A Thesis Submitted for the Degree of PhD at the University of Warwick

Library Declaration and Deposit Agreement

1. STUDENT DETAILS

Please complete the following:

Full name: ……………………………………………………………………………………………

University ID number: ………………………………………………………………………………

2. THESIS DEPOSIT

2.1 I understand that under my registration at the University, I am required to deposit my thesis with the University in BOTH hard copy and in digital format. The digital version should normally be saved as a single pdf file.

2.2 The hard copy will be housed in the University Library. The digital version will be deposited in the University's Institutional Repository (WRAP). Unless otherwise indicated (see 2.3 below) this will be made openly accessible on the Internet and will be supplied to the British Library to be made available online via its Electronic Theses Online Service (EThOS) service.
[At present, theses submitted for a Master's degree by Research (MA, MSc, LLM, MS or MMedSci) are not being deposited in WRAP and not being made available via EthOS. This may change in future.]

2.3 In exceptional circumstances, the Chair of the Board of Graduate Studies may grant permission for an embargo to be placed on public access to the hard copy thesis for a limited period. It is also possible to apply separately for an embargo on the digital version. (Further information is available in the *Guide to Examinations for Higher Degrees by Research*.)

2.4 *If you are depositing a thesis for a Master's degree by Research, please complete section (a) below. For all other research degrees, please complete both sections (a) and (b) below:*

(a) Hard Copy

I hereby deposit a hard copy of my thesis in the University Library to be made publicly available to readers (please delete as appropriate) EITHER immediately OR after an embargo period of ……..................... months/years as agreed by the Chair of the Board of Graduate Studies.

I agree that my thesis may be photocopied. YES / NO (*Please delete as appropriate*)

(b) Digital Copy

I hereby deposit a digital copy of my thesis to be held in WRAP and made available via EThOS.

Please choose one of the following options:

EITHER My thesis can be made publicly available online. YES / NO (*Please delete as appropriate*)

OR My thesis can be made publicly available only after…..[date] (Please give date)
YES / NO (*Please delete as appropriate*)

OR My full thesis cannot be made publicly available online but I am submitting a separately identified additional, abridged version that can be made available online.
YES / NO (*Please delete as appropriate*)

OR My thesis cannot be made publicly available online. YES / NO (*Please delete as appropriate*)

3. GRANTING OF NON-EXCLUSIVE RIGHTS

Whether I deposit my Work personally or through an assistant or other agent, I agree to the following:

Rights granted to the University of Warwick and the British Library and the user of the thesis through this agreement are non-exclusive. I retain all rights in the thesis in its present version or future versions. I agree that the institutional repository administrators and the British Library or their agents may, without changing content, digitise and migrate the thesis to any medium or format for the purpose of future preservation and accessibility.

4. DECLARATIONS

(a) I DECLARE THAT:

- I am the author and owner of the copyright in the thesis and/or I have the authority of the authors and owners of the copyright in the thesis to make this agreement. Reproduction of any part of this thesis for teaching or in academic or other forms of publication is subject to the normal limitations on the use of copyrighted materials and to the proper and full acknowledgement of its source.

- The digital version of the thesis I am supplying is the same version as the final, hard-bound copy submitted in completion of my degree, once any minor corrections have been completed.

- I have exercised reasonable care to ensure that the thesis is original, and does not to the best of my knowledge break any UK law or other Intellectual Property Right, or contain any confidential material.

- I understand that, through the medium of the Internet, files will be available to automated agents, and may be searched and copied by, for example, text mining and plagiarism detection software.

(b) IF I HAVE AGREED (in Section 2 above) TO MAKE MY THESIS PUBLICLY AVAILABLE DIGITALLY, I ALSO DECLARE THAT:

- I grant the University of Warwick and the British Library a licence to make available on the Internet the thesis in digitised format through the Institutional Repository and through the British Library via the EThOS service.

- If my thesis does include any substantial subsidiary material owned by third-party copyright holders, I have sought and obtained permission to include it in any version of my thesis available in digital format and that this permission encompasses the rights that I have granted to the University of Warwick and to the British Library.

5. LEGAL INFRINGEMENTS

I understand that neither the University of Warwick nor the British Library have any obligation to take legal action on behalf of myself, or other rights holders, in the event of infringement of intellectual property rights, breach of contract or of any other right, in the thesis.

Please sign this agreement and return it to the Graduate School Office when you submit your thesis.

Student's signature: ....…… Date: ....

Materials and Methods for Microstereolithography

by

Christopher Philip Purssell MEng (Hons)

Submitted in fulfilment of the requirements

for the degree of Doctor of Philosophy

to the

University of Warwick

School of Engineering

June 2012

Contents

List of Figures

List of Tables

Acknowledgements

I would like to thank Dr. James Covington and Dr Duncan Billson for their support, guidance and the lending of their invaluable expertise throughout the course of my PhD. I would also like to acknowledge the EPSRC (Engineering and Physical Sciences Research Council) for their funding.

I would like express my gratitude to my friend and colleague, Dr. Simon Leigh for keeping the lab a lively place and for his guidance on all things chemistry related. Thanks are also due to Frank Courtney, Ian Griffith and the rest of the technicians and support staff whose knowledge and assistance is always greatly appreciated.

I would also like to thank all my other friends, family and colleagues, particularly, Helen, Max, Matt, Phil, Charley and Fauzan for their support, encouragement and willingness to lend a hand when needed. Also deserving of thanks are Allard, Nigel, Oli, Ali, Louis, Kevin and the other metagrobologists for giving me an excuse to take a break every once in a while.

Finally, I would like to thank my parents for their continued love and support.

Declaration

This thesis is presented in accordance with the regulations for the degree of Doctor of Philosophy. The work described in this thesis is entirely original and my own, except where stated otherwise. Parts of this work have been published in scientific journals and presented at international conferences as listed below:

Journal Papers

C.P. Purssell, S.J. Leigh, M. Thomas, D.R. Billson, D.A. Hutchins, **Microstereolithography for Fabrication of Devices for Ultrasonic NDE Applications**, Ultrasonics (2012), Submitted for peer review.

S.J. Leigh, C.P. Purssell, J. Bowen, D.A. Hutchins, J.A. Covington, D.R. Billson, **A miniature flow sensor fabricated by micro-stereolithography employing a magnetite/acrylic nanocomposite resin**, Sensors and Actuators A: Physical 168 (2011) 66–71.

S.J. Leigh, J. Bowen, C.P. Purssell, J.A. Covington, D.R. Billson and D.A. Hutchins, **Rapid Manufacture of Monolithic Micro-Actuated Forceps Inspired by Echinoderm Pedicellariae**, Bioinspiration & Biomimetics (2012), Bioinspiration & Biomimetics 7 (2012) 044001.

D. Cheneler, J. Bowen, S.J. Leigh, C.P. Purssell, D.R. Billson, D.A. Hutchins, M.C.L. Ward, **Fabrication and analysis of cylindrical resin AFM microcantilevers**, Ultramicroscopy 111 (2011) 1214–1223.

S.J. Leigh, R.J. Bradley, C.P. Purssell, D.R. Billson, D.A. Hutchins, **A simple, low-cost conductive composite material for 3D printing of electronic sensors**, PLoS ONE (2012), Submitted for peer review.

Conference Papers

D.R. Billson, C.P. Purssell, S.J. Leigh, D.A. Hutchins, **Rapid Prototyping technologies for ultrasonic beam focussing in NDE**, 2011 IEEE International Ultrasonics Symposium Proceedings 2472-2474.

Summary

There is an increasing requirement to fabricate ever smaller components and micro-devices and incorporate them within all aspects of our lives. From a Wii controller to a car airbag, micro-technology is employed in a huge spectrum of applications. Within process control and sample analysis, micro-components are making a significant impact, driven by the desire to use smaller volumes, lower concentrations, less reagent, or simply to make the process quicker or cheaper. Currently, methods of fabrication for such devices are based predominantly on silicon processing techniques. While these techniques are suitable for mass manufacture / high volume applications, there are a number of disadvantages for situations requiring lower volumes or where the end system is continually evolving – such as for research applications. The primary drawbacks are cost, turnaround time and the requirement for expensive processing facilities. However, for these situations, additive layer manufacture presents huge promise as an alternative fabrication technology.

The field of additive layer manufacture has advanced greatly since its inception 25 years ago. While such technologies are still primarily focused on the field of rapid prototyping of purely mechanical structures, it is clear that their full potential is yet to be realised. This is particularly the case for stereolithography and microstereolithography, the latter of which provides the capability to create complex, true 3D structures (as opposed to pseudo 3D/extruded 2D of silicon techniques), measureable on the micron scale. This thesis shows that microstereolithography has the potential to become an alternative fabrication method for functional micro-devices and structures. This is due to the simplicity of its single-step fabrication process and the significant time/cost savings it presents. Therefore, making it an affordable technique for low volume production where a fast turnaround is required. However, the lack of functional materials compatible with microstereolithography, and hence the lack of examples of the technology being used to produce active components, currently limits it in this respect.

This project therefore focused on exploring the possibilities of using microstereolithography as an alternative to traditional silicon based techniques for the direct fabrication of functional micro-devices and sensors. This was achieved through the development of a number of microstereolithography compatible, novel materials, methods and applications. Here, presented for the first time are both conductive and magnetic composite photopolymers compatible with microstereolithography technology. The materials were developed with the use of a custom built, constrained surface system using a parallel projection method. The system used LED technology as a novel exposure source, tuned to the developed materials in an attempt to gain extra control over the curing process and hence achieve higher quality components.

These materials were characterised and then used to fabricate exemplar sensing devices using microstereolithography – a method not previously used for creating such devices. Microfluidic flow sensing devices were used to demonstrate the practical application of the magnetic material. One of which, a lab-on-chip type device, was demonstrated to have a working range of 5 to 70 ml/min when tested with a liquid medium. Similarly, a practical application of the conductive material was shown through the fabrication of MSL-printed conductometirc vapour sensors. The sensors showed favourable characteristics working in range of humidites (up to 50% RH) and temperatures (up to 70°C). The sensors also demonstrated a degree of selectivity to different analyte vapours. Finally, the technology was demonstrated as a feasible method of fabricating ultrasonic beam forming apparatus. Acoustic testing of a range of materials also suggested that the composite metal materials could be used to further improve performance.

The novel materials and techniques investigated, along with the exemplar devices produced, demonstrate further abilities and a wider range of applications than has been demonstrated with this technology to date. It is hoped that this research will lead to wider use of the technology and encourage further advances in the field of microstereolithography.

Abbreviations

ABS - Acrylonitrile Butadiene Styrene

ADC - Analog to Digital Converter

ALM - Additive Layer Manufacture

ALT - Additive Layer Technology

AMR - Anisotropic Magneto-Resistive

API - Application Programming Interface

DLP - Digital Light Processing

DMD - Digital Mico-Mirror Device

DSP - Digital Signal Processing

FDM - Fused Deposition Modelling

GC - Gas Chromatography

GPIB - General Purpose Interface Bus

IC - Integrated Circuit

ICP - Intrinsically Conductive Polymer

LCD - Liquid Crystal Display

LED - Light Emitting Diode

MEMS - Microelectromechanical System

MS - Mass Spectrometry

MSL - Microstereolighography

NDE - Non-Destructive Evaluation

NIR - Near Infrared

RM - Rapid Manufacture

RP - Rapid Prototyping

PCL - Poly Caprolactone

PLA - Poly (lactic acid)

PMMA - Poly (methyl methacrylate)

PNG - Portable Network Graphics

PTFE - Poly (tetrafluoro ethylene)

PVA - Poly (vinyl acetate)

PVP - Poly (vinyl pyrrolidone)

RFID - Radio-Frequency Identification

SFF - Solid Freeform Fabrication

SL - Stereolithography

STL - Standard Tessellation Language

USB - Universal Serial Bus

UV - Ultraviolet

VOC - Volatile Organic Compound

Chapter 1

1 Introduction

Microstereolithography is an advanced fabrication technology capable of creating a wide variety of micro-devices and structures. It is predominantly thought of as a rapid prototyping technology. However, it has enormous potential as a manufacturing method, but is currently held back due to a lack of functional materials and innovative examples of it uses and methods.

This chapter begins by describing some existing manufacture and fabrication methods. Next, an overview of additive layer manufacturing techniques and its advantages are presented. The later sections detail the aims and objectives of the research undertaken. Finally, there is a thesis outline detailing the contents of this thesis.

1.1 History of Manufacturing

Human's ability to design and manufacture complex tools has been a major distinction to the rest the animal kingdom. Archaeological research [1] has shown the use of tools by humans as far back as the ~2.5 million years ago, with the first evidence of manufacturing at ~1.76 million years ago, the "Acheulian". Throughout the ages, man has continued to discover new materials such as metals, and developed ways to utilise their properties. A huge leap was made during the industrial revolution where there was a large shift from manual labour to machine-based manufacturing. Ever since then, scientists and engineers have been striving to push the boundaries of technology in order to make things smaller, faster, lighter, and more efficient. Arguably one of the most significant developments in recent time is the use of silicon and its associated technologies and processes.

1.2 Microfabrication

There is a continuous drive in the fields of engineering and manufacture to produce ever smaller and more compact devices and systems. This is particularly important in the areas of biological synthesis, environmental monitoring and medical diagnosis. All of these demand either smaller sample volumes or lower concentrations. Therefore, the main reasons behind wanting to fabricate such micromechanical and microelectronic devices are to enable the processing of increasingly smaller sample volumes, or use less reagent material. Either of which can reduce running costs or increase the process speed. Indeed, this is also the driving force behind lab-on-chip devices, which are able to provide increasingly more integrated and compact solutions, that ultimately results in more efficient systems.

1.3 Microfabrication Methods

There are currently a variety of methods and techniques available to engineers to fabricate components on virtually any scale. Traditional manufacture and machining methods are generally forms of subtractive manufacture. This involves beginning the fabrication process with one or more pieces bulk raw material and producing the desired component by removing material from the bulk by drilling, milling, cutting, etc. The removed material is considered as waste and is either disposed or recycled. While these traditional machining techniques have been developed and adapted to increase precision and resolution, the requirements for micromechanical and microelectronic devices tend to be beyond the capabilities of such techniques. Fabrication of micro-devices and structures therefore commonly involve some form of silicon/micromachining based fabrication step.

This can be either for fabrication of the entire device or for one or more of the component parts.

In general, the term “micromachining” is used to describe a method of creating features on a substrate that can be measured in micrometres. The practice initially came about through the microelectronics industry as a means of creating mechanical microstructures such as beams, cantilevers, channels, springs etc either in, or on top of the silicon substrate [2]. However, silicon micromachining is a multi-step, multi-process fabrication technique, requiring a large range of expensive equipment, and depends almost exclusively on the patterning and subsequent developing of a photoresist material on top of a substrate.

The patterning is achieved through the use of a glass mask, selectively coated in a light-blocking material (chromium is a common choice), which is itself created using a lithography technique (by e-beam). Each mask can contain hundreds, even thousands of component patterns. The mask is used to create the two dimensional patterns in the photoresist, which is then developed. The developed photoresist is then used as a mask for the next step of the process, for which there are two options. In the case of bulk micromachining, the mask is used to define areas of the substrate to be etched. The etching process can either be performed chemically (known as “wet etching”), or by a plasma technique (known as “dry etching”). For surface micromachining, instead of modifying the substrate, the mask is used to define area of the substrate where a secondary material it to be deposited. These techniques can also be applied to other substrates too, such as ceramics.

Due to their widespread use in microelectronics, such silicon based fabrication techniques are generally well understood, and are therefore often considered as the “go-to” techniques for fabrication of micro-devices and structures. While such technologies are clearly well suited to high volume / mass manufacture applications such as integrated circuit (IC) manufacture, large numbers of devices are not always required. Indeed, when low volumes of devices are required, such as in a development or research environment, or where the expected device lifetime is such that they can be considered disposable, such processes still present a number of drawbacks.

Whether the fabrication is done in-house or externally, two of the major factors are cost of production and turnaround time due to the (often complex) multi-step nature of the process. Indeed the baking steps required for processing the resist can, on their own, take a number of hours. If the fabrication were to be done in-house then there are added considerations such as the requirement for expensive specialist equipment, handling of corrosive chemicals, and again the cost in man-hours to oversee the process. Therefore, due to the costs, and time involved in getting a design from idea to physical component it is imperative that the design is correct first time. If the design needs modifying because it is wrong or because it is unsuitable for the next iteration of the system design, then the process must be started over again. This rapidly becomes an expensive route though, as the masks alone can cost many hundreds of pounds to produce. These considerations can therefore often make this approach financially prohibitive for small scale operations.

As such, it is therefore felt that for situations where a relatively low volume of such functional micro-components are required at an affordable cost, an alternative method of fabrication is required. However, one advantage silicon based processing has over other technologies is the ability to create devices that have different functional layers (e.g. conductive) and embedded functional components. Any alternate technology to silicon based processing will be require to have the same functionality. It is, however, believed that a potential solution may lie in the use of additive layer manufacture (ALM) technologies.

1.4 Additive Layer Manufacture

Additive layer manufacturing techniques were initially developed as a rapid prototyping technique, and are commonly used in a number of industries, the largest being the automotive industry. In recent years, there has been increasing interest and development in the use of these technologies (sometimes also referred to as solid freeform fabrication (SFF) [3]). ALM is an interesting technology due its similarities with silicon technology (in terms of its layer approach to fabrication) that could be applied to the production of parts, but also offers a number of advantages over the use of silicon techniques. Initially, the most obvious advantage is ALM's ability to easily fabricate complex 3D structures. While this can be achieved with silicon processes it is difficult to do and components are instead restricted to having simple 2D geometry, or at best, a few superimposed layers.

In addition to not requiring expensive cleanroom facilities, the single-process, self contained fabrication systems require minimal chemical materials which present significantly less hazards that those of other micro-fabrication technologies. Due to the nature of their single-process, fully automated method of fabrication, ALM technologies also present a significantly more rapid method of manufacture (3-5 mm per hour), therefore dramatically speeding up the turnaround time of components for an iterative development process. While it could be argued that some ALM technologies require a certain amount of post-processing, effectively making it a multi-step process, the time and equipment required to perform these steps makes the argument largely irrelevant.

The main advantages of ALM over silicon based processing lie in the cost of the production of components. This provides the design flexibility, which ultimately makes it a far less financially prohibitive approach and enables the creation of components that are tuned to specific applications. It is therefore felt that ALM presents great opportunities that, to date, are yet to be fully explored.

1.5 The ALM Process

The ALM processes begins by using a computer aided design (CAD) package to create a 3D model of the intended component(s). The 3D CAD model is then sliced into a set of 2D cross-sections, each representing the component at a specific layer or z-height. The 2D cross-sections are then used by the ALM system to sequentially fabricate the layers one on top of another. Figure 1.1 gives a basic illustration of the concept. Due to the nature of the process, these fabrication methods usually generate little or no waste as material is only added, rather than being removed.

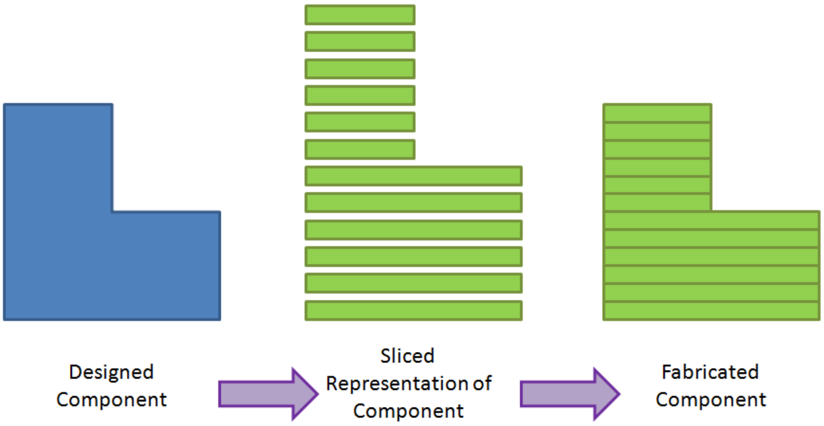

Figure 1.1 – Diagram illustrating the design to fabricated component flow for additive layer technology processes

1.6 ALM Methods

There is a wide variety of ALM systems currently available, each of which has its own advantages and disadvantages for different applications. They cover systems that can produce components ranging from headlight assemblies and toilet seats to microfluidic flow cells. All ALM systems can be further classified under one of three groups, based on their primary method of object generation: solid based, powder based, or liquid based.

1.6.1 Solid Based Fabrication Methods

Solid based methods are those that use a pre-formed, solid, bulk material as the primary method of fabrication. The two most notable methods solid-based systems are laminated object manufacture (LOM) and fused deposition modelling (FDM).

LOM, or layered object manufacture (with other names such as Plastic Sheet Lamination (PSL) and Paper Lamination Technology (PLT) given for more specific versions of the technology), builds up the model layers by using laminar sheets of material. Each layer is individually patterned using either a CO_2 laser beam, steered using galvanic mirrors or a blade. Before a layer is cut, adhesive is applied to the top of the previous layer so that the layers of the model are bonded. In theory, any laminar sheet material can be used providing it has a regular thickness and can be adhered. The excess material in the laminar sheets is not removed during fabrication. This means that the method cannot be used to fabricate hollow objects; however, the excess material is used as a support structure during fabrication. At the end of the fabrication process the excess material needs to be manually removed. Typical build resolutions for such systems are 100 µm in XY while the layer thickness is dependent on the thickness of the laminate used; 100-200 µm is typical.

FDM systems create layers by vectoring the outline and infill space of the object using an extruded thermoplastic material. A filament of the material (such as ABS, PLA (polylactic acid), or PCL (polycaprolactone)) with greater diameter than the desired extruded "string" is forced through a heated nozzle (usually between 150°C and 250°C depending on the material), which is moved around the build area using an XY stage (sometimes the extruder head is fixed and the build base is moved instead). Due to the means in which the material is extruded they are also often colloquially called "toothpaste machines". The potential build envelope for FDM systems is only limited by the size of motion carriages that hold the head, although dimensions on the order of 300 mm are typical. The resolution of FDM systems is limited by the diameter of the extruded material; therefore, the resolution in all three axes is around 100 µm to 200 µm. Due to the nature of the in-fill method, it is difficult to generate solid layers, as such, components fabricated using FDM have a degree of porosity.

1.6.2 Powder Based Fabrication Methods

Powder based fabrication methods are some of the most commonly used in industry due to self supporting nature of the fabrication process being able to produce large components with uneven, undulating surfaces – such as prototypes for car headlight assemblies. Selective laser sintering (SLS) and 3D printing (3DP) are the most common example of the technology.

In order to create layers, SLS begins by spreading a thin layer of powdered material (equal to one layer thickness) on top of the previous layer. A laser is then used to selectively sinter the defined areas within each layer. The non-sintered material is left in the build area and can therefore be used as a support structure. Similar methods which are derivatives of SLS are electron beam melting (EBM), which uses an electron beam in place of a laser, selective laser melting (SLM), which fills the fabrication chamber with an inert gas whilst building, and selective mask sintering (SMS) which uses a parallel irradiation method and masks that are generated by patterning toner onto a glass plate. The resolution of SLS systems is on the order of 0.5 mm.

In a similar manner to SLS, 3DP constructs each layer by spreading a layer of the powdered material on top of the previous. However, instead of melting or sintering the material, a print head (similar to those found in ink-jet printers) deposits a binding material onto the powder surface. The binder can also include inks that allow full colour models to be generated in one fabrication process. The resolution of such systems can be down to around 90 µm in layer thickness and up to 600 dpi (~45 µm) in XY.

1.6.3 Liquid Based Fabrication Methods

Liquid based fabrication methods are those that rely on the solidification of a photosensitive liquid polymer. There are a number of systems that use this principle to fabricate components, the most well-known of these is stereolithography apparatus (SLA). SLA is generally considered as being one of the first, if not the first, method of ALM. The earliest reference found was from a paper published in 1981 by Hideo Kodama [4] where the process was first outlined. Six years later, in 1987, 3D Systems (USA) produced the first commercial system [2, 5].

Traditional SLA systems operate by positioning a flat build platform in a vat of resin material such that one layer thickness material remains between the free surface of the material and the previously solidified layers. The layer is created by selectively manipulating light in order to polymerise a photocurable liquid polymer resin into a solid polymer in the desired pattern. This can achieved either by using galvanic mirrors to steer a laser beam (UV [6] or IR [7]), by employing a dynamic mask system [8]. Once the material is cured, it remains solid and will not re-dissolve in the monomer [9]. SL systems can achieve layer thicknesses of 100 μm with XY resolutions of 50 μm. Microstereolithography (MSL or μSL) is a form of SL that can be used to fabricate parts on the micron scale and therefore presents a possible alternative to silicon based fabrication methods. Depending on the system, layer thicknesses of 20 μm can be achieved with an XY resolution also down to 15 μm. The process is discussed in greater detail in the following chapter.

There is a further liquid based method, rather confusingly also referred to as 3D printing. This method again uses ink-jet technology to deposit measured amounts of material in the desired 2D pattern for each layer. The material is then immediately cured using a UV light source, which is attached to the print head. The systems employing this technology can have large build envelopes - up to 490mm x 390mm x 200 mm for the Eden 500v (Objet Ltd, USA) while still maintaining high resolutions - 50 μm in XY with 20 μm layer thickness.

	Method	Example System	Material(s)	xy Resolution (um)	z Resolution (um)	Typical Build Envelope (XYZ in mm)	Typical System Cost	Typical Material Cost	Surface Finish	Speed
LOM	Solid	SD300 (Solido Ltd, USA)	Paper / Plastic sheet	150	100	200 x 200 x 150	~$10000	$300 per kit	Poor	Average
FDM	Solid	Dimension Elite (Stratasys Inc, USA)	Thermoplastic Fillament	150	150	250 x 250 x 300	$3000 to $100000	$60 per kg	Average	Poor
SLS	Powder	Sinterstarion Pro (3D Systems Inc, USA)	Metals / Polymers	500	500	550 x 550 x 500	$200000+	$50 to $250 per kg	Good	Poor
3DP	Powder	Zprinter 850 (Zcorp/3D Systems Inc, USA)	Plaster composite / Elastomer	45	90	500 x 400 x 250	$15000+	$0.20 per cm^3	Average	Excellent
SLA	Liquid	ProJet 6000 (3D Systems Inc, USA)	Photopolymer	50	100	300 x 300 x 300	$75000+	$380 per litre	Very Good	Average
MSL	Liquid	Perfactory Mini (EnvisionTec GmbH, Germany)	Photopolymer	15	20	50 x 50 x 200	$20000+	$380 per litre	Excellent	Average
3DP	Liquid	Objet30 (Objet Ltd, USA)	Jetted Photopolymer	50	20	500 x 400 x 200	$20000+	$80 per kg $30 per kg -support material	Very Good	Good

	Post Processing	Advantages	Disadvantages
LOM	manual removing of excess material	cheap to run / no hazardous materials	large amount of waste / poor surface finish
FDM	removal of support structures (if used) / sanding	cheap to run / no harardous materials	slow / poor surface finish
SLS	particle blasting / sanding	no supporst required / minimal post processing	poor surface finish
3DP	air blasting to remove excess powder / sanding	fast / unused powder can be reused / multi coloured	weak parts / poor surface finish
SLA	removal of support structures (if used) / removal of excess material with solvent	large build envelope / good resolution / good surface finish	requires post-process cleaning and post curing
MSL	removal of support structures (if used) / removal of excess material with solvent	excellent resolution / excellent surface finish	limited build envelopes / requires post-process cleaning and post curing
3DP	water jet to remove excess material	very good surface finish	materials must be ink-jet head compatible / water jet post porcessing can damage parts / cannot fabricate any overhanging structures without support material

Table 1.1 – Comparison of different ALM technologies

Table 1.1 shows a comparison of systems, a number of which show promise as a potential solution to the issue of affordable fabrication of functional devices. However, it is felt that stereolithography and in particular, microstereolithography, show particular promise as an alternative method to fabricate functional micro-devices and components with micro-structures. The use of its micro-scale manufacturing capabilities have already been demonstrated through its use in the jewellery industry for creating moulds for the casting of rings etc. However, commercial system manufacturers appear to be content with this, and the current range materials and methods limit its use to purely structural or mechanical components. Therefore there are a great number of materials covering these applications, some including ceramics/glass particles for increased strength, others being wax based aimed at casting applications.

The combination of advantages that MSL has over other ALM technologies, specifically its resolution combined with the ability to use low material volumes and incorporate secondary, possible functional components within the material (as demonstrated by the commercially available ceramic materials), make it ideal as an alternative to silicon processing. While some researchers have begun to demonstrate the potential uses of MSL in more engineering related applications, such as basic air coupled ultrasonic transducers [10, 11] and micro-mechanical bellows [12], it is difficult to find any that present the material itself providing functional significance in an application. One exception to this is where researchers have begun to explore its uses in the medical field, for generation of bone and tissue scaffolds [13-18]. As such, there is a need to expand the range of available materials through the development of novel, functional materials. By increasing the range of materials to include those with additional functional properties, introducing new ideas for methods of fabricating existing components, and creating additional exemplar components using this technology, it is felt that the advantages of MSL could become more clearly seen. It is felt that this would lead to further development and research in the area and ultimately provide an invaluable future technology as a possible alternative to more traditional techniques of micro-manufacture.

1.7 Research Objectives

The recent advances of microstereolithography techniques (discussed further in Chapter 2) have bought the technology to a point where micro-mechanical structures can be fabricated with relative ease. However, to date, research has focused primarily on improvements in resolution and the fabrication of structural components, thus there is a great need for development in materials and their uses in order to expand the applications of the technology.

The aims of this work are therefore to attempt to overcome some of the current limitations of the technology by exploring the envelope of possibilities for MSL such that the potential uses of microstereolithography covers a wider range of applications. This will be done through the development of a number of microstereolithography compatible, novel functional materials and methods to find out what is achievable. This project will also aim to demonstrate potential applications of microstereolithography through the fabrication of exemplar functional devices.

Investigations will be carried out into the feasibility of creating both composite magnetic and conductive materials compatible for use in MSL apparatus. The potential of using microstereolithography to fabricate functional micro-devices using the new material will be examined through the design and fabrication of exemplar microfluidic flow and chemoresistive vapour sensing devices. Additionally, the use of microstereolithography for the fabrication of ultrasonic devices for use in non-destructive evaluation applications will be investigated. The acoustic properties of materials developed as part of the project will then be compared to that of commercial materials in an attempt to identify methods of increasing performance.

It is hoped that the research conducted in this thesis will increase the capabilities, scope and awareness of microstereolithography technologies, such that it widens the range of possible applications and enables an increase of its future use for the affordable, direct, rapid manufacture of a greater range of functional micro-devices and sensors.

1.8 Thesis Outline

Chapter 2 covers in greater depth the different variants of microstereolithography systems, including the specific steps involved in the fabrication process and the curing mechanism of the materials. There is a particular focus on constrained surface systems using parallel exposure methods. A number of limitations of the technology along with points that should be considered when attempting to fabricate using MSL are also covered, along with example structures.

Chapter 3 details the design and manufacture of two custom microstereolithography systems. Developed as part of this project, they employed LED technology as an exposure source, with the second system focused on the fabrication of multi-material component fabrication. The systems developed were used in the later sections of this work.

Chapter 4 discusses the development and testing of a novel photocurable magnetic composite material for use in the development of 3D printed sensors and micro-actuators. This chapter also describes mechanical testing as well as investigating the new material’s response to an applied magnetic field. A method of detecting the material’s magnetic field once poled is also presented.

Chapter 5 builds on the work in Chapter 4 by exploring the use of the magnetic composite material in the fabrication of bespoke flow sensing devices aimed at micro-fluidic applications.

Chapter 6 covers the investigation of a novel photocurable conductive composite material. The mechanical effect of using different filler loading levels is discussed along with the effects on the material's electrical conductivity.

Chapter 7 describe the use of a modified version of the conductive composite material covered in Chapter 6. The material is used as a method for the direct printing of vapour sensing devices. The sensors are characterised by testing with a range of vapours under different environmental conditions.

Chapter 8 discusses the use of microstereolithography for the fabrication of components for use in ultrasonic immersion NDE applications. An exemplar device is designed and tested. Analysis of the acoustic properties of a range of microstereolithography compatible materials is undertaken with the aim of increasing the performance of future fabricated components.

Chapter 9 collates together the main developments and conclusions brought about by this work. Suggestions for areas of further work are also put forward.

1.9 References

[1] C.J. Lepre, H. Roche, D.V. Kent, S. Harmand, R.L. Quinn, J-P. Brugal, P-J. Texier, A. Lenoble, C.S. Feibel, An earlier origin for the Acheulian, Nature 466 (2011) 82-85

[2] J.W. Gardner, V.K. Varadan, O.O. Awadelkarim, Microsensors, MEMS and Smart Devices, John Wiley & Sons Ltd (2007)

[3] P.K. Wright, 3: Product Design, Computer Aided Design (CAD) and Solid Modeling, 21st Century Manufacture, Prentice-Hall Inc. (2001)

[4] H. Kodama, Automatic method for fabricating a three-dimensional plastic model with photo-hardening polymer, Review of Scientific Instruments 52 (1981) 1770-1773

[5] P.F. Jacobs, Rapid Prototyping and Manufacturing: Fundamentals of Stereolithography, McGraw-Hill (1992)

[6] J.J.A. Barrya, A.V. Evseevb, M.A. Markovb, C.E. Uptona, C.A. Scotchfordc, V.K. Popovb, S.M. Howdle, In vitro study of hydroxyapatite-based photocurable polymer composites prepared by laser stereolithography and supercritical fluid extraction, Acta Biomaterialia 4 (2008) 1603-1610

[7] A.L.M. Jardinia, R. Maciela, M.A.F. Scarparoa, S.R. Andradea, L.F.M. Moura, Improvement of the spatial resolution of prototypes using infrared laser stereolithography on thermosensitive resins, Journal of Materials Processing Technology 172 (2006) 104-109

[8] C. Sun, N. Fang, D.M. Wu, X. Zhang, Projection micro-stereolithography using digital micro-mirror dynamic mask, Sensors and Actuators A: Physical 121 (2005) 113-120

[9] A. Bertsch, S. Jiguet, P. Bernhard, P. Renaud, A. Pique, A.S. Holmes, D.B. Dimos, Microstereolithography: a review, Materials Research Society Symposium Proceedings 758 (2002) 3-15

[10] K.S. Ho, R.J. Bradley, D.R. Billson, D.A. Hutchins, Micro-stereolithography as a transducer design method, Ultrasonics 48 (2008) 1–5

[11] D.A. Hutchins, D.R. Billson, R.J. Bradley, K.S. Ho, Structural health monitoring using polymer-based capacitive micromachined ultrasonic transducers (CMUTs),Ultrasonics 51 (2011) 870–877

[12] H-W. Kang, I.H. Lee, D-W. Cho, Development of a micro-bellows actuator using micro-stereolithography technology, Microelectronic Engineering 83 (2006) 1201–1204

[13] T. Torii, M. Inada, S. Maruo, Three-Dimensional Molding Based on Microstereolithography Using Beta-Tricalcium Phosphate Slurry for the Production of Bioceramic Scaffolds, Japanese Journal of Applied Physics 50 (2011) 06GL15 1-5

[14] T.M. Secka, F.P.W. Melchelsb, J. Feijenb, D.W. Grijpma, Designed biodegradable hydrogel structures prepared by stereolithography using poly(ethylene glycol)/poly(d,l-lactide)-based resins, Journal of Controlled Release 148 (2010) 34–41

[15] R. Cave, The Development and Characterisation of Photopolymerisable Resins for the Fabrication of Tissue Regeneration Scaffolds [PhD Thesis], University of Warwick (2008)

[16] W-Y. Yeong, C-K. Chua, K-F. Leong, M. Chandrasekaran, Rapid prototyping in tissue engineering: challenges and potential, Trends in Biotechnology 22 (2004) 643-652

[17] Q. Liu, M.C. Leu, S.M. Schmitt, Rapid prototyping in dentistry: technology and application, The International Journal of Advanced Manufacturing Technology 29 (2006) 317-335

[18] S-J. Lee, H-W. Kang, J.K. Park, J-W. Rhie, S.K. Hahn, D-W. Cho, Application of microstereolithography in the development of three-dimensional cartilage regeneration scaffolds, Biomedical Microdevices 10 (2008) 1387-2176

Chapter 2 - Microstereolithography

2 Microstereolithography

2.1 Introduction

Stereolithography is an additive layer manufacture (ALM) fabrication technology that utilises a light source to selectively solidify a photopolymer material. It is based on the principle of creating a 3D model using CAD (Figure 2.1(a)) that is then imported into specialist software (Figure 2.1(b)) designed to slice the component into a series of equally thick parallel slices (Figure 2.1(c)). Each slice represents one X-Y layer cross-section of the component at a specific Z height. The component is fabricated by recreating the slices one on top of another until the component is formed [1] (Figure 2.1(d)). As previously mentioned, the process was first described by Hideo Kodama [2] in 1981. In 1986, Charles W. Hull and Raymond S. Freed founded 3D Systems Corporation (USA). In the following year, the company released the first commercial stereolithography system [3-5] as a means of rapidly producing components.

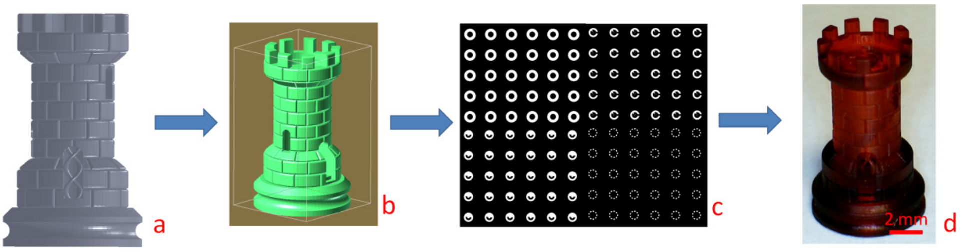

Figure 2.1 – Diagram illustrating the stereolithography process of taking (a) a CAD model, (b) transferring it to a slicer program, and (c) dividing the model into representative slice images, such that the model can be (d) recreated as a physical component

Microstereolithography is essentially the same as stereolithography with the exception that MSL systems can be used to fabricate components with features sizes down to the micrometer (10^{-6} m) scale (although more recently systems have been developed which can produce components with submicron resolution [6, 7]). Gardner et. Al. [4] states that in the micro version of the process, the laser beam (typically UV) is focused down to a 1 μm to 2 μm diameter spot whereas in the standard SL process the spot size is between 100 μm and 1000 μm. However, due to recent advances in the capabilities of SL systems, this definition is becoming less relevant as even the larger SL systems (such as 3D Systems iPro range) are capable of fabricating components with sub millimetre X-Y resolution and sub 200 μm layer thicknesses [8]. Therefore, the term is considered a description of the typical component size and as such is linked more to the build envelope of the system. As such, an SL system with a build envelope whose smallest dimension is around 100 mm or less is termed as a MSL system. There are 5 main commercial manufacturers of such systems:

- EnvisionTec GmbH (Germany) – Perfactory system range
- D-Mec Ltd. (Japan) – Acculas systems
- CMET Inc (Japan) – EQ-1 / RM-3000 / RM-6000 systems
- 3D Systems Inc. (USA) – iPro systems
- Rapid Shape GmbH (Germany) – S60 range

While previously, the technology has been predominantly synonymous with rapid prototyping, recent advances resulting in higher resolutions and falling system costs mean that it is increasingly being used as a method of rapid (or direct) manufacture for micro-devices [9] and other micro-feature components, such as jewellery.

This chapter provides background into the different variations of microstereolithography systems, focusing on the operation constrained surface systems utilising parallel mask projection, specifically using DLP technology. In addition, there is a brief discussion of the photopolymerisation process and overview of suitable materials. Finally, some considerations and limitations of the technology are discussed.

2.2 Types of SL and MSL

Stereolithography and Microstereolithography systems can come in three different forms depending on how the layers are presented for exposure; the more common are free surface and constrained surface systems. The third method is to fabricate the entire component within a vat of resin material. Throughout the range of systems there are also number of different exposure sources and fabrication techniques - serial exposure using lasers or parallel exposure using full layer masks using either liquid crystal display (LCD) modules or dynamic mirror devices (DMD). Table 2.1 shows some of the notable systems presented by other researchers. The following section explains further the differences between these various approaches.

Group	**Exposure Type**	**Type**	**Curing Method**	**Build Envelope**	**Resolution**	**Ref**
Farsari et al	Parallel	Free Surface	LCD, laser (351.1 nm)	50µm to 50 mm	1 x 1 x 50 µm	[10]
Kang et al	Parallel	Constrained Surface	DMD, UV lamp	14.6 x 10.9 mm	14 x 14 x 50 µm	[11]
Choi et al	Parallel	Free Surface	DMD, UV lamp (365 nm filter)	5.1 x 3.8 mm	5 x 5 x 1 µm	[12]
Choi et al	Vector	Free Surface	Laser (355 nm)	165.1 x 120.7 x 120.7 mm	not reported	[13]
Ikuta et al	Vector	In vat	Laser (442 nm)	~100 um3	~500 nm	[14]
Park et al	Parallel	Free Surface	DMD, lamp (visible)	not reported	2 x 2 x 2 µm	[15]
Kawata et al	Vector	In vat	2 Photon process	~10 µm3	~150 nm	[16]
Ikuta et al	Vector	Constrained Surface	Focused lamp	10 x 10 x 10 mm	1 µm (z)	[17]
Bertsch et al	Parallel	Free Surface	LCD, laser (515 nm)	not reported	~10 µm (z)	[18]
Devaux et al	Parallel	Free Surface	DMD, lamp (visible)	3 x 3 mm	20 x 20 x 20 µm	[19]

Table 2.1 – MSL systems presented by other researchers

2.2.1 Free Surface Systems

The original SL systems employed galvanic mirrors to direct ultraviolet lasers onto the top surface of a vat of photopolymer material. Such methods that cure the material on its top surface are more commonly referred to as the “free surface” methods [17, 20, 21]. Laser based systems selectively cure areas of the material by rastering the laser light on the resin’s surface. The build process is then as follows:

- A build platform that is suspended within the resin vat is positioned such that its surface is set below the surface of the material by one layer thickness - Figure 2.2(a).
- The layer image is then drawn/rastered onto the top surface of the material – Figure 2.2(b).
- The build platform is lowered such that there is again, one layer thickness between the top of the previously solidified layer and the surface of the resin material. – Figure 2.2(c).
- A levelling arm is then employed to level the resin surface – Figure 2.2 (d).
- The process is repeated until the component is built.

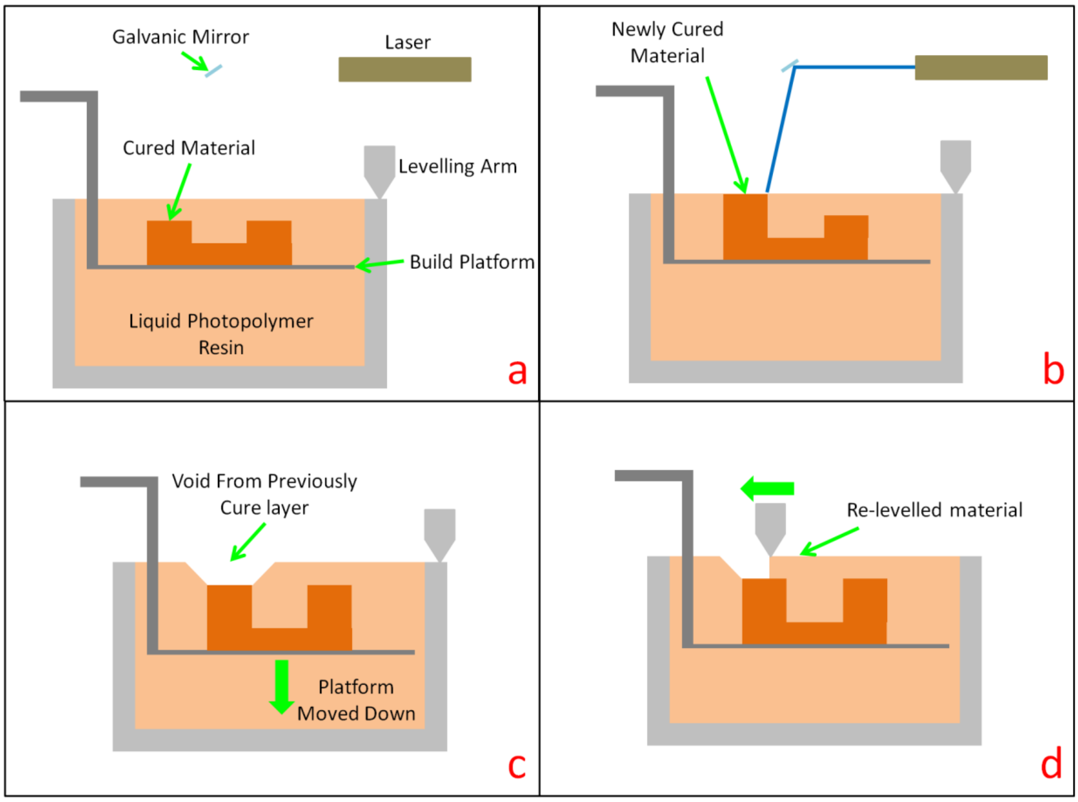

Figure 2.2 –Schematic diagram showing individual steps of a laser based, free surface stereolithography process. (a) 1 layer thickness is left between previously cured layer and surface of liquid material in resin vat, (b) a laser is used to photopolymerise the required pattern onto the surface of the resin material, (c) the build platform lower by 1 layer thickness, (d) the levelling arm recoats and levels the top surface of the material leaving a flat surface in preparation for the following layer

There are, however, a number of drawbacks to this type of system; the main two being the initial cost of the system (~£800,000 for 3D systems iPro 9000 XL) and the material cost (~£300 per litre). Due to the components being built within the resin vat, the system requires to be setup with a volume of material that is significantly greater than the final model volume. Additionally, the Z height of parts is limited not only to the depth of the vat itself but also to the quantity of material within the vat when the build process is started. There can also be inconsistencies in the spot profile of the laser depending on where on the resin surface the spot is directed to. Work by Deshmukh et al [22] shows that there can be as much at 10% variation in the peak intensity spot size when the spot position is off centre due to its elliptical profile. This can cause features towards the edges of components to be less defined and effectively have a lower resolution than features positioned directly below the scanning mirrors. However, the differences are generally so negligible that it is not considered to be a significant problem

An alternative, and increasingly popular method of exposure is to use parallel exposure. Here, instead of using a laser as an exposure light source to serially cure a series of lines, a mask is used with a wide angle exposure source such that all of the areas of a layer are exposed simultaneously [23]. The parallel exposure system is described in greater detail later in this chapter.

2.2.2 Two Photon / Dual Laser Stereolithography

Two less common forms of stereolithography employ “Two Photon” and “Dual Laser” based techniques [24] (sometimes also referred to as beam interference solidification (BIS) [25]). Neither method is currently available as a commercial system, and only a few research departments use them due to the cost of manufacture and maintenance required to keep the systems operational. Both systems utilise lasers in a serial fabrication process and both exclude the need to have a movable build platform. In both types of system the components are fabricated directly within the resin vat which therefore eliminates the need for support structures. Ordinarily, curing of the material in this manner would be impossible to achieve, however, both types of system employ techniques that allow for selective curing of a non-standard modified photopolymer within the vat.

The dual laser method uses two intersecting laser beams of differing frequency to cure the photopolymer. The first beam is used to excite the material into a reversible meta-stable state, the second intersecting beam then causes the meta-stable material to polymerise. However, as noted by Pham et al [25], there are no commercial applications for this method as there are still a number of unsolved technical problems including working around shadowed areas caused by previously built sections, inconsistent exposure intensity due to the light absorption of the material, along with diffraction of the beams making them hard to intersect [26].

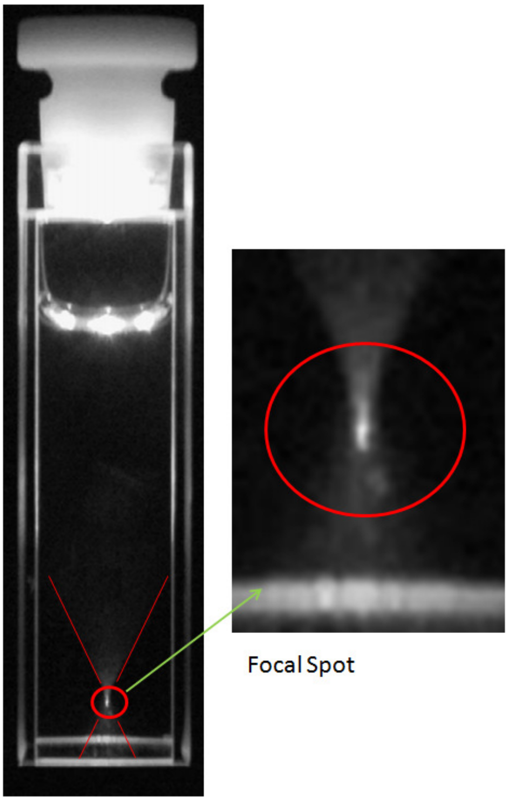

Figure 2.3 – A vial of fluorescent dye excited with NIR laser pulses demonstrating the selective curing of photopolymer in a 3D space (taken from Wu et al [27])

Two photon stereolithography, on the other hand, requires only one laser source to produce similar results. To achieve this, the wavelength of the laser is not of the correct wavelength to directly photopolymerise the resin - usually in the near infrared (NIR) region of the spectrum. Additionally, the beam is deliberately setup such that the beam only focuses at one point in the resin vat (Figure 2.3). At the focus of the beam the energy is sufficient to cause excitation of a fluorescent component within the resin, the secondary photon released from this excitation then causes the photo polymerisation of the material. The system can then cure material at any point within the 3D space of the resin vat by either altering the focal distance of the primary beam or more commonly, by moving the vat itself in 3D space by utilising an XYZ motion stage with sufficient resolution – this method is however much slower as movement of the vat must be sufficiently slow and smooth that any parts of the component already fabricated in the vat are not moved by sudden jolts or inertia (Figure 2.4). Groups such as Wu et al [27], Lee et al [28], and Sun et al [29] have all published extensive papers on two photon techniques, with Kawata et al [16] from the same group also publishing in Nature. All show great advances in achievable resolution for microstereolithography (Figure 2.5) with reported spatial resolutions of 120 nm to 200 nm. However, due to the custom materials required, and the difficulties associated with accurately positioning and focusing the primary laser, such systems are currently limited to research establishments.

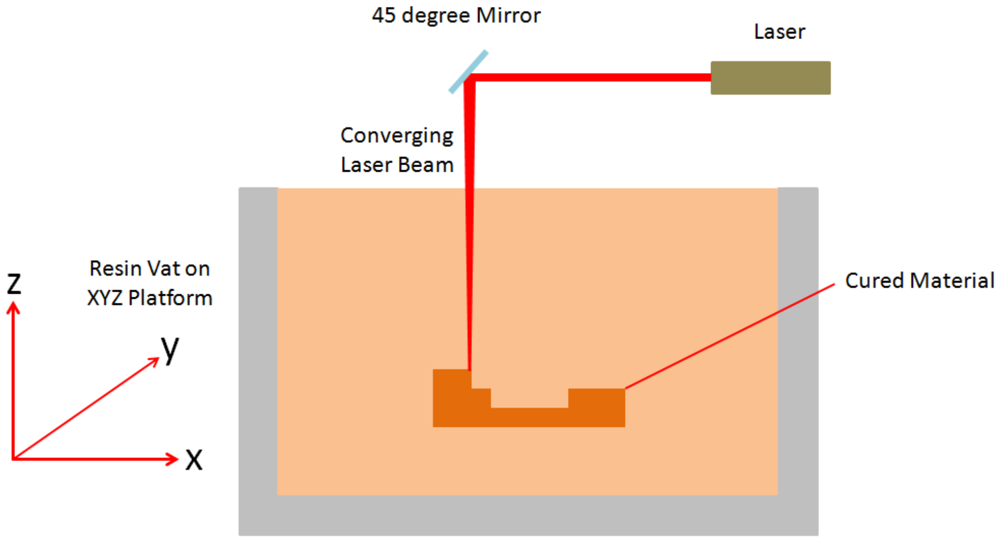

Figure 2.4 – Schematic diagram showing selective cutting method of two photon microstereolithography

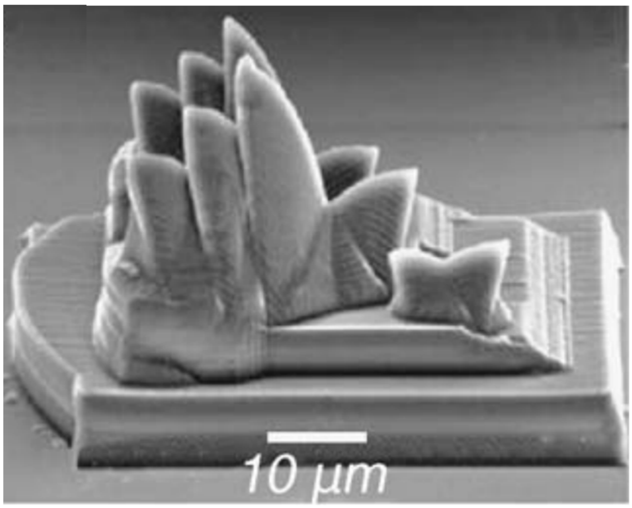

Figure 2.5 – A model of the Sydney Opera House fabricated using two photon microstereolithography (taken from Wu et al [27])

2.2.3 Constrained Surface Systems

The final technique of stereolithography apparatus is known as constrained surface systems. Such systems operate in a similar manner to free surface systems but instead of the exposure area being on the top, free, surface of the material, it is instead on the bottom of the material vat. In this case, the layer to be cured is constrained between the previously cured layer of material and the transparent base of the resin vat. The fabricated components are therefore built upside down vertically in the vat. As such, the depth of material in the vat is not required to be any deeper than a few mm, and in such systems the vat is more commonly referred to as a “resin tray”.

The build process for each layer begins by lowering the build platform into the resin such that there is one layer thickness remaining between the build platform and the bottom of the resin tray. There is then a short wait period (few seconds) to allow any trapped air bubbles within the space to escape before the exposure period. After the exposure, there is a further wait period followed by a peeling step; the peeing step can vary depending on the system. On systems with simple peel mechanisms the resin tray is held in a mechanism that allows the rear of the tray to raise by a few degrees while pivoting about the front edge. For this setup, the peel mechanism is then simply there to raise the build platform and allow the cured layers to peel from the surface of the resin tray. A more controlled method is to use an additional motion stage on the system to pull down the rear edge of the resin tray, which performs the peel. The build platform is then raised before the rear edge of the resin tray is raised again. Finally, the build platform lowers back into the resin such that one layer thickness is left between the surface of the previously built layer and the bottom of the resin tray. This process is repeated until the component is fully fabricated.

Although the exposure step is key to the curing the material, the levelling and peeling steps must also be well controlled in order to ensure the fabrication doesn’t fail. If the levelling speed is too great then air bubbles can become trapped in the exposure layer, causing unwanted voids in the component. Additionally, as the material is being compressed between the two flat surfaces of the base of the resin tray and the build platform, excess levelling speed can cause significant force to be required from the z-axis lowering the platform. When using viscous materials this force can become too great and so the platform fails to level properly, which causes either inconsistency in layer thicknesses, or causes the machine to detect an error and abort the build, or damage the motors of the machine itself.

More important than the levelling step is the peeling step. Here, if the peel is performed too quickly, then the force exerted on the component can cause it to pull away from the build platform; this become a greater problem as the height of the component increases. In order to prevent this happening, constrained surface systems tend to overexpose a number of the initial layers as this helps it to adhere to the glass build platform. In order to prevent the cured layer adhering to the base of the resin tray, the glass base of the tray is covered by a thin layer of silicon rubber. Conversely, if the system peels too slowly then the suction forces on the material can cause its components to separate. This is a particular issue with loaded composite materials (those which consist of a solid micro or nano particles homogenously mixed into the material) as the pumping effect of the repeated levelling and peeling causes the composite particles to fall out of suspension. Figure 2.6 illustrates the build process of a constrained surface system using a motorised peeling mechanism similar to that found in the Perfactory Mini systems [30] produced by EnvisionTec GmbH (Germany).

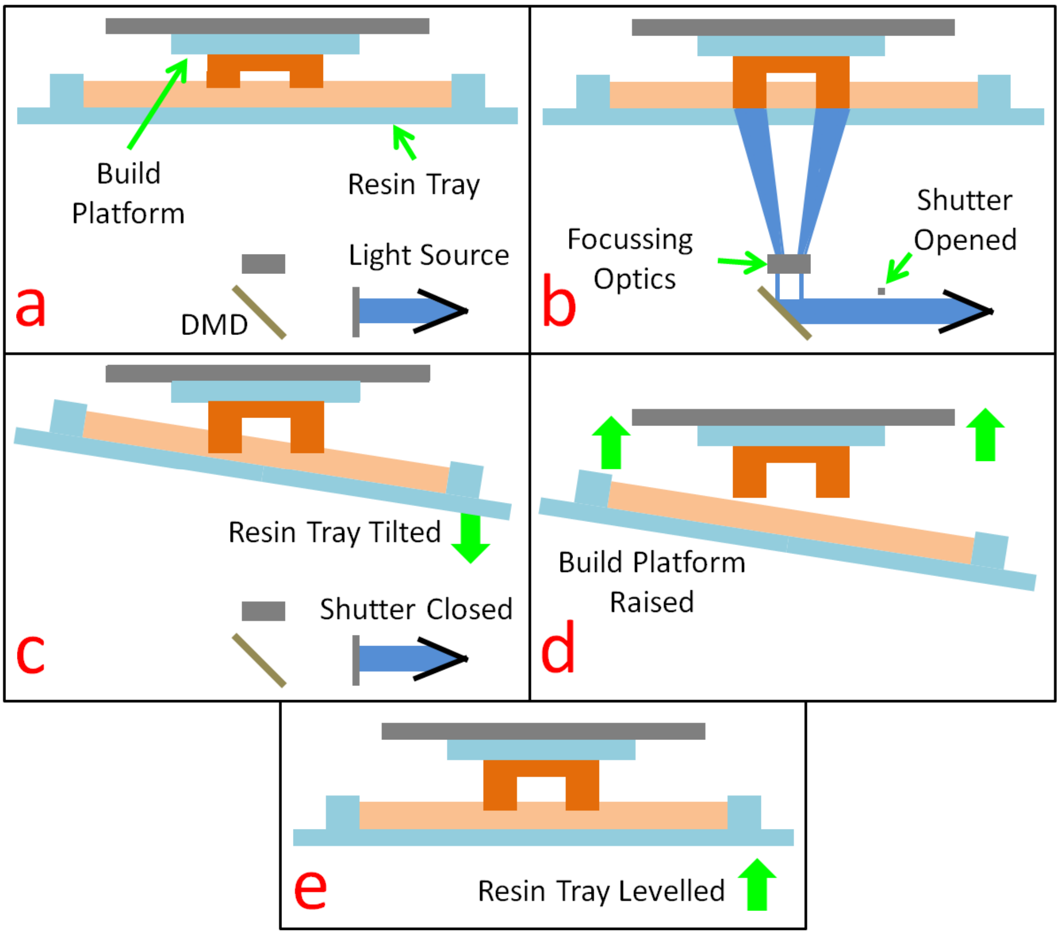

Figure 2.6 - Schematic diagram showing process steps for fabrication using constrained surface microstereolithography with parallel dynamic mask projection. (a) a gap of 1 layer thickness is left between the previously cured layer and the bottom of the resin tray, (b) the image is set on the dynamic mask and the exposure shutter is opened; curing the resin, (c) the front edge of the resin tray is lowered to peel the newly cured layer from the resin tray, (d) the build platform is raised by 1 layer thickness, (e) the resin tray is re-levelled ready for exposure of the following layer

The Microsensors and Bioelectronics Laboratory (MBL) within the School of Engineering has three EnvisionTec Perfactory systems, including a modified Perfactory

Mini D Multilens systems and Perfactory Desktop system (which employs the manual peel mechanism). Due to the known reliability, previous working knowledge of the operation of this type of MSL system, and the advantage of requiring smaller volumes of material than free surface methods, the work carried out in further chapters is based on the constrained surface approach using parallel exposure methods with dynamic mask technology, described below.

2.3 Parallel Exposure / Mask Projection Systems

Nakamoto et al [31] were some of the first researchers to describe the use of the mask projection method. In these early studies the method was used to fabricate high aspect ratio structures using a single fixed chrome pattern mask (i.e. the cross section through the component is in theory constant), a technique borrowed from the silicon processing world. Figure 2.7 shows one of the first examples.

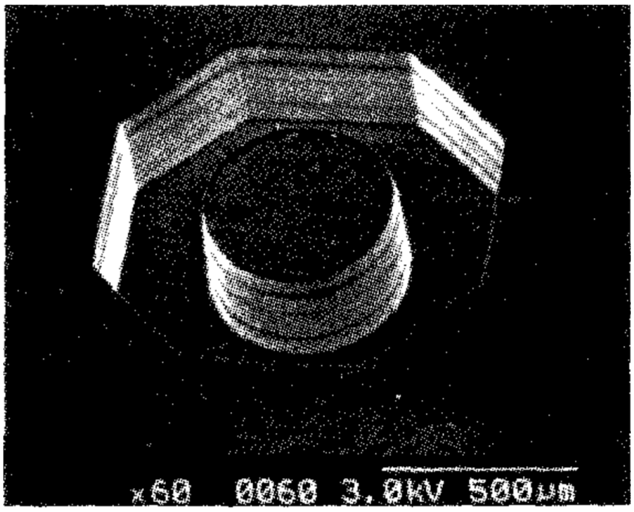

Figure 2.7 – A well micro structure fabricated using single mask parallel exposure method (taken from Nakamoto et al [31])

The key component in a parallel exposure system is the mask system [31]. As mentioned, parallel mask projection is a much faster method than serial scanning; however, for complex structures a large numbers of masks would be required. The fabrication of large numbers of masks is expensive (~£500 per mask) as well as time consuming. As such, systems using dynamic mask generators have become the standard method of mask generation in modern systems[32]. It is referred to as "dynamic" in order to distinguish it from the static chrome / glass mask typically used in silicon based fabrication processes.

By exposing complete layers in this parallel fashion, the fabrication time of a component (T_{BS} for a serial build method, T_{BP} for a parallel build method) can be dramatically decreased. The following equations are derived from analysis of the process steps for each method and describe the component build times for both exposure methods, where: N is the number of layers in the build, D_P is the peel distance of the build platform after each layer, S_L and S_P are the levelling speed of the platform in preparation for the following layer and the peel speed following an exposure of the layer respectively, T_{WL} and T_{WP} are the wait periods after levelling of the platform pre exposure and before peeling post exposure respectively, A_i is the area to be exposed on cross-sectional layer, R is the resolution of the system (pixels per unit area), and T_{EL} and T_{EP} are the exposure time for one layer (in the case of parallel exposure) or for one effective pixel (in the case of serial exposure) respectively.

$$T_{BS} = N\left(\frac{D_P}{S_L} + T_{WL} + \frac{D_P}{S_P} + T_{WP}\right) + \sum_{i=0}^{N} A_i R T_{EP} \tag{2.1}$$

$$T_{BP} = N\left(\frac{D_P}{S_L} + T_{WL} + \frac{D_P}{S_P} + T_{WP} + T_{EL}\right) \tag{2.2}$$

As the equations show, while the build time of the serial process is determined by the volume of the components to be built, the build time of the parallel process is determined only by the number of layers (and therefore the height) of the build. This means that providing there is sufficient space on the build platform, multiple components can be built simultaneously without any impact on the fabrication time.

While the name may suggest that mask generators are highly specialised pieces of equipment, in practice they are generally little more than modified digital presentation projectors. One of the first systems presented using dynamic masks was described in a paper by Bertsch et al[18]. Their described system operated by using a beam expander to first defocus the output of a laser. The defocused light was then passed through a liquid crystal display (LCD) module before using a beam reducer that then projected onto the resin surface. The pixel elements in the LCD were used to selectively block the exposure light from the laser, this allowed for easy manipulation of the exposure field such that each layer of the fabricated component could consist of a different pattern. Figure 2.8 shows a mechanical gear fabricated using this process. It is however noted in the same paper that there is a major disadvantage with using a laser as a light source. This is that the Gaussian distribution of its beam causes increased flux in the centre of the exposure field. The result of this is that there are features in the centre of the build that are over cured. To overcome this, the intensity of the source can be reduced; however this can then lead to under cure at the perimeter. The proposed solution was to use a lamp instead.

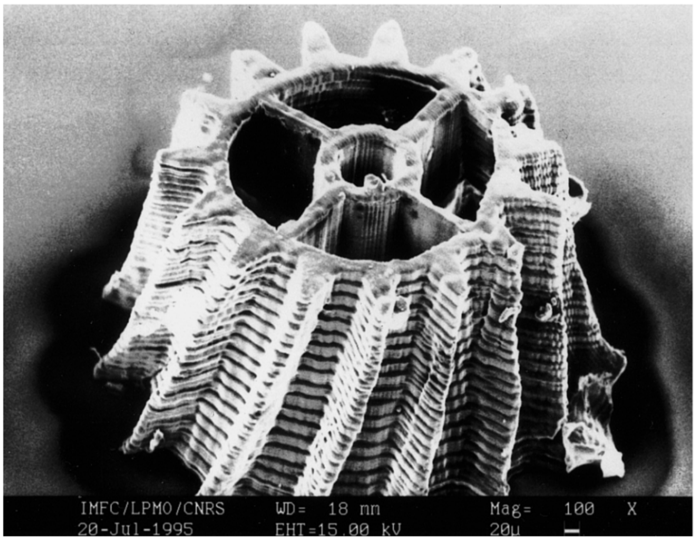

Figure 2.8 – A mechanical gear printed using an LCD dynamic mask with laser exposure source and laser (taken from Bertsch et al [18])

Even with the use of a bulb, it is not trivial to achieve an even light field across the exposure plane, additionally, using an LCD as a dynamic mask generator presents its own problems. Such issues include attenuation of the exposure light intensity (due to the beam having to transmit through the device), filtering of the wavelengths required for polymerisation (although some such as Monneret et al [33] have attempted to overcome this by working with materials outside of the LCDs opacity wavelengths), and diffraction effects. Due to these issues, digital light projection (DLP) systems took over as the generally favoured method of dynamic mask generation [11, 34]. DLP systems incorporate digital micromirror devices (DMDs) that operate on the principle of selective reflection of the exposure light to generate the masks. In 2005 Sun et al [35] presented a comparison (Table 2.2) of similar LCD and DMD based systems that illustrates a number of advantages of DMD technology. It showed that key parameters for MSL such as pitch size, UV compatibility and the contrast ratio between "on" and "off" pixels in the mask were all more favourable with DMD technology. DLP technology is discussed further in the following section.

	LCD	**DMD**
UV Compatibility	No	Yes
Modulation Efficiency	12.5% (transmission)	88% (reflection)
Pitch Size	26 µm x 24 µm	14 – 17 µm
Pixel Size	33 µm x 33 µm	13 – 16.2 µm
Filling Ratio	57%	91%
Contrast Ratio	100:1	350:1
Switching Speed	20 ms	20 µs

Table 2.2 – Comparison of key specifications between LCD and DMD based exposure systems (taken from Sun et al [35])

In a later paper, Bertsch et al [36] conducted further work that investigated the variation between edge profiles of layers created using the two patterning/irradiation methods. They highlight that vector-by-vector microstereolithography methods that employed a point laser as the irradiation source produced edges with curved profiles, whereas the dynamic mask methods were able to produce sharper edge features. Figure 2.9 shows the variation observed between the types of system.

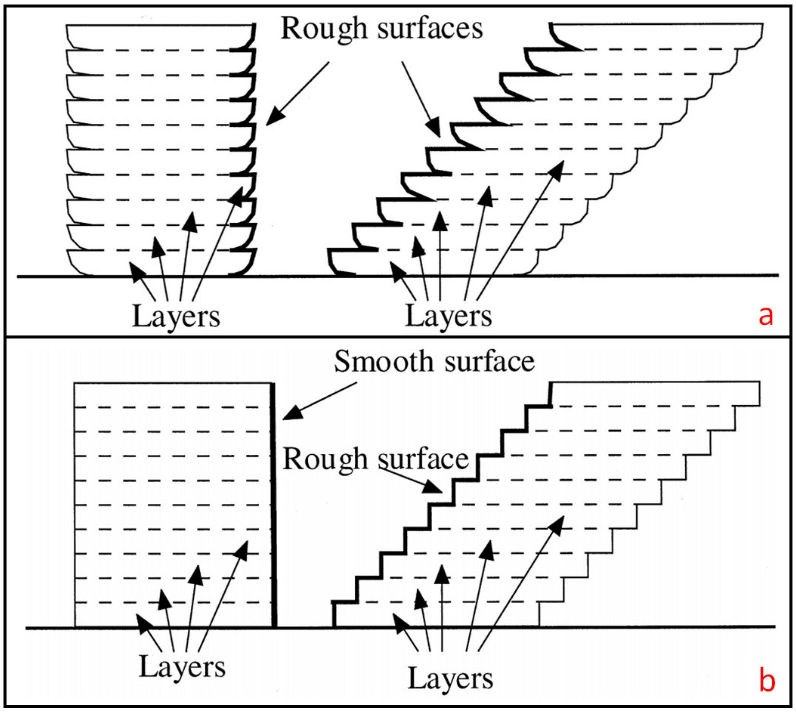

Figure 2.9 – Diagram showing differences in surface finish from (a) laser / vector-by-vector and (b) parallel / dynamic mask methods of irradiation (taken from Bertsch et al [36])

2.3.1 *Digital Light Projection (DLP) Technology*

Digital Light Processing Technology (DLP) is a parallel light manipulation technology that was originally invented by Dr. Larry Hornbeck and Dr. William Nelson while working for Texas Instruments in 1987 [37]. Their primary use is in conventional projectors used for rear projection televisions and office presentation displays. The key part of a DLP system is the digital micromirror device (DMD) which is, as the name suggests, a MEMS (microelectromechanical system) device consisting of a rectangular array of mirrors (Figure 2.10) each of which can be individually controlled using electrostatic attraction[38].

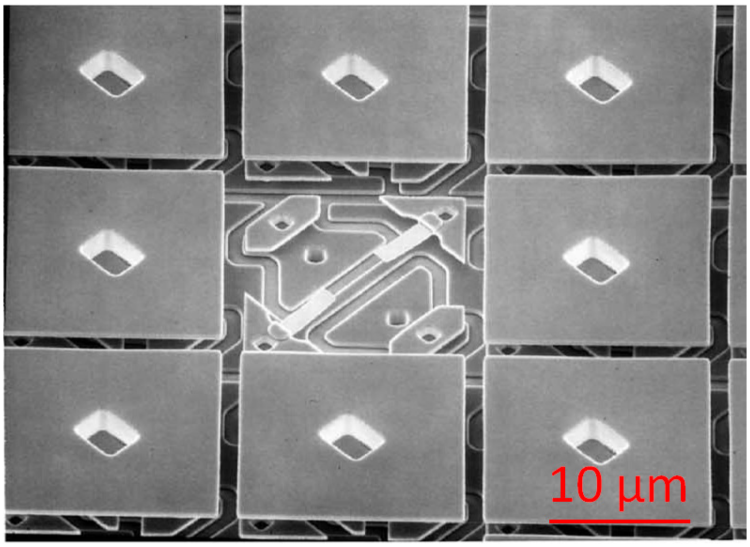

Figure 2.10 – SEM micrograph of a the mirrors on a DMD [39]

Each mirror on the DMD is ~16 µm x ~16 µm with a 1 µm gap between mirrors and are available in a number of common display array sizes including 640x480, 1027x768, 1280x1024, 1400x1050 and 1920x1200. Each mirror can individually be tilted up or down between 10 and 12 degrees, which allows the light source to be reflected towards or away from the projection lens, hence turning a pixel on or off. It is also possible to generate 1024 different "grey shades" from each pixel by modulating the tilt frequency. In conventional projectors, a colour wheel (which is located between the light source and the DMD) and the grey shade generating technique is used to produce the full colour images which the user sees. Figure 2.11 illustrates the key components in a DLP projection system.

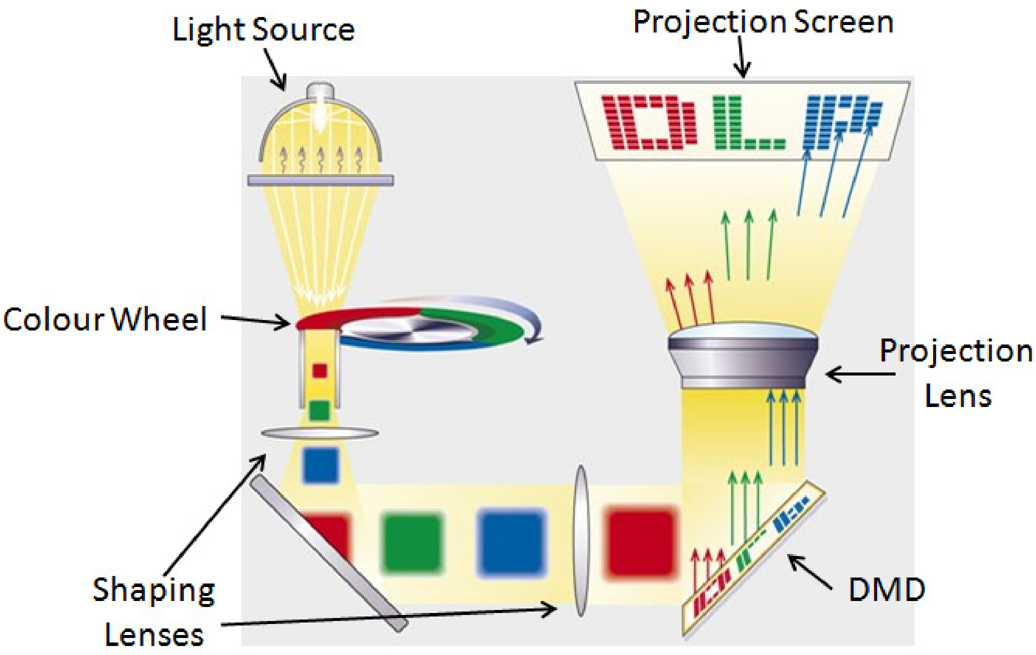

Figure 2.11 – Schematic diagram illustrating the operation of a DMD based projection system [40]

The main difference between a consumer projector and one used in an SL system is the removal of the colour wheel. This colour wheel is used to filter the light source in order to produce the desired colour shades on the image. As the photopolymers only respond to a small band of wavelengths (generally in the region between 300 nm and 500 nm), the use of a colour wheel would result in a proportion of the bulbs power being wasted when the filters on the colour wheel exclude the wavelengths required for polymerisation. The ability to control grey shades is however still used to correct for slight variations in light level across the exposure plane [15] (grey mask calibration is discussed further later in this chapter).

The projectors use metal-halide lamps as the exposure source and therefore remain on throughout the entire build process. In the cheaper systems (such as EnvisionTec's Perfactory Desktop) the mask generator is loaded with a blank, black image as an "all off" state. However, there is generally always a small amount of light leakage reflected through the system that can cause the resin material to degrade if the material is left in the resin tray while the machine is turned on but not in use. Higher end systems therefore further modify the projector to include a mechanical shutter, which sits between the light source and the DMD in order to completely block the exposure light when it is not needed.

An important point to note with dynamic mask projection systems is that there is a direct trade off in terms of build envelope and pixel size resolution. Thus, finer resolution can be achieved simply by adjusting the focusing optics of the system, but in doing so the maximum possible dimensions of a component in the XY plane decreases, the Z resolution however remains constant.

2.3.2 Enhanced Resolution Modules (ERM)

As the constant drive of system manufactures is to increase the resolution while maintaining desirable build envelopes, many companies are looking at alternative means to "boost" the resolution of their systems. The Enhanced Resolution Module (ERM) was originally developed by EnvisionTec GmBH as a way to artificially increase the resolution of their systems; the first systems to include this device were EnvisionTec's Perfactory Mini range.

ERM does not increase the number of available pixels on the DMD, but instead uses piezoelectric elements to shift the system's optics simultaneously in both and X and Y by half of a pixel width in each direction. This technique enables the system to resolve finer edge features in greater detail (illustrated in (a) and (b) in Figure 2.12) and in theory produce thinner channels or single pixel holes as illustrated in Figures 2.12 (c). In practice, though producing single pixel width holes and channels is limited by a number of other factors, including the quality of the focus of the image, the quality of the resin material and how well the exposure level of the system is setup. Generally attempts to fabricate such small features in the XY plane results in overcure causing the hole or channel to fill with a thin film of cured material. A key point is that the size of an on / cure state pixel remains the same when using ERM.

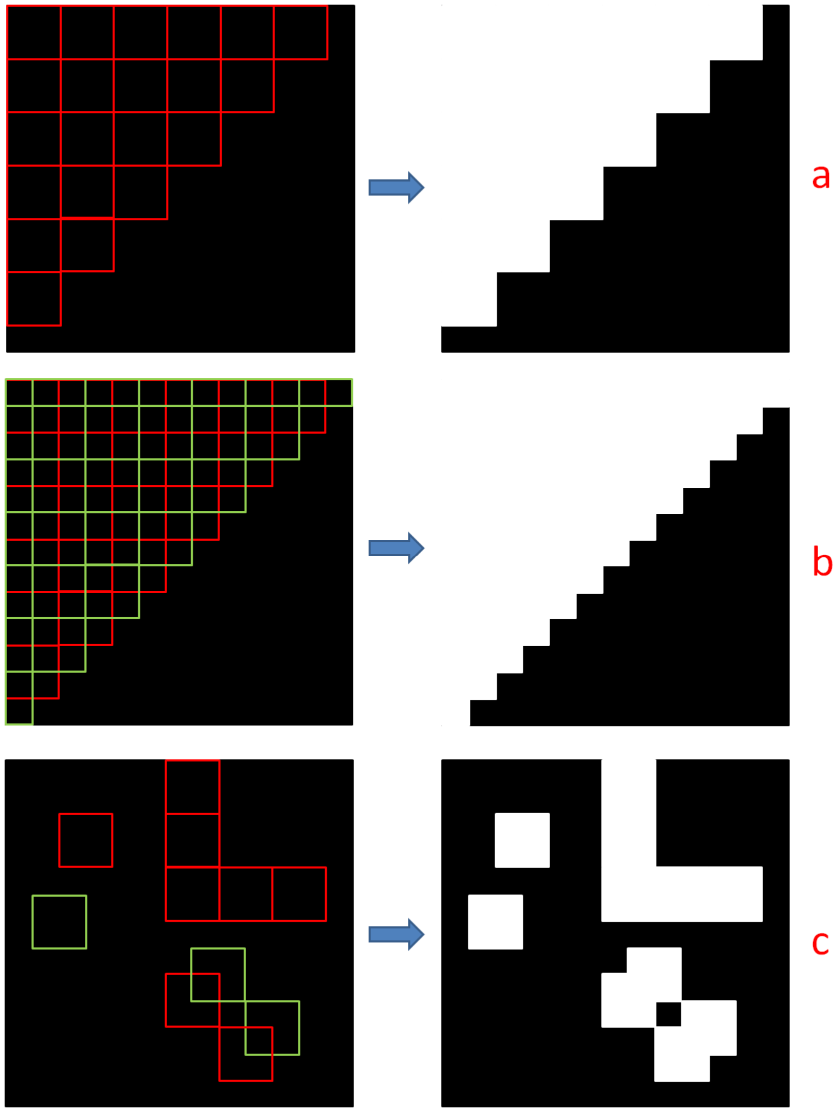

Figure 2.12 – Diagram illustrating the resulting mask output when fabricating an angled edge using (a) a standard system and (b) a system capable of pixel shifting using ERM (green). (c) demonstrates that while smaller holes can be fabricated, smaller cured areas cannot

2.4 System Operation

Although ALM systems all operate on the same layer-by-layer fabrication principle, their methods of operation vary from one technique to another – sometimes even between systems using the same technique. This section covers the operation procedures for a constrained surface microstereolithography system using projected dynamic masks.

2.4.1 Design to Object Process

The fabrication process begins by generating a digital model of the component using a computer aided design (CAD) software package. All designs produced throughout this thesis were generated using SolidWorks 2009 (Dassault Systemes, France) although any package capable of exporting the model in a "Standard Tessellation Language" (STL) format could be used. For example, AutoCAD, AutoDesk, Google Sketchup, Alibre, and Blender are popular alternatives. It is essential to ensure that the dimensions of the design are correct as these will be directly replicated when the components is fabricated.

The model can then be exported, from the CAD software, in a STL file format [37]. The STL file format was a format created by 3D Systems specifically as a universal method of representing 3D objects for stereolithography systems. However, it has now become the native industry standard file format for all additive layer manufacturing and 3D printing techniques. The STL format only stores information regarding the geometry of the object and no information about material type, colour or texture.

The STL file is then imported into a slicing program, which is used to convert the 3D object into a series of parallel 2D slices. The slicing program is usually specific to the machine that the model is to be built on. As laser based systems generate each 2D slice by rastering the image on the resin surface, each 2D layer is stored as a series of XY coordinates that the laser must track along in order to recreate the slice. For systems that utilise a parallel dynamic mask system, the 2D slices are stored as individual image files, often in a PNG (portable network graphics) format as it employs lossless data compression. Each slice image consists of both white and black regions that represent areas to either cure or leave uncured respectively. To ensure that is no scaling or deformation of the image during the exposure, the resolution of the PNG file is matched to the native resolution of the dynamic mask generator (be it LCD panel or DMD). Along with the mask images for each layer, an additional file is generated by the slicer that defines the individual exposure times, peel/level speed, wait times etc. for each layer. Depending on the system, the data is then either streamed to the system (typically over Ethernet or USB connections) during fabrication, or more commonly, all of the data is transferred to the system before beginning the process such that it cooperate in a “standalone” mode.

2.4.2 Post Processing

Once the fabrication process has completed the build platform along with the attached component is removed from the machine. The component is then removed from the build platform using a wide flat edge or hobby-knife. At this point the component is still in its “green” state as the fabrication process only cures the material to around 75% of its full hardness.

The component then goes through a number of washing steps to remove any excess, uncured resin material. The washing steps can vary depending on both the material used and the features on the components and are often largely dependent on the user’s prior experience and judgement of what method is best for each situation. Unless stated otherwise, the cleaning steps used for components discussed in this thesis are as follows: For most components acetone dispensed from a wash bottle is used to remove the bulk of the excess material, the component is then swilled in ~10 ml of acetone in a glass beaker until all of the excess material is visibly removed. The component is then transferred to a beaker of propan-2-ol to remove the acetone from the surface before being blotted dry on a cleanroom cloth. It is essential that the acetone wash lasts no longer than a few minutes and that it is removed afterwards as it has been observed to attack the resin material and cause delamination. For parts with small features (0.5 mm or less) the acetone wash step is skipped and propan-2-ol is used instead. Using acetone on such small features causes the soft, green-state, material to rapidly deform and destroy the part. For components with embedded fluidic channels, acetone is pumped through using a syringe unless the component contains thin membranes.

Propan-2-ol can be used as an alternative; however, using this solvent on liquid resin can cause the material to form a gel, which then blocks the channels.

After cleaning any drying of the component it is then post cured to ensure all the material is fully polymerised. The MBL group has two post curing units, an Otoflash G171 (NK-Optik GmbH, Germany) and a Metalight QX1 (Primotec, USA). The Otoflash unit is used for general post curing operations and operates by using two xenon flash tubes that emit a high intensity broadband spectrum making it suitable for curing all photopolymer materials. The controls on the unit allow the user to set the number of desired flashes, which occur at 10 Hz. For the R11 material, 500 to 1000 flashes are typically required. For smaller components this has to be done in blocks of flashes as the heat generated from the bulbs otherwise distorts the part. For large components the Metalight unit is used as it provides a constant output of a lower intensity, using ring of UV fluorescent bulbs. A typical cure time using the Metalight unit is between 15 and 30 minutes.

2.5 Microstereolithography Materials

Although when discussing the uses of SL and MSL technologies it is often the fabrication hardware that is focused upon, the photopolymer resin material itself is arguably as important, if not more so. This section provides an outline of the photopolymerisation process along with a number of photopolymer materials.

2.5.1 Photopolymerisation Process

The stereolithography process is based on a photopolymerisation process. Photopolymerisation is a solidification method whereby a liquid monomer is cross-linked by exposure to an incident light of suitable wavelength (usually in the ultraviolet region for MSL) [41]. There are two main types method of photopolymerisation, free-radical and cationic [42]. Cationic photopolymers include epoxy based materials and vinyl ethers.

However they are not often used for MSL operations due to the continuation of reactions post exposure as observed in cationic polymerisation which prevents the fabrication of accurate components with fine details [43]. As such, free-radical initiated photopolymerisation using an acrylate or methacrylate based material is generally preferred [44]. Figure 2.13 shows the generalised structure of monofuctional acrylate, epoxy and vinyl ether molecules.

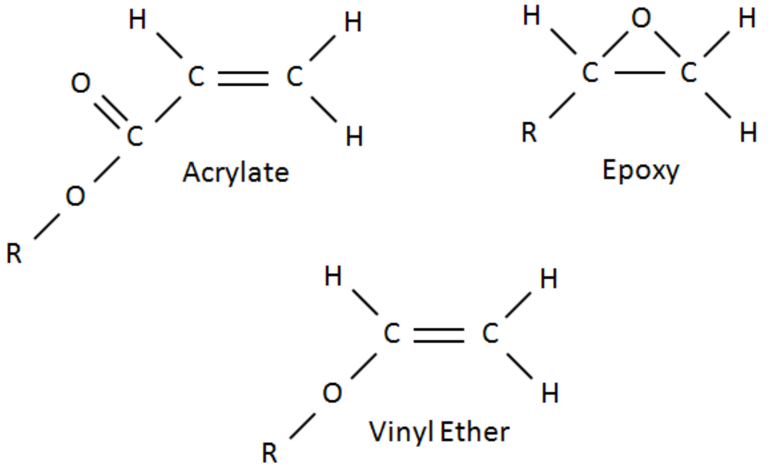

Figure 2.13 – General chemical structures of monofunctional acrylate, epoxy and vinyl ether molecules

As most monomers used for polymerisation are transparent, they do not absorb enough of the incident exposure light to produce enough free radicals for polymerisation. As such, photopolymer resins also include a photoinitiator whose sole purpose is to generate enough free radicals to induce rapid photopolymerisation[45] (known as the initiation stage). The free radicals generated then move between the acrylate monomer units, breaking the C=C bonds and causing crosslinking with adjacent units (known as the propagation stage). The termination stage occurs when all of the monomer units are cross linked and there can therefore no longer be radical transfer between chains. In order to increase cross linking it is also common to introduce an additional cross linking material into the resin formulation. A dye is also generally added to the material in order to absorb a certain percentage of the exposure light. This serves to improve layer control and to keep the exothermic polymerisation reaction under control in order to prevent overcure and edge distortion.

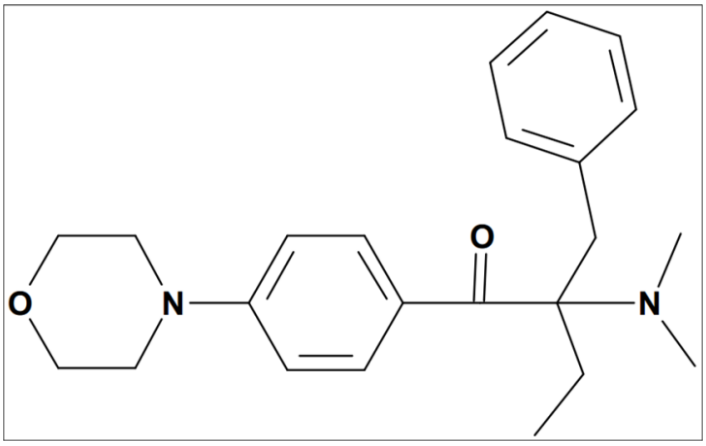

Figure 2.14 – Chemical structure of Irgacure 369

It should be noted that the curing properties of a material can vary slightly between systems due to the variations in wavelengths of the light emitted from the exposure source. Indeed, variations can also occur with a system through the life of the exposure source. Mask based MSL systems tend to use metal-halide lamps that have a high intensity broadband output, while most systems will filter out IR wavelengths to prevent heating of the material, the lower wavelengths are generally not restricted in order for systems to be used with a wide range of materials. Therefore, the wavelength of projector output isn't necessarily matched to the photoinitiator in the material. As an extreme example: According to the MSDS (material safety datasheet) for R11 [46] (EnvisiontTec's most popular, standard material), the chemical abstracts service (CAS) number (119313-12-1) shows the photoinitiator used is 2-benzyl-2-dimethylamino-1-(4-morpholinophrnyl)-butanone-1 (Figure 2.14), which also has the commercial name of Irgacure 369 (Ciba Speciality Chemicals Inc., Switzerland). Figure 2.15, taken from the compound's datasheet [47], shows that the peak excitation wavelength is approximately 320 nm. However, when this is compared to the spectral output of the Perfactory Mini system (measured using an Ocean

Optics HR2000+ spectrometer) in Figure 2.16, which R11 is the recommended material, it can be seen that the 320 nm lies outside of the output range of the system. The reason in this case that the material is still able to photopolymerise is due to the high level of photoinitiator used (up to 5%), which acts to increase the excitation region to include wavelengths up to ~500 nm, within the region of peak intensity output for the exposure source. Although this method appears to be an inefficient method, it is one that is often utilised to gain control over the curing process while taking into account the variations in output levels for different bulbs in the exposure source.

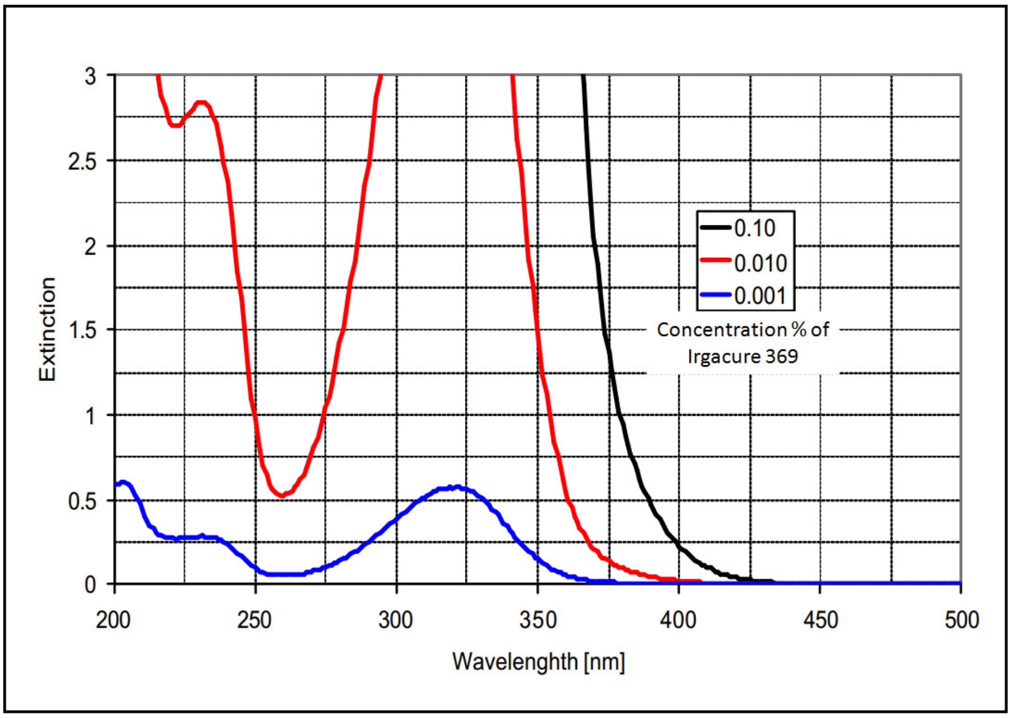

Figure 2.15 – Absorption profile for Irgacure 369 [47]

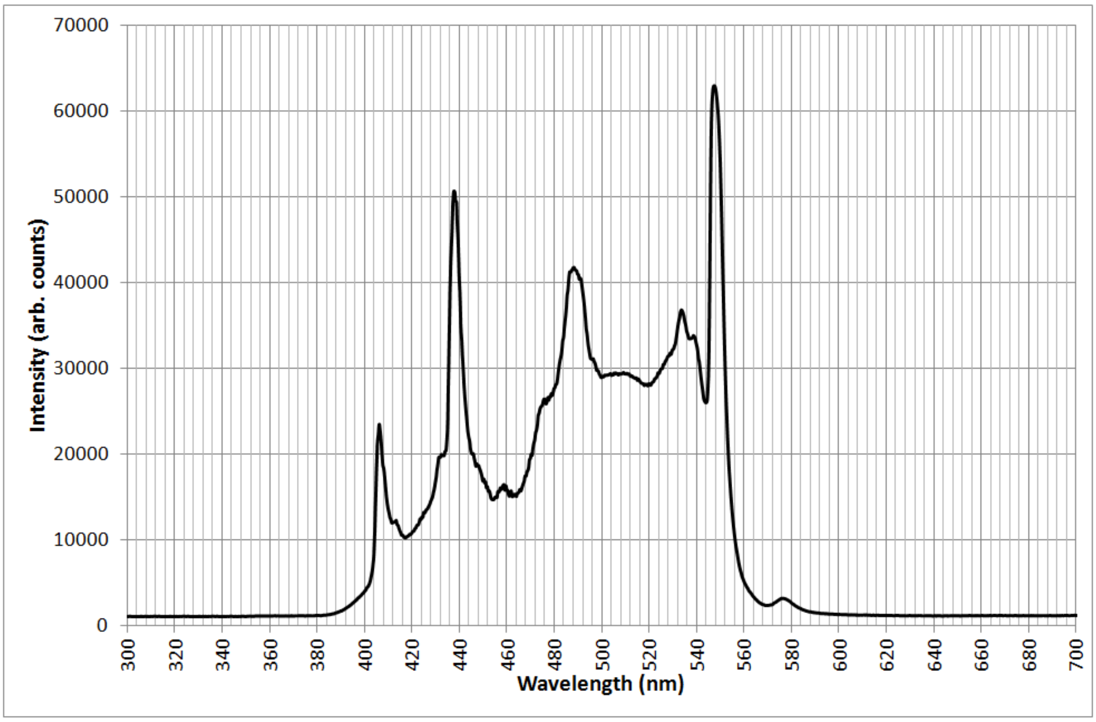

Figure 2.16 – Spectral output of Perfactory Mini (EnvisionTec GmBH)

2.5.2 Material Overview

As mentioned previously, the primary use for many ALM technologies, including SL, is rapid prototyping. Since prototypes are generally produced for aesthetic demonstration and form/fit verification of the component rather than any type of end use, the majority of materials available have been acrylate based and geared solely towards producing rigid structures, such as EnvisionTec's R11.

As MSL systems have become more advanced with increases in resolution, base photopolymer materials and photoinitiators, so more materials and techniques are being developed that expand the practical uses of the technology. There is, for instance, great interest in the field for utilising the technology for the casting of secondary structures. This is done either by using MSL to create a negative mould for casting of a secondary material, or by using materials such as EnvisionTec's specially designed range of materials for investment casting – WIC for general investment casting or the PIC range that is specifically for the jewellery market. Figure 2.17 shows a set of ring designs fabricated using EnvisionTec's WIC and PIC materials for sacrificial casting – a typical use of the technology.

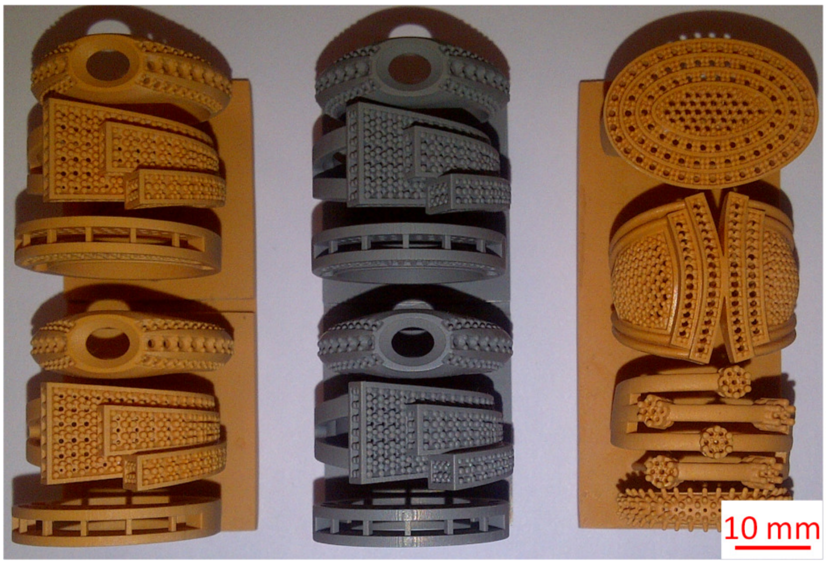

Table 2.17 – Ring designs for sacrificial casting fabricated using WIC and PIC materials (EnvisionTec GmBH)

It is clear that while the technology and its uses are progressing, its deployment is currently still focused on structural materials where the application's form is of most importance rather than any particular function of the material itself (such as it conductivity, or magnetic or optical properties). It is however the author's belief that the development of functional materials would greatly increase the range and possibilities of components that could be fabricated using MSL. Furthermore, due to the simplicity and low costs of the process when compared to existing fabrication such as silicon based processes, it presents an attractive alternative to research facilities and sectors where it is often desirable to be able to produce bespoke MEMS and other functional components in minimal fabrication steps.

One area where there has however been a great deal of research conducted by a number of groups is in the field on development of ceramic materials [20, 48-52] for MSL. Bertsch et al [48] have had particular success with working with ceramic fill levels up to

80% by volume however at this level of loading a recoating systems was required due to the viscosity of the material. Work on such ceramic material has also aided in the research of biocompatible [53-55] and biodegradable [56] functional materials [12]; a number have demonstrated the use of such materials for the fabrication of custom bone scaffolds as a bone regeneration techniques [57-60]. For such materials poly(ethylene glycol) is generally used as the base monomer due to its biocompatibility.

Work with ceramic composites has also led onto a small number of other groups beginning to develop materials that exhibit electromechanical properties. Jiang et al [61] for example have successfully created a piezoelectric composite material that was deposited directly onto a pre-prepared silicon wafer which they believe could lead to the direct fabrication of piezoelectric microsensors and microactuators using MSL. However, it noted that the process requires a post fabrication sintering step. On further investigation of the literature, little more can be found on functional materials with MSL or active uses of MSL fabricated components. Table 2.3 shows a summary of the alternative materials developed by other researchers.

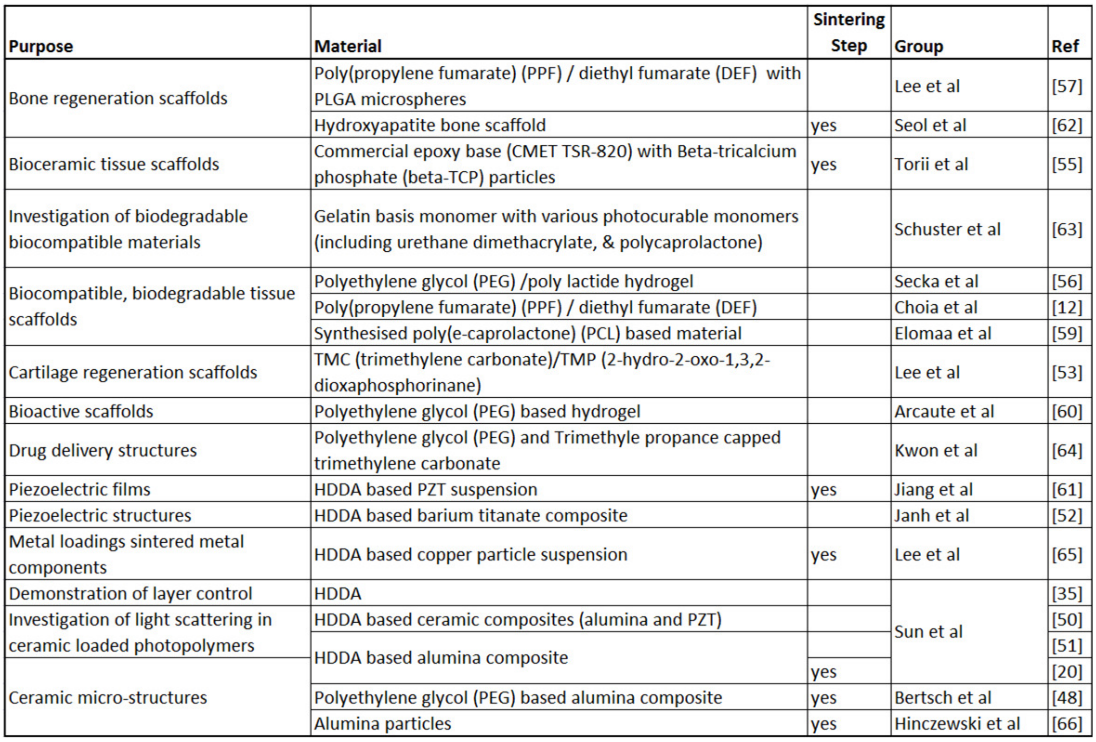

Purpose	Material	Sintering Step	Group	Ref
Bone regeneration scaffolds	Poly(propylene fumarate) (PPF) / diethyl fumarate (DEF) with PLGA microspheres		Lee et al	[57]
	Hydroxyapatite bone scaffold	yes	Seol et al	[62]
Bioceramic tissue scaffolds	Commercial epoxy base (CMET TSR-820) with Beta-tricalcium phosphate (beta-TCP) particles	yes	Torii et al	[55]
Investigation of biodegradable biocompatible materials	Gelatin basis monomer with various photocurable monomers (including urethane dimethacrylate, & polycaprolactone)		Schuster et al	[63]
Biocompatible, biodegradable tissue scaffolds	Polyethylene glycol (PEG) /poly lactide hydrogel		Secka et al	[56]
	Poly(propylene fumarate) (PPF) / diethyl fumarate (DEF)		Choia et al	[12]
	Synthesised poly(e-caprolactone) (PCL) based material		Elomaa et al	[59]
Cartilage regeneration scaffolds	TMC (trimethylene carbonate)/TMP (2-hydro-2-oxo-1,3,2-dioxaphosphorinane)		Lee et al	[53]
Bioactive scaffolds	Polyethylene glycol (PEG) based hydrogel		Arcaute et al	[60]
Drug delivery structures	Polyethylene glycol (PEG) and Trimethyle propance capped trimethylene carbonate		Kwon et al	[64]
Piezoelectric films	HDDA based PZT suspension	yes	Jiang et al	[61]
Piezoelectric structures	HDDA based barium titanate composite		Janh et al	[52]
Metal loadings sintered metal components	HDDA based copper particle suspension	yes	Lee et al	[65]
Demonstration of layer control	HDDA		Sun et al	[35]
Investigation of light scattering in ceramic loaded photopolymers	HDDA based ceramic composites (alumina and PZT)			[50]
	HDDA based alumina composite			[51]
Ceramic micro-structures		yes		[20]
	Polyethylene glycol (PEG) based alumina composite	yes	Bertsch et al	[48]
	Alumina particles	yes	Hinczewski et al	[66]

Table 2.3 – Alternative photopolymer materials developed by other researchers

2.6 Considerations and Limitations

When attempting to fabricate components using MSL there are a number of important factors that should be considered both when designing the component, using the slicer program to prepare the job file ready for fabrication and setting up the system. There are a number of obvious considerations, including the trade-off between built envelope and minimum feature size, and post fabrication part shrinkage [67]. Aside from these, one of the most important considerations that is often overlooked is that all ALM technologies recreate objects by splitting them into a finite number of representative layers. Indeed, each XY layer is further divided up into a finite number of pixels. A volume of one unit pixel in XY and of one layer thickness is often referred to as a volume pixel or “voxel”. This digitisation of components can sometimes cause a number of issues if a feature on a component is not an integer number of a voxel unit in either length, width or height as it becomes physically impossible for it to be fabricated perfectly as per the original design. Figure 2.18(a) illustrates a square which has lengths greater than 3 voxels, but less than 4, so the shape cannot be accurately replicated. Without unit dimensioned features, the results are imperfect slopes (Figure 2.18(b)) and rough edges, which can cause particular problem with lamina flow and optical applications. However, unless working with feature sizes on the order of tens of microns, then in most cases the error is considered negligible and therefore acceptable.

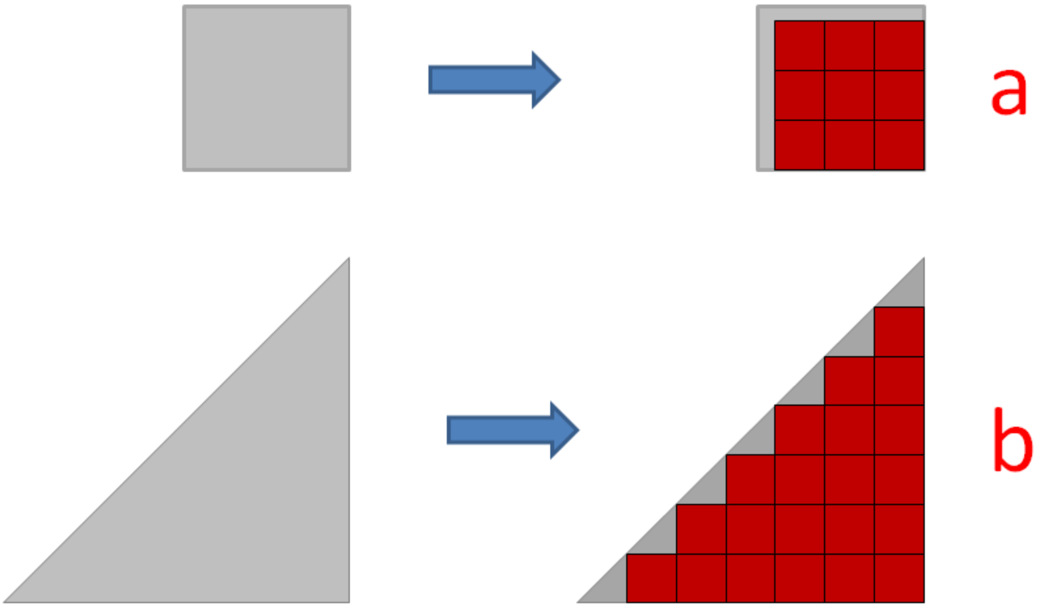

Figure 2.18 – Illustration of fabrication error due components by either (a) the dimensions not being an integer number of voxels, or (b) the edge features not being collinear with the voxel matrix

The issue can, however, become a problem when attempting to fabricate continuous smooth, shallow curves as series of large stepped planes will be the likely output from fabrication. The problem becomes less with steeper gradients relative to the plane of the build platform. As such, providing the curve isn't symmetrical about a rotational axis the operator can occasionally work around the issue by adjusting the orientation of the component in the slicer program – this method can work particularly well with flat planes by making the plane of the slope parallel to the build platform.

Another consideration when fabricating using MSL is when components have large areas that are supported only at the edges, long beams and overhanging structures, or areas that are only supported from above (i.e. by a subsequent layer that haven't yet been fabricated). In general such features are not possible to fabricate on either constrained or free surface systems. This is due to single layers unsupported layers being incapable of withstanding the forces involved in the peeling or levelling steps of the fabrication process. Figure 2.19 shows a test component with a series of bars with lengths of 1 mm to 5 mm, 1 mm width and 2.5 mm height, oriented at 0º, 45º and 90º to the build platform. It can be seen that both sets of bars at 0º and 45º were fabricated without error, however, the set at 90º (parallel to the build platform) failed. It can be seen that the initial layers of this set failed to fabricate – while it is likely that they cured, it is expected that they would have been torn away close to the bulk during peeling. Each subsequent layer then tears off further away from the bulk such that later layers will fabricate successfully – as shown by the ~15° angle highlighted on Figure 2.18. Additionally, it can be seen that in these regions layer-to-layer adhesion is less, often due to sections of previously build layers folding up during the peeling process.

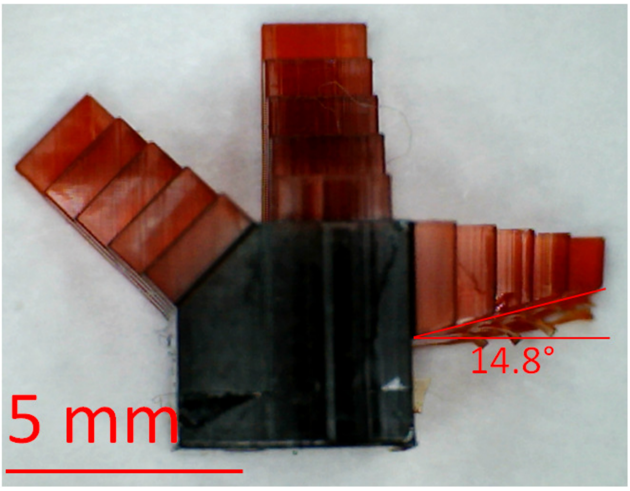

Figure 2.19 – Microscopy image of test build illustrating the failure of unsupported overhanging features

There are however a number of methods to work around this issue, including fabricating the component in a different orientation where the overhanging structure is oriented perpendicular to the build platform, or by splitting the component up into a number of smaller components. In some instances, neither of these options are viable, in which case additional support structures would be required.

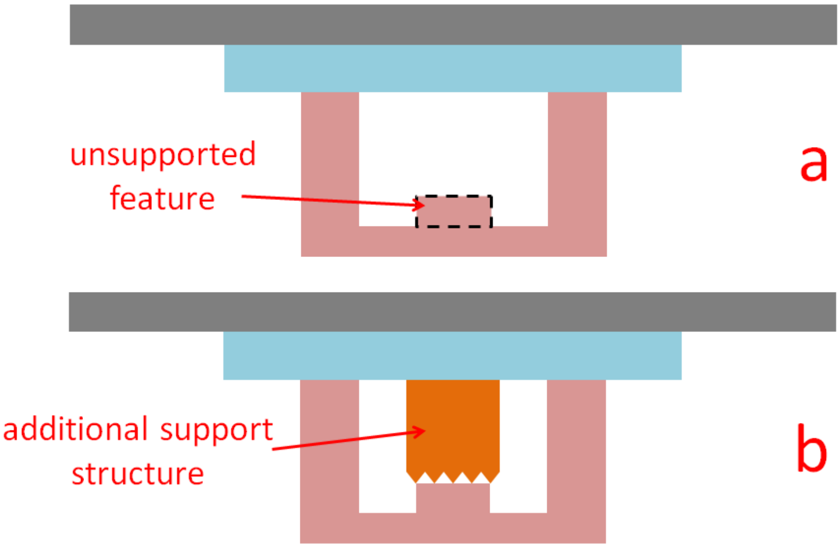

Figure 2.20 – Diagram showing the use of support structures to ensure the fabrication of otherwise unsupported features. (a) shows the intended component with an unsupported feature, (b) shows the same component with an additional support feature

Figure 2.20(a) illustrates a typical component with a bridge feature including an unsupported structure hanging below. If feasible, the component would ideally be positioned for fabrication such that horizontal member would be build first, however, if this is not possible then a support structure would be required, as illustrated in Figure 2.20(b). The support structure is generally a mesh structure that forms an array of point contacts with the component such that it can be easily be removed during post processing by snapping it away. Figure 2.21(a) shows the model of a sports car that required supports in order to fabricate. Here the point contacts between the component and the support structure can be seen. However, as illustrated in the extreme case in Figure 2.21(b), the use of support structures is not a perfect solution and often leaves the supported areas with deformities.

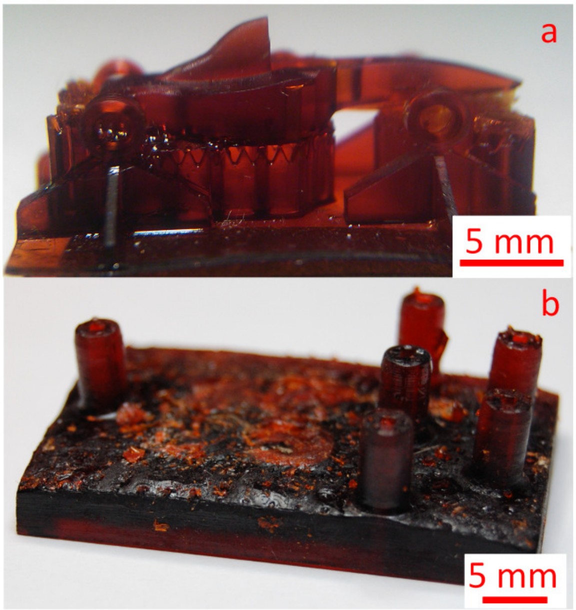

Figure 2.21 – Images showing (a) model vehicle with support structure, (b) a microfluidic component with surface deformities having removed the support structure

The final considerations, when fabricating using MSL, are related to the curing process itself, and more specifically the profile of the exposure field when using pixel based parallel exposure methods. Although the size of each projected pixel can in theory be calculated by knowing the dimensions of the build envelop in the XY plane and the resolution of the DMD, in practice each pixel has a Gaussian intensity profile. The profiles of adjacent pixels overlap such that there is a second intensity peak between the two pixels that produces a surface texture effect often observed on MSL parts fabricated using parallel exposure methods. Figure 2.22 shows the interference pattern observed when a point laser is shone through the reverse side of an apparently flat square of material fabricated using MSL and projected onto a wall. This pattern is not observed if the incident beam is shone through the front face (i.e. the last layer fabricated) and therefore confirms that the diffraction pattern is caused by a surface pattern rather than in the bulk material itself.

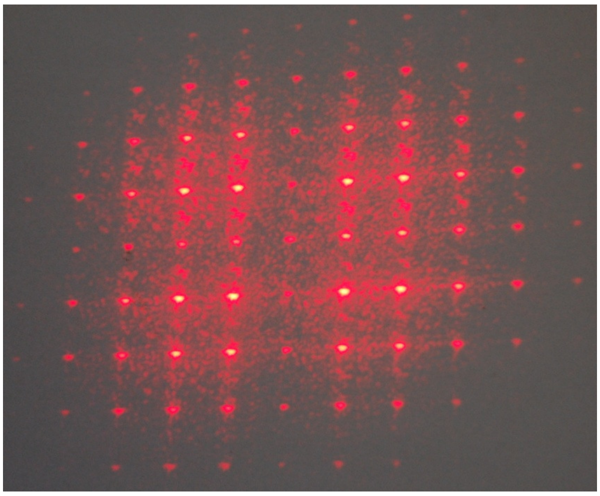

Figure 2.22 – Interference pattern observed when a laser spot is projected through a flat sample of material cured using a DMD based exposure

The effect is discussed by Sun et al [35]. It is demonstrated that when the width of the projected feature is greater than the Gaussian radius of a single pixel, “cross-talk between imaged light spots” occurs. It was noted that this causes the peak power in the centre of the area to be up to 6 times greater than if the area were just a single pixel. Their model showed that once the width of a feature was greater that approximately 3.5 times the width of a pixel, the peak intensity reached a maximum.

In order to maintain control of layer thickness, the peak intensity value must be no greater than the intensity required to cure one layer thickness of the material. This therefore illustrates that while the minimum feature size is dependent on the projected pixel size, it is not equal to the projected pixel size as a point will be reached where the intensity is insufficient to begin the photopolymerisation process. Ryoo et al [68] also investigated this by modelling the output of a DMD system to evaluate the exposure efficiency of a system with a projected XY pixel size of 4 µm. They reported that with feature sizes between 4 µm and 4.5 µm the exposure efficiency rapidly increases from 20% up to 73% and thereafter steadily increases up to 100% at 18 µm which concurs with the findings of Sun et al [35] and more recent work by Kang et al [11].

Sun et al [50] went on to investigate the effect of using additive particle materials in the polymer with respect to light scattering. Three types of ceramic particles were used; silica, alumina and lead zirconate titanate (PZT). Contrary to expectation, as the mean particle size increased (from 300 nm to 1 µm), the curing radius was found to decrease (from 7 µm to 4 µm) while the curing depth increased (from 50 µm to 80 µm). Scattering was found to be strongest when the size of the additive material approached the wavelength of the exposure source, additionally the greater the difference in refractive index between the polymer and the particles, the greater the light scattering effect was observed.

2.7 Conclusion

In this chapter the methods and techniques employed in microstereolithography systems were discussed. While it may at first appear that the process of microstereolithography is relatively simple when compared to traditional silicon based fabrication methods, there are many aspects of the process, particularly with regard to the setup and calibration of the system, which can determine the range and quality of components that can be produced.

It has been shown that recent research in the technology had resulted in great advancement within the past decade particularly with the incorporation of DLP projection technologies, which significantly reduce fabrication time and machine cost. The technology is such that now even larger systems are beginning to be capable of fabricating components with features on the micron scale. As improvements in techniques and materials continue, so the opportunities to fabricate ever more complex and higher quality parts increases.

While the technology has previously been used primarily for the production of prototype components, it is felt that it has now progressed to a stage where it can be begun to be used as a standard manufacturing technique alongside, or in preference to, existing methods. Some have found small niches where the technology has clear advantages over traditional methods, such as EnvisionTec with their material for sacrificial casting in the jewellery sector. However, by expanding the current range of materials to incorporate functional properties, rather than purely mechanical ones, it is predicted that the potential range of applications could be significantly broader. A number of considerations and limitations of the current technology were also covered, which must be taken into account by the system operators when attempting to fabricate using MSL.

Based on the review of the methods, it is concluded that a constrained surface system would present the most ideal development platform due to it not requiring large volumes of material. Additionally, the success of component fabrication can be verified throughout the component as the component rises from the material. Due to it compatibility with the constrained surface approach and the simplicity of setup, it is also concluded that a parallel projection method would be used.

The following chapter will cover the assembly of two custom MSL systems that allows for increased control over the build process when compared to commercial systems. These are then used develop new photocurable functional materials and techniques which allow investigation of further expansion of the technology's uses.

2.8 References

[1] A. Bertsch, P. Bernhard, P. Renaud, Microstereolithography: concepts and applications, Proceedings of 2001 8th IEEE International Conference on Emerging Technologies and Factory Automation 2 (2001) 289–298

[2] H. Kodama, Automatic method for fabricating a three-dimensional plastic model with photo-hardening polymer, Review of Scientific Instruments 52 (1981) 1770-1773

[3] P.F. Jacobs, Rapid Prototyping and Manufacturing: Fundamentals of Stereolithography, McGraw-Hill (1992)

[4] J.W. Gardner, V.K. Varadan, O.O. Awadelkarim, Microsensors, MEMS and Smart Devices, John Wiley & Sons Ltd (2007)

[5] L. Wood, Rapid Automated Prototyping: An Introduction, Industrial Press Inc. (1993)

[6] S. Maruo, K. Ik, Submicron stereolithography for the production of freely movable mechanisms by using single-photon polymerization, Sensors and Actuators A 100 (2002) 70–76

[7] L.H. Nguyen, M. Straub, M. Gu, Acrylate-Based Photopolymer for Two-Photon Microfabrication and Photonic Applications, Advance Functional Materials 15 (2005) 209-216

[8] iPro 8000 & 9000 Family Technical Specifications and Datasheet, [online] available from: http://production3dprinters.com/sites/production3dprinters.com/files/downloads/iPro-Family-USEN.pdf (last accessed 04/04/2012)

[9] H-W. Kang, I.H. Lee, D-W. Cho, Development of a micro-bellows actuator using micro-stereolithography technology, Microelectronic Engineering 83 (2006) 1201–1204

[10] M. Farsari, F. Claret-Tournier, S. Huang, C.R. Chatwin, D.M. Budgett, P.M. Birch, R.C.D. Young, J.D. Richardson A novel high-accuracy microstereolithography method employing an adaptive electro-optic mask, Journal of Materials Processing Technology 107 (2000) 167-172

[11] H-W. Kang, J.H. Park, D-W. Cho, A pixel based solidification model for projection based stereolithography technology, Sensors and Actuators A 178 (2012) 223–229

[12] J-W. Choi, R. Wicker, S-H. Lee, K-H. Choi, C-S. Ha, I. Chung, Fabrication of 3D biocompatible/biodegradable micro-scaffolds using dynamic mask projection microstereolithography, Journal of Materials Processing Technology 209 (2009) 5494–5503

[13] J-W. Choi, H-C. Kim, R. Wicker, Multi-material stereolithography, Journal of Materials Processing Technology 211 (2011) 318–328

[14] K. Ikuta, S. Mauruo, S. Kojima, New Micro Stereo Lithography for Freely Movable 3D Micro Structure, Proceedings of IEEE 11th Annual International Workshop on Micro Electro Mechanical Systems (1998) 290-295

[15] I-B. Park, Y-M. Ha, S-H. Lee, Still motion process for improving the accuracy of latticed microstructures in projection microstereolithography, Sensors and Actuators A 167 (2011) 117–129

[16] S. Kawata, H. B. Sun, T. Tanaka, and K. Takada, Finer features for functional microdevices, Nature 412 (2001) 697-698

[17] K. Ikuta, K. Hirowatari, Real Three Dimensional Micro Fabrication Using Stereo Lithography and Metal Molding, Proceedings from An Investigation of Micro Structures, Sensors, Actuators, Machines and Systems, Micro Electro Mechanical Systems (1993) 42-47

[18] A. Bertsch, S. Zissi, J.Y. Jezequel, S. Corbel, J.C. Andre, Microstereophotolithography using a liquid crystal display as dynamic mask-generator, Microsystem Technologies (1997) 42-47

[19] F. Devaux, A. Mosset, E. Lantz, S. Monneret, H. Gall, Image Upconversion from the Visible to the UV Domain: Application to Dynamic UV Microstereolithography, Applied Optics 40 (2001) 4953-4957

[20] X. Zhang, X.N. Jiang, C. Sun, Micro-stereolithography of polymeric and ceramic microstructures, Sensors and Actuators 77 1999 149–156

[21] K. Kobayashi, K. Ikuta, Development of Free-Surface Microstereolithography with Ultra-High Resolution to Fabricate Hybrid 3-D Microdevices, 2005 IEEE International Symposium on Micro-NanoMechatronicsand Human Science (2005) 273-278

[22] S. Deshmukh, P.S. Gandhi, Optomechanical scanning systems for microstereolithography (MSL): Analysis and experimental verification, Journal of Materials Processing Technology 209 (2009) 1275–1285

[23] B. Courtois, S.B. Crary, W. Ehrfeld, H. Fujita, J.M. Karam, K. Markus, L. Beluze, A. Bertsch, P. Renaud, Microstereolithography: a new process to build complex 3D objects, Proceedings of the Society of Photo-Optical Instrumentation Engineers, Design, Test and Microfabrications of MEMES and MOEMS 3680 (1999) 808-817

[24] J-J. Clair, Utilisation du procede biphotonique en stereolithographie: A biphotonic process in stereolithography, Pure and Applied Optics: Journal of the European Optical Society Part A 2 (1993) 169-172

[25] D.T Pham, R.S Gault, A comparison of rapid prototyping technologies, International Journal of Machine Tools and Manufacture 38 (1998) 1257-1287

[26] J.P. Kruth, Material Incress Manufacturing by Rapid Prototyping Techniques, CIRP Annals - Manufacturing Technology 40 (1991) 603–614

[27] S. Wu, J. Serbin, M. Gu, Two-photon polymerisation for three-dimensional micro-fabrication, Journal of Photochemistry and Photobiology A: Chemistry 181 (2006) 1–11

[28] K-S. Lee, R.H. Kim, D-Y. Yang, S.H. Park, Advances in 3D nano/microfabrication using two-photon initiated polymerization, Progress in Polymer Science 33 (2008) 631-681

[29] H-B. Sun, S. Kawata, Two-Photon Photopolymerization and 3D Lithographic Microfabrication, Advances in Polymer Science 170 (2004) 169-273

[30] EnvisionTec GmbH (Germany) company website, [online] available from: www.envisiontec.de/index.php?page=machines&id=43 (last accessed: 21/06/2012)

[31] T. Nakamoto, K. Yamaguchi, Consideration on the producing high aspect ratio microparts using UV sensitive photopolymer, Proceedings of the IEEE 7th International Symposium for Micro Machine and Human Science (1996) 53-58

[32] V.K. Varadan, X. Jiang, V.V. Varadan, Microstereolithography and Other Fabrication Techniques for 3D MEMS, John Wiley & Sons, Ltd. (2001)

[33] S. Monneret, H. Le Gall, V. Badé, F. Devaux, A. Mosset, E. Lantz, Dynamic UV microstereolithography, The European Physical Journal Applied Physics 20 (2002) 213–218

[34] S.J. Leigh, C.P. Purssell, J. Bowen, D.A. Hutchins, J.A. Covington, D.R. Billson, A miniature flow sensor fabricated by micro-stereolithography employing a magnetite/acrylic nanocomposite resin, Sensors and Actuators A 168 (2011) 66–71

[35] C. Sun, N. Fang, D.M. Wu, X. Zhang, Projection micro-stereolithography using digital micro-mirror dynamic mask, Sensors and Actuators A: Physical 120 (2005) 113–120

[36] A. Bertsch, H. Lorenz, P. Renaud, 3D microfabrication by combining microstereolithography and thick resist UV lithography, Sensors and Actuators 73 1999 14–23

[37] C.K. Chua, K.F. Leong, C.S. Lim, Rapid Protoytping: Principles and Applications 3rd Edition (2010), World Scientific Publishing Co

[38] F. Bitte, G. Dussler, T. Pfeifer, 3D micro-inspection goes DMD, Optics and Lasers in Engineering 36 (2001) 155–167

[39] "How DLP Works", Texas Instruments, [online] available from: www.dlp.com/technology/how-dlp-works (last accessed: 12/05/2012)

[40] Schematic of DLP front projector, Optics Blazers AG (Liechtenstein), [online] available from: www.opticsbalzers.com/en/236/DLP%C2%AE-front-projector.htm (last accessed: 15/06/2012)

[41] N.S. Allen, Photopolymerisation chemistry, Journal of Photochemistry and Photobiology A: Chemistry 159 (2003) 102

[42] P.F. Jacobs, Stereolithography and other RP&M technologies: from rapid prototyping to rapid tooling, Society of Manufacturing Engineers, USA (1996)

[43] R. Cave, The Development and Characterisation of Photopolymerisable Resins for the Fabrication of Tissue Regeneration Scaffolds [PhD Thesis], University of Warwick (2008)

[44] C. Decker, The use of UV irradiation in polymerisation, Polymer International 45 (1998) 133-141

[45] P.M. Johnson, J.W. Stansbury, C.N. Bowman, Kinetic Modeling of a Comonomer Photopolymerization System Using High-Throughput Conversion Data, Macromolecules 41 (2008) 230-237

[46] R11 Material Safety Datasheet, EnvisinTec GmBh, [online] available from: www.envisiontec.de/userfiles/Material%20R5%20R11.pdf (last accessed: 02/01/2012)

[47] Irgacure 369 Datasheet, Ciba Speciality Chemicals (Switzerland), [online] available from: www.xtgchem.cn/upload/20110629045432.pdf (last accessed: 15/05/2012)

[48] A. Bertsch, S. Jiguet, P. Renaud, Microfabrication of ceramic components by microstereolithography, Journal of Micromechanics and Microengineering 14 (2004) 197-203

[49] C. Provin, S. Monneret, H. Le Gall, S. Corbel, Three-dimensional ceramic microcomponents made using microstereolithography, Advanced Materials 15 (2003) 994–997

[50] C. Sun, X. Zhang, The influences of the material properties on ceramic micro-stereolithography, Sensors and Actuators A: Physical 101 (2002) 364–370

[51] C. Sun, X. Zhang, Experimental and numerical investigations on microstereolithography of ceramics, Journal of Applied Physics 92 (2002) 4796-4802

[52] J.H Jang, S. Wang, S.M. Pilgrim, W.A. Schulze, Preparation and characterization of barium titanate suspensions for stereolithography, Journal of the American Ceramic Society 83 (2000) 1804-1806

[53] S-J. Lee, H-W. Kang, J.K. Park, J-W. Rhie, S.K. Hahn, D-W. Cho, Application of microstereolithography in the development of three-dimensional cartilage regeneration scaffolds, Biomedical Microdevices 10 (2008) 1387-2176

[54] F.P.W. Melchels, J. Feijen, D.W. Grijpma, A review on stereolithography and its applications in biomedical engineering, Biomaterials 31 (2010) 6121-6130

[55] T. Torii, M. Inada, S. Maruo, Three-Dimensional Molding Based on Microstereolithography Using Beta-Tricalcium Phosphate Slurry for the Production of Bioceramic Scaffolds, Japanese Journal of Applied Physics 50 (2011) 06GL15 1-5

[56] T.M. Secka, F.P.W. Melchelsb, J. Feijenb, D.W. Grijpma, Designed biodegradable hydrogel structures prepared by stereolithography using poly(ethylene glycol)/poly(d,l-lactide)-based resins, Journal of Controlled Release 148 (2010) 34–41

[57] J.W. Lee, K.S. Kang, S.H. Lee, J-Y. Kimc, B-K. Lee, D-W. Cho, Bone regeneration using a microstereolithography-produced customized poly (propylene fumarate)/diethyl fumarate photopolymer 3D scaffold incorporating BMP-2 loaded PLGA microspheres, Biomaterials 32 (2011) 744-752

[58] R. Gauvin, Y-C. Chen, J.W. Lee, P. Soman, P. Zorlutuna, J.W. Nichol, H. Bae, S. Chen, A. Khademhosseini, Microfabrication of complex porous tissue engineering scaffolds using 3D projection stereolithography, Biomaterials 33 (2012) 3824-3834

[59] L.Elomaaa, S. Teixeiraa, R. Hakalab, H. Korhonenb, D.W. Grijpmaa, J.V. Seppälä, Preparation of poly(e-caprolactone)-based tissue engineering scaffolds by stereolithography, Acta Biomaterialia 7 (2011) 3850–3856

[60] K. Arcaute, B. Mann, R. Wicker, Stereolithography of spatially controlled multi-material bioactive poly(ethylene glycol) scaffolds, Acta Biomaterialia 6 (2010) 1047–1054

[61] X.N Jianga, C. Suna, X. Zhanga, B. Xub, Y.H. Ye, Microstereolithography of lead zirconate titanate thick film on silicon substrate, Sensors and Actuators A: Physical 87 (2000) 72–77

[62] Y-J. Seol, J.Y. Kima, E.K. Park, S-Y. Kimd, D-W. Cho, Fabrication of a hydroxyapatite scaffold for bone tissue regeneration using microstereolithography and molding technology, Microelectronic Engineering 86 (2009) 1443–1446

[63] M. Schuster, C. Turecek, J. Stanpfl, F. Varga, R. Liska, Biofunctional Photopolymers for Micro-Stereolithography, Proceedings of The 8th International Symposium on Laser Precision Microfabrication (2007)

[64] I.K. Kwon, T. Matsuda, Photo-polymerized microarchitectural constructs prepared by microstereolithography (mSL) using liquid acrylate-end-capped trimethylene carbonate-based prepolymers, Biomaterials 26 (2005) 1675–1684
[65] J.W. Lee, I.H. Lee, D-W. Cho, Development of micro-stereolithography technology using metal powder, Microelectronic Engineering 83 (2006) 1253–1256
[66] C. Hinczewski, S. Corbel, T. Chartier, Stereolithography for the fabrication of ceramic three-dimensional parts, Rapid Prototyping Journal 4 (1998) 104-114
[67] W. L. Wang, C. M. Cheah, J. Y. H. Fuh" and L. Lu, Influence of process parameters on stereolithography part shrinkage, Materials and Design 17 (1996) 205-213
[68] H. Ryoo, D.W. Kang, J.W. Hahn, Analysis of the line pattern width and exposure efficiency in maskless lithography using a digital micromirror device, Microelectronic Engineering 88 (2011) 3145–3149

Chapter 3

3 Custom Microstereolithography System Design

This chapter details the design and manufacture of two custom microstereolithography systems that enable complete control over the individual steps of the fabrication process. The first section details the design of a custom system that utilises an LED exposure source for increased control of the curing process for the development of alternative materials. The later section covers a second system that is based on the first but has the capability to fabricate components using multiple materials in a single build process and includes a LED source with greater power output. The rationale for this is discussed in the following sections.

3.1 Introduction

During the early stages of conducting the work presented in this thesis, preliminary experiments were conducted using the range of EnvisionTec Perfactory MSL systems that were available within the Microsensors & Bioelectronics Laboratory (MBL) group: a Perfactory Mini D, a Perfactory 3 SXGA+ Mini Multi Lens [1], and a Perfactory Desktop. The “Mini D” and Desktop systems both incorporate an XGA resolution DMD (1024 x 768) where as the “Mini Multi Lens” uses an SXGA+ resolution device (1400 x 1050). Additionally, the Mini system has been previously modified to operate with a reduced build envelope of 28 mm x 21 mm resulting in a pixel size of 20 µm. This system also includes the previously mentioned ERM module that reduces the theoretical minimum hole size to 10 µm.

While use of the commercial EnvisionTec system was adequate for fabrication using the materials supplied by EnvisionTec, the systems were not ideal for developing alternative materials and build techniques. In essence, they are designed to work with known materials using known parameters such that customers can easily fabricate components without requiring any great depth of understanding of the operation of the machine. Therefore, many commercial systems have numerous restrictions on the parameters used for fabrication, such as exposure time, motion speeds and levelling/wait times. Indeed, the EnvisionTec Perfactory systems supply RFID (radio-frequency identification) tags with the materials to ensure the correct parameters are used. While this is useful in a commercial environment, it presents a significant issue when using alternative materials. As the software used on the system's embedded computer is closed source the system could not be easily modified to enable more control over the parameters. Additionally, the resin trays, although requiring significantly less material than a system employing a free surface fabrication method, would still required many more times more material than was required for the fabrication of test parts. There was also the risk that new, previously untested materials could potentially contaminate and damage the surface of the resin trays that would then affect the operation of the system.

Due to the issues detailed, it was therefore decided that a custom, microstereolithography system would be built in house along with control software that would allow for complete control of the system in order to continue development of new materials and techniques. The hardware of the system was based on the principals of a standard constrained surface system using a mask projection technology exposure systems.

3.2 Custom MSL System – Hardware

A parallel projection microstereolithography system can be roughly broken down into 5 key components: an exposure light source, a DMD device with necessary optics, a motion stage for movement of the build platform, a framework to hold the resin tray in a set position, and a computer used to control the other elements of the system. This section covers the design of the hardware components for a custom microstereolithography system, as shown in Figure 3.1.

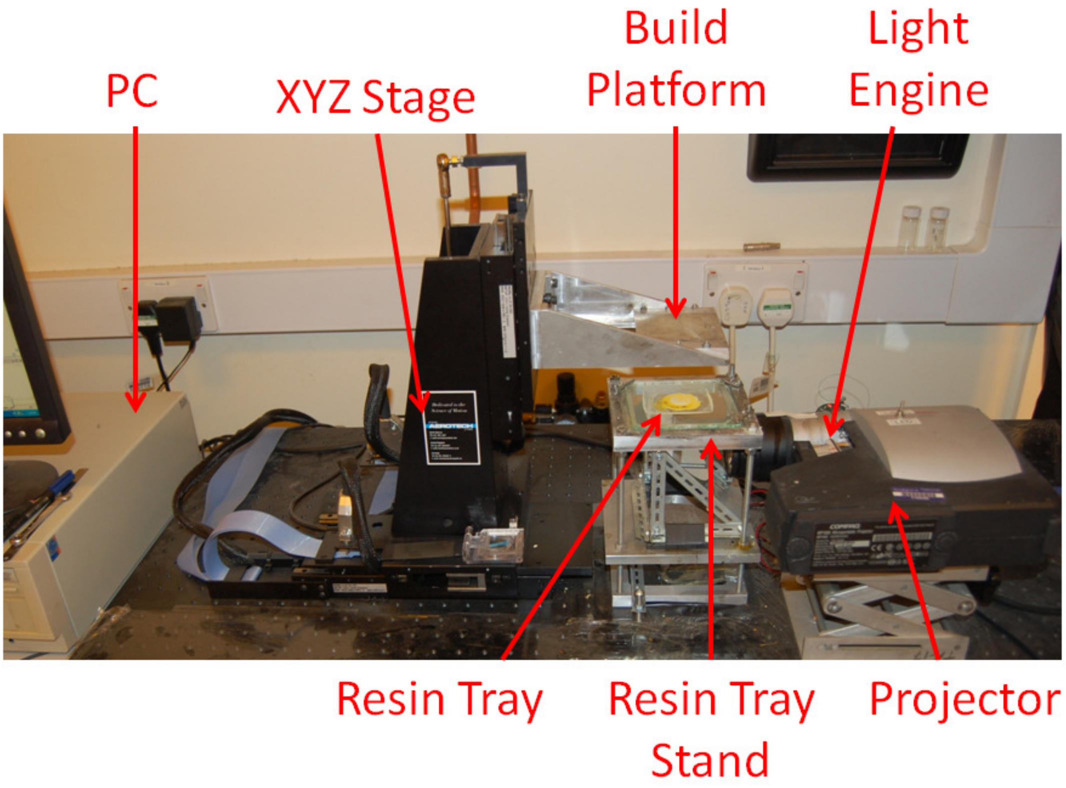

Figure 3.1 – Photograph of custom microstereolithography system

3.2.1 *XYZ Stage*

An Aerotech XYZ position stage consisting of 3 separate linear motors (x-axis: ALS130-150, y-axis: ALS130-100, z-axis: ALS130-050) was used for the raising, lowering and positioning of the build platform. The primary reasons for this choice were that it can not only easily exceed the required resolution for use in an MSL system but the associated A3200 motion controller also comes with a fully documented programming API (application programming interface) that allows for rapid and efficient integration in many common programming languages. It is not generally necessary to have the additional degrees of freedom along X and Y axis on an MSL system, however, the additional stages were already assembled from its previous use. During initial development of the system when adjustments and modifications were often being made, it was found useful to be able to manoeuvre the build platform and its support arm away from the main resin tray stand for calibration of the position, focus and keystoning of the exposure field. In a commercial MSL system this issue would not present as much of a problem as the adjustments would not need to be made regularly and the build platform in such systems rises up sufficiently to leave a suitable large workspace for the operator; the Z-axis of the Aerotech stage however only rises by 50 mm which is sufficient for normal operation but otherwise hinders access.

3.2.2 Arms

A pair of arms and clamps were designed (Figure 3.2) with a bracket in order to hold the build platform in place over the resin tray. The design for the arms was such that they included a wedge shaped clamping mechanism that made an interference fit with the matching angled edges on the build platform mount. This allowed for quick and easy removal and replacement of the build platform for the removal of fabricated components, while still providing adequate support to prevent unwanted movement during the build process. The bracket was then securely mounted to the face of the z-axis of the motion stage.

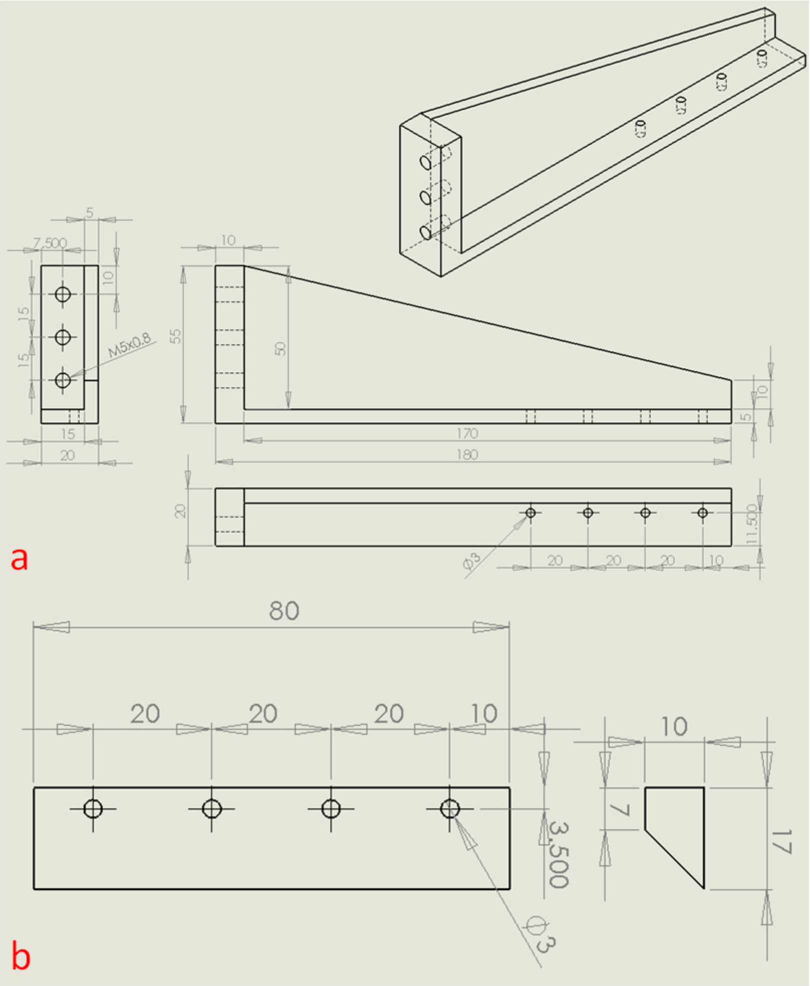

Figure 3.2 – CAD drawings of (a) left build platform support arm and (b) build platform clamp for custom MSL system (dimensions in mm)

3.2.3 Build Platform

The build platform itself consisted of a 60 mm x 60 mm polished glass block with a height of 10 mm. The glass was chosen to be thick enough such that it prevented interference with the assembly screws on the resin tray frame and any resin retainer walls that may be used on future resin trays. The block itself was then adhered to the underside of the build platform using double sided adhesive tape. A further build platform was later made that included an additional layer of 200 μm thick black plasticard between the glass block and the aluminium mount. This was done as it was found that when the original platform was used with resins containing low inhibitor dye levels, the first layers (up to ~300 μm) showed poor feature resolution. It was later discovered that this was due to a proportion of the light from the exposure field being reflected off the aluminium surface of the mount, causing unwanted curing in areas during the first layers. The addition of the black sheet prevented these reflections. Figure 3.3 shows the assembled build platforms.

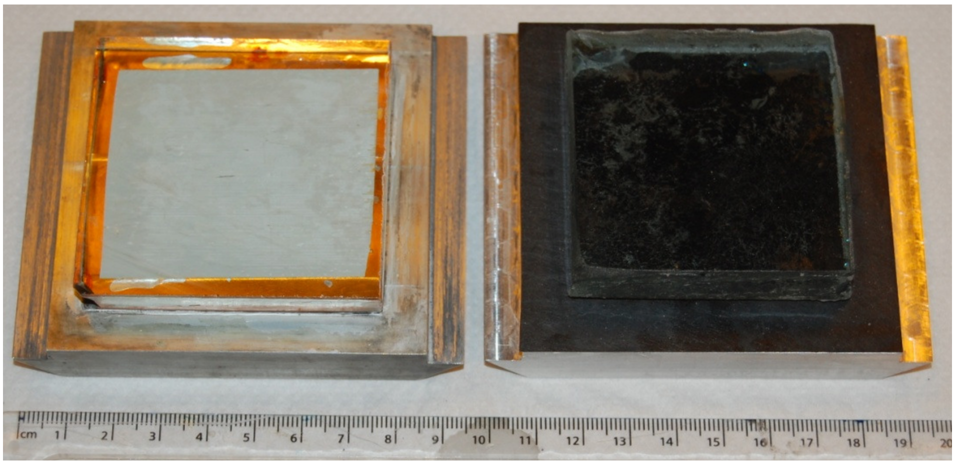

Figure 3.3 – Photograph of two build platforms manufactured for use with the custom MSL system, one (left) as a standard platform and a second (right) that includes a black backing to the glass build platform to prevent unwanted over cure when using un-dyed materials (scale shown in cm)

3.2.4 Resin Tray Stand

The resin tray stand (Figure 3.4) consisted of three machined 136 mm x 136mm x 15 mm aluminium plates aligned one over the other. Four lengths of M6 threaded bar were threaded through holes located in each corner of the plates. The bars were screwed through the lower of the three plates and then directly into the optics table with, nylock nuts used to set the relative heights of the upper plates. The middle of the three plates was used to position the 45 degree mirror used to direct the image produced from the projector mask generator onto the underside of the resin tray.

The higher plate incorporates a 5 mm deep recessed 110 mm x 110 mm square ring in the top face of the platform in which the resin tray can be located during normal operation. A further 90 mm wide square hole was then cut through the rest of this plate to allow the exposure light to reach the underside of the resin tray. Along both the front and back edges of the platform are two retaining clamps that serve to hold down the resin tray during the peeling steps of the fabrication process. The clamps are each held in place with a single screw that can be used to adjust the height at which they take effect. This mechanism is similar to that found on EnvisionTec's Perfactory Desktop [2] systems and allows for complete control over the tilt angle for the peeling process. The tilt angle could then be adjusted depending on the material being used.

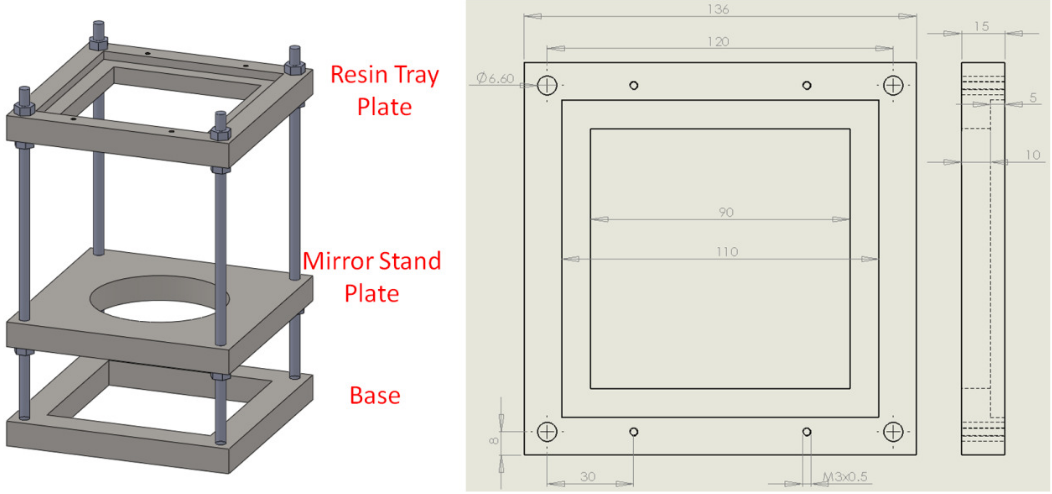

Figure 3.4 – CAD image of resin tray stand (left) and schematic drawing of resin tray platform for the custom MSL system (right) (dimensions in mm)

The initial height of the resin tray platform (Figure 3.4) was designed such that it allowed for optimal use of the full range of motion of the z-axis of the motion stage. It was set such that when the z-axis is fully lowered, the underside of the build platform would theoretically be ~5 mm below the top surface of the resin tray. The extra 5 mm was to allow for variations in thicknesses of different resin trays and build platforms, and to allow for calibration adjustment for levelling of the platform to ensure that the surface of the resin tray is parallel with that of the build platform.

3.2.5 Resin Trays

An attempt was made to fabricate bespoke resin trays by coating 100 mm square sheets of 8 mm thick glass with a layer of PDMS (Polydimethylsiloxane) material. However, it proved difficult to maintain a sufficiently flat surface as the forces exhibited during the peeling process were observed to lift the layer from the glass. Additionally, it was difficult to achieve a surface finish that promoted the peeling separation of the component from the PDMS, rather than the component from the build platform. Therefore, it was decided that used trays from the commercial EnvisionTec Perfactory systems would be recycled and used as they were known to work reliable and repeatably.

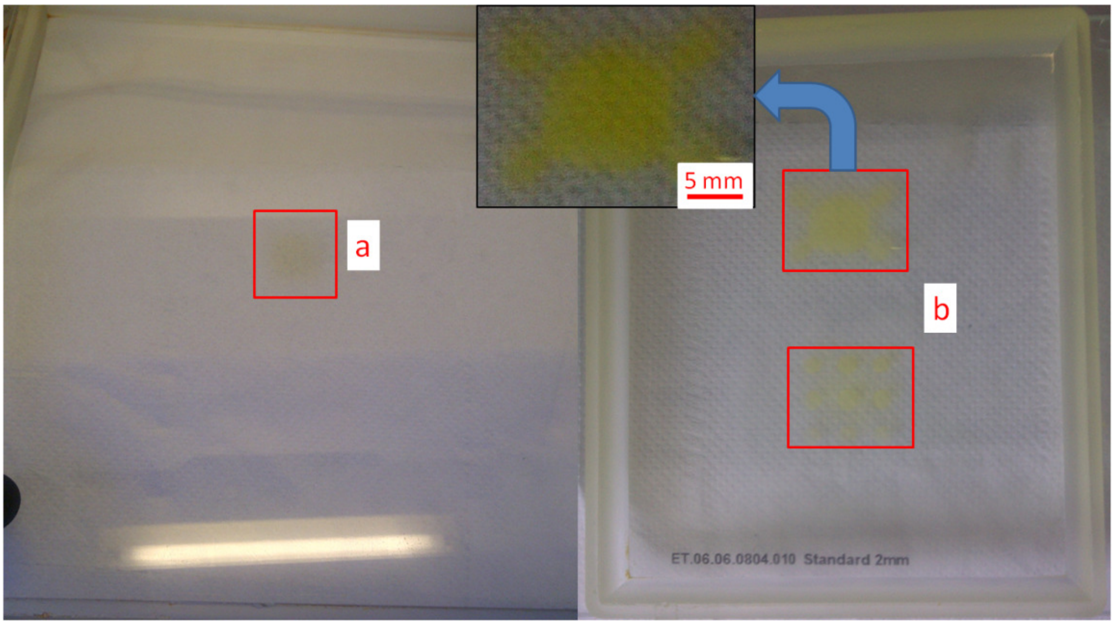

Figure 3.5 – Photograph showing used commercial trays that have absorbed dye material in the exposure area therefore no longer of use in the commercial EnvisionTec system

During the lifetime of a resin tray the process of polymerisation of the resin material attacks and degrades the silicone layer such that the material's dye is absorbed into it. This results in the area of silicone that is over the exposure area gradually becoming increasingly opaque to the exposure field (Figure 3.5). Eventually a point is reached where the degradation is such that it prevents the material curing. The resin trays used on the Perfactory Mini systems are a 340 mm x 270 mm, in which only the centre 28 mm x 21 mm is utilised as the exposure area. Once a tray had reach the end of its normal working life, the remaining undamaged areas were sectioned by using a ceramic tile cutter to cut the glass from the rear, followed by a scalpel to then cut the silicone layer. They were each cut in a set of smaller 100 mm x 100 mm trays that could then be used on the custom system (Figure 3.6).

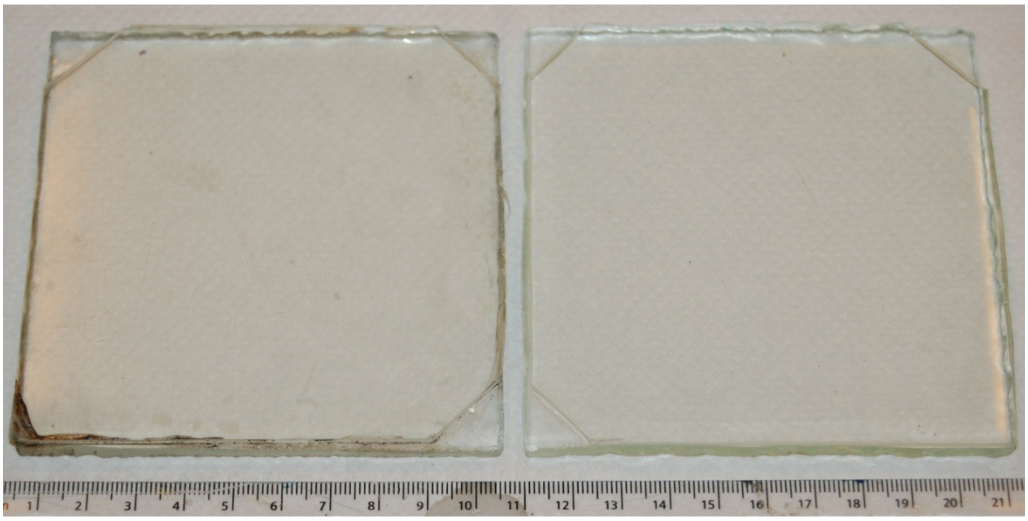

Figure 3.6 – Custom resin plates cut from used EnvisionTec trays. The corner cuts are used to ensure the plates are used in the correct orientation. (scale show in cm)

Calibration plates for the custom system were created in a similar manner by cutting up damaged calibration plates from the commercial system. Typically, these plates are used for calibration of the exposure field and when levelling the resin tray stand to the build platform. However, when conducting some of the work discussed later in this thesis, a calibration plate was mistakenly used as a standard resin tray. The resulting components that were fabricated, in general, were less prone to failure of small features (<1 mm^2) during fabrication. On further investigation, it was also noticed that a number of the materials tested also pooled more effectively during the peeling steps of the build process. It should however be noted that use of the calibration plates in this manner was sometimes unsuitable as the surface coating is noticeably more rigid and was therefore found not to be suitable for highly loaded composite materials (discussed later). It was also observed that use of calibrations plates as resin trays caused unwanted bleeding of the exposure light in non-loaded, un-dyed resins; this therefore reduced the edge definition of the components.

3.2.6 Exposure Light Source

As the intention was to use the new system for material development, some of which may have low or no percentage of dye to prevent overcure it was apparent that the system would require precise control of the dynamic mask system or light source in order to attain desirable results. As mentioned in the previous chapter, the “off” state (where the mask shows a dark pixel) of a pixel using a DMD is not truly black as there is a small quantity of light leakage. This means that while the system is on but not in an exposure step, there would be a small amount of unwanted background that could cause unwanted curing. Therefore, it was decided that the dynamic mask generator/projector (discussed in the following section) would require either a shutter mechanism to isolate the light source, or some means of controlling the state of the light source. The solution decided upon was to use a high power LED (light emitting diode) array. Further reasoning behind this choice was that the range of emitted wavelengths from an LED source is much narrower than that of a traditional bulb. Therefore, when matched with an appropriate photoinitiator, it should provide increased control of the photopolymerisation process. This is due to there being no fluctuating sideband wavelengths which are often found in lamp technology – indeed as the lamp ages, the fluctuations change too, resulting in altered characteristics over time.

A search of the literature shows that the use of LEDs as light source for curing photopolymers has only really been in dental applications for curing small quantities of material[3-7]. The information found in the references suggested, however that LED technology should be capable of being utilised for MSL systems.

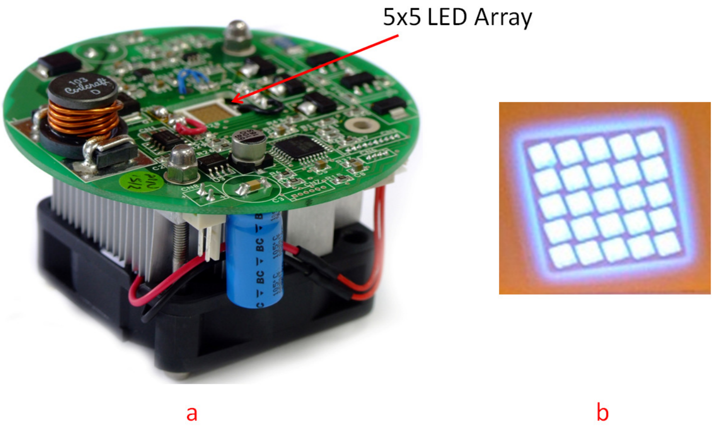

Figure 3.7 – A photograph of (a) an Enfis Uno Air Light engine [8] and (b) the observed array pattern when focused and projected onto a surface

Of the commercial LED arrays available, it was decided that an Enfis (part of Photonstar Technology Limited, UK) Uno Air LED array [8] as shown in Figure 3.7(a), also referred to as a "light engine", would be used. The device consists of a 5x5 LED array (Figure 3.7(b) shows the array's orientation pattern when projected) with integrated controller board. This choice was made primarily due the combination increased light output available compared to other available products, and also because the unit already included the necessary control electronics. The control electronics both regulate the supply current to the array, but crucially also provide a means to control the intensity of the output from 0% to 100% from within the custom software written for the system (discussed later) using a supplied API (application programming interface). The 465 nm variant of the device was chosen as it was believed that it would work efficiently with a readily available photoinitiator, Irgacure 784. The main absorption band for this material ranges from sub 200 nm up to ~340 nm, however, a secondary band lies between 380 nm and 550 nm that would be directly compatible with the LED array output. Table 3.1 provides further specifications of the unit.

		Minimum	**Typical**	**Maximum**	**Units**
Rated Current	I_f		2350		mA
Forward Voltage	V_f	14	16	20	V
Peak Wavelength	λ_p	455	465	475	nm
Spectral Width	$\Delta\lambda$	19	23	27	nm
Total Radient Flux	Φ_R	4000	5000		mW
Total Flux Density	$\Phi_R A^{-1}$	200	10000		mWcm^{-2}
Total Electrical Power	W		38		W

Table 3.1 – Enfis Uno Air Specifications taken from product datasheet [8]

The light engine also provides a more economical alternative to the traditional bulbs used in projectors as they have a lower initial cost (~£100 for a light engine compared to ~£900 for a replacement bulb for the EnvisionTec systems), and require much less energy when in operation. In addition to the cost and energy saving advantages, the light engine generates less heat when in operation such that at most, only a small fan is required for cooling if the device exceeds 40°C although passive cooling using a heat sink is generally sufficient. This has two advantages, firstly the system is less prone to heating the resin material that can increase the rate of aging, and secondly, there is no "warm up" time as there is with lamp based sources. As there is no warm up time involved with LED sources and the device can be controlled directly using software, the array can be rapidly turned off in-between the exposure of layers, therefore eliminating the risk of degrading the resin material due to light leakage through the DMD when the mirrors are set to their "off" .

The biggest advantage with using an LED source is the increased control over the exposure process. Unlike lamp sources, LEDs output a much narrower band of wavelengths that if selected with an appropriate photoinitiator in the resin can reduce the effects of overexposure. Additionally, by utilising the intensity control of the device, the exposure intensity can be adjusted during the build process in order to optimally fabricate using variable layer thicknesses or with multiple materials with differing curing profiles. Figure 3.8 shows the spectral output of the light engine measured using a USB2000+UV-NIR spectrometer (OceanOptics, USA) with a 5ms integration time and a 10 spectra average. The main drawback with using LED technology is that intensity is less than that of a standard lamp, therefore the exposure time of commercial materials is up to 5 times longer than a standard machine. This can be significant since the standard exposure time can account for up to 40% of the time to process a layer.

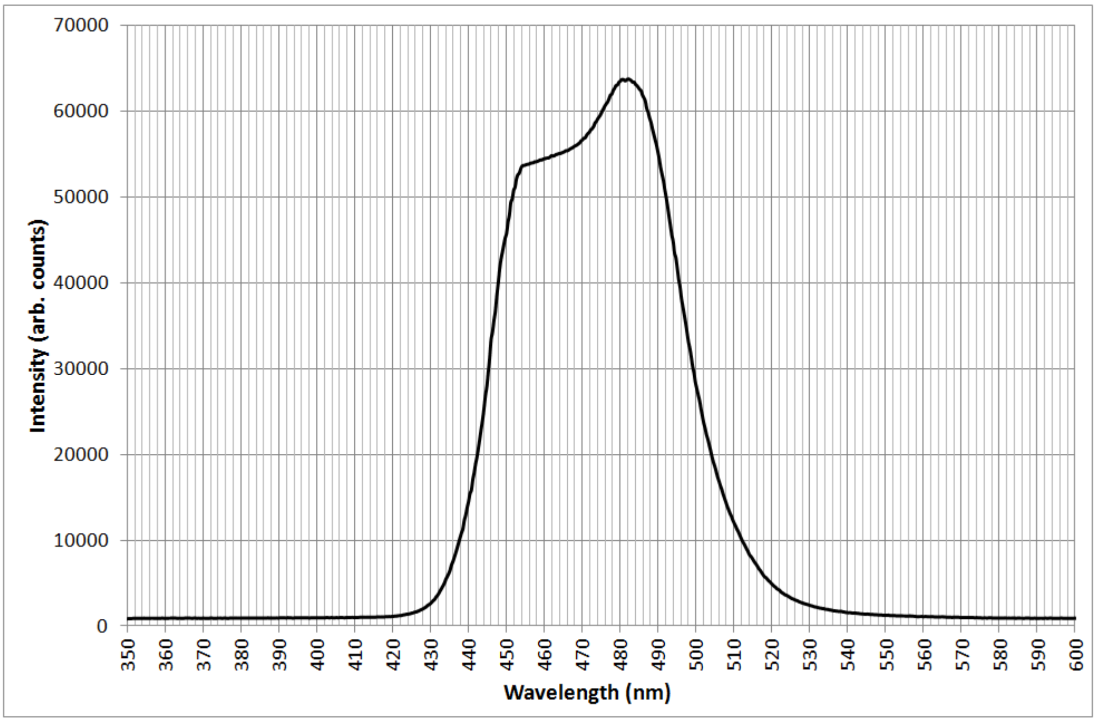

Figure 3.8 – Spectral output of Enfis Uno Air 465nm light engine

Since conducting this work, LED technology has now also begun to be used in commercial systems; both D-Mec (Acculas [9]) systems and EnvisionTec (Perfactory µicro [10]) now offer MSL systems utilising LED technology in their current range.

3.2.7 Dynamic Mask Generator

The projector used in the system was a standard, commercial HP Compaq (USA) MP1800. The reason for this choice was primarily due to its compact size that results in a short optical path length between the light inlet window and the focusing optics that it was hoped would prevent attenuation of the intensity of the output.

In order to utilise the light engine as the light source for the device, both the light engine and projector required modification. The modification of the light engine was required because the circuit board attached to the LED array and heatsink resulted in the unit being significantly larger in diameter than the lamp originally used in the projector. As such the LED array, heatsink and cooling fan were removed from the circuit board containing the control electronics. A mounting bracket was fabricated that allowed the heatsink for the LED array (to which the LED itself was adhered) to be directly mounted in place of the original lamp (Figure 3.9(a)). The bracket included a section of aluminium box tube to act as a light guide and integrator (Figure 3.9(b)) between the array and light entry window of the projector. Flying leads were then used to reconnect the array, temperature sensor and cooling fan to the light engine's control board that was mounted remotely.

The modification of the projector involved using a microcontroller to emulate feedback from a number of the projector's existing subsystems such that the systems could be disabled without the projector detecting an error and affecting the operation of the unit. The two systems that were emulated were the lamp driver (such that the projector would not detect the missing lamp), and the colour wheel position feedback as the colour wheel was disabled and its position fixed such that the clear filter segment of the wheel was in the light path. A single PIC12F675 (Microchip Technology Inc, USA) with code written in assembly language was used to accomplish both of these tasks. The code first waits for an input signal that detects whether the projector has instructed the bulb to turn on, once this signal is received, there is a wait period of 4 seconds (that was previously measured as the typical bulb start time) before the microcontroller pulls low the bulb acknowledge feedback line to instruct the projector that the bulb has ignited. At this point, the projector usually starts the colour wheel rotating, however, as the colour wheel was disabled, the microcontroller then outputs a further signal that emulates the opto device monitoring the rotation of the colour wheel. These modifications then enable the projector to function in an otherwise normal manner while the unwanted systems are disabled. The circuit is fully embedded within the projector and is powered by the projector's internal supplies. Figure 3.9 shows the projector complete with modifications.

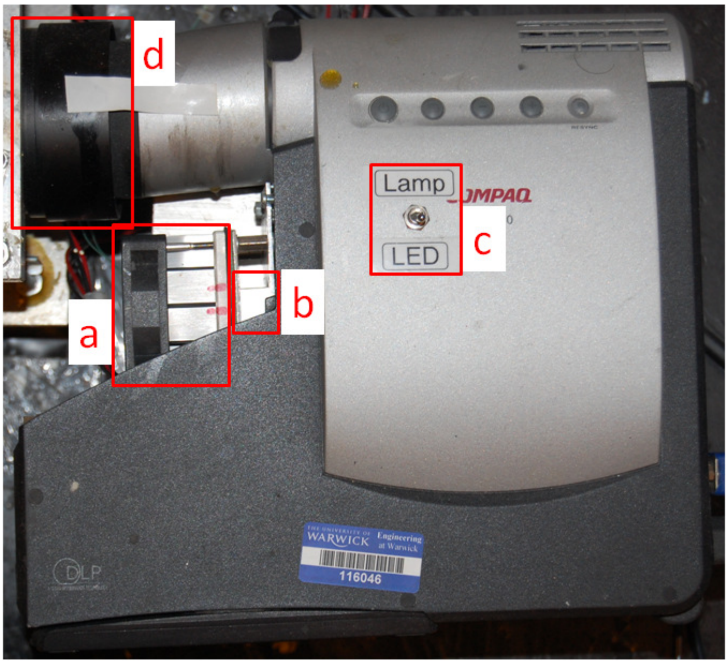

Figure 3.9 – A Compaq MP1800 projector with modified such that it continues to operate without after lamp has been replaced with (a) an alternate light source. Also highlighted are (b) the light guide to prevent leakage between array and the projector's input window, (c) the light source selection switch, and (d) modified optics to reduce the focal distance and size of the projected image

The modifications were preformed such that if the operator wished to return to using a lamp as the exposure source all that would be required would be to swap the LED array and lamp and to toggle the source select switch (Figure 3.9(c)), a further switch was used to toggle use of the colour wheel if required. Figure 3.9(d) shows an additional optics module used to reduce the dimensions of the image output from the projector. For normal operation, the system was setup with a build envelope of 30 mm x 22.5 mm which with the 1024 x 768 native resolution of the DMD within the projector produces an XY pixel size of 29 µm. The system has however been successfully tested down to a resolution of 15 µm pixels with a build envelope of ~15.5 mm x 11.5 mm.

3.3 Custom MSL System - Software

In order to control the system, custom software was written to run on the system's computer using the C# programming language in Visual Studio 2010 (Microsoft Corp., USA). The software was designed such that it allows control over every stage of the build process including modification and overriding of the build parameters and pausing of the process during fabrications.

The software requires the computer to have 2 display devices, one to display the user interface and a second that is shown on the projector as the dynamic masks. When the program initially starts it initialises the second screen with a blank, black image to prevent any exposure of the resin material while communication with the controller for the light engine is being established. The XYZ stage is then instructed to move to its home position. This locates the build platform centrally above the resin tray at its full height. The interface then waits for further user input while continually updating the display with the current feedback position of the XYZ stage along with the temperature and electrical parameters of the light engine (Figure 3.10(a)).

The software includes controls for manual movement of the XYZ stage (Figure 3.10(b)) that are used to manoeuvre the build platform away from the resin tray during exposure field calibration and for calibration of the origin (Figure 3.10(c)) (the absolute z height when the build platform is in contact with the resin tray). These controls can also be used in conjunction with the functions to manually load dynamic mask images (Figure 3.10(d)) from png (portable network graphics) image files, and control the light engine (Figure 3.10(e)) in order to manually fabricate components or individual layers.

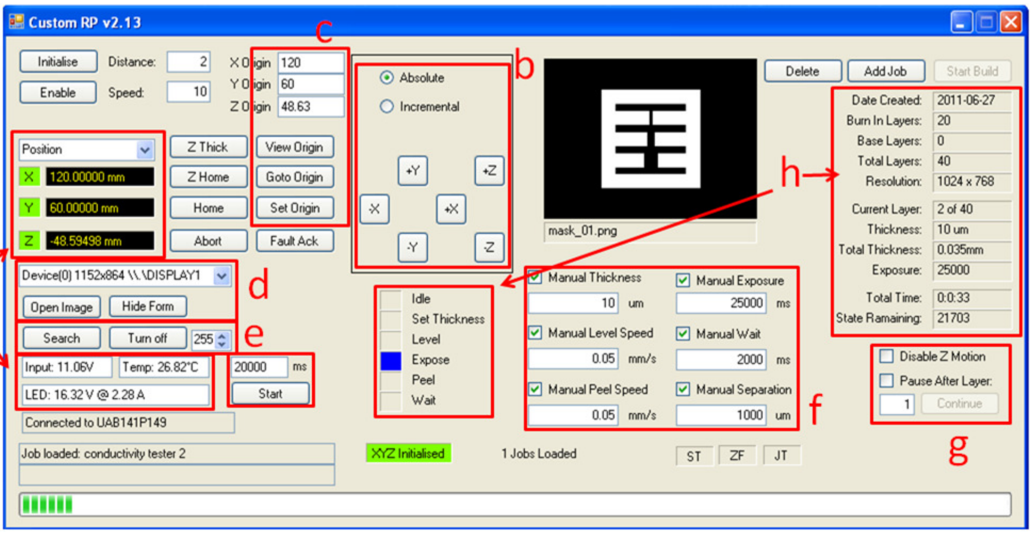

Distance: 2
Speed: 10
X O igin 120
Y O igin 60
Z O igin 48.63
Position
X 120.00000 mm
Y 60.00000 mm
Z -48.59498 mm
● Absolute
○ Incremental
Device(0) 1152x864 \\.\DISPLAY1
255
Input: 11.06V
Temp: 26.82°C
LED: 16.32 V @ 2.28 A
20000 ms
Connected to UAB141P149
Job loaded: conductivity tester 2
XYZ Initialised
1 Jobs Loaded
mask_01.png
☑ Manual Thickness 10 um
☑ Manual Exposure 25000 ms
☑ Manual Level Speed 0.05 mm/s
☑ Manual Wait 2000 ms
☑ Manual Peel Speed 0.05 mm/s
☑ Manual Separation 1000 um
Date Created: 2011-06-27
Burn In Layers: 20
Base Layers: 0
Total Layers: 40
Resolution: 1024 x 768
Current Layer: 2 of 40
Thickness: 10 um
Total Thickness: 0.035mm
Exposure: 25000
Total Time: 0:0:33
State Ramaining: 21703
☐ Disable Z Motion
☐ Pause After Layer: 1

Figure 3.10 – Custom MSL system user interface with key controls and indicators highlighted. (a) feedback for current motion stage position and light engine status, (b) manual controls for motion stage, (c) build platform calibration controls, (d) manual mask controls, (e) manual exposure controls, (f) build parameter override controls, (g) build pause control, and (h) current build status indicators

Under normal operation, the software utilises “job” files created by EnvisionTec’s Perfactory RP software that is used to convert the STL (Standard Tessellation Language) files produced by the CAD software into a slice “job” file. In this mode the system operates in a fully automated manner. Further controls allow the user to override the wait, motion speed, exposure and layer thickness settings before or during the build process (Figure 3.10(f)). These were included so that the optimum build parameters for different materials and techniques could be easily established without the need to reprocess the CAD file each time. Additionally, the process can be paused at any point during the process (Figure

3.10(g)). When the process is paused, the build platform raises to its home position to allow for inspection, or for the resin to be topped up or replaced. As the build progresses, the current state and progress of the process is also shown on the user interface (Figure 3.10(h)).

By using custom software written C# it allows for simple adaptation and updating of the software for custom applications, for example, modified versions of the software were also written specifically for fabrication of GRIN (Gradient-INdex) lenses and other optical devices. Figure 3.11 shows a selection of test components fabricated using this system. This includes an umbrella test component fabricated using both a PEG (polyethylene glycol) material and a commercial material, R11 (EnvisionTec GmbH, Germany). For comparison, also shown is the same umbrella component fabricated using R11 on an EnvisionTec Perfactory system where it should be noted that the systems were not capable of fabricating the handle section of the design.

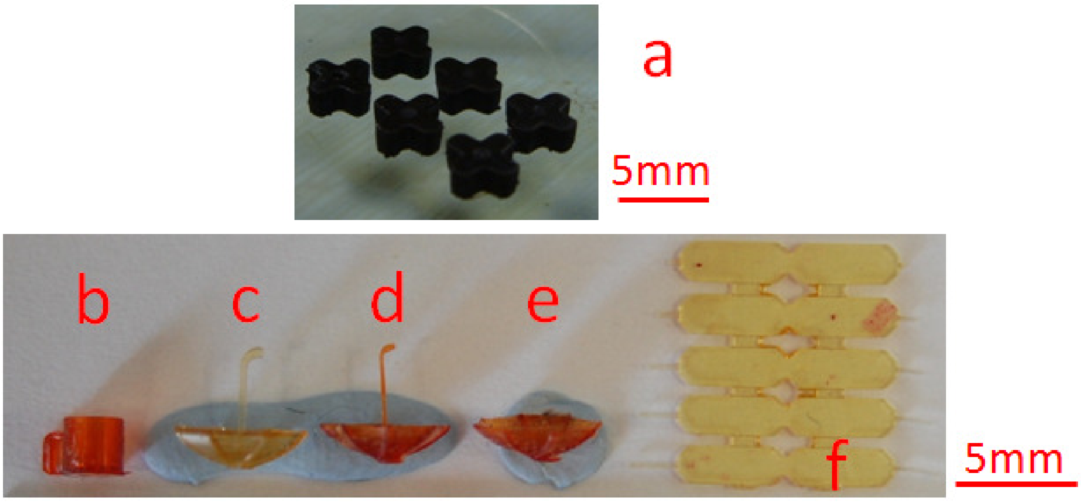

Figure 3.11 – Photographic images showing test components fabricated using the custom MSL system ((a)-(d) and (f)), and an EnvisionTec Perfactory Mini system (e). (a) shows micro-impellers fabricated using a magnetic composite material. Other test components shown are a mug (b), three umbrellas ((c), (d) and (e)) and a set of cantilever beams (f). The orange material in (b), (d) and (e) is a commercial material (R11), the lighter material in (c) and (f) is a custom PEG based material developed specifically for the custom system.

3.4 Custom Multi-Material MSL System

During the course of the research, it was found to be desirable to be able to fabricate components using multiple materials such that the functional materials (discussed later) could be embedded within housings such that fully functional components could be fabricated in a single build process. This functionality then makes MSL technology comparable to silicon process that can incorporate different functional layers on one device. A search of the literature shows that Choi et al have previously investigated multi-material fabrication using for both stereolithography [11] and microstereolithography [12] processes. However, these existing multi material systems utilise free surface fabrication using laser and projection exposure methods respectively. Although multi-material builds are demonstrated the materials used are purely structural and offer no further benefits beyond being able to fabricate multi coloured components. A disadvantage of both systems presented is that they both require large reservoirs of material, the MSL system in particular used a vat that is gradually topped up using a syringe pump throughout the process. Therefore the systems require a large excess of material and thorough cleaning of the component between materials that would result in damage to the component for complex components due to the repeated exposure to the cleaning solvents. In contrast, the multi-material system built for this work was again based on the constrained surface model that does not require large quantities of excess material to fill the resin vat and only requires the last ~2 mm of the components to be exposed to the cleaning solvent between changing of the materials.

The design for the multi-material system was based on the previously described custom system and as such used an Aerotech motion stage for the z-axis (ANT130-060-L-Z-25DU with Ensemble MP controller) that had an identical set of build platform arms mounted to its face such that the build platforms could be interchanged between systems. Similarly, the same model of HP Compaq MP1800 projector was used. For this system, an additional carriage was designed to replace the resin tray stand. The carriage (shown in

Figure 3.12(a)) incorporates 4 recessed areas for resin tray caddies (Figure 3.12(b)) that in turn have a resin tray/plate held in them using grub screws.

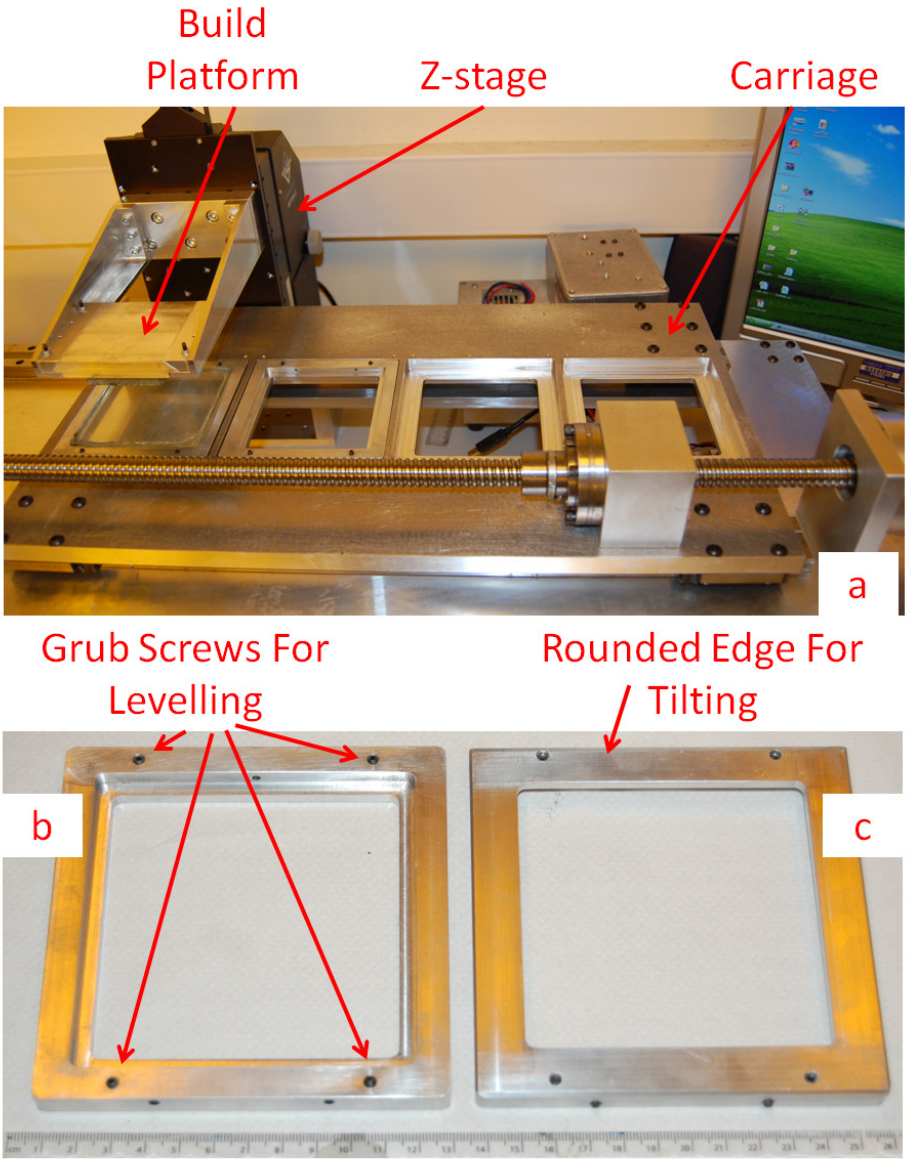

Figure 3.12 – Photographic images showing (a) carriage component of multi-material MSL system, (b) top and (c) reverse sides of resin tray caddies

An additional 4 grub screws are located along the front and rear edges of each caddy. These were to enable levelling of the plates to the build platforms. The back edge on the underside of the caddy (Figure 3.12(c)) was also chamfered to enable smooth tilting during the peeling step of the fabrication process. Currently, only 3 of the 4 trays are useable as the 4th recess is used to hold a small tray of propan-2-ol in order to wash off excess material between swapping material trays – this prevents cross contamination of the materials. The carriage was itself mounted via linear bearings to a table area that stood over the projector. A lead screw with an appropriate stepper motor was included such that the carriage could be instructed by the system's software and interface unit (discussed later) to move along the x-axis such that different resin trays (and therefore materials) could be positioned for use.

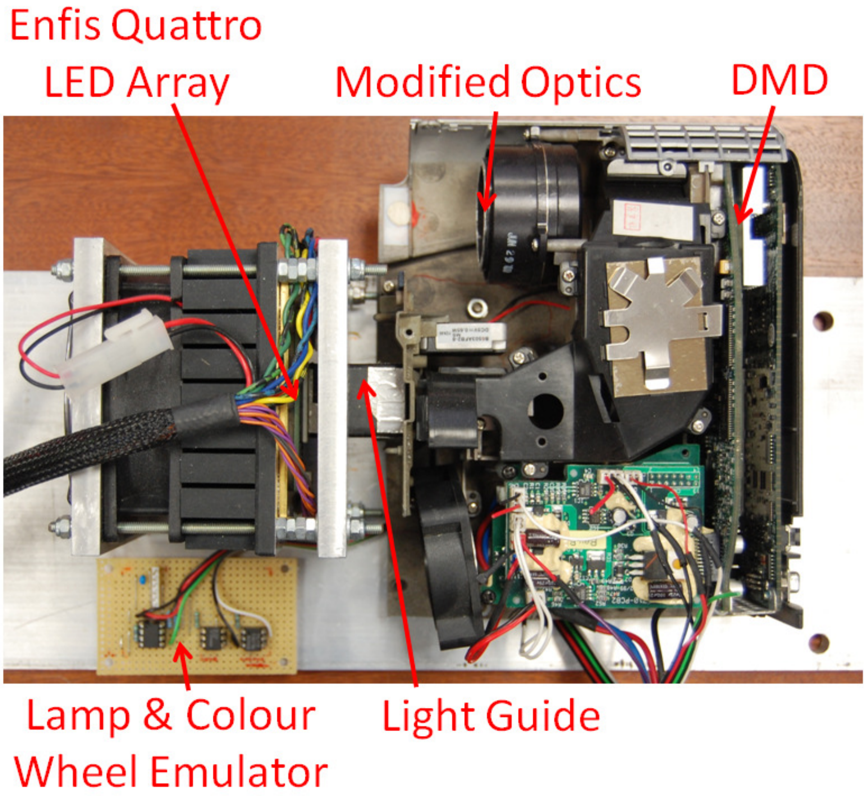

Figure 3.13 – Photograph showing a HP Compaq MP1800 projector modified to use an Enfis Quattro Mini Air LED array for use in the multi-material MSL system

A number of commercial resin materials tested on the single material custom system that include large dye percentages were found to take in excess of 30 seconds of exposure to cure the desired layer thickness. Therefore, in order to reduce this time, a higher power LED light engine was incorporated in the multi-material system. The light engine used was Quattro Mini Air (Enfis Limited, UK) with a typical light output of 16.5 W [13] (compared to the 5 W for the Uno light engine used in the single material system). However, due to the increased dimensions of the cooling apparatus required for this device, the housing of the projector required modification (Figure 3.13). Additionally, the area of removed housing incorporated the projectors power supply, therefore this was removed and housed separately.

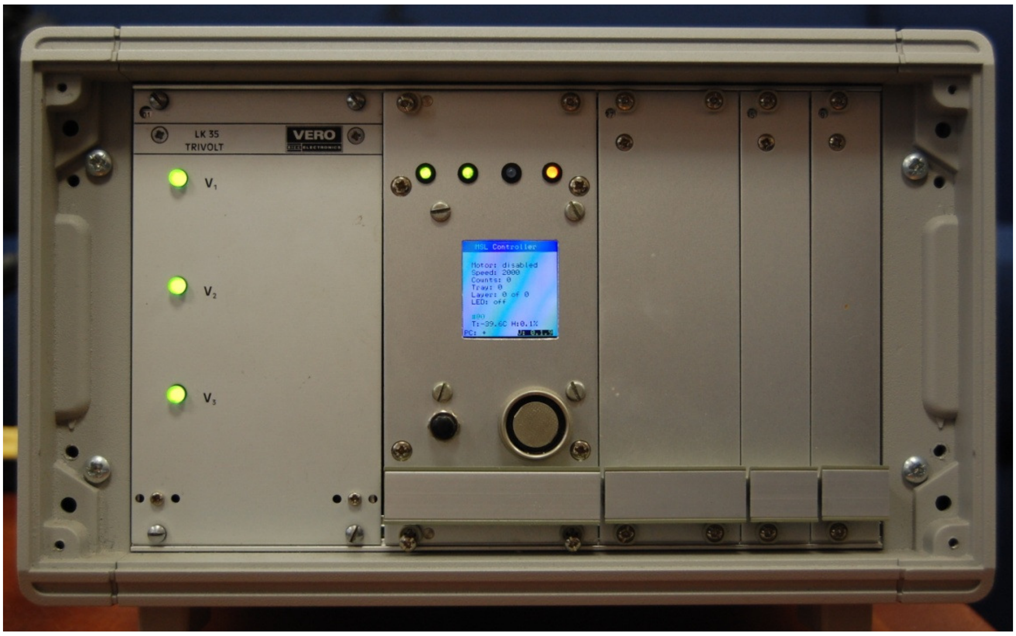

```
MSL Controller

Motor: disabled
Speed: 2000
Counts: 0
Tray: 0
Layer: 0 of 0
LED: off

#00
T:-39.6C H:0.1%
PC: +                V: 0.1.5
```

Figure 3.14 – Interface unit for controlling carriage motor and monitoring of sensors on the custom multi-material MSL system

The interface unit (Figure 3.14) is based around a PIC24HJ256GP610 (Microchip Inc, USA) microcontroller (schematic in Appendix A). Its primary purpose is to provide a simple interface between the control software on the PC and the additional hardware systems such as the motor controller for the carriage system. It therefore accepts ASCII based commands that can be used to select a particular resin tray, set the motion speed of the carriage or update the status information on the included graphic LCD screen for build job details and progress. Due to the number of moving parts on the system a number of security and safety features were also incorperated. This included an emergency stop button and an iButton interface (Maxim Electronics, USA) that was to prevent unauthorised users from operating the system. Both of which are managed by the interface unit. A Sensirion SHT75 is also mounted on the build platform arms in order to monitor the ambient temperature and humidity around the build platform.

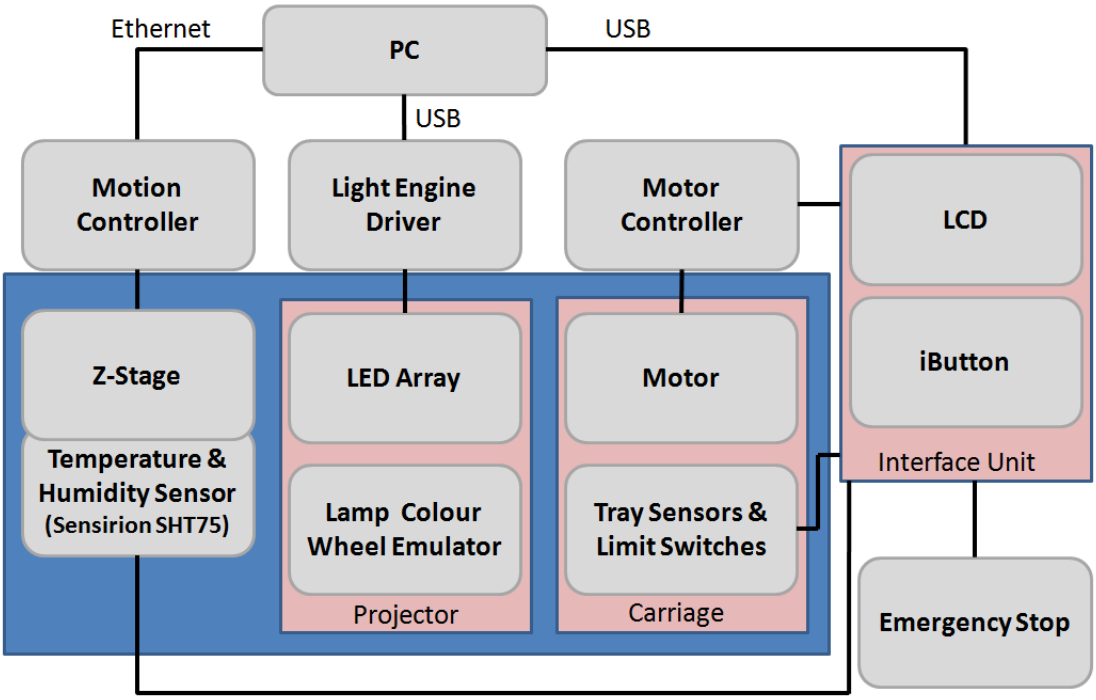

Figure 3.15 – Diagram showing the component parts of the custom multi-material MSL system

The carriage motor is controlled via the interface unit using a stepper motor chopper driver (Quasar Electronics Ltd, UK) that is based on L297 (stepper motor controller) & L298 (dual full-bridge) devices from STMicroelectronics (Switzerland). A set of 4 light gates were used by the interface unit as feedback to verify the position of the carriage. Additionally, lever arm micro switches were located at either end of the carriage as limit switches. While not fully implemented in the current iteration of the hardware design, the controller's software also includes functionality to use heated resin trays with temperature feedback and auxiliary outputs which it is envisioned could be used to control a more advanced washing system. A diagram of the system is shown in Figure 3.15.

In order to fabricate components using multiple materials, the PC control software from the previous system was modified such that is could communicate with the external interface unit and so that multiple build files could be simultaneously loaded. Each of the build files is required to contain the necessary information to fabricate a single material. The software allows each build file to be associated with a material. As the fabrication process is being run, the software sequentially steps through each image mask for each layer and determines which materials the layer contains.

Figure 3.16 shows a set of 6 simple demonstration dog-bone components fabricated using the system. Although this particular build was largely successful, it can be seen by the inconsistencies in layer structure in the second (yellow) material that it essential that all traces of solvent are removed from the partially built components before proceeding with the next material.

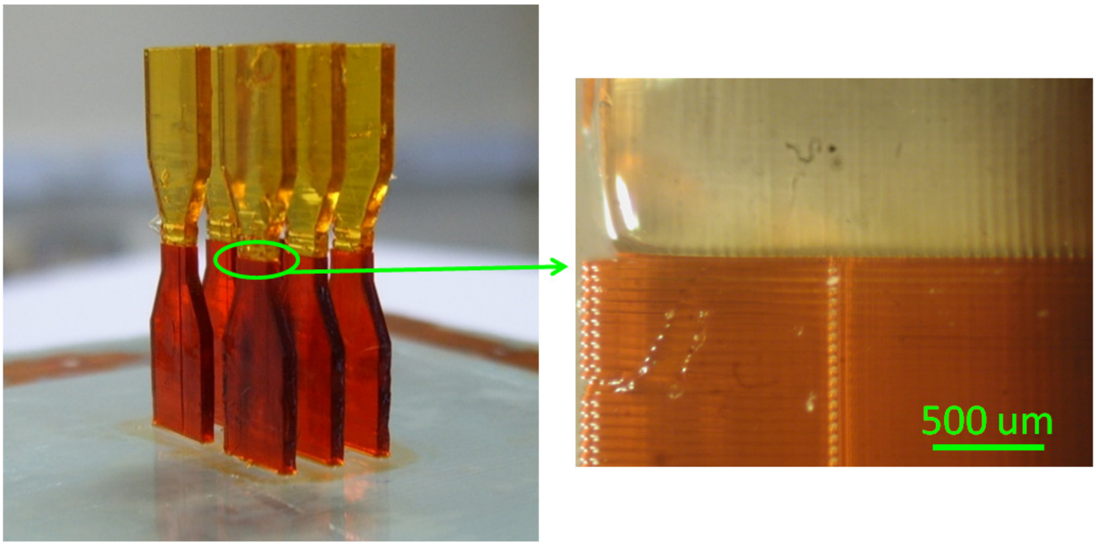

Figure 3.16 – A set of 6 example dog bone components fabricated using the multi-material MSL system

3.5 Conclusion

This chapter describes the design and assembly of two custom microstereolithography systems. Their purpose was to enable the use of custom photopolymer materials that require build parameters outside of the available range for typical commercial systems. Both of the systems utilise the constrained surface fabrication method using DMD based projection exposure systems and LED technology as an exposure source. The systems use build files generated by EnvisionTec's Perfactory RP software that enables seamless migration between existing methods of producing components from the CAD software and use of the new system.

The first custom system operates as a traditional MSL system would, but provides controls such that parameters such as exposure duration and intensity, motion speeds, layer thickness and wait times can be easily overridden or altered "on the fly" without the need to reprocess the original CAD drawings – significantly reducing development time.

The second of the systems, while based on the design of the first, incorporated an additional multi resin tray carriage system. The addition of the carriage system allows the system to fabricate components using up to 3 different materials. The intensity of the LED light source can be adjusted easily in the system's software such that materials with differing exposure intensity requirements can be used in the same build process.

3.6 References

[1] Perfactory3 SXGA+ w/ERM Mini Multi Lens Specification Sheet, EnvisionTec GmbH, [online] available from: http://www.envisiontec.de/admin/machine_datasheet/Datasheet_machine57.pdf (last accessed: 02/02/2012)

[2] EnvisionTec Perfactory Desktop datasheet, EnvisionTec GmbH (Germany), [online] available from www.envisiontec.de/index.php?page=machines&id=25 (last accessed: 18/06/2012)

[3] A. Uhl, R.W. Mills, K.D. Jandt, Polymerization and light-induced heat of dental composites cured with LED and halogen technology, Biomaterials 24 (2003) 1809–1820

[4] A. Uhl, R.W. Mills, K.D. Jandt, Photoinitiator dependent composite depth of cure and Knoop hardness with halogen and LED light curing units, Biomaterials 24 (2003) 1787–1795

[5] F. Stahl, S.H. Ashworth, K.D. Jandt, R.W. Mills, Light-emitting diode (LED) polymerisation of dental composites: flexural properties and polymerisation potential, Biomaterials 21 (2000) 1379-1385

[6] A. Uhl, R.W. Mills, A.E. Rzanny, K.D. Jandt, Time dependence of composite shrinkage using halogen and LED light curing, Dental Materials 21 (2005) 278–286

[7] G. LaTorre, L. Marigo, G.A. Pascarella, G. Rumi, Light-emitting diodes (LED) technology applied to the photopolymerization of resin composites, Minerva Stomatologica 52 (2003) 193-200

[8] Enfis Uno Air 465nm Light Engine Datasheet, Enfis UK

[9] Acculas Microstereolithography Systme Datasheet, D-Mec [online] www.d-mec.co.jp/eng/pdf/eng_acculas_catalog_new.pdf (last accessed: 08/03/2011)

[10] Perfactory µicro Specification Sheet, EnvisionTec GmBh, [online] available from: http://www.envisiontec.de/admin/machine_datasheet/Datasheet_machine68.pdf (last accessed: 24/05/2012)

[11] J-W. Choi, H-C. Kim, R. Wicker, Multi-material stereolithography, Journal of Materials Processing Technology 211 (2011) 318-328

[12] J-W. Choi, H-C. Kim, R. Wicker, Multi-material microstereolithography, International Journal of Advanced Manufacturing Technology 49 (2010) 243-551

[13] Enfis Quattro Mini Air Cooled Light Engine Datasheet, Enfis UK

Chapter 4

4 Development of an MSL Compatible Magnetic Material

This chapter details the development and characterisation of a novel composite magnetic polymer resin material for use with microstereolithography (MSL) systems. The developed resin incorporates a loading of magnetite nanoparticles, and provides a novel means to fabricate components with magnetic properties that can provide a functional use within the built components. An example of a practical application of the material is demonstrated in the following chapter.

The first section examines the basic development of the material. Some of the issues associated with producing an MSL resin material with magnetic filler particles is also covered. The second section covers basic mechanical testing in order to verify the material's ability to be used in applications involving sustained force or movement. Finally, a suitable means of detecting magnetic fluctuations caused by the material is presented.

4.1 Introduction

The magnetic properties of materials have been harnessed for practical uses for many hundreds of years [1]. Magnetic materials are widely used and can be found in many common everyday objects ranging from simple devices such as a compass to more complex devices including motors and actuators (CD/DVD players), alternators, digital storage media (Floppy Disks, Hard Disks), super conducting magnets (MRI scanners), and sensors (to activate reed switches or for flow sensors). Magnets can be manufactured in a wide variety of shapes, sizes and with varying strengths. However, the ability to quickly and easily design and fabricate custom micro-structures that can be made to exhibit magnetic fields or have specific properties (such as low coercively for producing magnetic memory media) are not currently available. The material demonstrated here uses magnetite – a ferrimagnetic material which can be magnetised post-fabrication. This ability to fabricate such components would provide an additional tool for use in rapid micro-fabricated systems such as lab-on-chip devices and micro actuators.

As discussed in Chapter 2, recent advances in microstereolithography technology mean that it is increasingly being seen as a manufacturing technology rather than purely as a rapid prototyping process. Although the range of available resin materials is steadily increasing, the current range is still heavily focused on structural resins for applications in, for example the manufacture of hearing aids [2, 3] or sacrificial casting [4, 5] for the jewellery industry [6]. However, the ability to fabricate components using MSL with functional properties creates potential for a much wider range of applications.

It is only within the past decade that research has begun to deal with the synthesis and fabrication of magnetic polymers. A particular area of recent rapid development is in the field of functional magnetic polymer beads and nanospheres [7, 8] that have applications in biomedicine [9] for cell separation, protein purification etc [10] to isolate magnetic materials from a biological solution.

It has been previously demonstrated that it is possible to fabricate both carbon [11] and organic polymer (PANiCNQ) [12] based materials that exhibit ferro- and antiferro- magnetic properties at room temperature. However, not only does their fabrication require specialist equipment, they are difficult to reliably reproduce and are currently limited in the magnitude of the field they can generate and the duration for which the field can be maintained (only a few hours). Therefore, they cannot be made use of in day to day applications.

A more common and reliable method to produce “magnetic plastic” is to create a composite consisting of a polymer containing a loading of a magnetic material [13-15]. N. Damean et al [16] have previously demonstrated the use of magnetic nickel nanoparticles / epoxy composite in a lithography processes. The work presented was based on an SU8-50 photoresist with suspended 80-150 nm diameter nickel nanoparticles. However, the loadings achieved were relatively low at only 13% by weight (only 5% by weight was demonstrated). SU-8 based polymers also require additional baking steps pre- and post-exposure stage along with a developer stage to remove excess material. Therefore, although it was demonstrated that it is feasible to create a magnetic/photopolymer composite, this would not be a feasible method in an MSL base process though as it would require the component with its build platform to be removed and baked before additional layers could be built.

A paper by Nonakova et al [17] investigated the magnetic behaviour of a polymer nanocomposite containing magnetite nanoparticles (~10 nm) in a polyvinyl alcohol matrix. While more recently, Kobayashi et al [18] discussed adding ferrite particles with a mean particle diameter of 1.3 μm to a standard photocurable polymer (SCR770 from D-MEC Ltd.). They used a laser based MSL system with loadings of ferrite material between 30% and 50% by weight. While actuation using such material was mentioned, it was not demonstrated.

4.2 Types of Magnetism

The magnetism of a material is a property that causes a response to an applied magnetic field. Similarly, a magnet is a component or object that exhibits a magnetic field either directly due to the material properties or by the flow of an electric current. Magnetic materials are traditionally associated with compounds containing metal ions, where the magnetism is a caused by the electron spins in the atoms of the material being aligned. There are a number of different types of magnetism, which are defined by the spin of the electrons in the material [19] (Figure 4.1); Table 4.1 provides a brief explanation of the different types of magnetism.

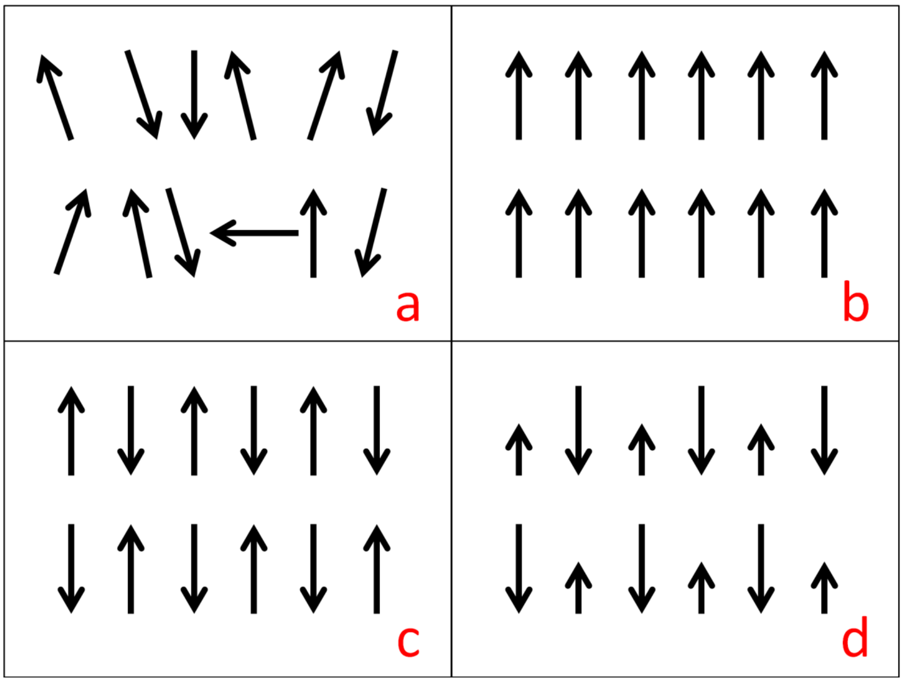

Figure 4.1 – Spin configurations for (a) paramagnetism, (b) ferromagnetism, (c) antiferromagnetism, (d) ferrimagnetism

Type	Description
Diamagnetism	A property that appears in all materials that causes the material to show a small magnetic moment that opposes an applied magnetic field. When no field is applied the material shows a net magnetic moment of zero [20]. If a material possesses paramagnetic properties then the paramagnetic properties will dominate.
Paramagnetism	A property that will cause the material to be attracted to the region of greater magnetic field, such as an electromagnetic field or a ferromagnetic material. It occurs when the material's atoms have unpaired electrons. The unpaired electrons can align its magnetic

	moment in any direction, so when an external magnetic field is applied the electrons align in the same direction. When the field is removed, the electron fields scatter and cancel each other out.
Ferromagnetism	Is similar to paramagnetism in that the material has unpaired electrons but the magnetic moments prefer to align themselves in a parallel fashion in order to maintain a low energy state. As the aligned magnetic moments are in the same direction, a ferromagnet can maintain a magnetic field without the influence of an external applied field. Ferromagnetic materials are the strongest and most common type of permanent magnets.
Antiferromagnetism	Is similar to ferromagnetism except that the parallel aligned magnetic moments of neighbouring electrons are in opposing directions, causing a net magnetic field of zero.
Ferrimagnetism	Is similar to antiferromagnetism however, the magnetic moment of the electrons in one direction is greater than those in the other direction. The resultant net magnetic moment is therefore non-zero. A ferrimagnet can therefore retain its magnetisation without the presence of a magnetic field but generally the field is weaker than that which would be found in a ferromagnet. The oldest known ferrimagnetic material is a mineral called ferrous-ferric oxide or iron(II,III) oxide - also commonly known as magnetite. Magnetite has the chemical formula Fe_3O_4 and is most magnetic of all naturally occurring minerals [21].

Table 4.1 – Different types of magnetism

An important property of any magnetic material is remanence. Remanence is a measure of the magnetisation that remains in a material after it has been exposed to an external magnetic field that has later been removed. It is effectively the magnetic memory of a material and as such is the basis behind all forms of magnetic storage media [22] such as computer floppy discs and hard drives. When a material is magnetised (or poled) it is said to have remanence if its magnetisation does not relax back to zero after the removal of the external field. In order to remove the magnetisation the magnet must be exposed to a field in the opposite direction.

4.3 Material Development

The idea of adding insoluble particles to a photocurable resin is not a new. This method is already used to create other commercially available materials such as ceramics (EnvisionTEC RC Nanocure Materials [23]) and more recently piezoelectric materials [24, 25]. The composite material developed consisted of two main components parts, a base photopolymer resin and a loading material. The base resin is similar to standard MSL resins used for building structural parts as it consists of a number of other component parts including, the monomer, crosslinker and the photoinitiator. Existing commercially available resins cannot be used as the base for a new loaded resin as a dye is invariably included in the formulation to prevent overcure outside of the intended areas and ensure accurate parts are produced. Due to the opacity of the loading material (in this case, nanoparticles), it also has the affect of attenuating the curing light. Therefore, using a base resin with a dye already included would result in an insufficient penetration depth of the exposure light. Even when using a dye-less material, there is a trade off between having a greater amount of loading (to increase the functional properties of the material), or having less loading in order to improve build performance (i.e. thicker/quicker to cure layers). The purpose of the loading material is therefore to ensure that the end resin exhibits the desired functional properties, but also to partially replace the function of the dye.

Another consideration when attempting to use higher loadings is the effect of material viscosity. Although thinner layers are required in order to successfully cure the full depth of the layer due to the attenuation of the exposure light, often highly loaded materials can cause issues with levelling of the build platform. The problem is caused by the increased force required to be applied by the z axis motion stage due to the increased viscosity of the material. Care also has to be taken when using small particles as loading materials, as the scattering effect that occurs due to the high refractive index difference between the particle and the resin increases as the particle size approaches the wavelength of the exposure light [26]. The effect is not only on cure depth but also cure radius, which affects the sharpness and quality of the fabricated parts. In light of these potential problems, some initial experiments were conducted in order to ascertain the feasibility of resins loaded with a magnetic filler material.

A number of powdered magnetic materials were tested including neodymium-iron-boron ($Nd_2Fe_{14}B$), aluminium-nickel-cobalt (AlNiCo) and magnetite (Fe_3O_4). To investigate whether different resin mixes were curable, samples of the materials (~0.1 ml) were cured using an Otoflash G171 (NK-Optik GmbH) which is generally used for post-curing components after fabrication. The samples were deposited using a micro-pipette onto standard glass slides which were then placed in an Otoflash device and flashed for a series of 50 flash cycles (at a rate of 10 flashes per second). After each cycle, the samples were tested to see whether they were cured simple by dragging another slide over the top of the deposited material to verify if any liquid resin remained. Fill loadings of particles between 1% and 50% by weight were used.

During the preparation of the materials it was quickly apparent that both the neodymium-iron-boron and aluminium-nickel-cobalt particles would be unusable. While mixing the material the neodymium-iron-boron powder rapidly aggregated due to its ease of aligning and the mixing procedure aligning the particles. Therefore, although the material exhibited favourable curing speeds, simple observation demonstrated that a homogenous mixture could not be achieved and therefore the material would not be suitable. By contrast, the aluminium-nickel-cobalt particles appeared to inhibit the curing mechanism of the resin even with relatively low loadings. This is thought to be caused by absorption of the exposure light by the filler particles. Therefore, further investigations were conducted using the magnetite nanoparticles (approximate diameter 50 nm, Sigma–Aldrich, UK). Initial experiments demonstrated homogenous initial mixing and curing properties that suggested that it would work with the custom MSL system. As mentioned previously, magnetite is a ferrimagnetic material and as such can be poled with the application of an external magnetic field; however, the remanence of the material would be less than that of the ferromagnetic materials.

Initial base resins were polyethylene glycol (PEG) based, as in other previous experiments they had previously proved easy to work with and generally accepted additive materials. Two problems were observed with the PEG based materials when used with the magnetite particles. Firstly, after curing, the material became brittle and difficult to handle; a hobby knife with a wide, straight edged blade is usually used to remove components from the build platforms, but when this was used with the PEG materials the edges of the samples easily chipped and crumbled. Secondly, as the magnetite particles were denser than other fillers previously used, it was found that a significant amount of the particles began to fall out of suspension only minutes after the material had been stirred. This would mean that resin would have to be continually stirred in order to stay usable. However, as a typical build time using MSL is usually greater than 30 minutes, the material would likely become unusable before the end of the build process.

As an alternative a HDEDA (1,6 hexanediol-ethoxylate diacrylate) monomer was used. Formulations using HDEDA proved to provide much more reliable and repeatable results. This was mainly due to the magnetite particles being held in suspension for much longer periods than the PEG material before showing signs of the material degrading - such as particles falling out of suspension or ambient room light causing unintentional curing of the material in the storage vial. It was however observed that due to the natural magnetic attraction of the magnetite nanoparticles there was still a tendency that over time they would aggregate together. As such, the ratio of monomer to crosslinker was biased towards achieving a slightly more viscous resin than would usually be used with MSL. Due to the increased viscosity, the resin produced was not only able to achieve a significantly greater magnetite content (50 wt% was achieved where as only 15 wt% was achieved using PEG), but the material also showed better structural integrity on removal of the samples from the glass slides.

Both mixing order and the duration of mixing of the resin components were discovered to be important factors in being able to produce a usable resin. The method found to produce the most satisfactory and repeatable results began by measuring the monomer into a mixing vial using a pipette followed by the cross linker. To reduce the stir time for this first stage of the mixing process, the crosslinker was warmed in a separate vial in a water bath heated to 35 degrees with the aim of reducing its viscosity. The two components were then mixed using a magnetic stirrer & bar for 30 minutes. After this period the photoinitiator was added and the vial was completely wrapped in aluminium foil to prevent any ambient light in the room from degrading the mix. This was then stirred for a further 60 minutes to ensure that the photoinitiator was completely and evenly dispersed.

Before adding the magnetite nanopowder, the vial was taken off the magnetic stirrer and the stirring bar removed. Mixing of the material with magnetic particles posed an issue since stirring could not be done using a magnetic stirrer as it caused the material to aggregate in the bottom of the vial. Once this happened it proved virtually impossible to re-disperse. To avoid this, a non-magnetic, perforated paddle was used. It was also observed that if the paddle width was too small, the magnetic particles began to aggregate in the corner area of the vial. The paddle was attached to a small 12v DC motor with a 100mm long shaft to ensure that the motor didn't interact with the magnetite particles in the resin. The magnetite powder was then slowly added and mixed for a final 10 minutes. The duration of the final "stir time" was one of the most critical points of the process. If the mixing time was insufficient then the built components contained regions with little or no filler. If however, the material was over mixed then the nanoparticles begin to aggregate. Although the areas of aggregation appear evenly throughout the sample, the increased radius of the aggregate cluster caused build failures as the cluster can be wider than the thickness of the desired layers. At best, this gives a "lumpy" finish and texture to the part; at worst it will prevent the MSL system from being able to set the layer thickness correctly. Figure 4.2 shows microscopy images a magnetite resin mix after a selection of final stir times.

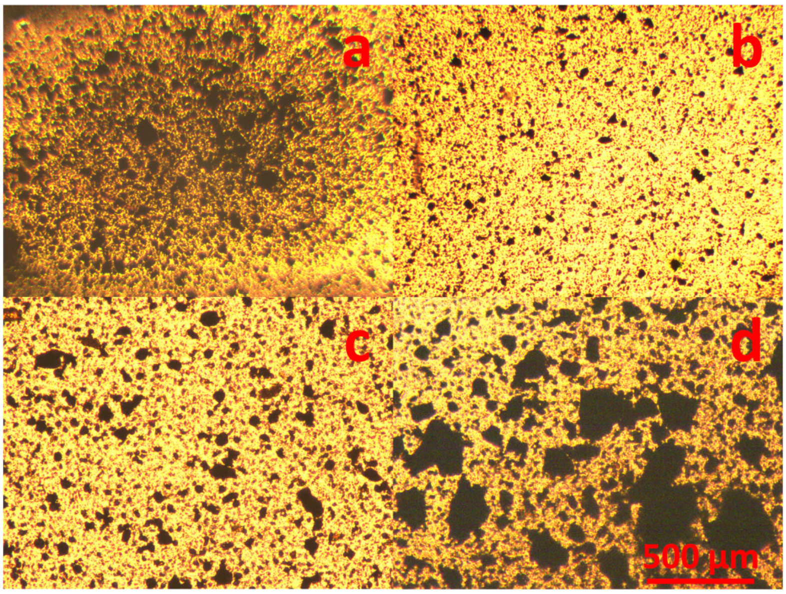

Figure 4.2 – Microscopy images of magnetite resin samples after (a) 5 minutes, (b) 10 minutes, (c) 15 minutes, and (d) 25 minutes of stirring

The final stable formulation that enabled reliable building and generated repeatable results was a custom magnetite/acrylic resin formulation which was composed of a 1:2 ratio of the monomer HDEDA (1,6 hexanediol-ethoxylate diacrylate) to the crosslinker, DPPHA (dipentaerythritol penta-/hexa-acrylate). Irgacure 784 was selected as a suitable photoinitiator as its peak sensitivity is in the wavelength region of maximum intensity for the light engine being used in the custom MSL machine. The quantity of photoinitiator used was 5% by weight.

4.4 Initial Build Tests

Following on from the initial curing experiments, further investigations were conducted to discover the workable cure depth of single layers that could be used to provide consistently reliable and repeatable results. A component was designed that would be used to observe the effect of the magnetite particles in the resin.

4.4.1 Design and Fabrication

A component with a comb shaped structure was designed (Figure 4.3a) in order to conduct a basic test to investigate cure depth and the mechanical response of the material in a magnetic field. The dimensions of the components were chosen such that there was a large bulk area which could be used to clamp the device when testing, and an adequate length such that a number of “fingers” could be included and equally spaced (in this case 10). The “fingers” of the component were designed with a long aspect ratio to test the adhesion of small areas to the build platform during fabrication, and to ensure that a measureable deflection of the tips occurs when exposed to a permanent magnet. The part was designed in CAD and exported to the slicer program, however, in this instance, the build only required a single layer so after the part had been sliced, and a single image mask (Figure 4.3b) was extracted from the created build file. The custom machine was then used in its manual operating mode so that each step of the build procedure could be verified. For each build a small amount (~0.2 ml) of resin was manually deposited using a syringe onto the resin tray of the custom MSL system, directly under the build platform. The material used a loading of 35% by weight of the magnetite nanoparticles.

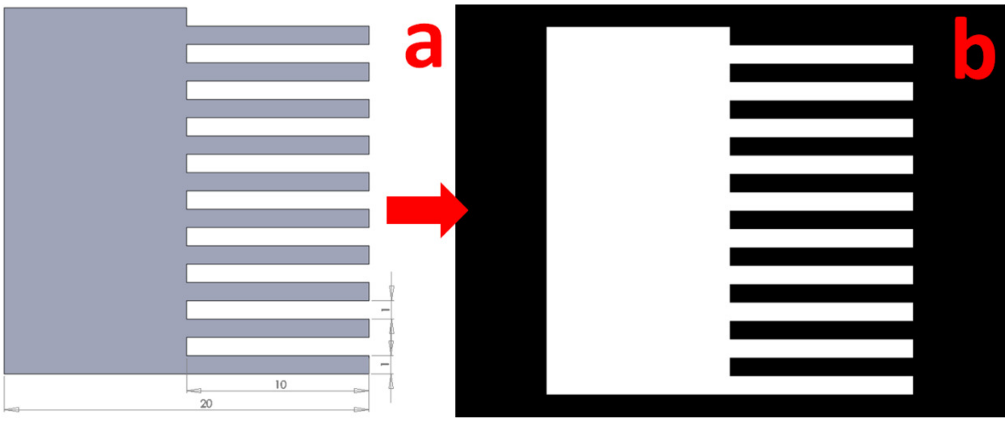

Figure 4.3 - (a) CAD image (dimensions in mm) and (b) png of single layer for comb device (dimensions in mm)

Firstly, a series of single layer builds were attempted using a combination of different exposure times and layer thicknesses. The experiment began by attempting a layer thickness of 15 µm as this is conventionally a standard lower bound thickness for MSL. Further layers were then attempted with increasing thicknesses of 5 µm until the quality of the builds became unacceptable.

It was observed that attempting to use layer thicknesses of 20 µm or less was not possible. This conclusion was made by observing the feedback readings from the linear drive, which was used to set the layer thickness, showing that the force required to set such a thickness was at the limit of what the machine could achieve. As such, the thickness of the layers was often unpredictable or in some cases the over-current protection of the linear drive prevented levelling at the desired level. It is thought that this is due to both materials having a greater viscosity than more conventional resins and also areas of aggregation of the magnetite particles. Layer thicknesses between 25 µm and 40 µm were possible providing that the resin was free of aggregate clusters, while layer thicknesses between 40 µm and 60 µm were tolerant of a small amount of aggregate clusters.

At layer thicknesses of 65 µm or greater the layers began to exhibit signs of failure, which is not uncommon, even with standard materials, if they are pushed to the limits of their operating range. Voids in the intended build area occurred where an air pocket had not been properly forced out; this is often caused by the levelling speed being too great, the wait time being too short, or the material being too viscous for the set layer thickness. While a slower levelling speed could have been attempted, it was felt that this was unnecessary as the speeds being used were 90% slower than standard levelling speeds to ensure that the success or failure of the build was primarily a factor of layer thickness and exposure parameters.

While conducting the work for other groups, it was observed that even when using a commercially available system with an approved compatible material, similar voids caused by trapped air bubbles can occur when the resin becomes viscous. In these cases the increased viscosity was due to either using older resin that had begun to degrade, or where the resin batch being used had experienced one or more builds fail during its use (failures occur due to poor/incompatible component designs or by insufficient exposure).

It was also observed that in a significant number of cases, areas of the layer became delaminated from the build platform during or after the peeling stage of the process. This occurs when an insufficient level of the exposure light has reached the rear side of the layer, due to the light from the exposure source being significantly attenuated by the magnetite nanoparticles such that photopolymerisation cannot fully occur. While this could potentially be overcome by increasing the exposure light intensity, or by extending the exposure time of the layer, it was felt that these were not viable options in this case. This was because it could be seen that the front side of the layer (the side in contact with the resin tray) had been successfully fully exposed, and therefore further exposure would lead to overcure in these areas. This also indicates that the cure level was significantly inconsistent through the thickness of the layer, which is undesirable when fabricating a part consisting of multiple layers as the mechanical behaviour of the part becomes unpredictable.

The optimal layer thickness for the material was therefore found to be between 20 µm and 60 µm – although resin mixes from older batches (> 24 hours) still proved to be unreliable with 60 µm layers. As such, further work continued using layer thicknesses of 25 µm, or if the material began to show signs of aging with aggregate clusters, then 50 µm layers were used. These are also standard layer thicknesses used for MSL fabrication; therefore the results obtained should be comparable to other existing setups. At these thicknesses, the optimum exposure times per layer were found to be 60 seconds for 20 µm layers and 90 seconds for 50 µm layers.

A final comb test part was built consisting of four 25 µm layers (Figure 4.4). After fabrication the part was carefully removed from the build platform using a craft knife and rinsed with propan-2-ol to wash away any uncured resin material that may have been present on the surface. The part was then post-cured in the Otoflash unit with 100 flashes.

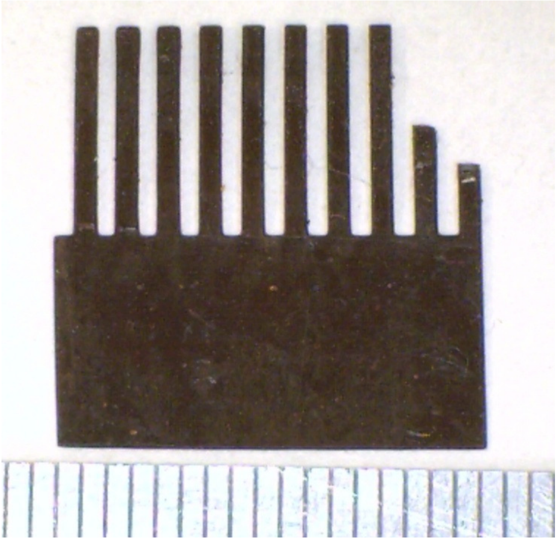

Figure 4.4 – Microscopy image of comb device fabricated using magnetite composite material (units in mm)

4.4.2 Testing

After fabrication, it could be seen that the component exhibited ferrimagnetism as it was easily attracted to a permanent magnet held at a distance of ~15mm, and showed small amounts of attraction to other ferrous objects. A mechanical rig was setup in order to conduct a test of the deflection of the fingers at different standoff distances from the permanent magnet. To do this, the Z-axis motion stage of the custom built MSL machine was utilised as a means to accurately position the magnet at the desired distance from the component. The magnet was an N42 neodymium permanent magnet whose remanence, Br, was measured to be ~1.2T. This value was calculated by measuring the field strength, F, at a distance, z, using a Bell (Bell Labs, USA) 640 Incremental Gaussmeter (assisted by Dr Yichao Fan, Department of Physics) and the using Equation 4.1 where L is the thickness of the magnet, and D is the diameter of the cylindrical magnet.

$$F = Br\left(\frac{z+L}{\sqrt{4(z+L)^2+D^2}} - \frac{z}{\sqrt{4z^2+D^2}}\right) \tag{4.1}$$

The permanent magnet was mounted to the glass underside of the MSL machine's build platform using double sided adhesive tape, while the bulk area of the component was securely clamped to the surface of the resin tray using a length of aluminium bar. A vertical scale was setup next to the build platform in order to measure the deflection of the fingers with different offsets (Figure 4.5).

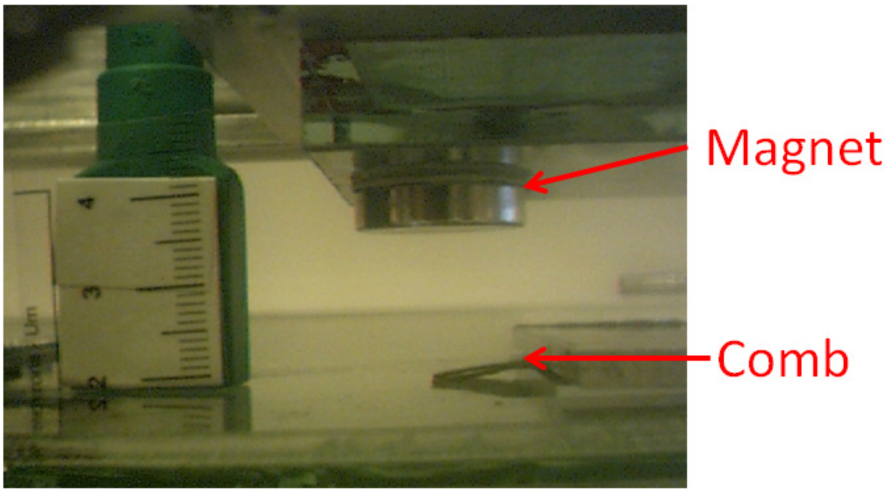

Figure 4.5 – Photographic image showing test setup for measuring B-field effect of a permanent magnet on the magnetic comb test part (scale in cm)

The control software for the MSL system was used in its manual mode so that the build platform (attached to the Z-stage) of the machine could be moved up and down by set distances by entering commands. The initial distance between the magnet and the comb structure was 16 mm ±0.2 mm. Figure 4.6 shows the average displacement of the tips of the fingers as the magnet is moved closer to the structure and then away again. On the first run, one of the fingers had noticeably greater deflection up to 6.5 mm, at which point it broke away from the structure. The test was repeated after the fingers had been manually pushed back to a flat position. Here it can be seen that displacement of the fingers was greater than on the previous run and the standard deviation at each point was also less. This suggests that the material may have fatigued at the pivot points and hence allowed a greater displacement. The maximum deflection observed was on the second run where one finger achieved an inclination of 58.2°. The graph also demonstrates the approximate exponential relationship between the force and distance from the magnet. It is also clear that there is a hysteresis effect in the motion of the fingers. It is felt that there are two reasons for this, firstly that the fingers do not return to their original position due internal mechanical stresses within the part causing a memory effect in the polymer. Secondly, it is felt that as the distance between the magnet and device decreases, the magnet is poling the magnetic particles within the material. Indeed when the displacement of the magnet was 8 mm from its initial position, the fingers of the device became in contact with the magnet. Therefore when the magnet is moved back to its initial position, the fingers are still showing sufficient attraction that they remain slightly raised.

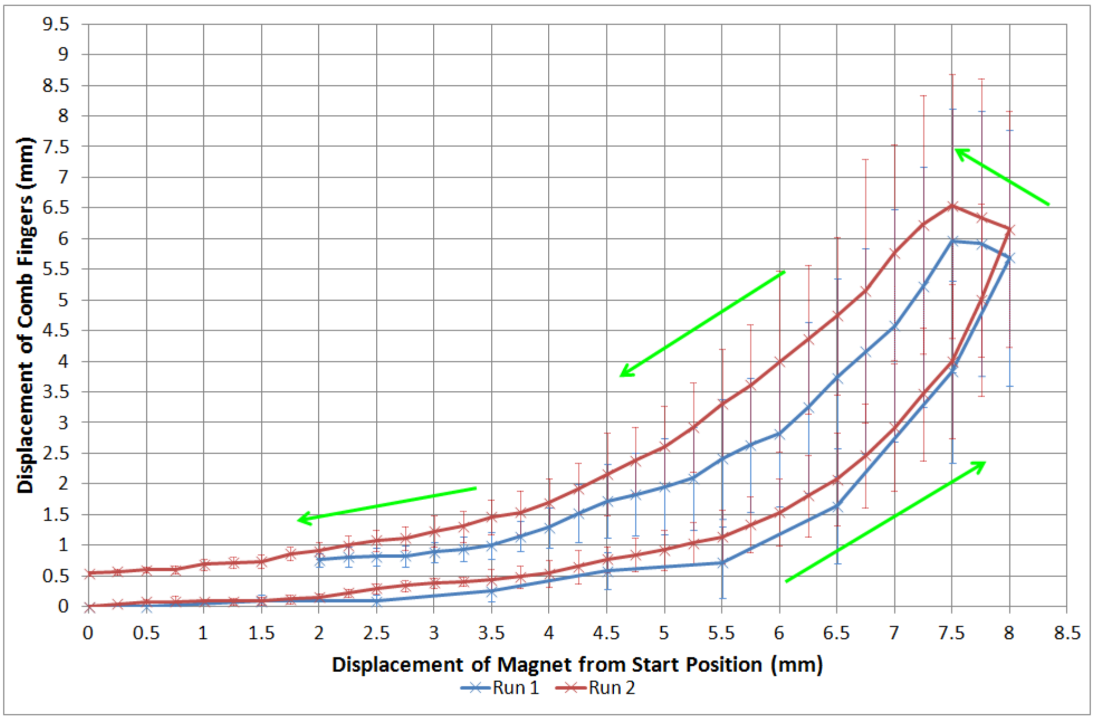

Figure 4.6 – Average displacement of 10 fingers against magnet stand-off. At a magnet displacement of 8 mm, the fingers touched the magnet.

As mentioned, during the experiment one of the fingers of the component broke off due to the force of the magnetic attraction being too great for the interface where the finger comes out of the bulk area. As only one finger broke with up to 3 others demonstrating signs of fatigue, it indicates that there may have been inconsistencies in the structure of the fabricated part. Such a thin part may also have been prone to damage during the process of removal from the build platform or during post-processing. The same specimen was fabricated using both R11 (Envisiontec GmbH) and the base material used for the composite, but the same weaknesses were not observed. However, the R11 version did exhibit severe deformation as the solvent (propan-2-ol) used during post processing evaporated from the part's surface. It is therefore apparent that the addition of the magnetite nanopowder had increased the components rigidity, but made it more prone to fatigue.

4.5 Multi- Layer Components

Following the successful building of the comb specimen, a larger component consisting of multiple layers was designed. The design was a simple cube with 5 mm long vertices. The dimensions were chosen as it was felt they were representative of typical components being built using the material. Due to their size, a set of 4 cubes could be fit onto a platform during fabrication. The purpose of these components was to test whether the material could be used to build components using the standard MSL technique – rather than just fabricating single or double layer parts as the comb device was.

While the magnetic comb component used a magnetite loading of 35% by weight, it was observed that this level of loading the repeated levelling and peeling action of the build platform caused the material to aggregate throughout the build process. The extent of the aggregation was not sufficient to cause the build process to fail; however, the aggregates caused an uneven distribution of the filler within the resin. This meant that as the build progressed, the later layers had areas without loading (Figure 4.7). In addition, this resulted in an uneven surface finish and prevented the material from flowing properly between layers. Therefore, in order to complete the fabrication the wait time had to be increased and the levelling speed reduced.

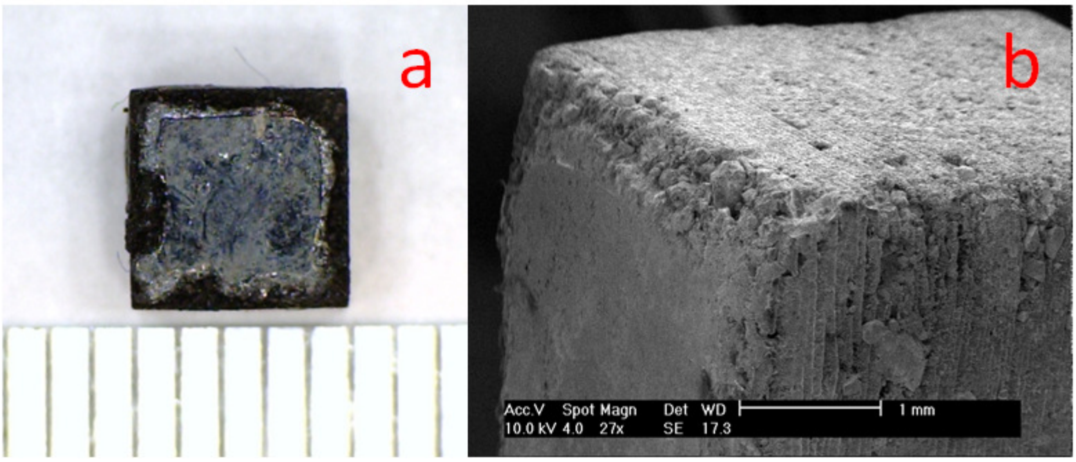

Figure 4.7 – (a) microscopy (scale in mm) and (b) SEM images showing filler voids in final layers of cube due to aggregation

By reducing the loading to a level of 25% by weight produced the aggregation effect was dramatically decreased such that it only began to occur once the resin was more than 6 hours old or if 1000 or more layers were attempted. While a loading of less than 25% would also work (providing the exposure time or intensity was reduced), it was thought that the strongest magnetic field possible (and thus, highest loading) would be the most useful for the majority of applications.

4.5.1 Fabrication of Multi-Layer Test Cubes

Using this adapted resin, a series of solid cubes were built successfully. The cubes were 5 mm x 5 mm x 5 mm and built with 100 layers each with a thickness of 50 μm using a 90 second exposure. To ensure that no voids were present in the complete component and to reduce the aggregation of the magnetite particles in the resin during the build process, the motion speeds for levelling and peeling were set to 0.1 mm/s, with a 2 mm separation distance and a post level wait time of 2 seconds per layer. The build therefore took 3 hours and 40 minutes to complete. Figure 4.8 shows a cube from the completed build.

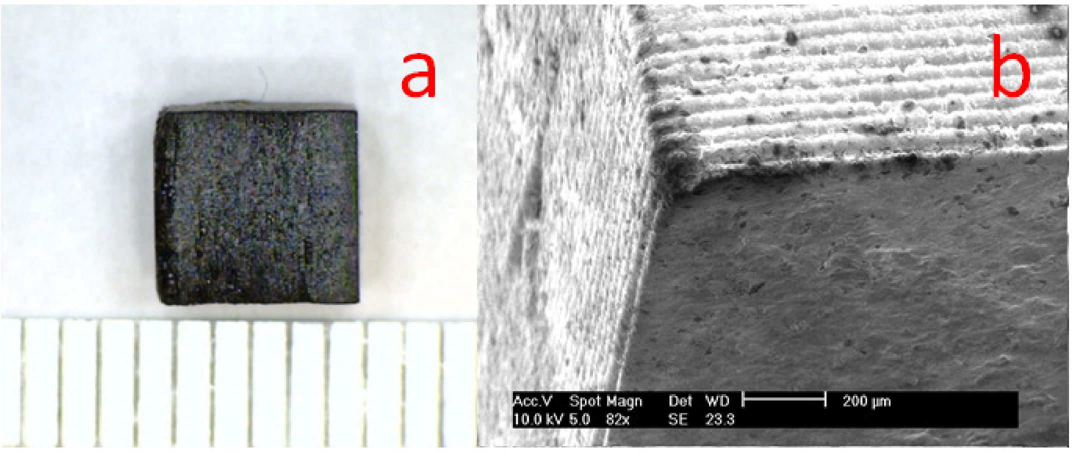

Figure 4.8 – (a) microscopy (scale in mm) and (b) SEM images showing successful build of cube with lower loading

After the cubes had been built and were still in their "green" state, they were manually rinsed with isopropanol to remove any cured resin remaining on the surface. They were then blotted dry on paper towel to remove the excess isopropanol before being post cured. The post curing was done with the Otoflash using a setting of 500 flashes on each face of the cube to ensure the parts were sufficiently cured throughout. Figure 4.9 shows that the cubes were attracted to a neodymium magnet and were able to support themselves being hung upside down from the magnet.

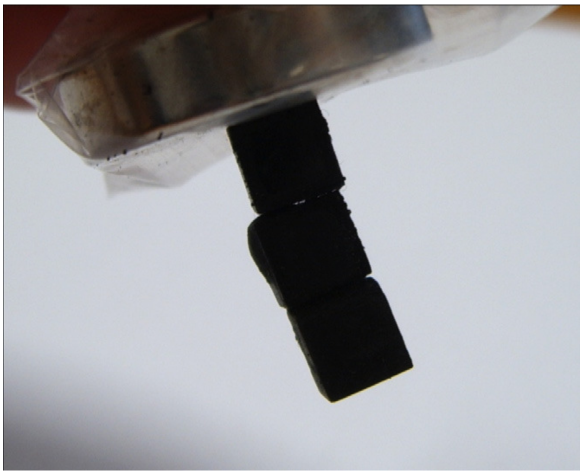

Figure 4.9 – Three cubes fabricated using magnetite composite material being attracted to a neodymium permanent magnet

4.5.2 Mechanical Analysis

As the intention for the magnetic material was for it to be used in applications where forces may be applied, a further set of cubes were fabricated to be used to test the mechanical compression properties of the material, while two sets of dog bone shaped components were fabricated for tensile testing with 25 µm and 50 µm layer thicknesses. So that a comparison can be drawn from a known reference, a set of components were also fabricated using a commercially available material, R11 (EnvisionTec GmbH) at 25 µm.

Compression testing was conducted using a Z030 (Zwick/Roell) mechanical tester at the University of Birmingham (UK). The tester was setup to run with a constant velocity of

1 mm/s and measure force-displacement data at a rate of 10 samples per second. As the MSL process produces anisotropic components, compression tests were conducted both along (Figure 4.10(a)) and through (Figure 4.10(b)) the layer plane on both materials. The specimens were tested until they failed. A compression test can be used to determine a material's behaviour under a crushing load. The data obtained was then used to plot appropriate stress/strain graphs (Figures 4.11 and 4.12).

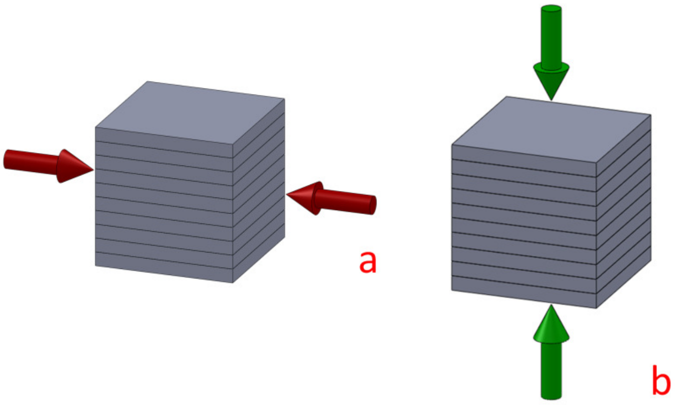

Figure 4.10 – Schematic showing direction of applied force for (a) along (parallel) plane and (b) through (perpendicular) plane compression testing

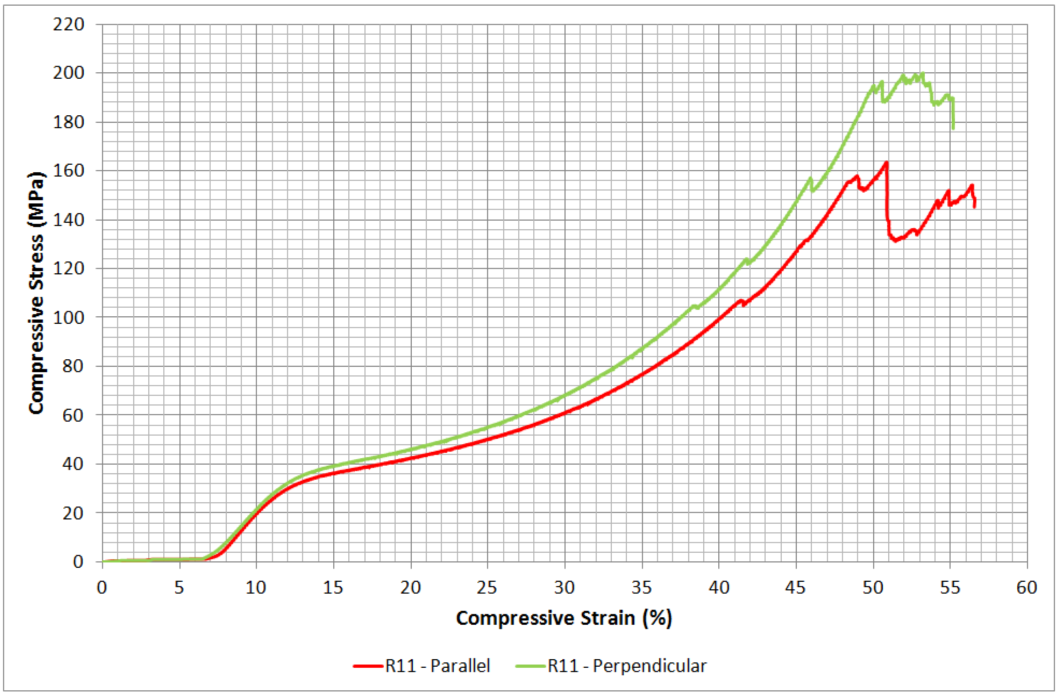

Figure 4.11 – Stress/strain graphs for compression tests of test cubes fabricated with R11

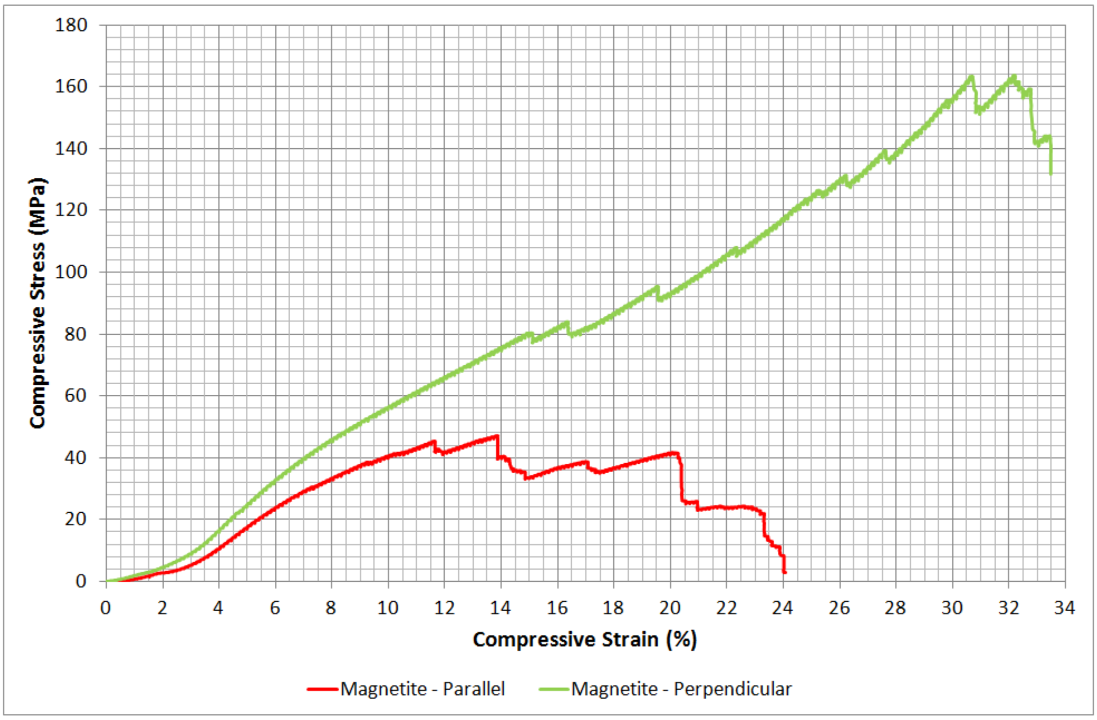

Figure 4.12 – Stress/strain graphs for compression tests of test cubes fabricated with magnetite composite material

Using this data, the compressive yield strength for each material and orientation can be obtained (Table 4.2).

	Yield Strength (Parallel) (MPa)	**Yield Strength (Perpendicular) (MPa)**
Magnetite	47.0	163.8
R11	163.5	200.2

Table 4.2 – Compressive yield strength of test cubes fabricated with magnetite composite and R11 materials with force applied both parallel and perpendicular to the fabricated layers

Tensile testing was then conducted using a Deben 2KN (Deben UK Ltd, UK) tensile mechanical tester. Again, the samples were tested until they failed. The tester was set at an extension rate of 0.1 mm/min with a data sampling rate of 10 samples per second. Figures 4.13 to 4.15 show the tensile results for the R11 and magnetite materials at 25µm and 50 µm respectively.

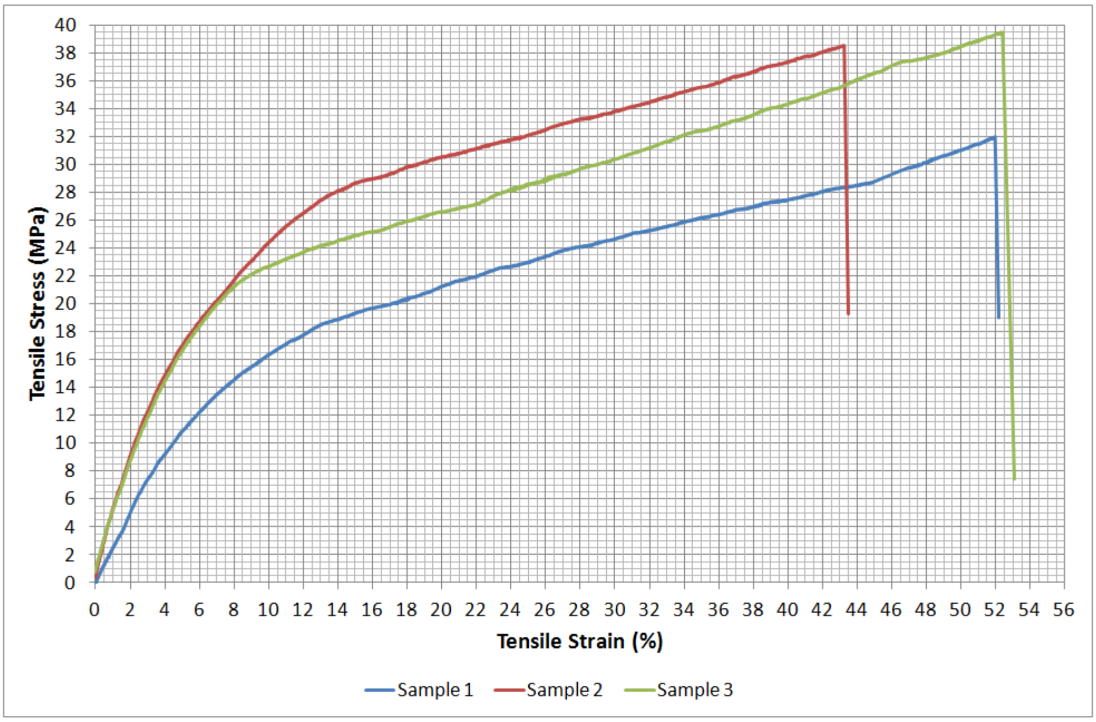

Figure 4.13 – Stress/strain plot for R11 tensile test parts (25 µm layers)

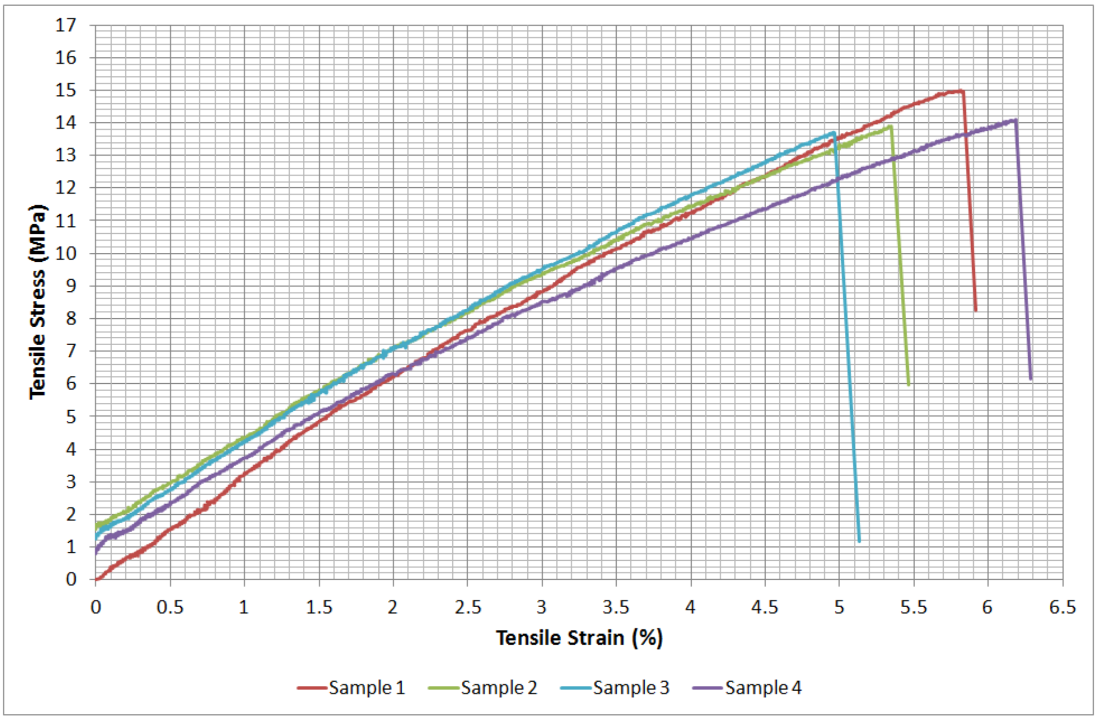

Figure 4.14 – Stress/strain plot for magnetite composite (25 µm layers) tensile test parts

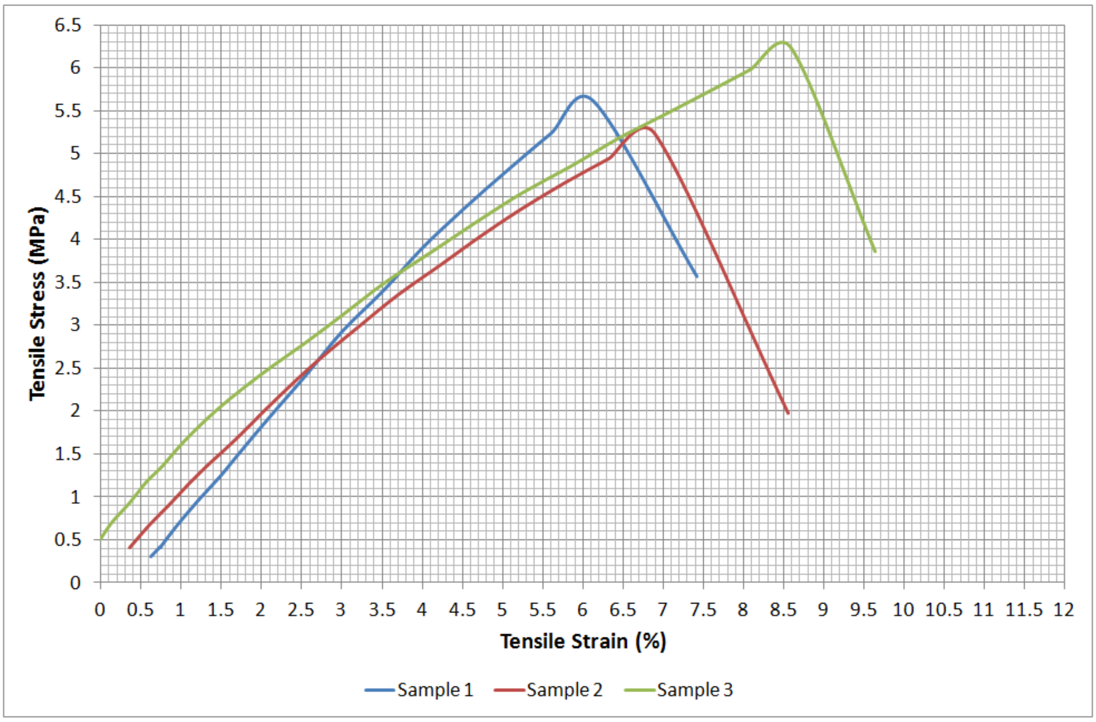

Figure 4.15 – Stress/strain plot for magnetite composite (50 µm layers) tensile test parts

Again, using the stress / strain data, values for the tensile strength and Young's Modulus of the each material were obtained (Table 4.3).

	R11 25µm	Magnetite 25µm	Magnetite 50µm
Tensile Strength (MPa)	36.7 ±4.1	14.2 ±0.6	5.7 ±0.5
Young's Modulus (MPa)	353.7 ±98.5	278.8 ±7.6	82.7 ±14.6

Table 4.3 – Measured average tensile strength and Young's modulus for R11, and magnetite composite materials

A paper by Quintana et al [27] notes that due to the process in which components are fabricated using MSL, the strength of the component is heavily dependent on the orientation that it was built (or the axis along which force is applied), making parts anisotropic. This is confirmed by the results obtained from the compression testing experiments as for both the composite and commercial resin materials. It can be seen that in both cases the stronger axis is the one parallel to the plane of the build layers. It can also be seen that the commercial material, which is intended primarily for structural components (R11), out performs the magnetite material in both orientations. However, the difference between the two, particularly in the perpendicular orientation, is not large (a factor of 3.5 at most). This shows that the current formulation of magnetite material has comparable compressive strength to a standard resin.

The results from testing the components in a tensile mode show that the magnetite resin has a lower tensile strength than R11. This suggests it may be less suitable to use to fabricate structural features and regions of components. This was to be expected though as the nanoparticles suspended within the magnetite material will reduce cross-linking of the polymer chains within those regions. It can also be seen that layer thickness plays a significant role in the strength of the magnetite material, with thinner layers producing a stronger part but at the cost of having a much longer build time. The difference in values for the Young's Modulus of the two magnetite samples demonstrates that using thicker layers produce more flexible components. This difference is thought to be due to the magnetite particles being in higher concentration at the lower part of each layer. Therefore, in thicker layers, there is a larger percentage of the layer with less filler material, causing greater flexibility of the component.

4.5.3 Poling and Field Detection

For the material to be of use in a sensing application, an appropriate sensor for detecting the orientation and magnitude of the material's magnetic field must be used, Honeywell's HMC1001 part is such a device. The HMC1001 is an anisotropic magneto-resistive (AMR) sensing device. Such devices are fabricated using thin film Permalloys (NiFe) which can change in resistivity when exposed to a magnetic field [28]. AMR sensors are highly accurate devices which are capable of detecting the magnitude of external magnetic fields and are suitable for a wide variety of magnetometry applications [29, 30]. The sensing part of the device is based around a simple Wheatstone bridge configuration consisting of four magneto-resistive elements. Therefore, when a potential is applied across the bridge, a differential voltage proportional to the magnitude of the applied field is produced across the output. When the elements are not subjected to a magnetic field they are electrically identical.

The differential output of the AMR sensor was buffered and amplified using the circuit shown in Figure 4.16 to enable the signal to be easily recorded. The values of the resistors chosen are to give a gain close to 6.25 such that with the AMR device sensitivity of 3.2 mV/V/Gauss, the circuit then has a sensitivity of 0.1 V/Gauss when the potential applied across the bridge is 5 V. R4 and R7 were included so that further adjustments could be made to the offset and gain respectively if required. The output from the amplifier circuit was then captured using a Tektronix TDS2022B oscilloscope.

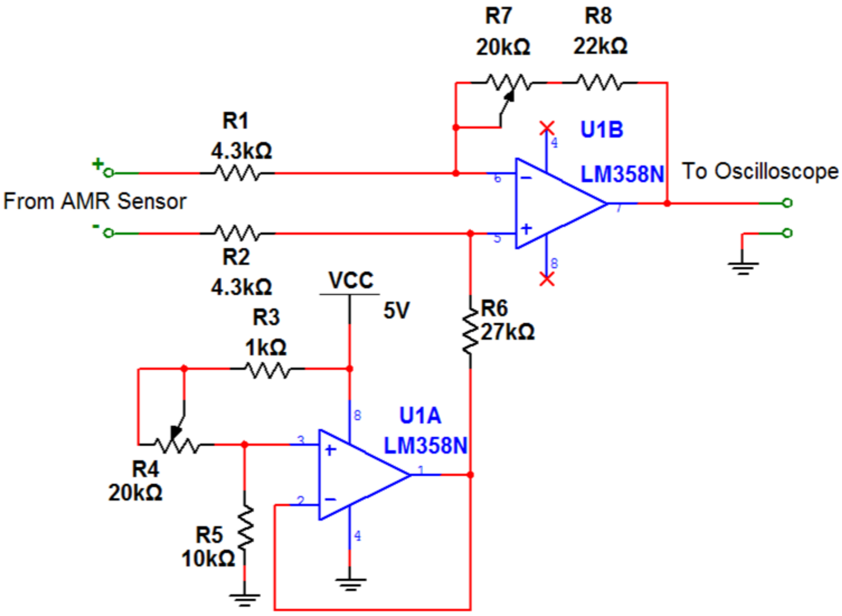

Figure 4.16 –Circuit diagram for the using the Honeywell HMC1001 AMR device for field detection of the magnetic composite material

As with the testing of the comb device previously, the XYZ-stage of the custom MSL machine was utilised to accurately move the AMR sensor over the composite cube. One side of the cube was adhered using standard acrylate based superglue to a glass slide which was then clamped securely to the mount usually used to hold the system's resin tray, while the circuit board with the attached AMR sensor was then mounted to the Z stage of the machine. A system diagram is shown in Figure 4.17. The motion stage was then manually adjusted so that the AMR sensor was aligned over the centre line of the cube in both X and Y orientations, this was then set as the origin in the software. The sensor was then run back and forth over the cube at a number of standoff distances while the output from the sensor's circuit was recorded using the oscilloscope. A digital output from the stage's controller (an Aerotech UK Ltd, A3200) was programmed to be used as an external trigger for the oscilloscope so that the relative position of the sensor could be accurately mapped to the recorded data.

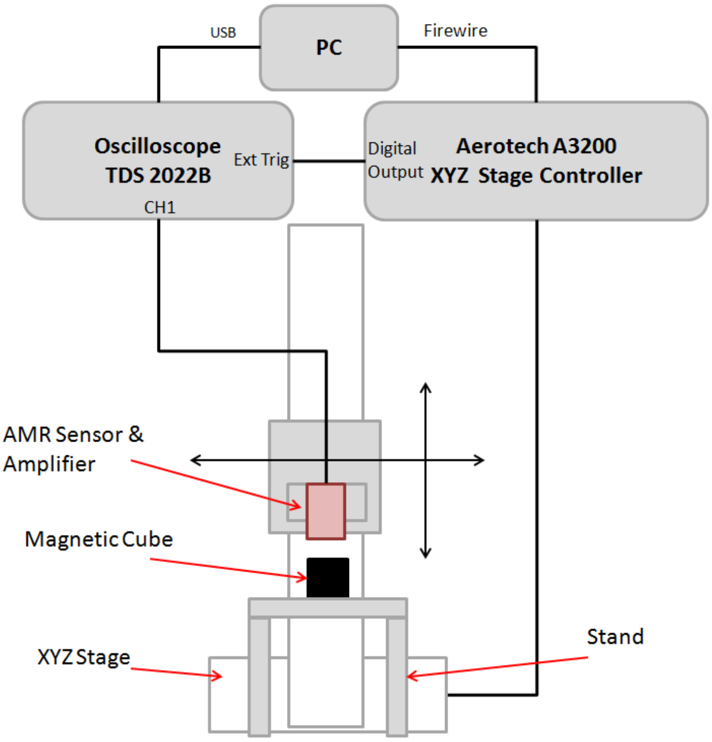

Figure 4.17 –Schematic diagram showing experimental setup used to map the B-field of the poled magnetite composite cube

To begin with, the cube was tested as fabricated. However, the magnetic field was not sufficient to be accurately measured beyond a distance of 1.5 mm. The cube was then poled by simply placing it on the N42 neodymium magnet for 2 seconds and the experiment repeated. After poling, the signal level observed was in approximately 500 times larger. Figure 4.18 shows the data obtained with stand-off distances between 0 mm and 5 mm.

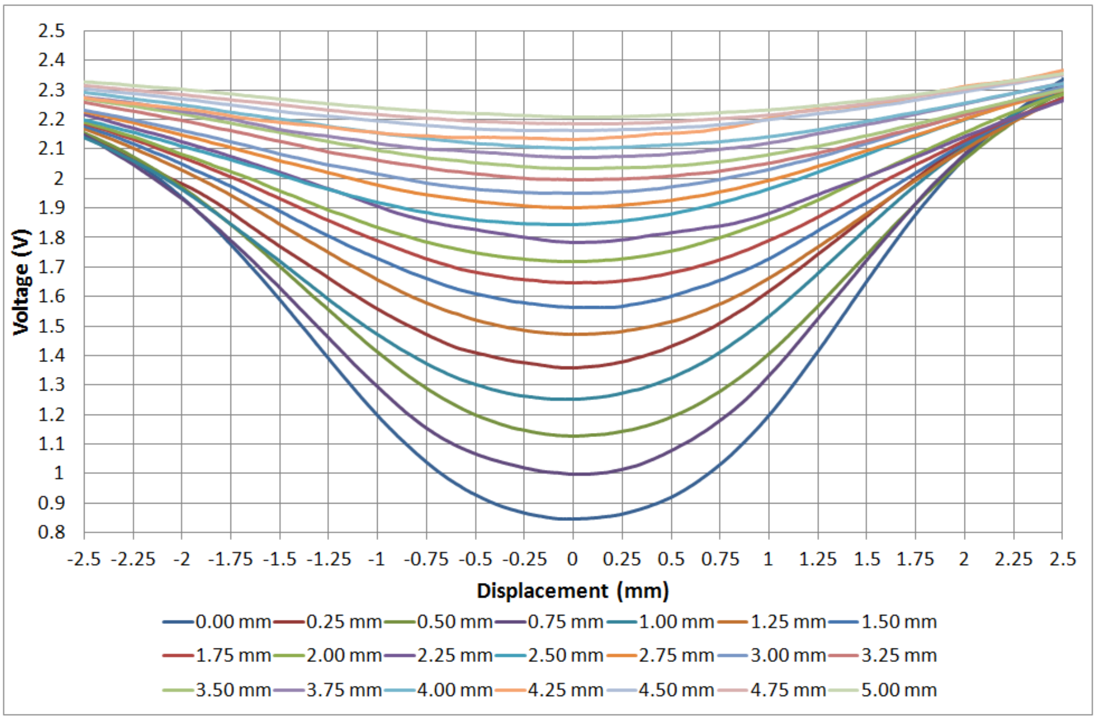

Figure 4.18 – Response of scanning AMR sensor over poled cube at increasing standoff

As is clearly shown by the graph, the separation distance between the material and the sensor has a significant impact on the amplitude of the signal. However, by increasing the gain of the amplifier circuit it was possible to observe a usable signal with a stand-off of up to approximately 15 mm, which the author believes to be sufficient for the intended flow sensing applications.

For the purposes of using the material in a practical application it is also important to know the rate of decay of the material's remanence. In order to measure this, the AMR sensor was used again to measure the magnitude of the field at a fixed point above the surface of the cube. The voltage from the output of the AMR sensor circuit was measured using an ATMEGA328P microcontroller (Atmel Corperation, USA) which was connected to a PC in order to log the data. The data was logged over a period of 10000 minutes (~7 days). The magnetic composite cube was poled using an N42 neodymium permanent magnet before its initial field was measured using a Bell (Bell Labs, USA) 640 Incremental Gaussmeter at the same standoff distance of as the AMR sensor in order to calibrate the output of the datalogger. The measured field strength at a standoff of 1 mm was measured as 40.4 ±2 Gauss. The initial remanence, Br, was calculated using Equation 4.2. F is the field strength at height z from the surface, A and B are width and length respectively, L is the height of the cube and Br is the remanence. The initial remanence was therefore calculated to be 142 Gauss. Figure 4.19 shows the recorded data where a decay of 17.8% from the initial reading can be seen. It is felt there are two possible reasons for the observed decay of field strength - either intrinsic decay of the polling of the magnetic particles within the material, or reorientation of the magnetic particles within the polymer matrix (through physical rotation of the particles).

$$F = \frac{Br}{\pi}\left[\tan^{-1}\left(\frac{AB}{2z\sqrt{A^2+B^2+4z^2}}\right) - \tan^{-1}\left(\frac{AB}{2(z+L)\sqrt{A^2+B^2+4(z+L)^2}}\right)\right] \tag{4.2}$$

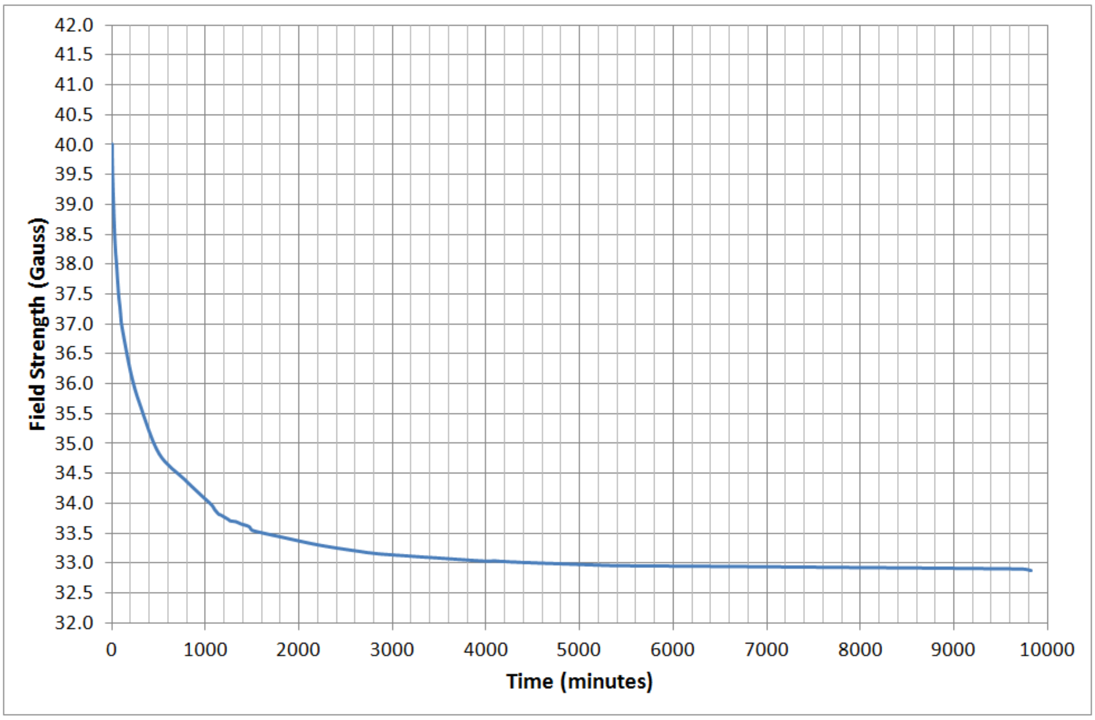

Figure 4.19 – Graph showing measured magnetic field strength over time of a poled magnetite cube with 50 μm layers

4.6 Conclusion

In this chapter, the development of a novel, functional, composite magnetic polymer material for use in a dynamic mask based microstereolithography system was described. The material consisted of a monomer (HDEDA) and crosslinker (DPPHA) in a ratio of 1:2. The material also contained 5% by weigh of Irgacure 784, which was used as a photoinitiator due to its sensitive region is compatible with wavelength of the light source and magnetite nanoparticles loading of 25% by weight for multi-layer components and 35% by weight for components consisting of 20 layers or less. While magnetite was used in these experiments due to compatibility with the MSL system and its ease of being magnetised post-fabrication, it is felt that other intrinsically magnetic fillers could be used with a free-surface MSL method.

Experiments were conducted which demonstrated that the material can be easily manipulated with the use of an externally applied magnetic field and can also be simply poled such that it can be used in a sensing application with an appropriate magnetic field sensing device. The material therefore provides the ability to quickly and easily fabricate bespoke components with favourable magnetic properties using a technology that is already well established in the microfabrication field. The following chapter examines one of the uses of the material in a practical microfluidic application.

4.7 References

[1] J.M.D. Coey, Magnetism in future Journal of Magnetism and Magnetic Materials, 226-230 (2001) 2107-2112

[2] K. Sickel, S. Baloch, R. Melkisetoglu, V. Bubnik, S. Azernikov, T. Fang, Toward automation in hearing aid design, Computer-Aided Design 43 (2011) 1793–1802

[3] F.P.W. Melchelsa, J. Feijena, D.W. Grijpma, A review on stereolithography and its applications in biomedical engineering, Biomaterials 31 (2010) 6121-6130

[4] H. Wu, D. Li, Y. Tang, B. Sun, D. Xu, Rapid fabrication of alumina-based ceramic cores for gas turbine blades by stereolithography and gelcasting, Journal of Materials Processing Technology 209 (2009) 5886–5891

[5] G. Casalino, L.A.C. De Filippis, A. Ludovico, A technical note on the mechanical and physical characterization of selective laser sintered sand for rapid casting, Journal of Materials Processing Technology 166 (2005) 1–8

[6] EnvisionTEC GmBH, Perfactory Mini Systems For the Production of Jewellery, [online] Available from: http://www.envisiontec.de/index.php?page=app&id=7 (last accessed 04/04/2012)

[7] W. Zheng, F. Gao, H. Gu, Magnetic polymer nanospheres with high and uniform magnetite content, Journal of Magnetism and Magnetic Materials 288 (2005) 403-410

[8] O. Philippova, A. Barabanova, V. Molchanov, A. Khokhlov, Magnetic polymer beads: Recent trends and developments in synthetic design and applications, European Polymer Journal 47 (2011) 542-559

[9] X. Zhang, W. Jiang, Y. Ye, Z. Feng, Z. Sun, F. Li, L. Hao, J. Chu, A facile method to synthesize magnetic polymer nanospheres with multifunctional groups, Journal of Magnetism and Magnetic Materials 323 (2011) 1440-1444

[10] I. Safarik, M. Safarikova, Use of magnetic techniques for the isolation of cells, Journal of Chromatography B 722 (1999) 33-53

[11] T. Makarova, Magnetism of Carbon –Based Materials, To be published in: Studies of High-T_c Superconductivity 44-45

[12] N. A. Zaidi, S. R. Giblin, I. Terry, A. P. Minkman, Room temperature magnetic order in an organic magnet derived from polyaniline, Polymer 45 (2004) 5683-5689

[13] K. Sonoda, N. Teirikangas, J. Jutti, Y. Moriya, H. Jantunen, Effect of surface modification on dielectric and magnetic properties of metal powder/polymer nanocomposites, Journal of Magnetism and Magnetic Materials 323 (2011) 2281-2286

[14] S.L. Lu, J. Ramos, J. Forcada, Self-stabalized magnetic polymeric composite nanoparticles by emulsifier-free miniemulsion polymerisation, Langmuir 23 (2007) 12893-12900

[15] F. Wua, Q. Li, X. Z, L. Liu, S. Wua, D. Sun, F. Li, W. Jiang, Fabrication and characterization of thermo-sensitive magnetic polymer composite nanoparticles, Journal of Magnetism and Magnetic Materials, 324 (2012) 1326-1330

[16] N. Damean, B.A. Parviz, J.N. Lee, T. Odom, G.M. Whitesides, Composite ferromagnetic photoresist for the fabrication of microelectromechanical systems, J.Micromech. Microeng. 15 (2005) 29‑34

[17] A.A. Novakovaa, V.Yu. Lanchinskayaa, A.V. Volkova, T.S. Gendlerb, T.Yu. Kiselevaa, M.A. Moskvinaa, S.B. Zezina, Magnetic properties of polymer nanocomposites containing iron oxide nanoparticles, Journal of Magnetism and Magnetic Materials 258-259 (2003) 354-357

[18] K. Kobayashi, K. Ikuta, Three-dimensional magnetic microstructures fabricated by microstereolithography, Appl. Phys. Lett. 92 (2008) 262505

[19] C. Timm, Theory of Magnetism, Lecture Notes from International Max Planck Research School: Dynamical Processes in Atoms, Molecules and Solids, [online] available from: http://www.physik.tu-dresden.de/~timm/personal/teaching/thmag_w09/lecturenotes.pdf (last accessed 01/04/2012)

[20] C. Westbrook, C. Kaut, MRI in Practice (2nd Edition), Wiley-Blackwell, (1998) p217

[21] Handbook of Mineralogy, vol. III, Mineralogical Society of America, 1997, 333

[22] T. Mizoguchi, R. Inamura, T. Sorimachi, K. Sato, Remanence in high-density recording media, Physica B 275 (2000) 270-273

[23] Envisiontec RC25 (NanoCure) Material Datasheet, [online] Available from: http://wp11009247.wp291.webpack.hosteurope.de/userfiles/Material%20RC25%20NanoCure(1).pdf (last accessed 10/05/2012)

[24] X.N. Jiang, C. Sun, X. Zhang, B. Xub, Y.H. Ye, Microstereolithography of lead zirconate titanate thick film on silicon substrate, Sensors and Actuators 87 (2000) 72-77

[25] P. Singh, S. Smith, M. Bezdecny, M. Cheverton, J.A Brewer, V. Venkataramani, Additive Manufacturing of PZT-5H Piezoceramic for Ultrasound Transducers, Proceedings IEEE Ultrasonics Symposium (2011) 1111-1114

[26] C. Sun, X. Zhang, The influences of the material properties on ceramic microstereolithography, Sensors Actuators A: Phys. 101 (2002) 364–370

[27] R. Quintana, J.-W. Choi, K. Puebla, R. Wicker, Effects of build orientation on tensile strength for stereolithography-manufactured ASTM D-638 Type I specimens, Int. J. Adv. Manuf. Technol. 46 (2010) 201–215

[28] Honeywell Application Note – AN213, [online] available from: www51.honeywell.com/aero/common/documents/myaerospacecatalog-documents/Defense_Brochures-documents/Magnetic__Literature_Application_notes-documents/AN213_Set_Reset_Function_of_Magnetic_Sensors.pdf (last accessed: 25/05/2012)

[29] D. Jurman, M. Jankoveca, R. Kamnika, M. Topic, Calibration and data fusion solution for the miniature altitude and heading reference system, Sensors Actuators A: Phys. 138 (2007) 411‑420

[30] F. Verpillat, M.P. Ledbetter, S. Xu, D.J. Michalak, C. Hilty, L.-S. Bouchard, S. Antonijevic, D. Budker, A. Pines, Remote detection of nuclear magnetic resonance with an anisotropic magnetoresistive sensor, PNAS 105 (2008) 2271‑2273

Chapter 5

5 MSL for the Direct Fabrication of Flow Sensors

In the previous chapter, the development of a novel composite photopolymer with magnetic properties was presented. In this chapter the practical use of the material is demonstrated by the fabrication of a flow-sensing device. The magnetic properties of the new material were used to produce a device that exhibits a rotating magnetic field whose frequency is proportional to the flow rate of a liquid through the device. The rotation (and therefore flow rate) is externally detected using a magnetic field sensor.

The first section of this chapter briefly details a number of potential uses for such a material, in particular its use in microfluidics. An outline of existing flow sensing techniques is covered along with the advantages of being able to rapidly manufacture such devices in both laboratory/research environments and for applications requiring an affordable method of fabricating disposable devices.

The second section describes the design, fabrication and testing of two exemplar flow sensing devices that utilise the composite magnetic photopolymer to allow for the entire flow device to be printed – a method not previously reported for fabricating such devices. The miniature flow cells were designed and tested as a proof of concept, to show that such a material could be of use in miniaturised systems. It is hoped that this will ultimately bring MSL technologies a step closer to being able to produce lab on chip devices and total analysis systems. Sections of the work described here have been published in “Sensors and Actuators A: Physical” [1].

5.1 Introduction

As discussed previously, MSL has already been proven to be a suitable technology for fabricating a range of devices for practical applications in a laboratory or research environment [2, 3]. However, the ability to rapidly take a micro-scale design with magnetic elements from CAD to fabricated component using MSL opens up many new research avenues in areas such as bespoke measurement, actuation and even rudimentary information storage applications. It is believed that there is potential to use such materials in applications relating to micro force/distance measurement techniques using micro cantilevers and devices containing simple magnetic storage media. For example, a 2D matrix barcode could be embedded into components using magnetic material for the purposes of device identification etc.

There is a constant drive for new electronic devices to become ever more compact, for microfluidic applications this is usually due to the desires to test lower sample volumes, or use less reagent to reduce running costs, or simply to make the testing process quicker. As such, the requirement of the microelectromechanical systems (MEMS), and microfluidic systems within them are required to be increasingly smaller, lightweight, and integrated. The Microsensors and Bioelectronics Laboratory (MBL) group at the University of Warwick utilise the current commercial MSL systems to fabricate a wide range of microfluidic components such as flow channels, gas sensor chambers, and micropumps (Figure 5.1).

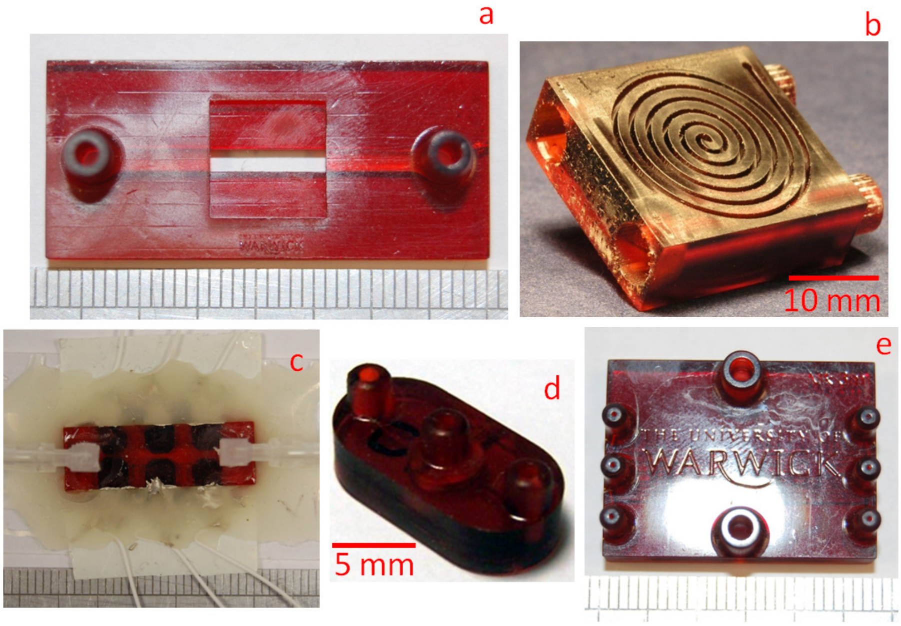

Figure 5.1 – Example flow devices made in the MBL group (units in mm) (a) flow cell with observation window, (b) spiral micro-retentive column [4], (c) electroanalytical flow cell, (d) pneumatically drive micropump [5], (e) DNA synthesis device

With all such systems, be they for gas sensing, micro-mixing [6], droplet merging etc, the rate of flow of the fluid through the system is an important factor that needs to be monitored. Flow is currently measured using commercially available flow sensors, however, it has often been desirable to have a more bespoke solution that integrates the sensor more compactly into the system.

5.2 Flow Sensors

There is a wide range of commercially made flow sensors available for both gas and liquid applications. Commercial devices are generally designed such that they can be used in a wide variety of systems and environments and as such are usually housed in packages with standardised fittings. While this is advantageous in a wide variety of situations, the device exists as a separate entity in the fluidic "circuit", requiring tubing to connect the various components. The result is then extended path lengths and increased dead volume, both of which are undesirable in micro fluidic systems as it leads to extended response times and can reduce temporal resolution. In addition to this, the fittings used are often bulky when used in compact applications. Commercial units are expensive (£150+) and are therefore not generally considered as single use or throw away devices, as such they are not always suited to single/low usage applications or where the required specifications are subject to change, such as in research environments.

By fabricating a bespoke flow sensor, not only can the device be tailored to the needs of the system but it can be designed to integrate more compactly into the system. As the MSL process is relatively inexpensive, it provides a realistic method of fabricating such bespoke devices that can be iteratively modified or improved as needed. Such an affordable means of manufacture also means that devices could be fabricated for single use which is useful in biological applications and those which require contamination from analytes in previous tests to be removed. Lab-on-chip type devices which house the moving parts of the flow sensor within the device itself can easily be created – reducing part count, dead volume and the need to seal the impeller against leaks.

5.2.1 Micro-Flow Measurement Techniques

The three most common methods of bespoke flow measurement are thermal, piezoresistive, and less commonly, optical. The most popular of these methods is measurement by thermal convection through the flow medium itself.

There are three methods of thermal flow measurement [7, 8], which are hot film, calorimetric and time-of-flight. All thermal flow sensors operate on the principal of heat being transferred from a heating element (usually polysilicon [9], nickel [10] or platinum [11]) into the fluid, and require either a knowledge of the heat capacity of the fluid or for the flow meter to be calibrated for the chosen fluid. In the cases of both calorimetric and time of flight methods, a resistive temperature sensor is used to detect the subsequent change in temperature of the fluid. In all cases, the heaters and sensors are located in or on the inside wall of the flow channel.

In the case of the hot film method, a constant current is applied to the resistive heater and the potential across the sensor is measured. A flow of fluid carries heat away from the heater, causing the resistance, and therefore the measure voltage across the device to vary.

With calorimetric measurement, two identical sensors are located upstream and downstream of a heating element; one device acts as a reference while the other as the sensor [12, 13]. The sensors are arranged with two external resistors in a Wheatstone bridge configuration (one sensor on each half of the bridge) and in a similar way to the hot film method, a constant current is applied to the bridge. The differential voltage across the bridge is measured in order to ascertain the differential resistance of the tracks. As the track is heated its resistance will vary and as such the change in temperate can be measured. With zero flow the heat will dissipate equally to each of the sensors and therefore their differential will be zero. As flow increases, less heat will be transferred to the sensor upstream of the heater, and more heat will be transferred to the sensor downstream, therefore the differential will increase. The flow rate is therefore proportional to the differential voltage observed.

The final thermal method of measurement is time-of-flight [14, 15]. Here, a heater is used to inject a pulse of heat into the fluid; this causes only a region of the fluid to heat. Downstream, a temperature sensor (the same as in the calorimetric method) is used to monitor the arrival time of the heated region. By knowing the separation distance of the heater and sensor, the flow rate can be directly calculated.

Due to their small dimensions, such devices generally used to measure low flow rates from microlitres down to nanolitres per minute. Tanaka et al [16] present a wide operating range device (0.01-10 ml/min) for use in small scale chemical processing. It achieves the wide operating range by using two detection methods; for the lower flow rates, the calorimetric method is used where as for the higher flow rates a time of flight method is used.

Such devices are advantageous due to their compact size and not having any moving parts, however, all of the production methods are based on multistep silicon fabrication technology. Additionally, the use of thermal techniques is not always possible, for instance when heating of the medium is undesirable. While the method could be used to generate bespoke designs, it would be prohibitively costly and time consuming to fabricate a new device for each new application.

Optical methods have also been developed as a means of measuring fluid flow. However, the flow rates tend to be on the order of litres per minute and be liquid based; therefore, not suitable for microfluidic applications [17, 18].

A method more similar to that used in MSL was presented by Song et al [19] and Zhang et al [20]. Here, the piezoresistive properties of a material are used to measure the deflection of a cantilever, which it is bonded to. The cantilevers are positioned in the fluid flow such that the mechanical force of the fluid bends the cantilevers. While a similar device could be easily fabricated using MSL, significant testing would be required in order to verify the reliability of the cantilevers in terms of both repeatability and device lifetime.

5.2.2 Mechanical Flow Measurement Techniques

The devices mentioned above are based on measuring an electrical characteristic of the sensing material; this approach is not applicable to the magnetic materials described here. Instead, the measurement technique must involve the sensing of the displacement of a mechanical component within the device with the use of a suitable magnetic field sensor.

One of the simplest methods of measuring volumetric flow rate is to use a rotameter design (Figure 5.2). A rotameter is a type of variable area meter which operates by the fluid medium exerting a force on a float, which is held within a tapered tube. The tube is mounted vertically such that the float is pulled to the base of the tube by gravity. The fluid is then pumped up the tube causing the float to rise. Due to the tapered profile of the tube, as the float is forced upwards, the gap between the float and the tube increases, therefore, increasing the cross-sectional area that the fluid can flow through, allowing more fluid to pass around. An equilibrium point is reached between the upward force of the fluid acting on the surface of the float and the downward force of gravity. Therefore, the float holds a stable position in the tube depending on the flow rate and viscosity of the fluid. Rotameters are commonly used for measuring air and water although can also be used with a range of other fluids. Such a device could be easily fabricated on a micro scale, using MSL to create the tube and a float from the magnetite composite material. The vertical displacement of the float could then be measured using the AMR sensor and circuit described in the previous chapter. However, the issue with this method is that for correct operation the device must be oriented vertically. While this isn't necessarily an issue in a laboratory development environment where orientation can be carefully setup, this is not the case for portable applications.

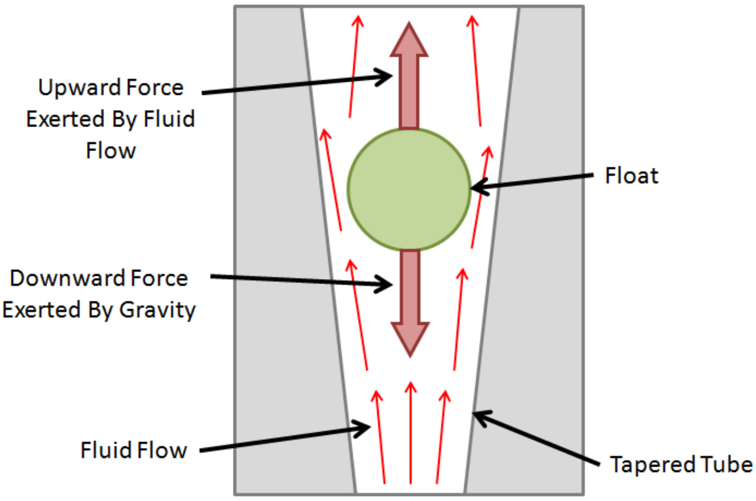

Figure 5.2 – Schematic showing theory of operation of a float-type variable area meter

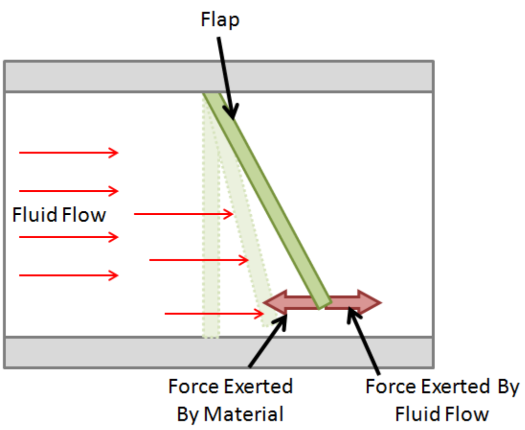

Figure 5.3 – Schematic showing theory of operation of a flap-type variable area flow meter

Another method that was considered, which overcomes the orientation dependency problem, was to use a flap which is inserted into the path of fluid flow (Figure 5.3). This is another form of variable area meter that again operates on the basis of an equilibrium point being reached. The force of the fluid flow exerts force on the flap, which is suspended in the flow channel. This causes the flap to raise and allow fluid to pass by. The internal stresses generated in the flap material caused by this displacement are used to generate an opposing force that tries to return the flap to its original position. As such, this method is heavily dependent on the mechanical properties of the material the flap is fabricated from. As the flap could be required to open and close many thousands of times during its operating life it was felt that this would not a suitable method due to potential fatigue problems with thin layers of the magnetic composite material. During material testing (as detailed in the previous chapter) the magnetic material demonstrated brittle properties and it was felt that this could dramatically affect the lifetime of the device. Calibration of each new device would also be required as it is felt that at this point, the mechanical properties of low layer count components could not be repeated accurately enough for such an application.

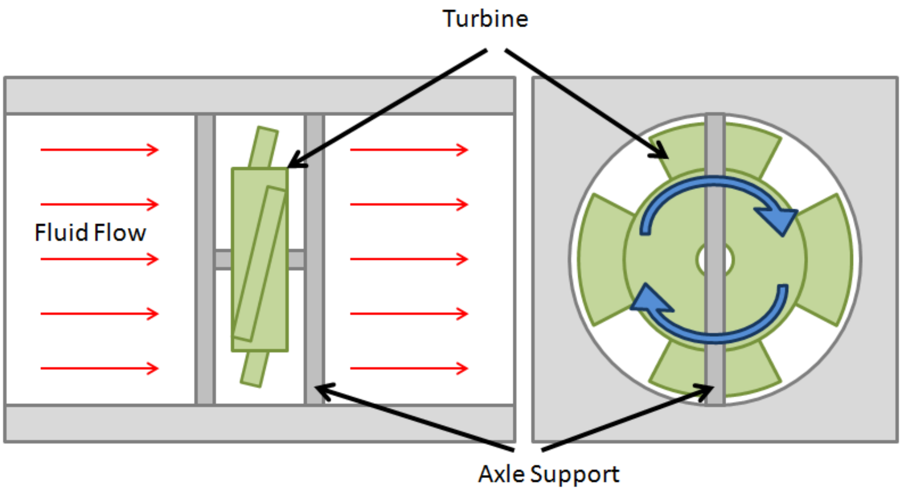

Figure 5.4 – Schematic showing theory of operation of a flow meter utilising a magnetic turbine

Other options considered were those which made use of rotating turbines and impellers. There is little difference between these two methods, one employs a turbine with shaped angled blades that is oriented perpendicularly to the direction of flow (Figure 5.4), while the other uses an impeller with simple, flat blades and is oriented in the plane of the flow (Figure 5.5) with the fluid flowing around the circumference of the rotor. The force imparted on the blades of the rotors causes them to rotate at a frequency proportional to the fluid velocity. Both designs are commonly used on larger scales for commercial devices and make use of either Hall Effect sensors or optical rotary encoders to measure the frequency of rotation of the rotors.

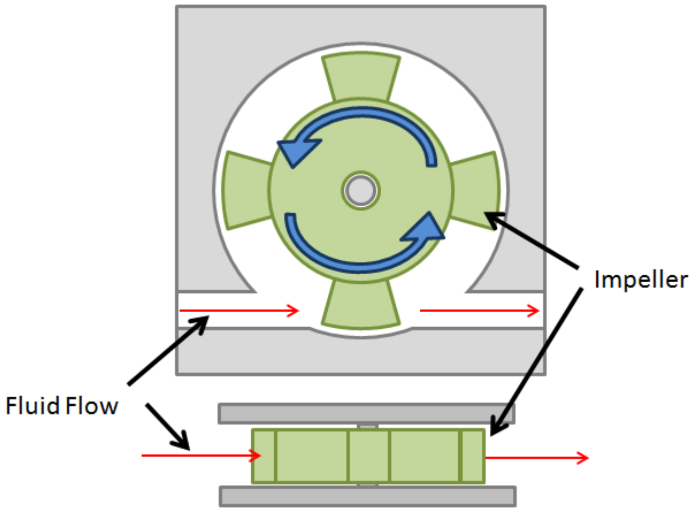

Figure 5.5 – Schematic showing theory of operation of a flow meter utilising a magnetic impeller

The turbine method does however provide two complications when it comes to manufacturing. The first is that because the axle of the rotor is required to be oriented concentrically with the tube, this results in one or more supporting beams being required in order to support the axle. This would make the design inherently difficult to fabricate using and MSL process even if the component were to be built in multiple parts. The second problem is that the inner diameter of the channels used in such fluidic systems is typically between 0.8 mm and 3 mm, which would significantly restrict the dimensions of the turbine. While the MSL systems available have resolutions between 50 µm and 20 µm, based on previous experience, fabricating a channel with a rotating part inside with such dimensions would have a high failure rate due to the fragility of the internal structures.

The flat impeller design, however, does not suffer from these restrictions as the fluid flows radially around the impeller. This means that the impeller's dimensions are not so restricted by the diameter of the fluidic channels. Therefore, the design chosen to base the flow sensing device on was that with a rotating impeller fabricated using the magnetite composite material.

5.3 3D Printed Flow Sensors

By utilising existing commercial MSL materials and the magnetic composite material, described in the previous chapter, together, all of the microfluidic components of a flow sensor can be fabricated on one system. This has a number of advantages, the main advantage being that the device can easily be integrated as a component in larger, more complex system. Therefore this brings the possibility of fabricating affordable lab on chip type devices. By being able to achieve such custom integration, other issues mentioned previously, such as excess dead volume and the ability to fabricate totally enclosed monolithic systems, are overcome.

5.3.1 2 Port Flow Sensor – Design

The model for a flow sensor utilising the magnetic material was designed using SolidWorks 2009 computer aided design (CAD) package. Figure 5.6 shows a schematic of the device. The dimensions of the design were chosen to reflect a device that might be used in a typical application in a laboratory setting. The ports of the device were designed such that a glass capillary tube could be easily adhered inside the tube. This could then be used to interface to PTFE (polytetrafluoroethylene) tubing used with the other microfluidic devices in the laboratory. The model was designed such that it would be built in three component parts which would be assembled post-fabrication. The main body of the device (a) includes the housing for the impeller (b), a centre axle to locate the impeller and two ports implemented as pipe fittings that act provide means to connect the device to a pneumatic source and an exhaust. Due to the position of the ports, it was also necessary to build a support under each to ensure that they would be fabricated correctly during the build process, as they would otherwise be unsupported.

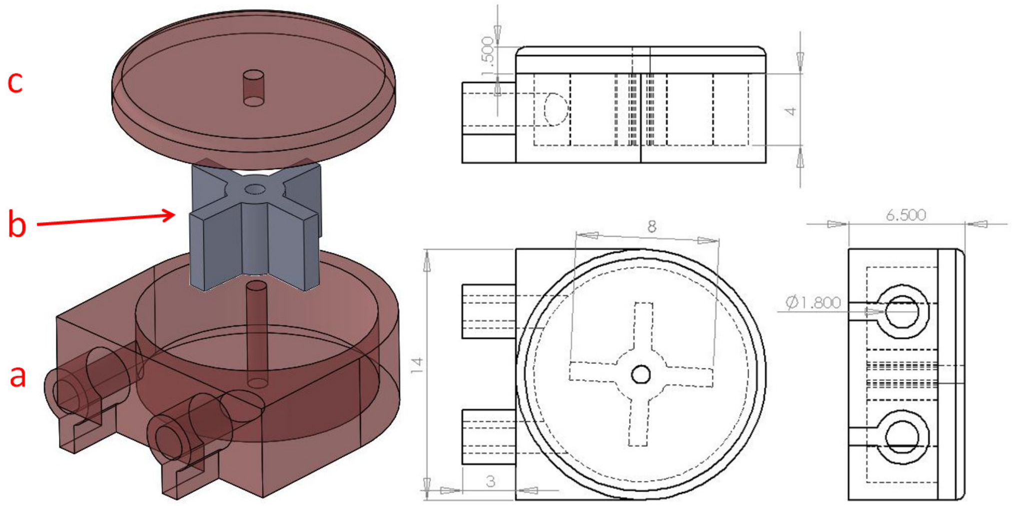

Figure 5.6 – CAD image and schematic of 2 port flow meter showing (a) the main body of the device, (b) the impeller, (c) the device's lid

5.3.2 2 Port Flow Sensor –Fabrication

Both the housing (a) and the lid of the device (c) were fabricated using a commercially available MSL resin suited to building structural parts, EnvisionTEC's R11 material. These parts were fabricated using an EnvisionTEC Perfactory Mini D with the layer thickness set to the standard setting of 25µm. The standard build settings were adjusted such that all layers had the same exposure time, rather than having a burn in range and standard range as discussed previously.

The impeller for the device (b) was fabricated using the magnetite composite material and was built using the custom MSL system described in Chapter 3, while the body (a) and lid (c) were fabricated using Perfactory Mini system (EnvisionTec GmBH, Germany) The impellers were built with a 25 µm larger thickness at 60 s expose per layer. Table 5.1 below details the machines, materials and build settings used to build each component.

Component	Body	Lid	Impeller
Component Height (mm)	6.5	1.5	4
MSL System	Perfactory Mini	Perfactory Mini	Custom Built System
Material	R11	R11	Magnetite Composite
Layer thickness (µm)	25	25	25
Number of Layers	260	60	160
Exposure time (s)	9.5	9.5	60
Separation (mm)	7	7	2
Peel speed (mm/s)	0.8	0.8	0.1
Levelling speed (mm/s)	0.8	0.8	0.1
Wait time after level (s)	2	2	2
Wait time after peel (s)	1	1	2
Total build time	2h 10m	30m	4h 37m

Table 5.1 – Fabrications settings for components of 2 port flow meter

After fabrication the body and lid of the device were rinsed thoroughly in Acetone in order to remove any excess uncured material and then post cured using an Otoflash G171 (NK-Optik GmbH) for 500 flashes on each side. Similarly, the magnetite components were washed in propan-2-ol in an ultrasound water bath for 30 minutes. It was found that this was necessary to remove both any uncured resin material and excess magnetite nanoparticles from the surface of the part. It was considered essential to remove any excess nanoparticles as it would be unacceptable to have them wash out into the fluid flow as this would both contaminate the fluid and risk increasing the abrasive wear between the impeller and the body. Simply rinsing the components with solvent was not enough to adequately clean the parts. As with previous experiments, after the magnetite loaded impeller was fabricated it was placed on a neodymium permanent magnet in order to pole its magnetic field across the width of the device. The specific orientation of the field across the width isn't crucial in this instance as fluctuations will be measured digitally to ascertain the rotational frequency of the impeller. The assembled device before the lid was adhered is shown in Figure 5.7.

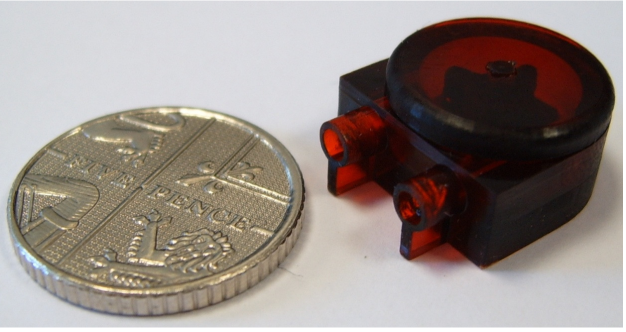

Figure 5.7 – Photographic image of assembled flow meter (5 pence piece shown for size reference)

5.3.3 2 Port Flow Sensor – Testing

As can be seen in Figure 5.8, the design for the flow sensor incorporated two external ports to be used as an input and output, the device is symmetrical so either port can be used as input or output. To test the device, the input port was connected to the laboratory's compressed air supply via a manual regulator. The input port was also connected to a Honeywell 26PC series pressure sensor via a T-junction. This was so the applied pressure could be accurately set; the signal from the sensor was processed using an Atmel ATmega328 microcontroller, which also provided power for the sensor. The microcontroller then communicated using serial emulation over USB to the host PC which displayed the measured pressure. For the purposes of the experiment, the output port was left unconnected.

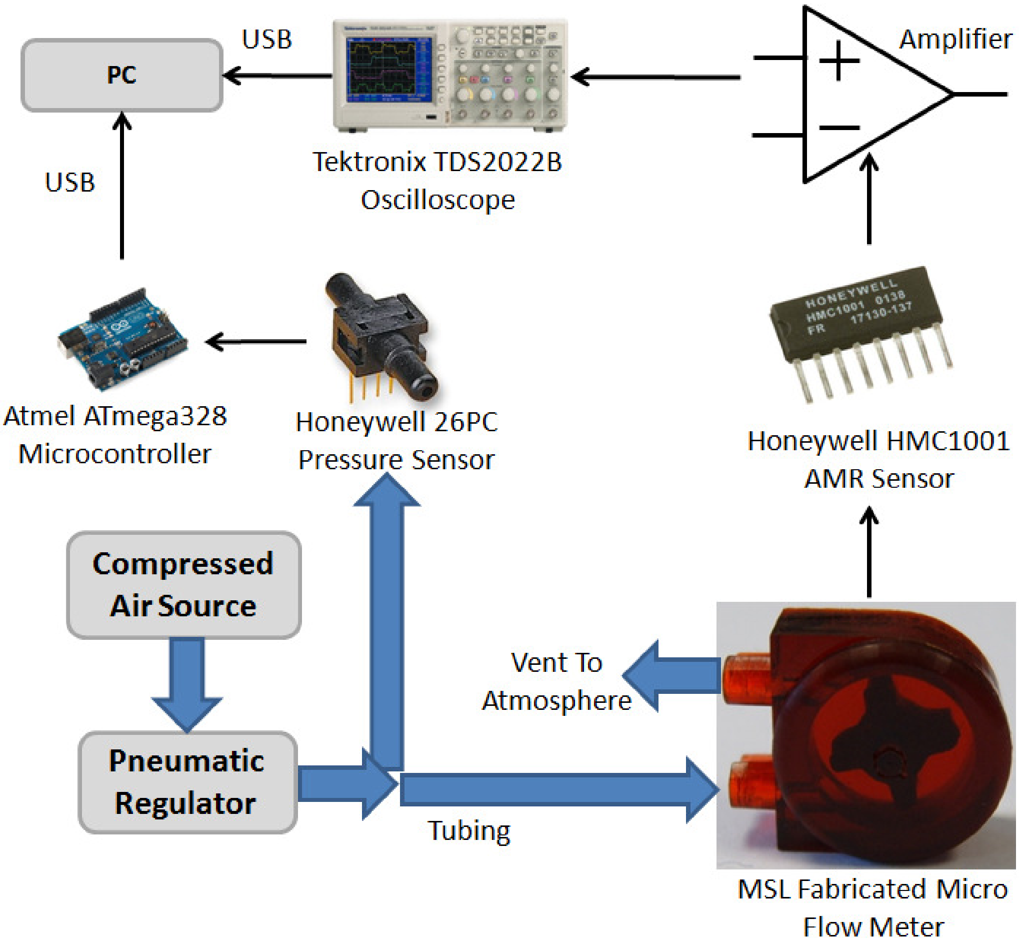

Figure 5.8 – Schematic of system setup for testing of 2 port flow meter

When the tap of the compressed air line was opened, the air flow through the device caused the impeller to rotate. The impeller was fabricated using the poled magnetite composite material, so as the impeller rotates so does the magnetic field surrounding it. The fluctuating magnetic field was then detected using a suitable sensor, a Honeywell HMC1001. For each revolution of the impeller, the sensor detects one count. As previously mentioned, the AMR sensor works as a Wheatstone bridge consisting of four magneto-resistive sensing elements. The differential output was then amplified using a simple circuit based on an OPA2123 operational amplifier so that a digital storage oscilloscope (Tektronix TDS 2022B) could then be used to observe and record the signal. Figure 5.8 shows a schematic of the system. The advantage of using this method is that the changing magnetic field can be detected remotely without any direct or mechanical coupling having to be made with the impeller. This eliminates the need for either integrated mechanical or electronic components and doesn't require any sealed bearings in the flow device itself.

In this case, the AMR sensor was mounted at a position 2 mm away from the body of the flow sensor (although as demonstrated in the previous chapter, a distance of 10 mm or more could be used if required in other applications). Due to the nature of the device, it is only sensitive in one axis and so care was taken to make sure it was oriented correctly to the plane of the magnetic field wanting to be measured. The setup can be seen in Figure 5.9 below. As the sensor is orientation specific, it allows for the possibility for multiple flow devices to be used simultaneously within the same sensing area. Indeed, the Honeywell HMC1002 contains two sensing devices with their dies oriented in orthogonal axis and so feasibly, it could be used with two flow sensor sensing devices in compact applications.

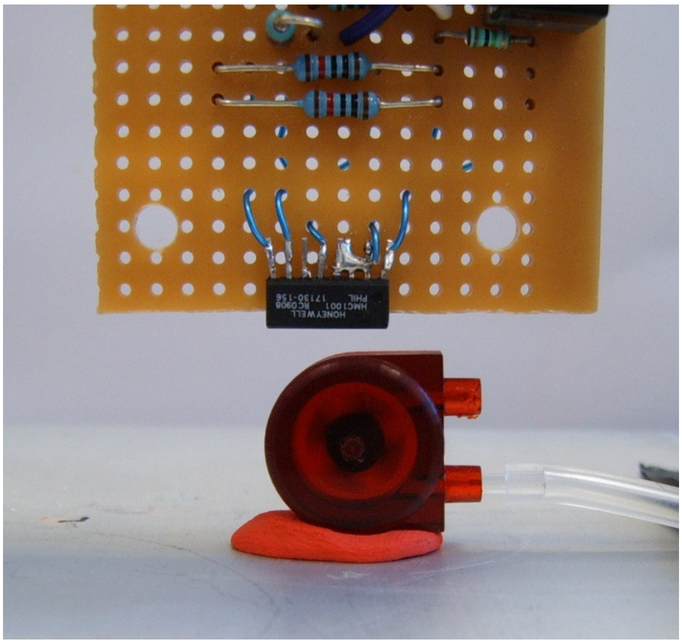

Figure 5.9 – Photographic image showing experimental setup of the testing of 2 port flow meter. The input port of the device is connected to a regulated compressed air supply and the AMR sensing device is mounted above with the required amplifier circuit.

The device was tested with a range of input pressures from 0.5 PSIG up to 7.5 PSIG in 0.25 PSIG steps. For each pressure step the waveform and frequency of rotation were collected from the oscilloscope (Tektronix OpenChoice software) for later analysis. In order to relate the applied input pressure to the flow rate, a calibration curve was made. This was done during a later test that used a rotameter immediately after the pneumatic regulator such that flow rate could be recorded at different applied pressures.

While conducting the experiment, one potential issue discovered was that the AMR sensor was susceptible to external interference. The sensor was affected by both static fields from other sources, such as metalwork in the laboratory desks, and oscillating fields such as interference caused by mains supply noise. Interference from static fields was removed by using the potentiometer on the AMR sensor's amplifier circuit (Chapter 4, Figure 4.14) to adjust the DC offset. A shield made of mu-metal (a nickel-iron alloy) was also constructed around the sensor to assist in negating interference from static and low frequency interference, however, the improvement seen was negligible in comparison to good adjustment of the DC offset. Strong external fields can cause poling of the sensing "straps" within the AMR sensor. Poling can either be partial, which has the effect of decreasing the amplitude of the detected signal, or total, which causes complete loss of signal. This polling effect can be easily removed by making use of the AMR sensor's strap reset and a suitable reset circuit; in this case the suggested design in the device's datasheet [21] was used. This design involved modifying the original circuit by adding the necessary components. By using a simple pushbutton switch on the circuit board, the effects of polling could be removed if they were observed. While this approach was sufficient in this case, an automated approach would be required for more permanent applications.

5.3.4 2 Port Flow Meter – Results

Figure 5.10 shows a typical measured signal from the system, in this case with an input pressure of 2 PSIG. Although it can be seen that the amplitude of the signal is not constant throughout the duration of the sample time, the variation observed is minimal (a standard deviation of 4.2% of the average peak-to-peak amplitude) and therefore was considered acceptable for such an application.

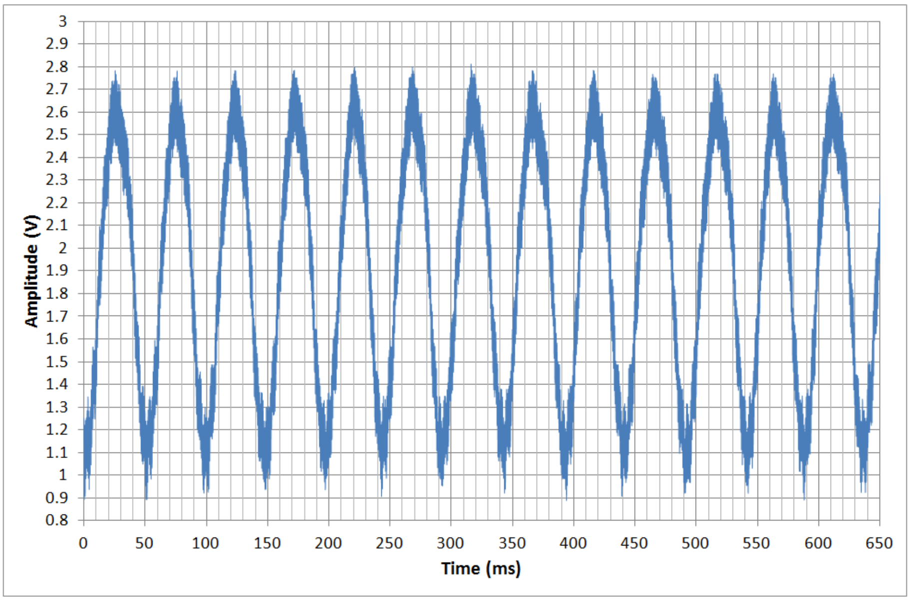

Figure 5.10 – Measured signal from 2 port flow meter using AMR sensing device and an input pressure of 2 PSIG. 1 cycle per revolution.

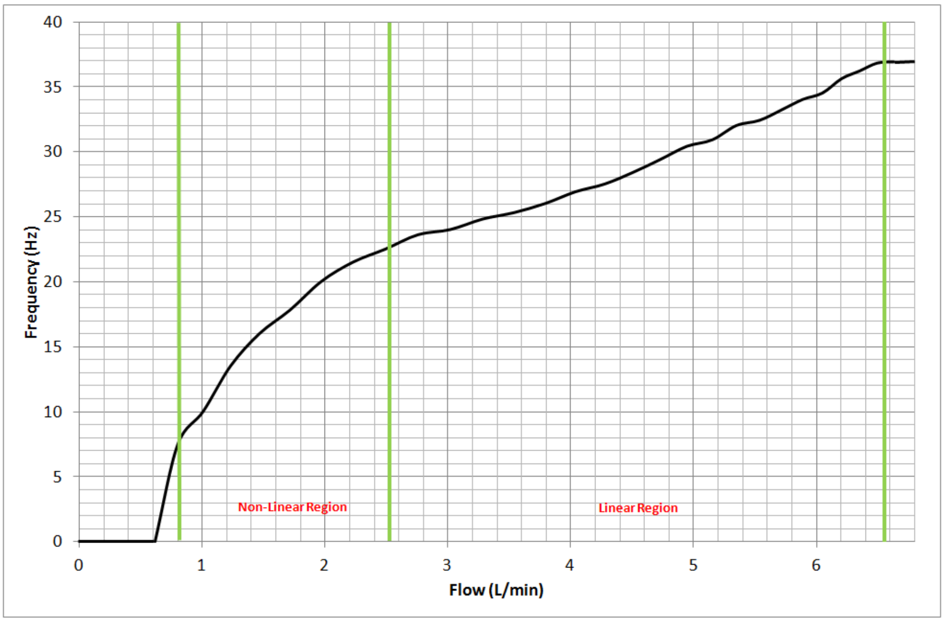

Figure 5.11 – Measured frequency with varying flow rate using 2 port flow meter

Figure 5.11 shows the measured results. It was observed that the sensor exhibits a non-linear response up to 2.45 l/min (rotational frequency of impeller: 22.6 Hz), but from ~2.5 l/min up to 5.5 l/min a linear region was observed. It is believed that below 0.9 l/min the frictional forces between the impeller and the body both on the base and around the axel were simply too great for the air flow to move the impeller. At ~0.9 l/min the impeller began to rotate, and although not detailed on the graph, the flow could reduced to ~0.75 l/min and the impeller would continue to rotate, albeit not smoothly. It is therefore believed that once the impeller begins rotating, it is raised slightly by a small air flow underneath which reduces the friction between to the base of the body and an inertial force then assists in it maintaining rotation at lower pressures.

With an applied flow of above 6.8 l/min, the rotational speed of the impeller was seen to level out at ~37Hz. This is again thought to be due to friction forces resulting in the impeller reaching a terminal velocity. As mentioned, it is believed the main contribution of the friction lies between the bottom of the impeller and the base of the flow device. As such, this effect could be significantly reduced by optimising the design of the cell's components. By simply adding a small diameter ring around the base of the axle ~200 μm in height the impeller would be raised off the base, greatly reducing the contact area (Figure 5.12). Also, by making the impeller chamber smaller and therefore reducing the gap around the edge of the impeller would allow less fluid to escape around the edge of the impeller and make the device more efficient at higher flow rates. This device and associated results were published as part of a paper submitted to Sensors and Actuators A: Physical [1].

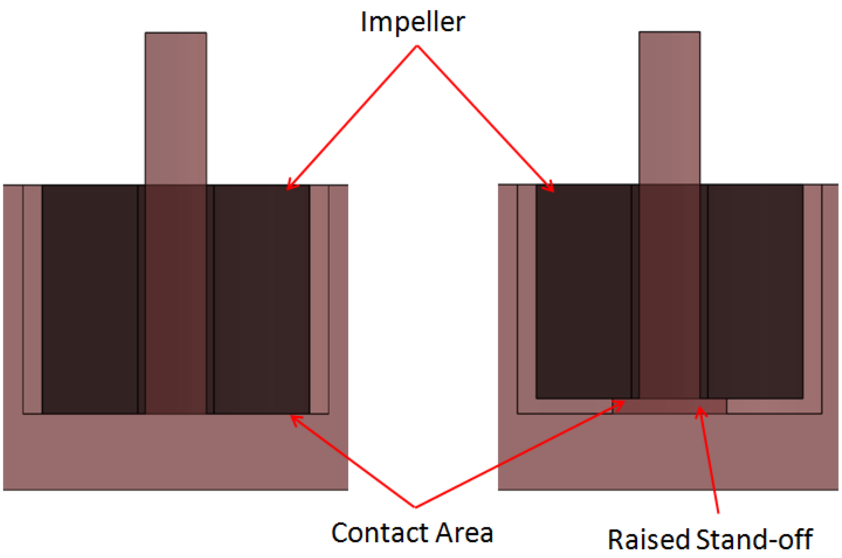

Figure 5.12 – Suggested design improvement for MSL fabricated flow meters using rotating impellers

5.3.5 Compact Lab-on-Chip Device Example - Design and Fabrication

Following on from the simple two port flow sensor, a smaller version was designed. The design was felt to be a good example as the dimensions used were similar to those on microfluidic devices typically fabricated using the existing MSL system by members of the University's Microsensors and Bioelectronics Laboratory (MBL) group. Additionally, the design incorporated a number of input ports which then mix and pass through the flow sensor chamber before exiting through the port. Although not necessary for this work, the addition of the further ports and mixer were included to demonstrate the possibility of fabricating more integrated lab-on-chip type devices. The 4 ports are designed to fit a standard 18 gauge plastic Luer-Lok needles to enable easy integration into a microfluidic system. In order to reduce the friction effects seen in the previous design, the design of the body also includes a small ring at the base of the axle which has a diameter 400 μm larger than the axle and a thickness of 200 μm with the aim to raise the impeller and so reduce the contact area between the impeller and the body. Figure 5.13 shows a CAD image and schematic of the device.

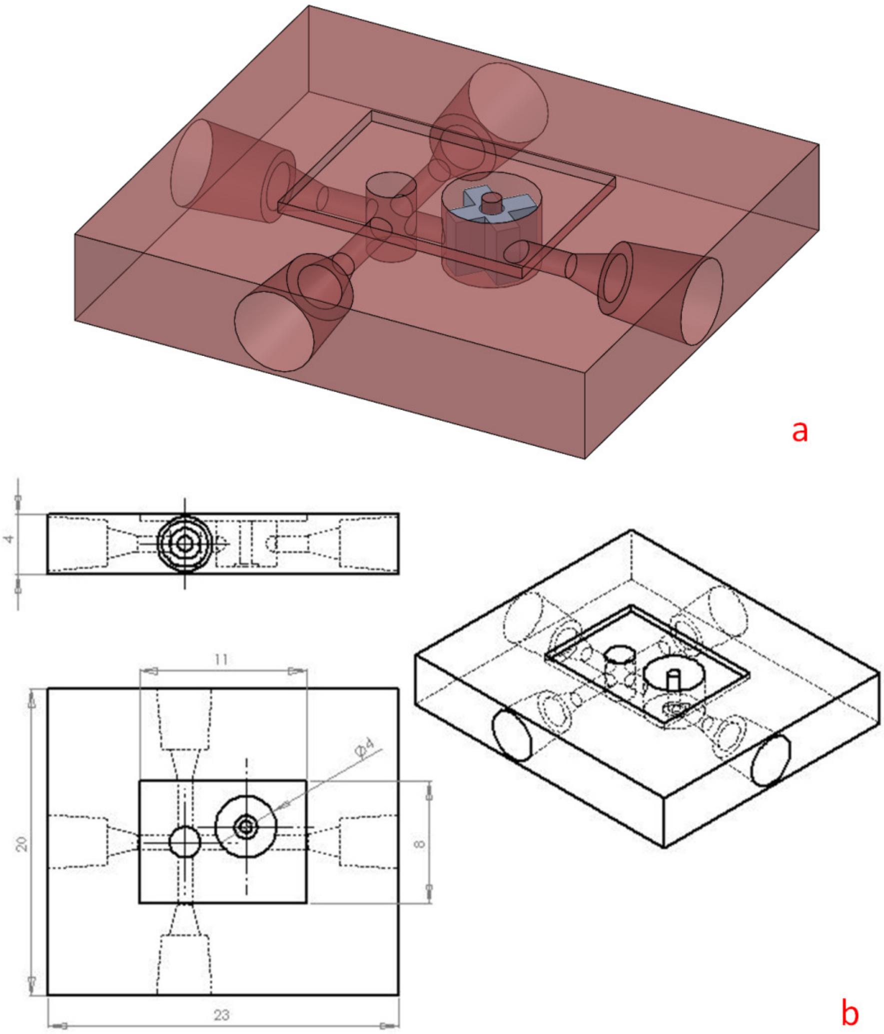

Figure 5.13 – (a) CAD image and (b)schematic of 2 port flow meter (dimensions in mm)

The device was again designed to be fabricated in two materials, the body from a structural material and the impeller from the magnetite composite. The smaller design of this sensor resulted in a smaller impeller. As such, the design tests both whether the magnetic field exhibited by the smaller impeller is sufficient to be reliably detected, and the ability of the composite material to be able to maintain its integrity in use when used on such a scale.

The device was built from two component parts, which were fabricated separately using MSL along with a glass viewing window the parts were then assembled post fabrication. The window could also have been printed but for testing purposes it was desirable to have a clear view of the impeller. Table 5.2 details the build settings used for each component, it should be noted that due to the smaller size of the impellers, a slower peel speed was required to prevent the build failing. Due to the smaller surface area of the impellers there is less adhesion to the glass build platform, therefore slower peel speeds are required to prevent them being pulled off during fabrication. The separation distance was also reduced in an attempt to minimise failure rate. Levelling speed was maintained at 0.1 mm/s.

Component	Body	Impeller
Component Height (mm)	4	2.65
MSL System	EnvisionTec Perfactory Mini	Custom MSL System
Material	R11	Magnetite Composite
Layer thickness (µm)	25	25
Number of Layers	160	106
Exposure time (s)	9.5	60
Separation (mm)	7	1
Peel speed (mm/s)	0.8	0.5
Levelling speed (mm/s)	0.8	0.1
Wait time after level (s)	2	2
Wait time after peel (s)	1	2
Total build time	1h 20m	2h 14m

Table 5.2 – Fabrication settings for components of multi port flow sensor

A window was made to fit in the recessed area by cutting an 11 mm by 8 mm section from a standard 1.2 mm thick glass slide. Using an adhesive, applied to the recessed area of the device, the window was adhered it to the recessed area of the device. It was important to seal the window effectively in order to ensure that the device is leak free. Initially an acrylate based super glue was used. While this method effectively secured the glass to the R11 body, due to the tight tolerances between the window and the impeller, it proved very difficult to glue the window without small excesses of adhesive flowing into the impeller cell and causing it to jam (Figure 5.14(a)). Using smaller amounts of glue was attempted but this often caused improper sealing of the device (Figure 5.14(b)).

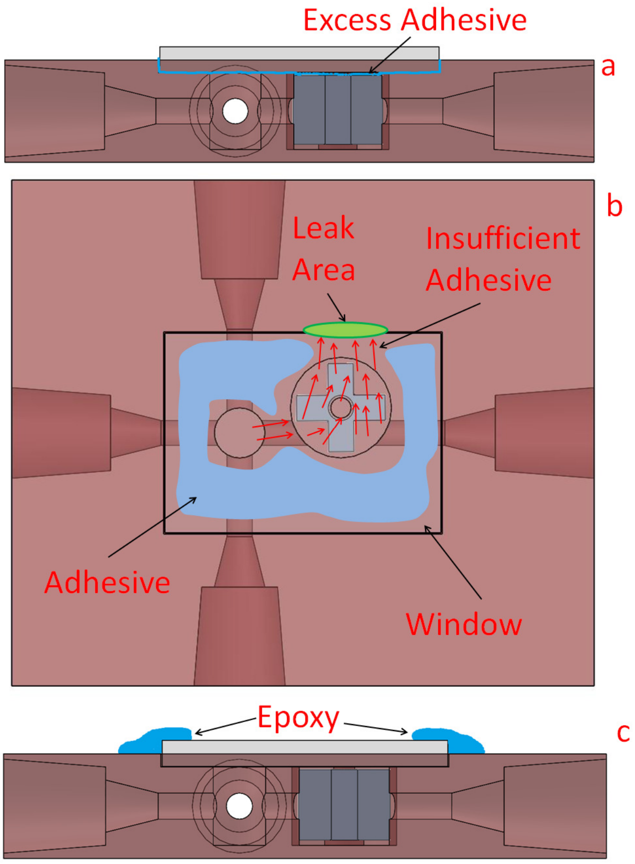

Figure 5.14 – Adhesion methods using: (a) an excess of superglue, (b) an insufficient amount of superglue, (c) a viscous epoxy adhesive

Instead, an epoxy base adhesive was used to securely hold down the window (Figure 5.14(c)). As the epoxy glue was more viscous it didn't seep into the flow cell. Unfortunately, the epoxy based method produced a less aesthetic result (Figure 5.15) and took considerably longer to set then the components took to fabricate.

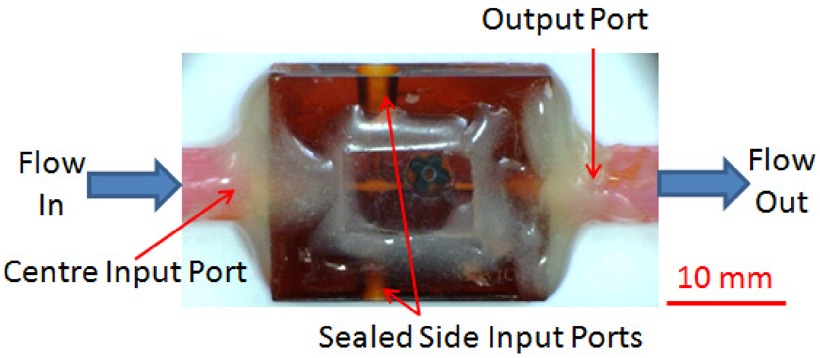

Figure 5.15 – Multi port micro flow meter with window (scale in mm)

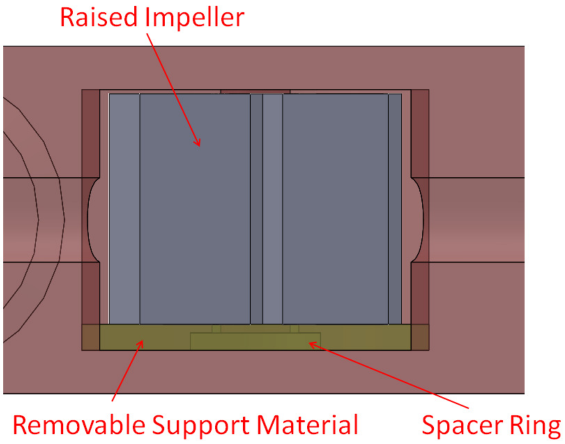

Figure 5.16 – Possible use of support material to enable device to be fabricated in a single, multi-material process

A more ideal solution would be to build the part as a single multi-material fabrication process. This way, there would be no need for the window as the impeller would already be build into the part. However, while the custom multi-material system would be fully capable of such a process, a third material would be required as a temporary support. The support material would be required between the base of the flow cell and the underside of the impeller to give a surface for the first layer of the impeller to build onto (Figure 5.16). The material would also need to be able to be dissolved in a solvent that didn't attack any other materials in the device. Part of the post-processing step would then be to wash away the support leaving the impeller to rotate freely. This is discussed further in Chapter 9 as further work.

5.3.6 Compact Lab-on-Chip Device Example - Testing

The device was tested with a liquid flow input into the centre input port (Figure 5.15). The two extra side ports were blocked off as the mixing capabilities of the device were not being tested. The fluid supply system consisted of a container filled with deionised water which was pressurised using the laboratory compressed air supply. The output of the container was connected to the input port of the flow device using PTFE tubing with an inner diameter of 0.76 mm. The output port was connected to PTFE tubing that fed into a glass beaker where the water was collected. The beaker was placed on a Precisa 310M digital measuring balance so that the weight of liquid passed could be measured during the test. When the tap of the compressed air line is opened the pressure in the reservoir container forces the water out and through the flow sensor. The flow rate was adjusted by varying the pressure applied to the container.

In order to accurately measure the frequency of rotation of the impeller a new amplifier circuit was designed for the AMR sensor. The circuit (Figure 5.17) converts the analogue sinusoid signal of the AMR sensor into a digital square wave signal. The circuit has three stages, the first stage is to buffer the differential output of the Wheatstone bridge sensor within the HMC1001 AMR device. This consists of two unity gain amplifiers. A third operational amplifier was then used as a simple differential amplifier with gain and an offset adjustment using a potentiometer to compensate for any static magnetic fields which cause the signal to be out of range of the op-amp. A capacitor then decouples the signal so that a reference can be generated from the AC signal and used as a reference for the final, fourth op-amp. The fourth op-amp is used without feedback and hence acts as a comparator. As the AC signal rises above and falls below the reference (the average of the AC signal), due to the internal gain of the device, the output swings from rail to rail, generating a TTL level version of the detected sinusoid wave.

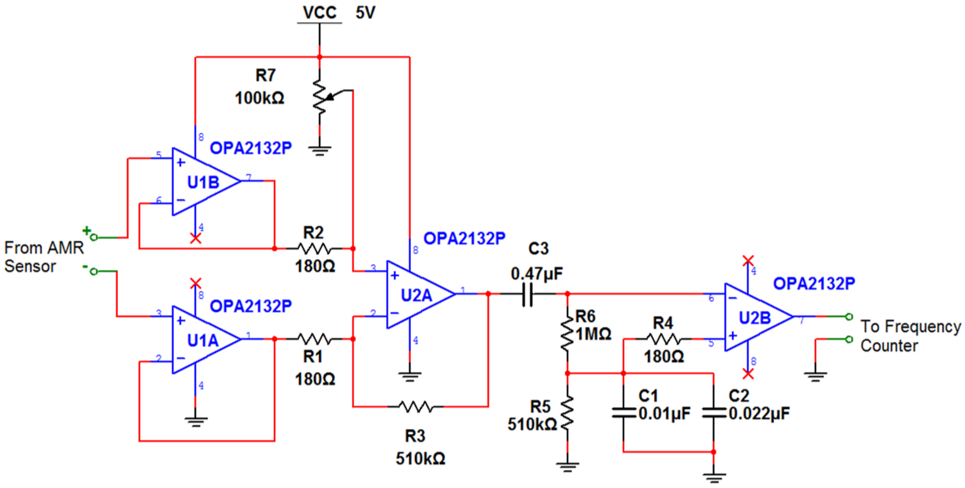

Figure 5.17 – Circuit diagram of amplifier with square wave output for direct frequency measurement of impeller rotation

The frequency of the digital signal was then measured using a HP5381A frequency counter device. The circuit also used a PIC microcontroller (Microchip, USA). This was used to periodically pulse the reset strap on the AMR sensor to ensure that the device doesn’t become poled (as discussed previously) to prevent inaccurate readings due to the lower amplitude of the signal. As the system was also to be used as a demonstration device, the controller also provided a visual output to indicate the detection of rotation of the impeller. This was simple to achieve by using the square wave output from the amplifier circuit as a clock input to sequentially illuminate a series of LEDs.

To measure the operating range of the device, water was passed through the device at a range of flow rates. The flow rates were set by adjusting the regulator on the air supply to the liquid container until the impeller was seen to be rotating at the desired frequency. The impeller frequency range used was from 20 Hz up to 200 Hz in 10 Hz steps. The frequency steps did not have to be exact as they were only used to gather enough information to characterise the sensor, however, the flow rate (and therefore measured frequency) must remain stable in order to obtain reliable results. The air supply was then turned off using the isolation tap while the measuring balance was zeroed. Then air pressure was then re-applied for a period of 60 seconds. During this time, a reading was taken from the frequency counter every 10 seconds to ensure that any variation in flow rate was accounted for. At 60 seconds the reading on the balance was recorded. Figure 5.18 shows the setup used.

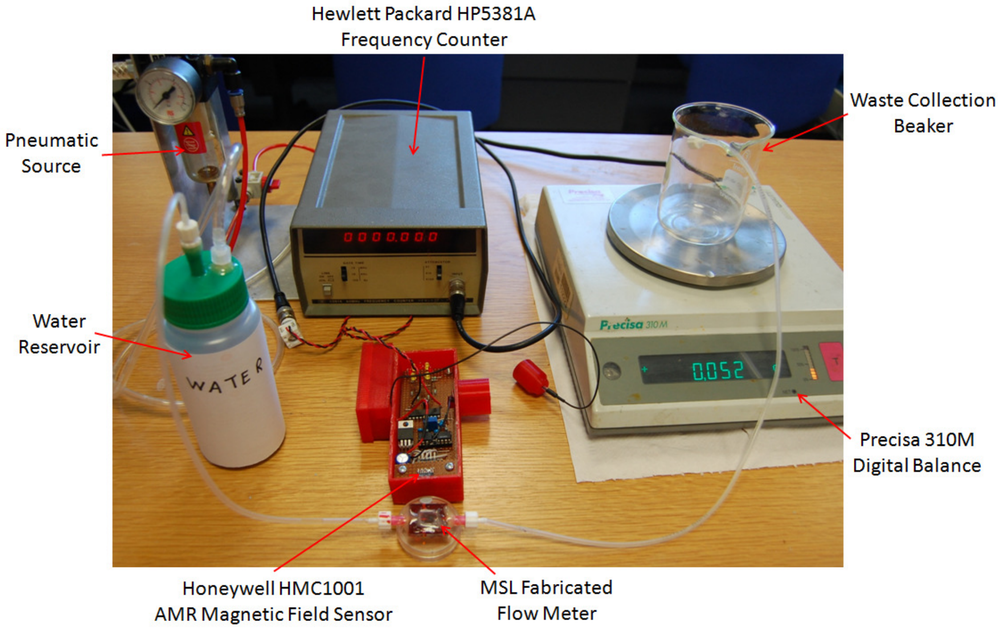

Figure 5.18 – Experimental setup for testing multi-port device

During testing of the device it was observed that the performance could be significantly reduced by the presence of trapped air bubbles in the impeller chamber, it was therefore essential to purge the device before testing. Often air bubbles could be purged by simply forcing liquid through the device using a syringe before connecting it to the test system. However, if the air bubble was large enough to encapsulate the entire impeller then the bubble had a tendency to simply rotate around the impeller or get stuck in the corners of the impeller. In order to overcome this it was necessary to briefly operate the device with the exit port pointing upwards until all bubbles were purged. Providing no more air bubbles entered the system while being used the device could then be operated in any orientation. At flow rates above 60 ml per minute it was observed that the seal between the Luer-Lok needles and the ports on the device were not sufficient to prevent leaks. As such, further epoxy adhesive was used to stop the leaks and prevent the pressure of the fluid from forcing the needle out of its compression fitting.

5.3.7 Compact Lab-on-Chip Device Example - Results

The data collected from the testing of the device is shown in Figure 5.19. Here, the results from three individual runs are shown. In all three runs the device was observed to have a near linear relationship between the flow rate and observed frequency over the majority of the test range. As with the 2 port flow device, below a certain range, the flow was not sufficient to cause the impeller to rotate. The minimum flow rate required for the device to operate was approximately 6 ml per minute; however it was felt that only rates of 8 ml per minute and above could be measured with any great confidence. No measurements were taken beyond a rate of 70 ml per minute as the integrity of the sealing of the device began to fail. At this point the impeller began to fail as the force of the fluid caused the material to disintegrate. Therefore the upper limit of the usable rage was found to be approximately 68 ml per minute, although for longterm it is suggested that 60 ml per minute would be more appropriate.

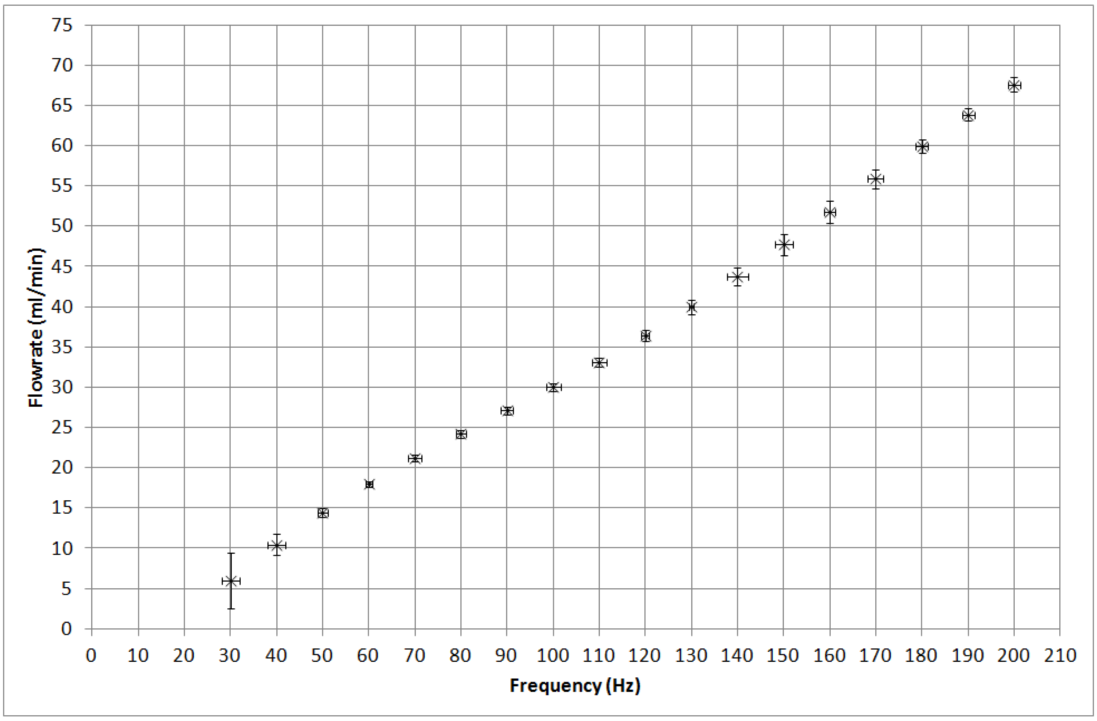

Figure 5.19 – Observed relationship between measure flowrate and frequency of impeller rotation for multiport device

As the device exhibited a near linear relationship over the working area, it could therefore be characterised and the relationship between the detected frequency and flow rate could be established. Equation 5.1, determined using the least squares method, approximates the behaviour of the device, where f is the detected frequency in Hz and r is the flow rate in ml/minute.

$$f = 2.8304\,r + 12.593 \tag{5.1}$$

To verify the quality of the observable signal from the rotating 4mm diameter impeller, the AMR circuit previously used to conduct the initial field strength test on the cube components in the previous chapter was used with the small impeller setup. Figure 5.20 shows the measured signal for one rotation of the impeller at 190 Hz (approximately 60 ml/minute) from this test. The signal shows two possible noise elements, firstly, a ripple of 1.1% of the peak-to-peak amplitude was present throughout the signal at a frequency of approximately 6.2 kHz, which is thought mainly to be a factor of the sampling capabilities of the oscilloscope. Secondly, there was also a larger noise component of ~6%, at 330 Hz which was consistently observed halfway through the rotation. This second noise element is thought to be caused by transition of the magnetic field lines of the poled material passing through the sensing device as the impeller rotates. This highlights that care needs to be taken when polling the material to ensure that it is done uniformly. While the error is not significant enough in this case to cause erroneous readings, it could cause inaccurate results in more sensitive applications.

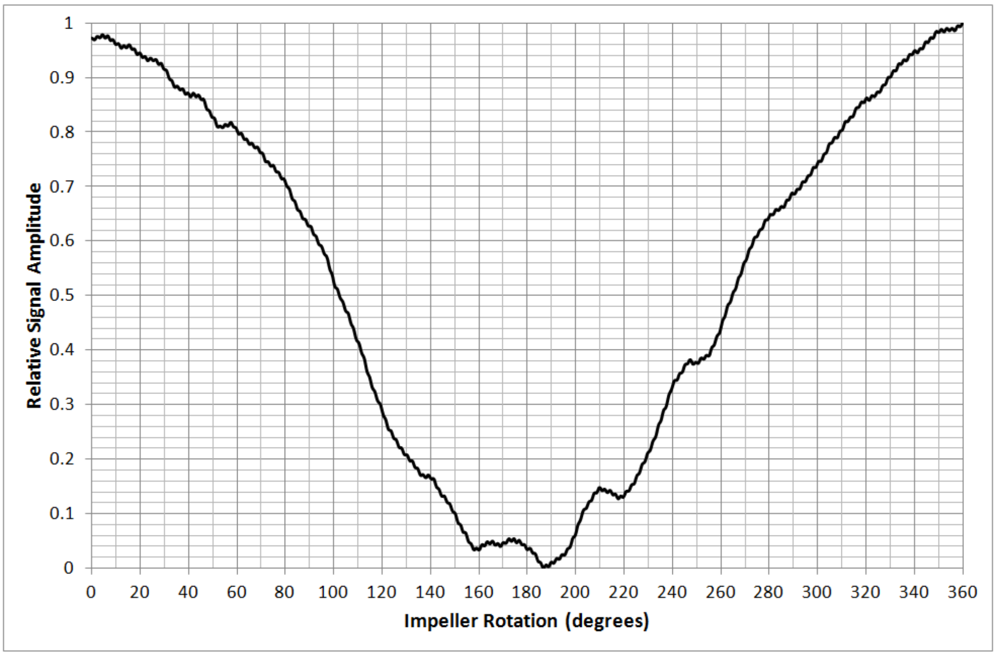

Figure 5.20 – Measured signal from a single rotation of the 4mm diameter impeller

5.4 Conclusion

In this chapter, the designs of two MSL fabricated miniature flow sensors have been outlined. The devices were fabricated as proof of concept that the novel magnetic composite material could be utilised in practical measurement applications. The two devices were successfully fabricated on different scales to demonstrate both standalone and possible lab-on-chip applications. It was also demonstrated that an impeller based sensing technique is suitable for use with both gas and liquid test mediums. Both devices demonstrated regions of linear response with the lab-on-chip device showing a proportional response over an entire working range of 5-70 ml/minute using a liquid medium.

During the development of the devices a number of initially unforeseen problems were encountered. These included friction between the planar surfaces within the device that resulted in limiting the operating range and issues with sealing the device post fabrication. To avoid the issue of sealing and to improve the capabilities of the technique, it is felt that ideally such a device would be fabricated in one process to avoid post fabrication assembly. However, while this is possible with devices with entirely static features, designs with dynamic and moving parts such as the impeller may require a further material to act as a dissolvable support. Analysis of the received signal showed that care must be taken when the material is being poled to ensure that all regions are magnetised as intended. It is suggested that a more effective and repeatable method of achieving this would be an area for further investigation.

While the use of the magnetic composite material was demonstrated here by using it to successfully fabricate micro flow sensing devices, this is just one example of its potential uses and it is suggested that further research could lead to the material potentially being utilised in a wide range of other measurement and actuation applications.

5.5 References

[1] S.J. Leigh, C.P. Purssell, J. Bowen, D.A. Hutchins, J.A. Covington, D.R. Billson, A miniature flow sensor fabricated by micro-stereolithography employing a magnetite/acrylic nanocomposite resin, Sensors and Actuators A 168 (2011) 66–71

[2] P. King, J. Covington, A novel monolithic microactuator fabricated by 3D rapid direct manufacture Procedia Chemistry 1 (2009) 1163–1166

[3] I.I. Leonte, G. Sehra, M. Cole, P. Hesketh, J.W. Gardner, Taste sensors utilizing high-frequency SH-SAW devices, Sensors and Actuators B 118 (2006) 349–355

[4] F.K.C. Harun, Mimicking the Human Olfactory System: A Portable e-Mucosa, PhD Thesis, University of Warwick, UK, 2009

[5] P.H. King, towards Rapid 3D Direct Manufacture of Biomechanical Microstructures, PhD Thesis, University of Warwick, 2009

[6] Z.-X. Guol, Q. Zeng1 , M. Zhang, L.-Y. Hong, Y.-F. Zhao, W. Liu, S.-S. Guo, Z.-Z. Zhao, Valve-based microfluidic droplet micromixer and mercury (II) ion detection, Sensors and Actuators A 172 (2011) 546– 551

[7] E. Menga, P.-Y. Li, Y.-C. Tai, A biocompatible Parylene thermal flow sensing array, Sensors and Actuators A 144 (2008) 18–28

[8] B.W. Oudheusden, Silicon thermal flow sensors, Sensors and Actuators A, 30 (1992) 5-26

[9] S. Wu, Q. Lin, Y. Yuen, Y.-C. Tai, MEMS flow sensors for nano-fluidic applications, Sensors and Actuators A 89 (2001) 152-158

[10] M. Esashi, Integrated Micro Flow Control Systems, Sensors and Actuators A21-A23 (1990) 161-167

[11] L. Scholer, B. Lange, K. Seibel, H. Schafer, M. Walder, N. Friedrich, D. Ehrhardt, F. Schonfeld, G. Zech, M. Bohm, Monolithically integrated micro flow sensor for lab-on-chip applications, Microelectronic Engineering 78–79 (2005) 164–170

[12] S. Billat, K. Kliche, R. Gronmaier, P. Nommensen, J. Auber, F. Hedrich, R. Zenge, Monolithic integration of micro-channel on disposable flow sensors for medical applications, Sensors and Actuators A 145–146 (2008) 66–74

[13] T.S.J. Lammermk, N.R. Tas, M. Elwenspoek, J.H.J Flultman, Micro-liquid flow sensor, Sensors and Actuafors A, 37-38 (1993) 45-50

[14] M. Shikidaa, T. Yokotab, S. Ukaib, K. Satob, Fabrication of monolithically integrated flow sensor on tube, Sensors and Actuators A 163 (2010) 61–67

[15] M. Ashauer, H. Glosch, F. Hedrich, N. Hey, H. Sandmaier, W. Lang, Thermal flow sensor for liquids and gases based on combinations of two principles, Sensors and Actuators A: Physical 73 (1999) 7–13

[16] Y. Tanaka, M. Terao, T. Akutsu, K. Isozaki, Micro Flow Sensor for Microreactor, Yokogawa Technical Report English Edition No. 47 (2009) 37-40

[17] C. Dam-Hansen, S.R. Kitchen, Holographic optical element for laser time-of-flight flow sensor, Optics and Lasers in Engineering 44 (2006) 954–964

[18] J. Lim, Q.P. Yang, B.E. Jones, P.R. Jackson, DP flow sensor using optical fibre Bragg grating, Sensors and Actuators A 92 (2001) 102-108

[19] C. Songa, A.R. Aiyarb, S.-H. Kima, M.G. Allena, Exploitation of aeroelastic effects for drift reduction, in an all-polymer air flow sensor, Sensors and Actuators A 165 (2011) 66–72

[20] Q. Zhang, W. Ruan, H. Wang, Y. Zhou, Z. Wang, L. Liu, A self-bended piezoresistive microcantilever flow sensor for low flow rate measurement, Sensors and Actuators A 158 (2010) 273–279

[21] 1- and 2-Axis Magnetic Sensors HMC1001/1002/1021/1022 datasheet, Honeywell International, USA, [online] from: www51.honeywell.com/aero/common/documents/myaerospacecatalog-documents/Missiles-Munitions/HMC_1001-1002-1021-1022_Data_Sheet.pdf, last accessed: 25/05/2012

Chapter 6

6 Development of an MSL Compatible Conductive Material

This chapter details the development of an electrically conductive composite photopolymer resin material. Such materials allow for the fabrication of fully 3D micro structures that have conductive properties using microstereolithography. Existing methods to generate such components using ALM generally involve separate fabrication of structural and conductive components with a later assemble step such as that presented by DeNava et al [1]. Here, the group presented a pseudo multi material device whereby a structural body was first fabricated using ALM techniques and the components and electrical interconnections were added later manually.

The aim of this work was to develop a photopolymer based material that has electrically conductive properties using rapid manufacture technologies such that it can be used to explore fabrication of devices and sensors. Indeed, given sufficiently high conductivity, such materials could also provide a means of electrically interfacing to other embedded devices within a component using microstereolithography. This would have numerous benefits due to the reduced cost and rapid production of devices without the need for complex processing or additional post processing steps such as sintering. It is felt that the capability to rapidly produce such monolithic lab-on-chip devices could be particularly useful for research groups who may frequently want to alter designs and have a rapid turnaround of components, or applications where the devices have limited usage time.

The first section provides a brief explanation on material conductivity, in particular the methods available to produce polymer based materials with electrically conductive properties. Following on is a discussion of the development of a conductive composite photopolymer material. The final section covers testing and characterisation of the material.

6.1 Introduction

In metals, the outer electrons of the atoms can disassociate from their nucleus and are free to move throughout the material's lattice. This allows clouds of disassociated electrons to form which are then easily moved when a potential is applied across the lattice. The electron disassociation that occurs in metals does not generally occur in traditional polymers, therefore, while some polymers can store charge as static electricity, polymers are generally considered to be insulators.

Polymers with conjugated backbone [2-4] structures (which results in promoting delocalised electrons and therefore conductivity) known as intrinsically conductive polymers (ICPs) can be synthesised - McCullough et al [5] demonstrated conductivities of 10^5 S m^{-1} by doping PDDT (poly(3-dodecylthiophene)) with iodine vapour. However, while ICP materials may appear to have the desired properties (being formable and having good conductivity), aside from being difficult to synthesise, ICPs have a tendency to be unstable and have their conjugated backbone easily degrade [6]. Additionally, the requirement of having conjugated bonds results in the materials being incompatible with the photopolymerisation process used in MSL systems.

As discussed previously and demonstrated in the previous chapters, it is possible to mix functional filler materials into polymer materials to enhance either their structural or functional properties. Therefore, by adding filler particles to an insulating polymer that are of an electrically conductive material, a conductive polymer composite can be produced. This way, the polymer is used to form the 3D structure while the embedded particles from a conductive path through the material.

6.2 Conductive Polymer Composites (CPCs)

A less complex method of producing a polymer based material with conductive properties is to produce a composite. Unlike an ICP, where the material properties of the polymer allow them to be conductive, in a conductive polymer composite the polymer acts as an insulator. It is the presence of an additional electrically conductive component that forms numerous electrical pathways through the polymer that give the overall material conductive properties. As the bulk of the material (the polymer) is an insulator, conductive polymer composites are semiconducting materials. The conductivity can then be controlled by altering either the ratio of polymer to filler material, or the type of filler material itself [7-10]. One of the main uses of CPCs are for electromagnetic interference (EMI) shielding and electrostatic discharge (ESD) protection applications [8, 11] although they are also often used in gas and vapour sensing [12-14] applications, in both cases the material is usually deposited by spraying the dissolved composite mixture [14].

Providing the filler material doesn’t interfere with the polymerisation process either chemically or physically (i.e. by excessively obscuring the exposure light), it allows for a simple yet effective method of producing a conductive material which was compatible with the MSL process. Additionally, it has the advantage that the conductivity of the overall material can be controlled by altering the filler volume. As such, this was the method that was investigated for the purposes of this work.

Unlike the magnetic composite material discussed in previous chapters, a polymer/conductor composite of any kind will not exhibit the desired functional properties until a critical proportion of filler material is reached. The threshold is based on the statistical probability that a conductive path will be formed through the matrix structure of the polymer assuming that the filler is homogeneously distributed through the structure. For a simplified 2D model, theoretically, assuming that the particles are spherical and of identical size, it is possible that the minimum filler volume necessary is simply the width of the component divided by the diameter of the filler particle size (Figure 6.1(a)). However, this does not represent a homogenous material and it is unlikely that this situation will occur. Figure 6.1(b) shows a simplified example of the condition that more likely to occur with the same fill volume. In this case, despite there being the same fill ratio, there is no electrical path between the two ends of the specimen (assuming the polymer is a perfect insulator). By increasing the ratio of filler particles in the composite, the probability that a series of adjacent conductive particles will form a continuous chain between two opposite faces increases. The critical threshed is the point at which this happens (Figure 6.1(c)), known as the percolation threshold [15, 16].

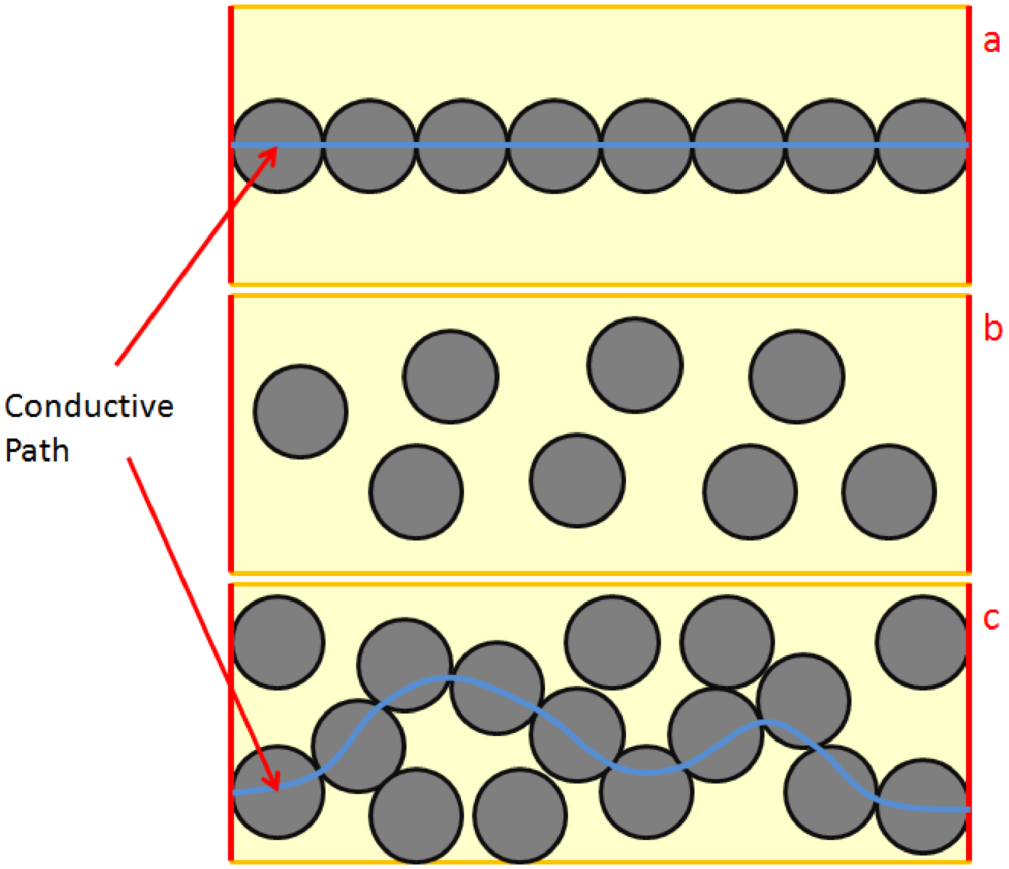

Figure 6.1 – Particle distribution with (a) absolute minimum number of filler particles in order for conduction to occur, in an ideal situation, (b) absolute minimum number of filler particles in order for conduction to occur in a realistic situation, therefore no conduction due to the filler particles, (c) the realistic minimum number of particles in order to overcome the percolation threshold

Once the critical threshold is exceeded, multiple chains can then join which creates a lattice structure throughout the material, at this point the conductivity can increase greatly with only small increases in filler percentage. This effect is detailed by Mamunya et al [17] who defined the percolation threshold as the point that an "infinite conductive cluster" [18] is formed and therefore, the material begins to exhibit conductive properties. Their work was conducted using an epoxy and PVC (polyvinyl chloride) based polymers with copper and nickel fillers with average particle sizes of 100 μm and 10 μm respectively. Figure 6.2 shows their results for a PVC/Nickel composite with three different filler contents. The lowest resistivity achieved in their study was with a copper filled PVC composite where at maximum fill (30% by volume) the measured resistivity was 1.58 x 10^{-6} Ωm (conductivity of 6.31 x 10^{5} Sm^{-1}) with the resistance at the critical threshold being 1.58 x 10^{13} Ωm (conductivity of 6.31 x 10^{-14} Sm^{-1}).

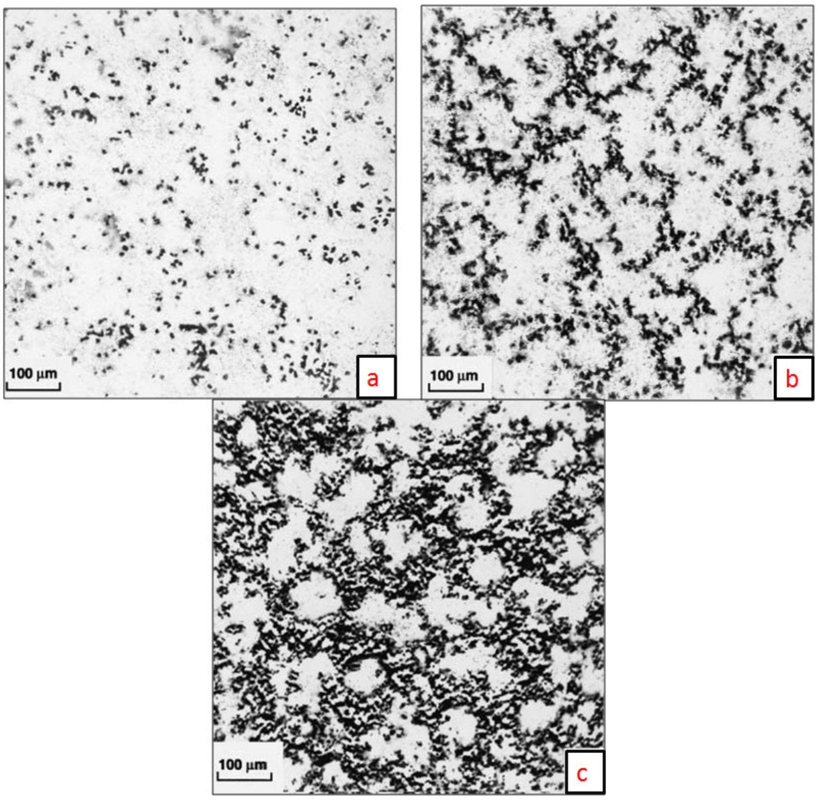

Figure 6.2 – 10 μm Nickel particle distribution in PVC where the filler content is (a) less than the critical threshold, (b) equal to the critical threshold, (c) greater than the critical threshold (taken from Mamunya et al [17])

6.3 Conductive Composite Material Development

Based on previous experience working with the MSL system and other similar composite materials, the use of three different monomers as possible base photopolymer formulations for the composite material was explored:

- PEG (polyethylene glycol)
- HDDA (1,6-hexanediol diacrylate)
- HDEDA (1,6 hexanediol-ethoxylate diacrylate)

All formulations used DPPHA (dipentaerythritol penta-/hexa-acrylate) (Sigma–Aldrich, UK) as a crosslinker while Irgacure 784 (Sort Chemicals Ltd, UK) was used as it's active region covers the custom MSL system's peak output wavelength. Both metal and carbon based filler materials were explored as possible conductive filler materials.

6.3.1 Metals

Initial investigations experimented with using a metal powder as an additive to the basic resin so that the bulk final material would show conductive properties. In these tests copper and nickel powders were used as other [17, 19, 20] researchers had success with these and similar additives. The copper powder used had average particle sizes of 10 µm (Sigma–Aldrich, UK), while the nickel the nickel powder was submicron with particle size < 1 µm (Sigma–Aldrich, UK).

As the previous magnetite composite had required a base resin with a greater viscosity than that of a standard MSL resin, due to the mass of the filler particles, it was expected that a similarly viscous base resin would be required in order to successfully hold the metal filler particles in suspension. In order to ensure that the filler ratios were sufficient to overcome the minimum threshold for conduction, as a starting point, fill loading ratios of 1:1, 1.5:1 and 2:1 by weight of filler to polymer were mixed with the base resins using a range of monomer to cross-linker ratios. While it quickly became clear that the PEG based material would not be suitable for the heavy metal filler as the filler material was observed to fall out of suspension rapidly, both the HDDA and HDEDA showed promise but a high ratio of cross linker was required in order to achieve a homogenous suspension. In many of the resin formulations previously used with the system, which do not include a filler material, the typical ratio of monomer to cross-linker required was between 10:1 and 1:1. However, in order to hold the filler particles in suspension with filler ratios of 1:1 by weight or greater, a ratio of 3:4 (monomer to cross-linker) or greater was required to achieve a sufficient viscosity. At this level, the particles were observed to stay in suspension for a period of around 2 hours which was considered a sufficient amount of time as, depending on the height of the parts being built, it allows for the material to be used a number of times. Beyond this period the filler material was observed to begin falling out of suspension and so the fill fraction cannot be guaranteed, therefore re-mixing was required in order to continue using the material.

With these levels of filler loadings, both the copper and nickel materials in both HDDA and HDEDA material began to exhibit a viscous coarse texture. The Nickel filled resins in particular exhibited this issue due to the ferromagnetic properties of the Nickel particles causing them to attract together and aggregate [21]. While the Nickel resins could be mixed to a smooth consistency, when used in the MSL system the repetitive peeling and levelling action of the build platform caused the resin to begin to separate after only 5 layers. By 10 layers, the resin had separated to an extent where the Nickel particles had completely dropped out of suspension and so both obscured the exposure light from the system and caused the build platform to fail to reach the desired layer thickness during the build process due to the large aggregates formed. It is felt that this was largely due to the ferromagnetic properties of the Nickel particles that encouraged the formation of aggregates.

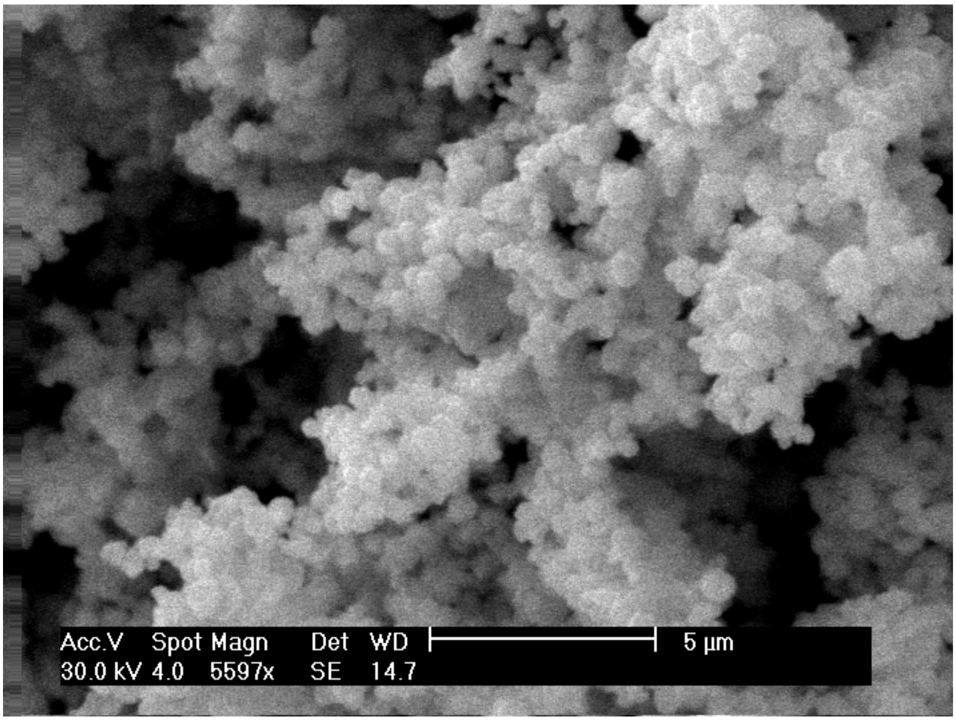

Figure 6.3 – SEM micrograph showing aggregation of Nickel nanoparticles due to their ferromagnetic properties

Figure 6.3 shows an SEM micrograph of the Nickel particles. It was observed that although the individual particles were consistently on the order of 500 nm +/- 50 nm, none were observed to be separate from a larger cluster due to the magnetic attraction between the particles. Indeed, due to their ferromagnetic properties the particles were difficult to image using the SEM even with the assistance of an experienced operator. The cluster sizes varied greatly in size from 10 μm up to 500 μm. As such further investigations proceeded with only the copper particles.

Similar aggregation problems that caused the MSL system to fail to reach the required layer thickness were encountered with the materials using Copper filler particles. However, it was observed that the aggregation was far less than both the Nickel and Magnetite filled resins discussed previously, also, the levelling failures were not seen to be occurring at any one point during the build process. It was therefore felt that the levelling problem with the Copper filled materials was due to the size of the particles in the filler.

Although the average particle size of the copper powder being used was 10 µm, this meant that potentially there were particles in the filler whose size was greater than the thickness of the layer being attempted. In order to reduce the average particle size, attempts were made to remove the larger particles from the powder before being mixed into a fresh batch of resin. The separation was performed in two steps; firstly the larger particles were removed using a woven wire mesh sieve with a certified aperture size of 38 µm, secondly, the sieved particles were further separated using a liquid suspension technique. The suspension technique involved vigorously mixing the smaller sieved particles in isopropanol in a round bottomed flask, waiting a short period to allow the large particles to settle, and then decanting the isopropanol with the remaining smaller particles into a beaker. The waiting time between mixing and decanting in this case was 5 seconds. This step was repeated 5 times to ensure that all larger particles had been removed. The selected particles were then filtered from the isopropanol and left to dry in an evaporating dish. Figure 6.4 shows images taken using a scanning electron of particle size difference between the selected fine particles (a) and removed larger particles (b). The images show that the selected powder now has an average particle size of approximately 20 µm with a maximum size no larger than 30 µm +/- 5 µm.

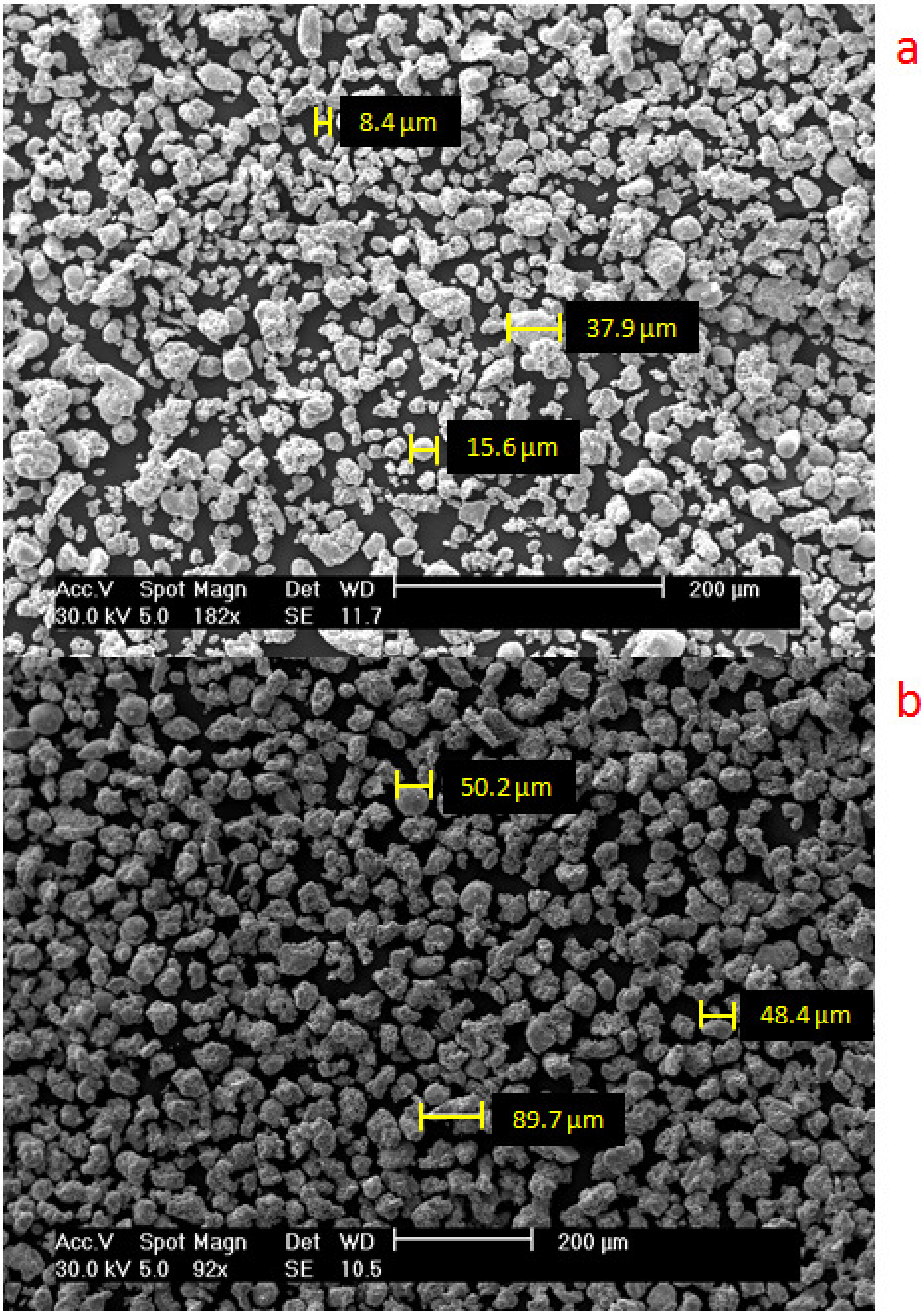

Figure 6.4 – SEM micrograph of (a) sieved and (b) excess copper particles

Following the sieving procedure, the copper based materials were found to be more stable and reliable. Although the time between mixing and the filler material being observed to be beginning to fall out of suspension was not seen to increase, the previous issue with the MSL system failing to level its build platform due to large particles and aggregates no longer occurred until around 100 level/peel cycles had occurred when using the HDDA based resin.

Around 120 cycles could be achieved with the HDEDA material but this material required much lower levelling velocity in order to ensure that the build platform reached the desired layer thickness without causing a position error, and lower peel velocities to ensure the components were not pulled off the build platform. Table 6.1 shows the difference in velocities between the two materials.

Monomer	HDDA	HDEDA
Peel Velocity (mm/s)	0.05	0.01
Levelling Velocity (mm/s)	0.1	0.01

Table 6.1 – Fabrication peel and level velocity settings used for copper composite materials with fill ratios of 1:1to 2.5:1 (filler to polymer) depending on monomer used

Although the HDEDA material showed to be able to produce more layers before needing to be replaced or re-mixed, the difference was small and due to the slower movement velocities. Therefore, there was seen to be no advantage to using the HDEDA material. When taking into account reliability of the fabrication, quality of the produced parts and achievable fabrication time, the optimal component ratio for the base resin was determined to be 2:3 monomer (HDDA) to cross-linker using with 5% photoinitiator. This base material was found to be suitable for copper filler loading of between 1:1 and 2.5:1 (filler to polymer) by weight for standard 25 μm layer thicknesses. Table 6.2 shows the build settings used with the final HDDA based material.

Layer thickness (μm)	25
Exposure time (s)	45
Separation (mm)	2
Peel speed (mm/s)	0.05
Levelling speed (mm/s)	0.1
Wait time after level (s)	5
Wait time after peel (s)	5

Table 6.2 – Fabrication settings used for 1:1 to 2.5:1 HDDA based copper composite materials

Although the copper composite material could be used in the MSL system, when test components (measuring 5 mm x 5 mm x 0.5 mm) were measured for their resistance (measured using a Solartron 7075 Digital MultiMeter) across and of the opposing sides, they exhibited no obvious conductivity (maximum measureable resistance of 14 MΩ). Using the multimeter an attempt was made to measure the resistance of a sample of the unused powder. Unexpectedly, no reading could be obtained from the copper powder as the resistance was seen to be beyond the range of the meter (14 MΩ).

It was thought that the high resistances observed were due to the small particle size, indeed, Lu et al [22] discuss with reference to magnetic nanoparticles, that pure metals (Iron, Cobalt, and Nickel are given as examples) and their metal alloys are very sensitive to oxidation in air. It is also highlighted that as the particle size decreases, the susceptibility to oxidation increases. A number of possible solutions are presented to prevent the surface oxidation; however, all involve coating the particles in a protective layer. While many of the suggested methods involve using a coating that would provide undesirable electrically insulating properties, it is thought that the methods of coating the particles in another oxidation resistant metal, or carbon would be possible solutions to prevent the oxide layer forming.

Lee et al [23] have reported success in producing a conductive photocurable material for MSL using 3 µm copper particles. However, they also note that their method requires a post fabrication sintering step (up to 950 °C) of the components under vacuum in order for the components to exhibit the desired conductive properties. While this initially may appear to be a solution, the required sintering step then presents a number of issues aside from the requirement of access to the necessary sintering equipment. Firstly, sintering prevents the fabrication of components with monolithic conductive and non-conductive elements as the non-conductive elements would be destroyed in the sintering step which would rule out the possibility of creating fully integrated devices in a single processing step. Secondly, the components undergo a size reduction when sintered as the polymer binder is burnt off.

While this may in some cases be favourable in order to effectively achieve a higher resolution that the fabrication system may be able to achieve, the process must be carefully controlled in order to ensure uniform shrinkage to prevent the deformation of the component. As such, sintering of the components was not considered to be a viable option.

To verify whether this was the case, the copper particles were acid washed in hydrochloric acid in order to remove the oxide coating. After washing, the powder resistance was again measured by measuring across a sample of the powder (~ 5mm diameter x ~0.5 mm height) with a multimeter. A resistance of ~2ohm +/-25% was measured initially, although within a period of 5 minutes, this value rose steadily until the resistance passed beyond the measuring range of the meter. This indicated that the high resistance observed previously was cause by an oxide coating on the particles.

Due to the issues with material stability and conductivity it was therefore decided that concentration would move to the use of a non-metallic filler, carbon black. However, it is felt that with further research, which would be beyond the scope of this thesis due to the time taken to develop such a material, it may be possible to achieve a conductive composite using metal powders.

6.3.2 Carbon Black

While working on the metal based composites, the use of amorphous carbon black being used to produce a partially-conductive composite photopolymer was also being explored. While the main aim was still to produce a material that could be directly utilised as a conductor, due to the lower conductivity of amorphous carbon (approximately 1.5×10^5 Sm^{-1}) when compared with metal conductors (between 10×10^6 Sm^{-1} and 60×10^6 Sm^{-1}) it was also expected that the material could be effectively used to fabricate resistive elements for mechanical or chemical sensing applications.

Carbon filled polymer composites are already well established in the field of conductive polymer composites [24, 25]. Their use has been explored variety of applications such as in fuel cells [26, 27], EMI and ESD protection[8], gas and vapour sensing [12, 13, 28, 29, 30], and strain/pressure measurements[31, 32]. These applications make use of the materials either as thin films, deposited coatings, extruded 2D structures, or simple injection moulded 3D structures.

Unlike the magnetic material discussed previously, where the desire was to achieve the highest possible loading in order to have a stronger signal and hence reduce the signal to noise ratio of the system, for a semiconductor material it is just as desirable to be able to produce components where the electrical characteristics can be tuned to a specific range. In this way, the resistance of the material, for example, could be matched to the application.

The simplest use of such a material is as a printable resistor or as an electrode in an electroanalysis setup for measuring the electrical properties of a fluid analyte. It is felt that such materials would also serve well to provide a means of fabricating structures such as strain gages that could be printed directly onto membranes in order to produce simple pressure sensors – a technique not previously seen before with MSL technologies. For these purposes, a HDDA based material was explored. Finally, it is felt that the most appealing use for such a material is in the novel method of utilising MSL to fabricate gas sensors. This was achieved by utilising the swelling properties of a PEG based material and is discussed further in the following chapter.

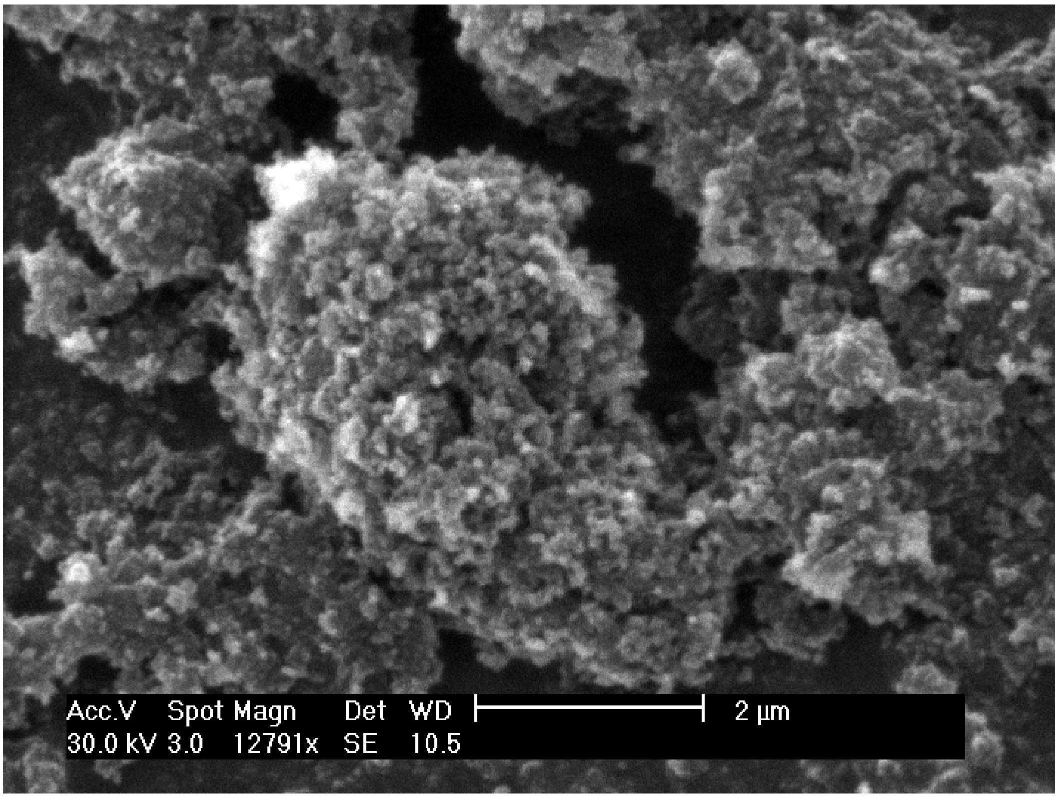

Figure 6.5 – SEM micrograph of aggregated carbon black particles

The HDDA monomer material was explored for use as a basic conductive material that would serve as a means to produce conductive 3D structures. The carbon black material used was based on carbon black pearls (Cabot, USA). The powder used was made by crushing the pearls using pestle and mortar. An SEM image (Figure 6.5) shows that the powder consists of particles on the order of 100 nm to 500 nm with aggregates on the order of 2 µm to 10 µm, most of which appear to break up and disperse when mixed into the liquid resin.

As the carbon black material was much less dense that the metal fillers used previously, the previous issue experienced regarding holding the filler in suspension was not seen to the same extent and was to be far less susceptible to separate. Indeed, with the formulation used, the filler particles were observed to remain in suspension for in excess of 10 hours before requiring re-mixing (5% by volume of carbon black). With high % loadings (up to 10% by volume) this period was less although was never observed to be less than 5 hours. The formulation used was 3:1 of HDDA to DPPHA as it was found to provide satisfactory results using a wide range of both filler percentage and settings for exposure time, peel speed and levelling speed. Figure 6.6 shows samples of 10% loaded resin that have been subjected to 200 level/peel cycles to 25 µm thickness with peel/level speeds of 1 mm/s (a) and 0.05 mm/s (b). It can clearly be seen that at the higher velocities the filler particles are more susceptible to dropping out of suspension.

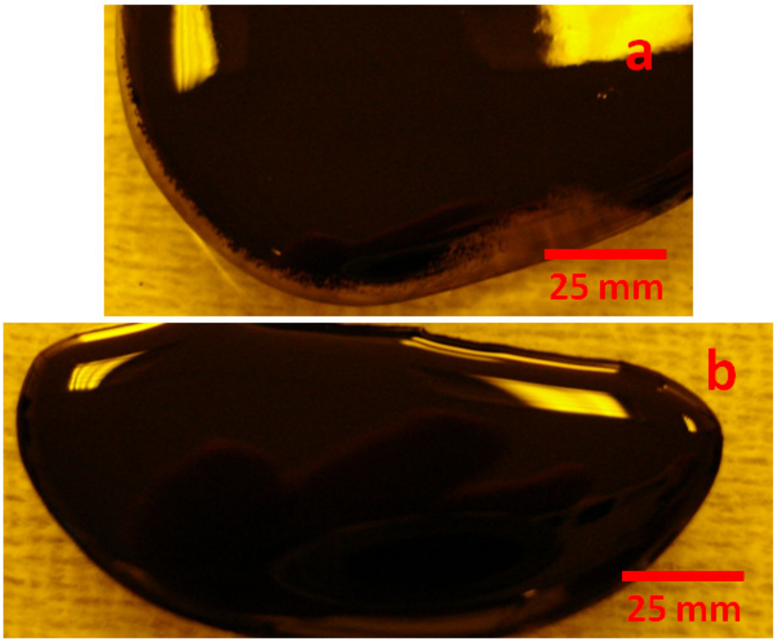

Figure 6.6 –Photographic image of resin material with filler of 10% by volume of carbon black using a monomer (HDDA) to cross-linker (DPPHA) in 3:1 ratio after 200 level peel cycles (5mm at 25µm layer thickness) at (a) 1 mm/s, (b) 0.05 mm/s

As mentioned in previous chapters, the MSL system uses two types of resin tray/plate, a resin tray for use during fabrication, and a calibration plate for use during calibration of the z-axis and focusing of the projected dynamic mask. The resin tray used during the development of material has no sidewalls as generally only a small amount of material is used and having no sidewalls makes cleaning the remaining resin from the plate easier, this however results in the test resin tray and calibration plate appearing almost identical. During the development of the HDDA and PEG based (discussed in the following chapter) carbon black composites, the calibration plate was used in error at one point.

However the components produced when using the calibration plate as the resin tray in general had visibly better defined features and appeared less prone to becoming unattached from the build platform during fabrication. It is thought that this is due to the calibration plate having a harder surface coating that prevents any adhesion between the component and the tray during the exposure step. Further tests using the calibration plate also found that the resin material pooled more easily after the peeling step, this resulted in the material being largely unaffected by separation height and peel speed. The droplets of material shown in Figure 6.6 (above) show the beading effect of the resin material when on the calibration plate. Materials with higher filler volumes (7.5% and 10% by volume) were however still used with lower peel speeds to prevent components becoming unattached during fabrication (Figure 6.7). For the remainder of the work using the conductive carbon black composite photopolymers, the calibration plate was used as the resin tray for the fabrication process.

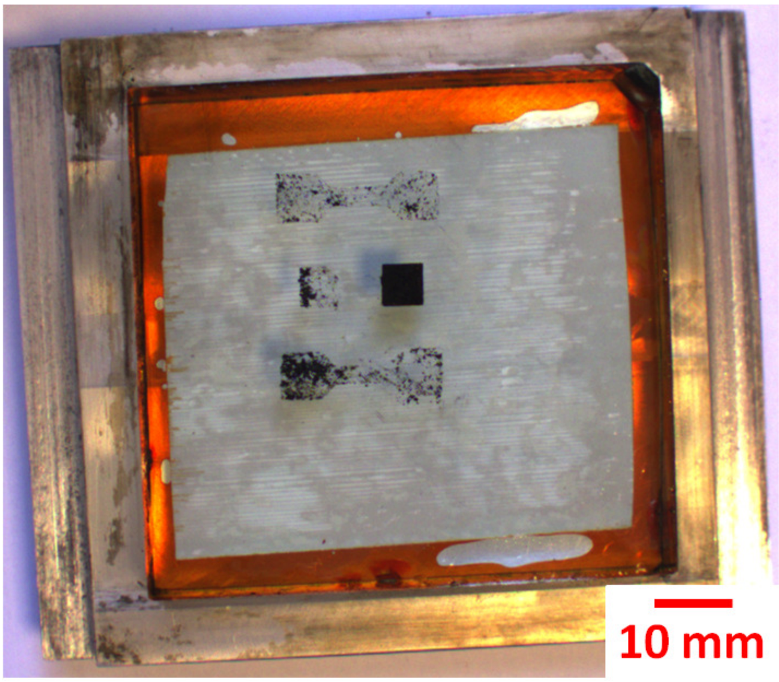

Figure 6.7 – Photographic image showing remains of failed components using 10%vol carbon black loading which became unattached from the build platform during fabrication do to too high peel speed

As with the magnetic composite material, it was observed that choosing the correct duration of stir time after adding the filler material was one of the more crucial parts of the fabrication process that had a significant effect on the success or failure of a build. If the stir duration was too short then the larger clumps of particles were not broken down and dispersed properly, which lead to some parts of the material being very thick and other areas with little or no filler material. A thick resin material is caused by incomplete dispersion of the filler and is caused by aggregates not being broken down. The aggregates prevent the build platform from reaching the desired level; this was particularly apparent when using the calibration plate as the resin tray as its surface coating is harder, which prevented it conforming to larger particles. Insufficient mixing also resulted in greatly reduced, or in some cases no, conductivity of the component. Conversely, if the stir period was too long then the resin covered carbon black particle began to aggregate again. The aggregation leads to similar problems to under stirring. Figure 6.8 shows the typical pattern observed on the surface of the build platform if the resin material has been over stirred. It should also be noted that similar effects were also observed if the material had reached the end of its usable period - either due to being used to fabricate many layers or components, or purely if there was a long time since the batch was originally mixed. The aging effect is due to partial polymerisation of the material from both ambient light and from scattered light during the exposure process which causes solids to form in the liquid material. In either situation, once this was observed the batch was not recoverable. It was found that the ideal duration for stirring the material was between 10 and 15 minutes and that any time in excess of 15 minutes would show the effects of over-stirring.

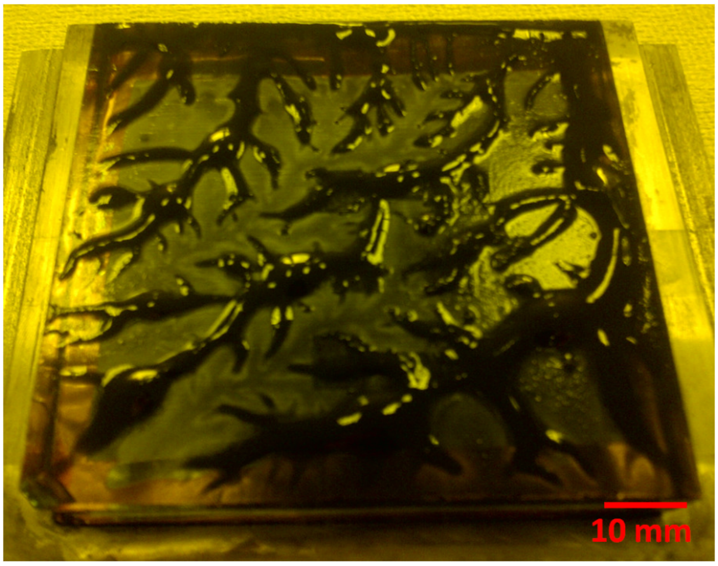

Figure 6.8 –Patterns observed on build platform after using over-stirred carbon composite material

6.4 Testing of the Material

6.4.1 Test Parts

In order to ascertain the relationship between the loading level of carbon black in the material and both the resistivity and mechanical properties of components fabricated using the HDDA based material, a set of test components were designed.

For mechanical testing of the material, a standard dog-bone shaped specimen was designed with dimensions that were suitable for use in the mechanical tensile testing system (Deben UK Ltd, UK). The parts had a total length of 20 mm with a clamping area width of 6 mm. The dimensions of the central test section were 6.5 mm by 2.5 mm (Figure 6.9(a)). The parts were 1 mm in thickness. For testing of the electrical properties of the material, a simple square shaped part was designed (Figure 6.9(b)). A square shape was chosen to enable easy measurement of the resistance both across the planes of the components layers and through the stack of layers (i.e. between the first and last layers fabricated.

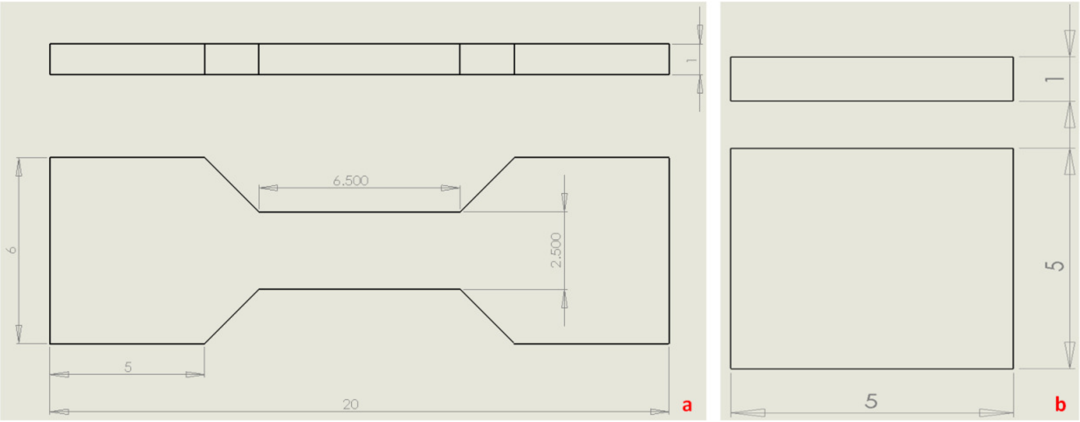

Figure 6.9 – CAD schematic of specimens for (a) tensile mechanical testing, (b) testing of electrical conductivity

Both the tensile test piece and the square piece were designed to be 1 mm in thickness. This thickness was chosen both because it was an appropriate dimension for the clamps of the tensile testing unit and so that contact could easily be made with the edges of the square parts for conductivity measurements. By designing the components to be the same thickness they could take advantage of the MSL process' ability to fabricate multiple components in one build and therefore also compare the mechanical and resistive properties of each build if required. Figure 6.10 shows the mask generated for the build job; note that as the components do not change structure through their height, all layer masks are identical.

Figure 6.10 – Dynamic mask for fabrication process for test pieces generated by slicer program

The components were fabricated using the single material custom MSL system discussed in Chapter 3. In total, materials with 6 loadings levels were produced with 1.25%, 2.5%, 3.75%, 5%, 7.5%, and 10 % by volume of carbon black. The build settings for these components are shown in Table 6.3.

% CB by volume	1.25	2.50	3.75	5.00	7.50	10.00
Component height (mm)	1	1	1	1	1	1
Layer thickness (µm)	25	25	25	25	25	25
Number of Layers	40	40	40	40	40	40
Exposure time (s)	30	45	60	90	90	90
Separation (mm)	1	1	1	1	2	2
Peel speed (mm/s)	0.20	0.20	0.20	0.10	0.05	0.05
Levelling speed (mm/s)	0.20	0.20	0.20	0.20	0.20	0.20
Wait time after level (s)	2	2	2	2	2	2
Wait time after peel (s)	1	1	1	1	1	1
Total build time	29 m	39 m	49 m	1 h 12 m	1 h 35 m	1 h 35 m

Table 6.3 – Fabrication settings and times for carbon composite materials with various filler ratios

6.4.2 Testing of Electrical Conductivity

As mentioned previously, thin, square specimens were fabricated in order to measure the resistivity both along the layer planes and perpendicularly through the layers. In order to achieve this, the resistance of each specimen was measured across both sides of the square and between the top to bottom faces. The dimensions of each specimen were also measured as there is often a small amount of deviation in x, y and z dimensions between the original CAD model and the final fabricated component. Using these measurement along with the resistance (R), the resistivity (ρ) of the component can then calculated along each dimension using Equation 6.1 (where A is the cross sectional areal and l is the length between the two electrodes).

$$\rho = R\,\frac{A}{l} \tag{6.1}$$

The resistance of the specimens was measured using a Solartron 7075 Digital Voltmeter (Schlumberger Measurement Control, UK) which is a precision 7.5 digit auto ranging meter. In order for the meter to measure the resistance of the specimens effectively, electrical contact needed to be made with the entire length of the sides of the specimens. Two methods were investigated to achieve this: using a conductive silver paint along the edges of the specimen, and using probes with a larger surface area.

The method involving coating the sides with silver paint was investigated first; however two issues were immediately apparent. Firstly, even after the silver paint had been applied, the cured carbon composite polymer was observed to have a brittle structure, and so when the voltmeter's point probe was used against the material's surface it was observed to disintegrate and crumble very easily. Once the material had begun to disintegrate the conductive path made by the silver paint failed and so there was no real advantage to the method. While with great care it was possible to obtain a measurement, the reliability of the approach was not considered good enough because it could not confidently guaranteed that the silver tracks were not being broken on the more brittle specimens with higher loadings. Additionally, if one edge was painted then the adjacent edge could not then be used for a further measurement as the path of least resistance was through the silver paint of the adjacent edge and was of significantly lower resistance than the polymer composite itself, as such, the readings from the second edge pair would be inaccurate.

To overcome this problem, a pair of probe pads with large flat surface areas were made to replace the voltmeter's existing point probes. It was felt that this approach would achieve better a contact area without the need for pre-treating the edges with conductive paint. Each pad probe was produced by adhering a length of copper tape around the short end of a standard glass slide. This produced a conductive pad with a large surface area that could used to easily make contact with the entire length of a specimen. A length of wire was soldered directly to the copper tape on each pad and connected to the voltmeter. Figure 6.11 shows the test pads then being used to measure the in plane resistance by pushing against opposing sides of the test specimens (a) and the through plane resistance by clamping the specimen top to bottom between the two plates (b). Clamps were used to secure the electrodes whilst measurements were being taken so that there was no movement of the part during measuring. To improve the accuracy of the measurement the meter's integration time setting was set to 10 seconds.

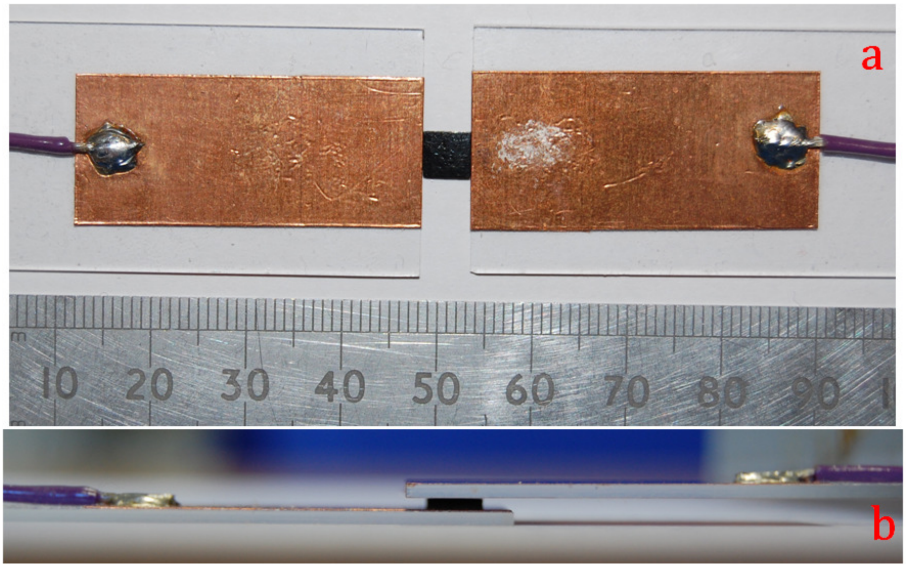

Figure 6.11 –Photographic image illustrating method of testing (a) in plane resistance, (b) through plane resistance of test specimens (scale in mm)

During testing, it was discovered that the contact between the top and bottom surfaces of the specimens and the test pads were not consistent due to surface imperfections on a number of the specimens. Figure 6.12 shows the polished surface appearance on a 10%vol loaded part with small indentations. The component was coated with 90 nm of gold so that its surface could be imaged using a WKYO NT2000 white light interferometer. A scan was conducted for a depth of 100 μm using the 2.5x objective lens over one of the pitted areas. Figure 6.13 is the resulting scan from the measurement that shows numerous imperfections and surface cracks that were typically between 5 μm and 10 μm although in some areas were up to 44 μm. As the layer thickness used to fabricate the parts were 25 μm, it would suggest that the failed areas are 2 layers deep. The width of the areas was around 50 µm in width with the larger cavity measuring 480 µm in diameter. A similar surface profile image of a 5% vol loaded specimen was taken (Figure 6.14), the objective lens was changed to 5x as the imperfections were far fewer and smaller than the 10% specimen. For the 5% specimens the largest imperfections were 30 to 50 µm in diameter with measured depths of 10µm while the average was around 2 µm. This suggests that these imperfections were minor failures in the layer rather that areas of total failure within the layers. It is felt that the most likely cause is from small aggregates of the carbon material being washed out during the post processing cleaning steps.

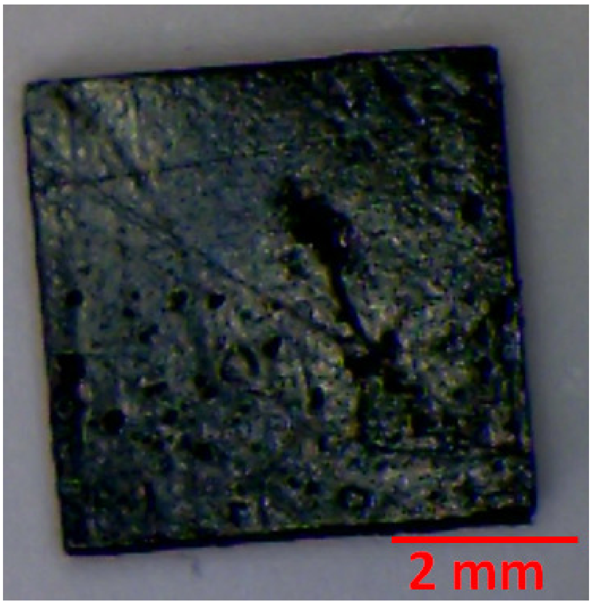

Figure 6.12 – Photographic image showing glassy surface with numerous small indentations on bottom surface (final fabrication layer) of 10% vol carbon black specimen loaded square

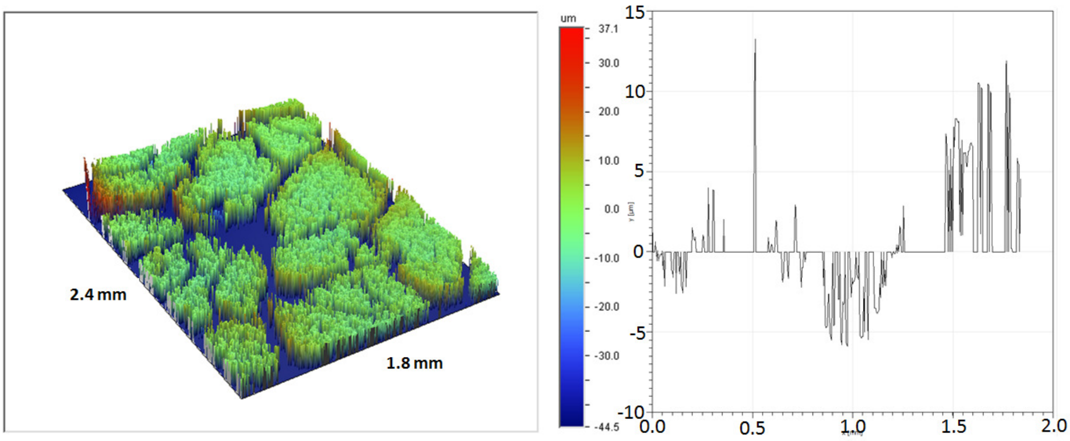

Figure 6.13 – Surface profile data from an interferometer scan of 10% vol loaded carbon black test specimen

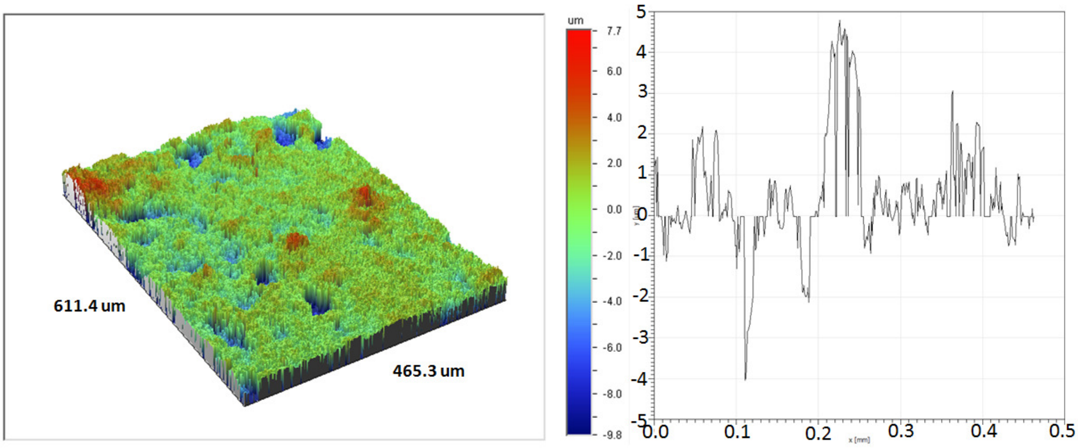

Figure 6.14 – Surface profile data from an interferometer scan of 5% vol loaded carbon black test specimen

As the observed imperfections were no more than the equivalent of 2 layer thicknesses on any of the samples, silver paint was applied to both top and bottom surfaces in order to improve the electrical contact between the faces and the test pads. This step was only done after measurements had been taken across the two side dimensions to prevent erroneous readings.

Along with measuring the resistance across each of the opposite faces, the physical dimensions of each specimen were also individually measured using a micrometer. The measurements then allow the resistivity (or conductivity) or each specimen to be calculated. In theory, if the specimen is isotropic, the resistivity should have been the same for each dimension, however there was found to be some variation.

The data presented in Figure 6.15 shows the conductivity of the specimens when measured across the long edges of parts (i.e. along the planes of the layers). There were no results obtained for the specimens with loadings of 1.25% by volume as there was no measureable resistance (Solartron multimeter measurement limit was 14 MΩ), this indicates that at this level of loading the fill ratio is below the previously mentioned critical level for conduction to occur. With loadings of 2.5% and above there was a clear correlation between the loading level and the measured resistivity of the material; indeed the variation in conductivity increases by several orders of magnitude over the range of loadings examined. The data does, however, also highlight that although there is certainly a correlation between loading and conductivity, there is a measurable amount of variation between samples of the same group. In some cases, the standard deviation exceeded 40% of the mean of the set. Potentially, this variation is caused by a number of factors including inconsistent contact area between the test pads and the specimen, incomplete initial mixing of the material, or partial material dropout during fabrication (an extreme case previously shown in Figure 6.6). However, on inspection of the specimens associated with the outlying data points, the surface structure of the affected specimens did not all appear to have irregular surfaces. Additionally, it is not felt that incomplete initial mixing was the main cause either as other specimens fabricated at the same time did not appear as outliers. Therefore, the main cause of conductivity variation between samples of the same loading is thought to be due to small quantities of filler particles falling out of suspension during fabrication - resulting in localised non homogenous areas. It is also felt that this effect could be increased by aging of the material causing areas of the resin to increase in viscosity as gel-like solids are formed.

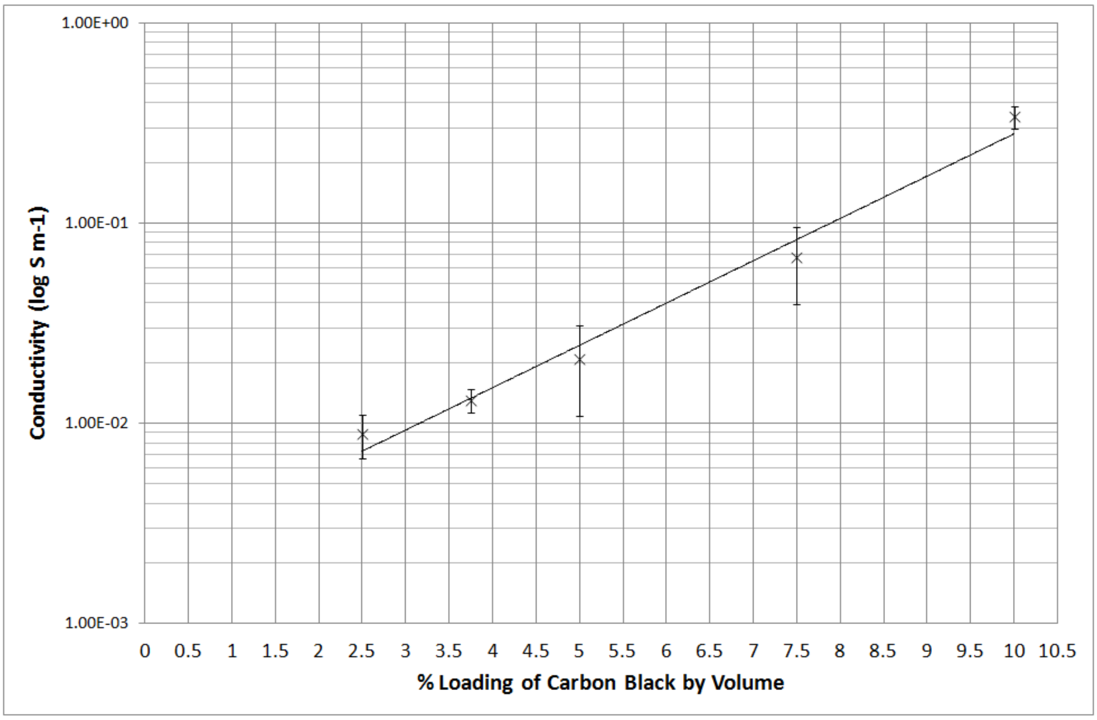

Figure 6.15 – Measured in plane conductivity of test specimens fabricated with a range of carbon black filler percentages

Figure 6.16 shows data from the same specimens but with the resistance measurement being taken between the top and bottom faces of the specimen. The results follow the same trend as the measurement taken across the sides of the specimens. However, on average, the conductivity was approximately 10 times less - with an overall range being between approximately 3.8 times and 28.0 times less than the in plane measurement of the same specimen. It was also observed that as the loading level increased, the difference in conductivity between side-to-side and top-to-bottom measurements increased exponentially.

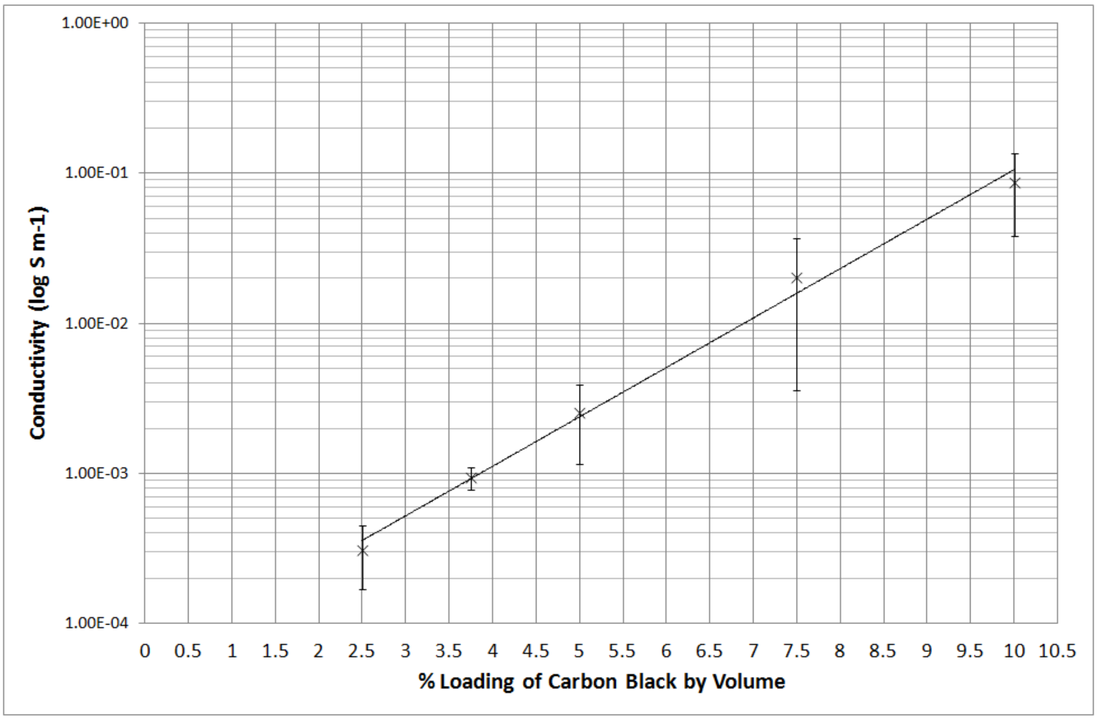

Figure 6.16 – Measured through plane conductivity of test specimens fabricated with a range of carbon black filler percentages

The reason for this variation is thought to be due to the layered structure of the component. It is believed that after the levelling step there is a gradient of particles present throughout the thickness of the layer where the filler particles have a tendency to settle near the bottom of the layer as illustrated in Figure 6.17. Figure 6.18 shows an extreme case with a 10% loaded material where the effect has also prevented full layer penetration of the exposure light, this causes poorer layer to layer conductivity. Therefore, when multiple layers are built on top of each other the difference in conductivity through the layers is seen to increase when compared to the conductivity across layers.

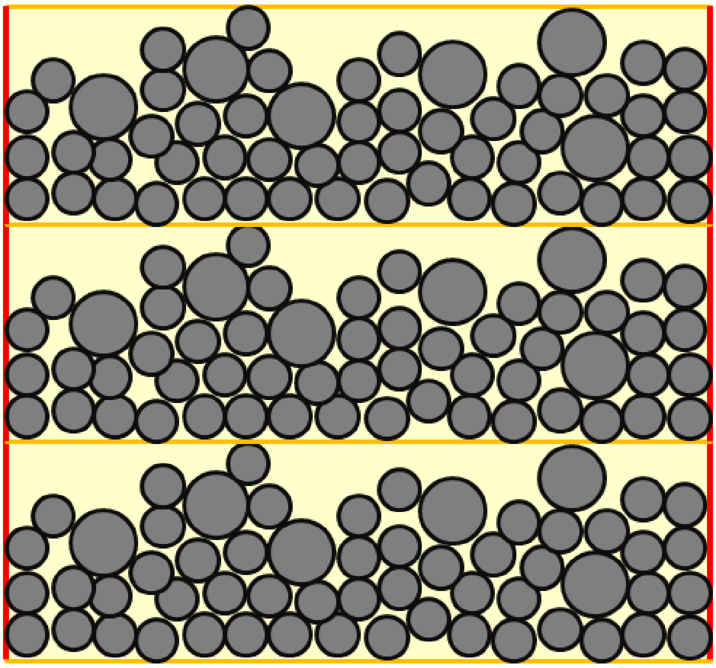

Figure 6.17 – Illustration of particle setting effect within layer structure

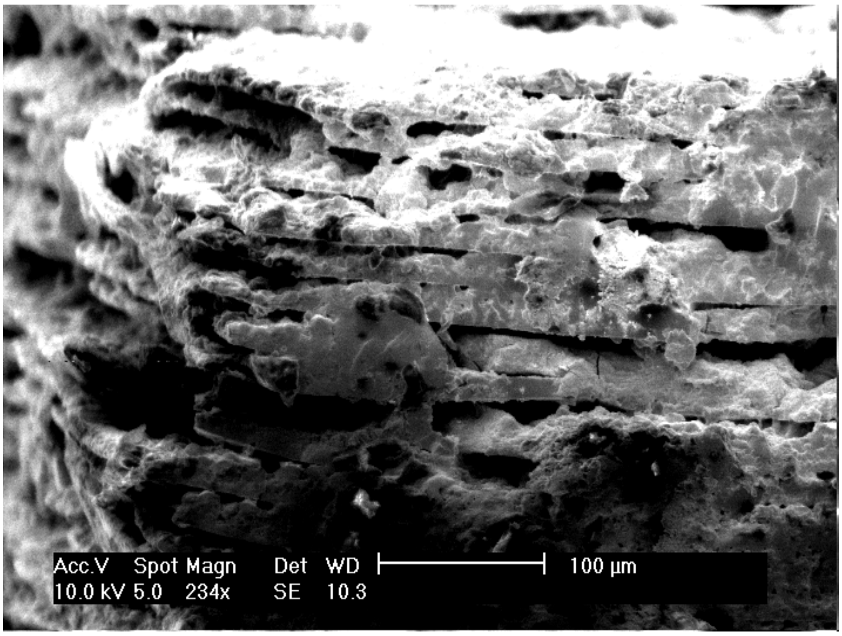

Figure 6.18 - SEM micrograph of a sample with a 10% CB loading showing the effects of particle settling

6.4.3 Mechanical Testing

As mentioned previously, in addition to the square test parts used for assessing the resistance of various resin mixtures, dog bone shapes were also fabricated during the same build process so that the mechanical properties of the material could also be assessed. A Deben 2KN Microtest unit was used to perform tensile testing of the specimens, to ascertain any correlation between loading percentage and the resulting ultimate tensile strength and Young's modulus of the materials. The tester was set to operate with an extension rate of 0.1 mm/min with a sampling rate of 10 samples per second.

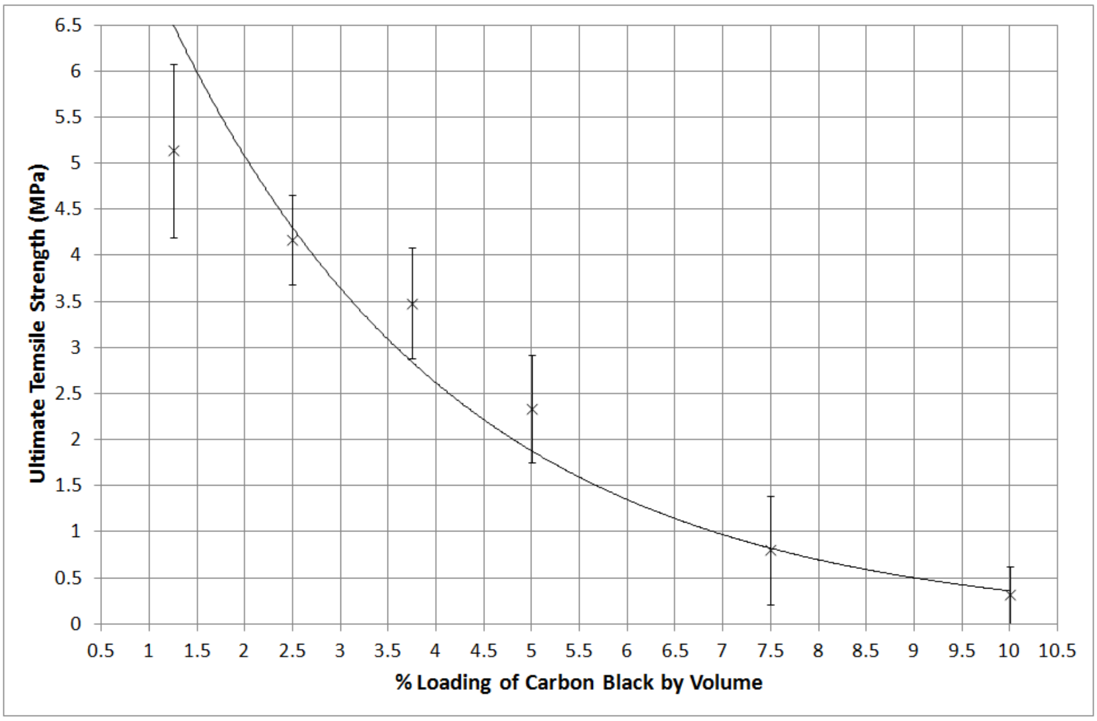

Figure 6.19 – Measured ultimate tensile strength of PEG based test specimens fabricated with a range of carbon black filler percentages

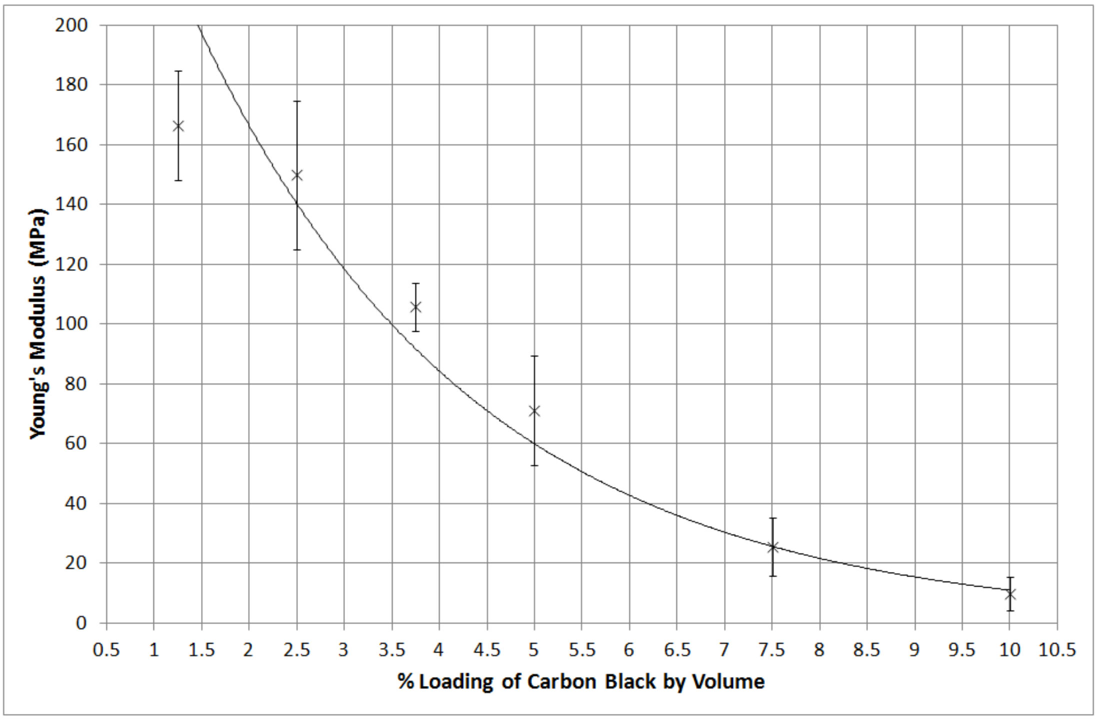

Figure 6.20 – Young's Modulus of PEG based test specimens fabricated with a range of carbon black filler percentages

Figure 6.19 and 6.20 show the results for the tensile strength and Young's modulus respectively. As expected, a clear correlation between loading level and mechanical properties was observed, although with some significant variation for some samples, which suggests there are inconsistencies in the mechanical properties between different batches of the same resin formulation.

Tensile results show that samples with less loading can withstand greater forces before failing. This is thought to be due to the carbon filler particles interfering with the cross-linking process of the photopolymerisation process and therefore introducing weaknesses within the structure of the layers. This also decreases the layer to layer adhesion with the higher loaded materials and as such will allow for minor movement between the individual layers of the structure. This is confirmed by the data recorded for the Young's modulus of the samples that shows that structures fabricated using high loading are also less stiff.

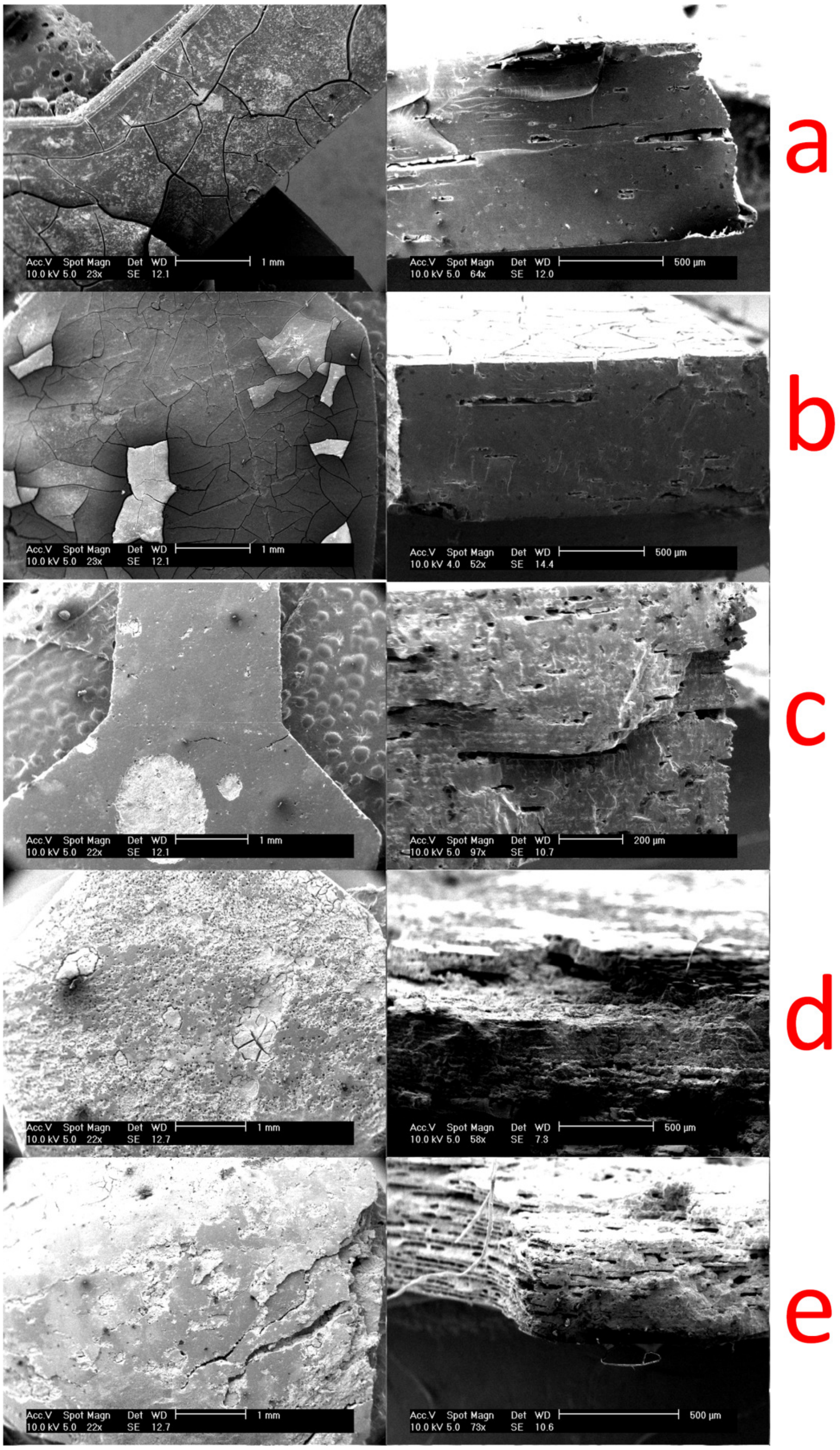

Figure 6.21 – SEM micrographs of tensile test pieces with loadings of (a) 1.25%, (b) 2.5%, (c) 5%, (d) 7.5% and (e) 10%

Figure 6.21 shows the difference in mechanical structure of samples with different loadings and shows the delamination effects caused by poor layer-to-layer adhesion in higher loaded specimens. The lower loaded materials showed poor surface integrity following tensile testing, although the cross-sections of the fracture plane shows little or no definition of individual layers. This indicates good layer-to-layer adhesion. The specimens with higher loading, however, performed worse in this respect. Loading levels of 5% were seen to be the point at which the first signs of delaminating occurred. The SEM micrographs of the higher loaded materials (7.5% and 10%) show that the delamination and poor inter layer bonding is partially due to incomplete layer curing, which is particularly noticeable along the edges of the layers. To investigate whether this problem could be overcome by longer exposure times a range of tests were conducted with a 7.5% material with extended exposure periods up to twice the period (180 seconds). The results showed that increasing the exposure period did not significantly improve the problem and instead introduced issues due to overcure. Figure 6.22 illustrates a case of severe delamination and failures within the layers due to internal stresses caused by over cure. Although not demonstrated here, such material failures could potentially be overcome by using an acrylate with a greater number of functional groups. However, this could also adversely affect the viscosity and mixing properties of the liquid resin.

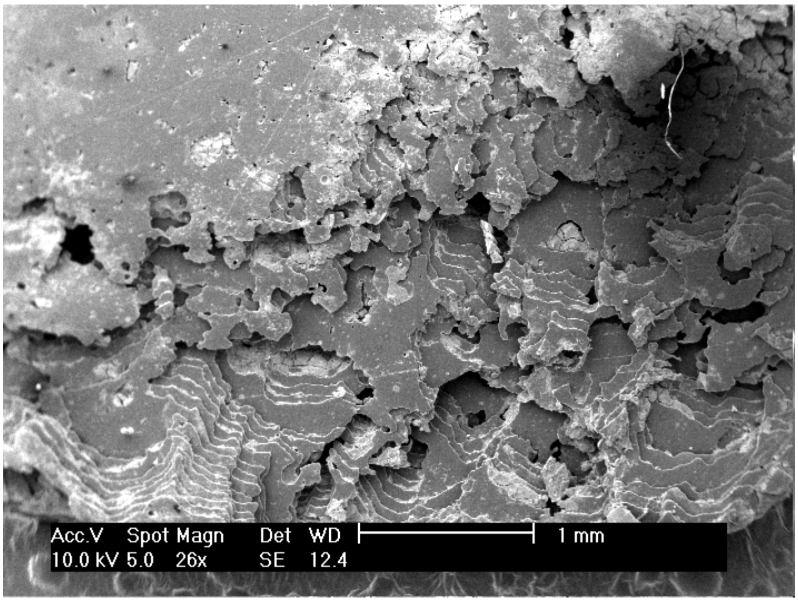

Figure 6.22 – SEM micrograph showing severe delamination caused by a combination of high loading (7.5%) and long exposure periods (180s)

6.5 Conclusion

In this chapter the development of a novel conductive composite photopolymers for manufacturing components using microstereolithography was reported.

A number of polymer formulations were initially explored along with a selection of filler materials including metals and a carbon black. While metal fillers were explored in an attempt to produce a highly conductive material capable of producing low resistance tracks, similar to those typically found on a printed circuit board, it was discovered that surface oxidation of metal particles due to their size prevented adequate conduction.

A conductive photopolymer composite was however successfully created by utilising carbon black as a filler material. By varying the percentage of carbon black in the material it was shown that the conductivity of the cured material could be altered within a range of 4.21×10^{-1} Sm^{-1} to 1.65×10^{-4} Sm^{-1} for loading levels of between 10% vol and 2.5% vol respectively. However, the relative standard deviation within the sets of the same loading was typically 39% and up to 82%, which has negative implications for the ability to achieve desired conductivities in precision applications. While a more viscous base polymer could be used to better hold the filler materials in suspension, this is likely to greatly increase the preparation time of the material due to the additional mixing time and may also increase the minimum layer thickness. An alternative solution may however be to use an additional component in the resin material to act as a dispersant.

Mechanical testing of the material also implied that increased loading levels have a negative impact on the structure of the fabricated components. The best compromise between achievable conductivity and structural ability of the material for “standalone” components (i.e. a component build solely using the conductive composite) occurs with carbon black filler loading of 5% vol. However, it is suggested that the mechanical limitations of the higher loaded materials could be overcome if the material was built as part of a larger structure consisting of less fragile materials.

It is suggested that with further investigation, more advanced semiconductor materials could be produced by blending other semiconductor materials such as zinc oxide and manganese dioxide [33] with the carbon black.

The next chapter describes the fabrication and characterisation of components suitable for gas and vapour application using MSL by altering the polymer component of the material discussed in this chapter.

6.6 References

[1] E. DeNava, M. Navarrete, A. Lopes, M. Alawneh, M. Contreras, D. Muse, S. Castillo, E. MacDonald, R. Wicker, Three-dimensional off-axis component placement and routing for electronics integration using solid freeform fabrication, Proceedings of Solid Freeform Fabrication Symposium, The University of Texas, Austin (2008) 362–369

[2] Adam Pron, Patrice Rannou, Processible conjugated polymers: from organic semiconductors to organic metals and superconductors, Progress in Polymer Science 27 (2002) 135–190

[3] S Yoshimura, M Murakami, H Yasujima, S Mizogami, New polyconjugated systems for intrinsically conductive polymers, Synthetic Metals 18 (1987) 473-478

[4] S. Tanaka, Y. Yamashita, A Novel Monomer Candidate for Intrinsically Conductive Organic Polymers Based on Nonclassical Thiophene, Synthetic Metals 84 (1997) 229–230

[5] R.D. McCullough, S. Tristram-Nagle, S.P. Williams, R.D. Lowe, M. Jayaraman, Self-Orienting Head-to-Tail Poly(3-alkylthiophenes): New Insights on Structure-Property Relationships in Conducting Polymers, Journal of The American Chemical Society 115 (1993) 4910-4911

[6] C. Pratt, Conducting Polymers, http://homepage.ntlworld.com/colin.pratt/cpoly.pdf (2006), last accessed: 03/03/2012

[7] J.F. Feller, Y. Grohens, Evolution of electrical properties of some conductive polymer composite textiles with organic solvent vapours diffusion, Sensors and Actuators B: Chemical 97 (2004) 231–242

[8] M.H. Al-Saleh, U. Sundararaj, A review of vapor grown carbon nanofiber/polymer conductive composites, Carbon 47 (2009) 2–22

[9] A. Tsirimpis, I. Kartsonakis, I. Danilidis, P. Liatsi, G. Kordas, Synthesis of conductive polymeric composite coatings for corrosion protection applications, Progress in Organic Coatings 67 (2010) 389–397

[10] M.E. Galvin, G.E Wnek, Electrically conductive polymer composites: polymerization of acetylene in polyethylene, Polymer 23 (1982) 795–797

[11] A. Das, H.T. Hayvaci, M.K. Tiwari, I.S. Bayer, D. Erricolo, C.M. Megaridis, Superhydrophobic and conductive carbon nanofiber/PTFE composite coatings for EMI shielding, Journal of Colloid and Interface Science 353 (2011) 311–315

[12] Y.S. Kim, Influence of carbon black content and film thickness on vapour detection properties of polyvinylpyrrolidone composite sensors, Current Applied Physics 10 (2010) 10–15

[13] Y.S. Kim, S-C. Ha, Y. Yang, Y.J. Kim, S.M. Cho, H. Yang, Y.T. Kim, Portable electronic nose system based on the carbon black–polymer composite sensor array, Sensors and Actuators B 108 (2005) 285–291

[14] J. Lu, B. Kumar, M. Castro, J-F. Feller, Vapour sensing with conductive polymer nanocomposites (CPC): Polycarbonate-carbon nanotubes transducers with hierarchical structure processed by spray layer by layer, Sensors and Actuators B 140 (2009) 451–460

[15] M.C. Lonergan, E.J. Severin, B.J. Doleman, S.A. Beaber, R.H. Grubbs, N.S. Lewis, Array-Based Vapor Sensing Using Chemically Sensitive, Carbon Black-Polymer Resistors, Chemistry of Materials 8 (1996) 2298-2312

[16] S. Kirkpatrick, Percolation and Conduction, Reviews of Moder Physics 45 (1973) 574-588

[17] Y.P. Mamunya, V.V. Davydenko, P. Pissis, E.V. Lebedev, Electrical and thermal conductivity of polymers filled with metal powders, European Polymer Journal 38 (2002) 1887–1897

[18] R.K. McGeary, Mechanical Packing of Spherical Particles, Journal of the American Ceramic Society 44 (1961) 513-522

[19] R.A. Mrozek, P.J. Cole, L.A. Mondy, R.R. Rao, L.F. Bieg, J.L. Lenhart, Highly conductive, melt processable polymer composites based on nickel and low melting eutectic metal, Polymer 51 (2010) 2954-2958

[20] L. Li, D.D.L. Chung, Electrical and mechanical properties of electrically conductive polyethersulfone composites, Composites 25 (1994) 215–224

[21] G-Y. Huang, S-Mg. Xu, G. Xua, L-Y. Li, L-F. Zhang, Preparation of fine nickel powders via reduction of nickel hydrazine complex precursors, Transactions of Nonferrous Metals Society of China 19 (2009) 389–393

[22] A.-H. Lu, E.L. Salabas, F. Schuth, Magnetic Nanoparticles: Synthesis, Protection, Functionalization, and Application, Angewandte Chemie 46 (2007) 1222-1244

[23] J. Lee, I.H. Lee, D-W Cho, Development of micro-stereolithography technology using metal powder, Microelectronic Engineering 83 (2006) 1253–1256

[24] R. Andrews, D. Jacques, M. Minot, T. Rantell, Fabrication of Carbon Multiwall Nanotube/Polymer Composites by Shear Mixing, Macromolecular Materials and Engineering 287 (2002) 395–403

[25] J. C.Huang, Carbon black filled conducting polymers and polymer blends, Advances in Polymer Technology 21 (2002) 299–313

[26] C. del Rjo, M.C. Ojeda, J.L. Acosta, Carbon black effect on the microstructure of incompatible polymer blends, European Polymer Journal 36 (2000) 1687-1695

[27] M. Wu, L.L. Shaw, A novel concept of carbon-filled polymer blends for applications in PEM fuel cell bipolar plates, International Journal of Hydrogen Energy 30 (2005) 373 – 380

[28] B.C. Sisk, N.S. Lewis, Comparison of analytical methods and calibration methods for correction of detector response drift in arrays of carbon black-polymer composite vapour detectors, Sensors and Actuators B: Chemical 105 (2005) 249-268

[29] S. Maldonado, E. García-Berríos, M.D. Woodka, B.S. Brunschwig, N.S. Lewis,Detection of organic vapors and NH_3(g) using thin-film carbon black–metallophthalocyanine composite chemiresistors, Sensors and Actuators B: Chemical 134 (2008) 521–531

[30] B.C. Sisk, N.S. Lewis, Estimation of chemical and physical characteristics of analyte vapors through analysis of the response data of arrays of polymer-carbon black composite vapor detectors, Sensors and Actuators B: Chemical 96 (2003) 268–282

[31] C. Cochrane, M. Lewandowski, V. Koncar, A Flexible Strain Sensor Based on a Conductive Polymer Composite for in situ Measurement of Parachute Canopy Deformation, Sensors 10 (2010) 8291-8303

[32] L. Wang, T. Ding, P. Wang, Thin Flexible Pressure Sensor Array Based on Carbon Black/Silicone Rubber Nanocomposite, IEEE Sensor Journal 9 (2002) 1130-1135

[33] E. Preisler, Semiconductor properties of manganese dioxide, Journal of Applied Electrochemistry 6 (1976) 311-320

Chapter 7

7 MSL for the Direct Fabrication of Vapour Sensors

In the previous chapter, the development of a novel photopolymer resin was investigated for the purpose of fabricating conductive 3D microstructures using microstereolithography. The purpose of this chapter is to build upon that work by using a modified version of the material to investigate the direct fabrication of vapour sensing device using microstereolithography.

The first section covers the background of sensing techniques, followed by sections covering the modification of the resin material along with fabrication of chemical sensors using this material. The final section then covers performance testing and characterisation of the fabricated sensors.

7.1 Introduction

There is wide interest in gas and vapour sensing technologies covering a wide variety of applications including, environmental monitoring [1, 2], process control, military [3], food safety [4-6], disease detection [7, 8], perfume classification [5] and even for mimicking the mammalian olfactory system [9]. There are a number of techniques to identify and detect of gases and vapours. These can be broadly divided into two categories; analytical techniques or discrete chemical sensors as described in the following sections.

7.1.1 Analytical Based Detection

Analytical methods are ones such as mass spectrometry (MS) whereby the sample gas or vapour is ionised and broken down into smaller fragments in order to be detected. Components are then identified depending on their charge-mass ratio using one of a number of detectors such a sector instrument, time of flight analyser, or quadrupole mass filter. Ionisation is achieved either by bombarding the sample with electrons or by chemical ionisation (also known as soft ionisation) using a reagent gas such as methane or ammonia. As such methods only work well with pure samples (as mixes of complex vapours could break down into similar sized fragments). A gas chromatography (GC) stage [10-12] is often used between the sample and before the MS detector as an orthogonal separation method. A GC column separates out a complex mix of chemical components by their interaction with a thin retentive layer, whereby each molecule is delayed by a different amount. Thus as the end of the column the complex mixture of chemical components leaves as a series of single chemical pulses [13, 14].

7.1.2 Sensor Based Detection

Compared to traditional analytical techniques, sensor based detectors are far more compact and affordable - a GC/MS setup can typically cost in excess of £30000, whereas a gas sensors are less £200. They are transducer devices that convert the chemical interaction of the analyte gas or vapour with a second material, which is part of the sensor, into an electrical signal of some type (be it, for example, conductance, reactance, capacitance, frequency). In general they do not offer the same quantitative resolution or ability to identify a great number of compounds as analytical techniques. However, they can be used to detect the presence of particular groups of gases and vapours to a limited quantitative accuracy, in some cases providing better concentration information than would be achievable with analytical methods. Since such devices tend to focus on the detection of just one or a small group of similar compounds (which is all that is needed in some applications), where more complex mixes of vapours are present, a selection of different sensors are used. Typically these are air quality applications where monitoring for the presence of toxic gasses (such as CO, CO_2, Cl_2, H_2S, SO_2, NO_2, NO, etc), flammables (such as hydrogen, propane, butane, nonane, acetylene, etc), or levels of O_2, CO_2 or other vapours is necessary.

There are numerous electronic chemical detection methods as shown in Table 7.1. The most commonly used sensing materials are metal oxides (MOX) which often preferred due to their fast response and recovery times [15, 16]. Commonly used metal oxide materials include WO_3 [17], SnO_2 [18], ZnO [19], TiO_2 [20], $BaTiO_3$ [21], or blends of two or more [22]. However, metal oxide sensors need to be heated to between 200°C to 500°C in order to operate [17, 23, 24] (although will only be sensitive to a target gas over a small temperature range). Due to the heating requirements of the devices, they tend to have much higher power requirements (generally a few hundred mW [25]) than other technologies such electrochemical sensors or chemoresistive devices; this makes them impractical for use in portable applications.

Type	Method	Advantages	Disadvantages	References
Acoustic Wave Devices	Mechanical	-high sensitivity -fast response time	-complex support circuitry -poor reproducibility	[26-29]
Metal Oxide	Conductometric	-cheap -fast response and recovery time	-high power consumption	[17, 23, 24]
Conducting Polymer	Conductometric	-good response time -cheap -low power	-poor reproducibility -baseline drift -humidity sensitive	[30, 31]

Carbon Black Composite	Conductometric	-cheap -low power -diverse range	-baseline drift -humidity sensitive	[32-37]
Fibre Optic	Optical	-fast response -repeatable	-expensive	[38-40]
Pellistor	Thermal	-low cost	-slow response -high power	[41-43]

Table 7.1 – Types of gas/vapour sensor technology

Arguably the simplest method of detection is with the use of a chemical resistor (also often referred to as a Chemiresistor or Chemoresistor) which have the advantage of operating at room temperature. Common types of chemoresistors use conducting polymers and composite polymer materials. Typically, such devices are produced using screen printing silicon processes onto a ceramic substrate, although silicon, glass and polymer [44] are also used. In its simplest form, the sensor involves bridging a gap of between 10 µm and 10 mm between two metal electrodes with a conductive gas sensitive material (sometime referred to as the "active material") as illustrated in Figure 7.1. The resistance of the conductive material then varies as it is exposed to different analytes (i.e. the film behaves as a semiconductor).

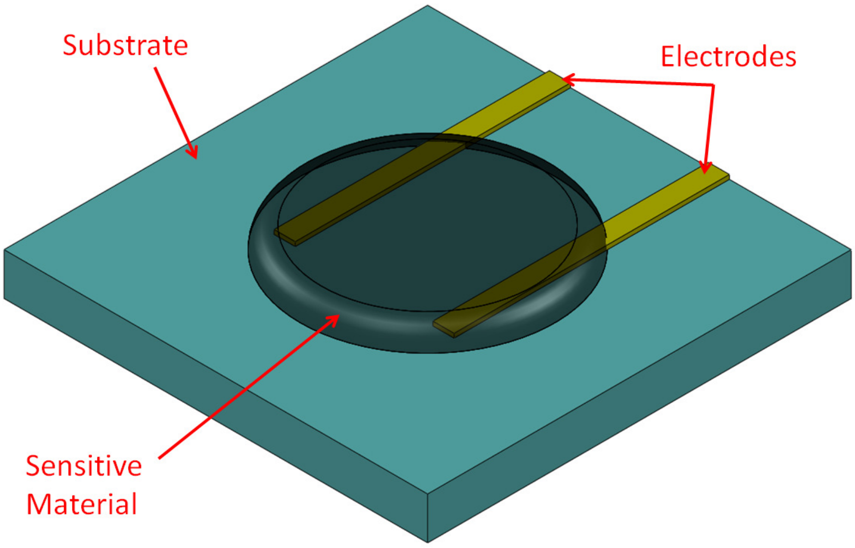

Figure 7.1 – Diagram of a chemoresistive gas sensor (for illustration only – not to scale)

7.2 Conductive Polymer Sensors

As discussed in the previous chapter, two types of conductive polymer exist, intrinsically conducting polymers (IPCs) and composite conducting polymers. Such materials have a number of advantages over the use of metal oxides, the main one being that they can operate at room temperature and therefore have lower power requirements. Additionally, they have a greater sensitivity to volatile organic compounds (VOCs) and generally are able to detect lower concentrations than metal oxide devices (down to 10 ppm), however are less responsive to oxidising and reducing gases such as CO or NO_2.

Intrinsically conductive polymers are those such as polypyrroles [45], thiophenes, indoles [46] or furans. Their detection mechanism is due to chemical interaction between the analyte gas or vapour with the charge carrying elements in the backbone of the polymer material (explained in the previous chapter). The interaction affects the movement of electrons through the material, and therefore, its conductivity. As mentioned previously, ICPs are also often unstable and are easily destroyed by irreversible reactions with analytes. Due to the difficulties of fabricating the devices, their susceptibility to drift, their increased response to changes in humidity, and their degradation by background UV irradiation, they are not often used either commercially or for research.

With a composite material, the polymer parts acts as one would traditionally expect i.e. as an insulator. It is then the filler material that provides the conductive path. The change in conductivity of the material, when in the presence of a vapour, is achieved through a swelling effect [47] of the polymer. The swelling occurs due to chemical interactions between the vapour and the material and therefore, by using different polymers, the sensor can be tailored to respond to different vapours. The mechanism is described by Ruschau et al [48] and notes that when the polymer swells, it causes some of the conductive paths in the material to break as the conductive particles are no longer in contact with each other. This results in the resistance increasing when it is exposed to an appropriate vapour. This is a reversible process, so when the material relaxes back, the conductivity returns to its previous value.

An ideal response would be an instantaneous increase in resistance to a ΔR value linearly dependent on the concentration of the analyte of interest and with little or no cross sensitivity to other vapours that were not of interest. Additionally, it would recover rapidly back to its initial value when the sample analyte is purged from the test chamber. Vapours are therefore analysed depending on the magnitude of the response of the sensors over a set time period or by the amount of time taken to reach an observed level - either the maximum or t_{90} (the time take to reach 90% of the maximum). It is typically the magnitude of the response that is used to calculate concentration. Figure 7.2 illustrates the typical response profile of a chemoresistive sensor such a carbon black composite. It shows that both the response and recovery times of the devices are gradual and is normally described by a two component exponential. The test cycle begins by ascertaining the baseline (R_0) of the sensor. This is achieved by exposing the device to a reference or carrier gas which can either be air (which doesn't include any concentration of the sample gas), argon or nitrogen. Next, the device is exposed to the sample air, which is a mix of the carrier gas with the sample vapour for a set duration. This causes the sensing material to swell and so increase the resistance of the device. An equilibrium is reach where the vapour that has permeated into the polymer is balanced to that in the sample air at which point the polymer ceases to swell further. Depending on the sensitivity/geometry of the device and the concentration of the sample gas it can take a significant amount of time to reach this level, hence it is common to expose for a set period. Once the exposure period has elapsed, the sensor chamber is then purged again with the carrier air until the initial baseline resistance level is reached. Due to the device true recovery time often being significantly longer than the exposure period [48], in practice, it is sometimes more practical to wait only until the reading drops to within a few percent of the original baseline value before proceeding with the next sample.

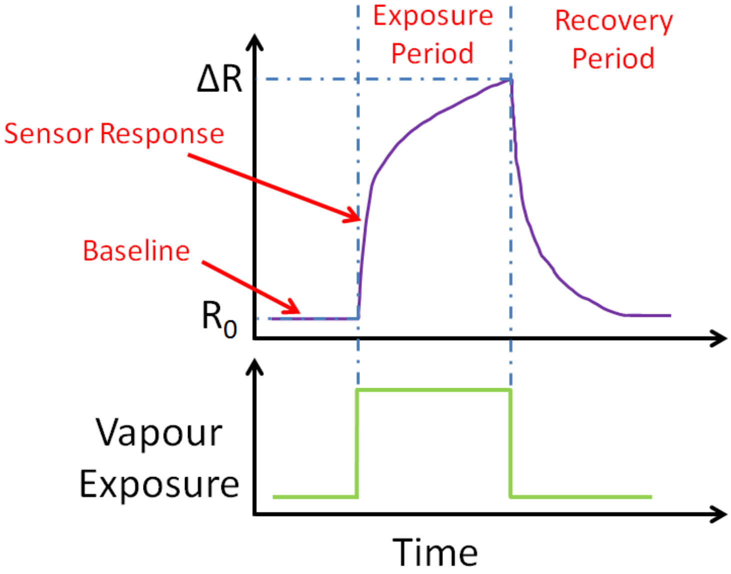

Figure 7.2 – Simplified timing diagram illustrating the typical response profile of a chemoresistive sensor

There are a wide variety of polymer materials that can be used for vapour sensing applications, some of the more common include PCL (poly caprolactone), PMMA (poly methyl methacrylate), PVP (poly vinyl pyrrolidone), PEG (poly ethylene glycol), PVA (poly vinyl acetate). Similarly, there are a number of additive materials which are typically used for the conductive filler particles, the most common of which are carbon black [48-51] and gold nanoparticles [52], although carbon nanotubes [53] have also been used along with a similar copper based composites which have been used for strain sensor applications [54]. To form the composite material, the polymer is generally first dissolved in a solvent such as ethanol, toluene, or dichloromethane, then, once dissolved the conductive particles are then added to the solution. The material can then deposited onto the substrate using one of a number of methods including spin coating, vapour growing [53, 55], plasma deposition [54], spin casting [56], electrospraying [33], dip coating [57], syringe depositing [58] or spray coating [59] . The most common method is to deposit the material by spray coating as it is a good method of producing thin films of material. Deposition masks are usually required for selective placement of the material, however, it is felt that by utilising the selective curing properties of MSL, multiple devices could just as easily be accurately fabricated in one step with virtually any specified geometry without the requirement to first fabricate a physical mask.

The resistivity of carbon black composites can be broadly predicted using percolation theory [51, 60], which has a number of advantages. Firstly, it allows the materials conductivity to be controlled by varying ratio of filler to polymer. Secondly, using filler ratios that are near the percolation threshold increases the sensitivity for low vapour concentrations as the change in conductivity will be a larger percentage of the initial conductivity. However, this method is rarely used as the responses are generally highly non-linear and often unrepeatable due to the sensing material not fully recovering.

Depending on the deposition method used for the fabrication of the devices, there can often be some variation of the initial resistance (baseline, R_0) of the sensor. Additionally, the baseline of the devices can drift with age, exposure to analytes or temperature. It is therefore normal to express the response of such sensors by their differential (R/R_0) or fractional $(\Delta R/R_0)$ resistance response. Doleman et al [49] note that a typical response is between 1% and 5% depending on the vapour, the concentration of the vapour, and the polymer used. The paper also notes that polymers can be mixed or "blended" in order to increase the devices selectivity. It was also shown that by altering the ratio of filler (in this case, carbon black) when used in sensor arrays, increased diversity was achieved. More complex vapour and odour detection systems use arrays of sensing devices, which utilise a selection of different polymers and blends with different selectivities in order to create a fingerprint of the vapour [61]. This identification technique is utilised in devices such as the Cyranose 320 (Smiths Detection, UK) which incorporates an array of 32 carbon black polymer composite devices.

Further research by Doleman et al [62] confirmed that the response times for carbon black based composite conductive polymers can vary between 20 seconds and 200 seconds and is heavily dependent on the thickness of the deposited layer of active material. Later research conducted at here at the University of Warwick by Iwaki et al [63] describe using a using carbon black / PVP composite devices in conjunction with a novel signal processing technique which records response times of 50 ms, 1 s and 30 s for water, methanol and ethanol vapours respectively.

7.3 Modification of the Conductive Composite Material

The previous chapter covered the development of a composite photopolymer that consisted of 4 components: a monomer, a crosslinker, photoinitiator, and a conductive filler material. It was thought that by replacing the monomer (HDDA) with a different monomer that experiences swelling when exposed to vapours, the material can then respond to exposure to vapours in the same way a traditional spray/vapour deposited sensing material would. The initial motivation was to investigate the rapid manufacture of gas sensing devices, however it also allows for the active materials to be deposited in any 3D structure therefore opening up the possibility to investigate the effect of geometry on the sensitivity and selectivity of the devices. A paper by Andreadis et al [31] described a similar photocurable composite polymer using carbon black, however their methods used polymers which required multiple processing steps (spin coating, pre-baking, exposure, post-baking, then finally developing) and created only 2D structures. Additionally, the devices showed relatively poor selectivity.

Polyethylene glycol (PEG) was chosen as the replacement monomer as it is known to work in such applications using other polymerisation processes [50, 61, 64, 65]. It had previously been used with the custom MSL system for other non-composite materials, so was known to work. The new material therefore consisted of PEG (polyethyleneglycol), DPPHA (dipentaerythritol penta-/hexa-acrylate), Irgacure 784, and carbon black nanopowder (crushed pearls, Cabot USA) as the conductive filler. Based on the results with the previous conductive composite in the previous chapter, it was decided that a filler level of 5% by volume would be used as it was felt that this would produce baseline resistances in a desirable region (~50 KΩ) for the dimensions used for the device (discussed later). It was determined that the optimal component ratio for fabrication of the devices was a 4:1 mix of PEG to DPPHA (crosslinker).

7.4 Device Design and Fabrication

7.4.1 Design

The initial design of the sensors was as a flat square with similar dimensions as the test specimens in the previous chapter (Figure 7.3(a) & (c)). As conducting polymer gas sensors operate on the principal of the analyte gas interacting with the polymer itself (which then causes it to swell), an additional design was produced in order to verify whether modifying the geometry of the sensor could be used as a method to improve sensitivity over the simple solid, square design.

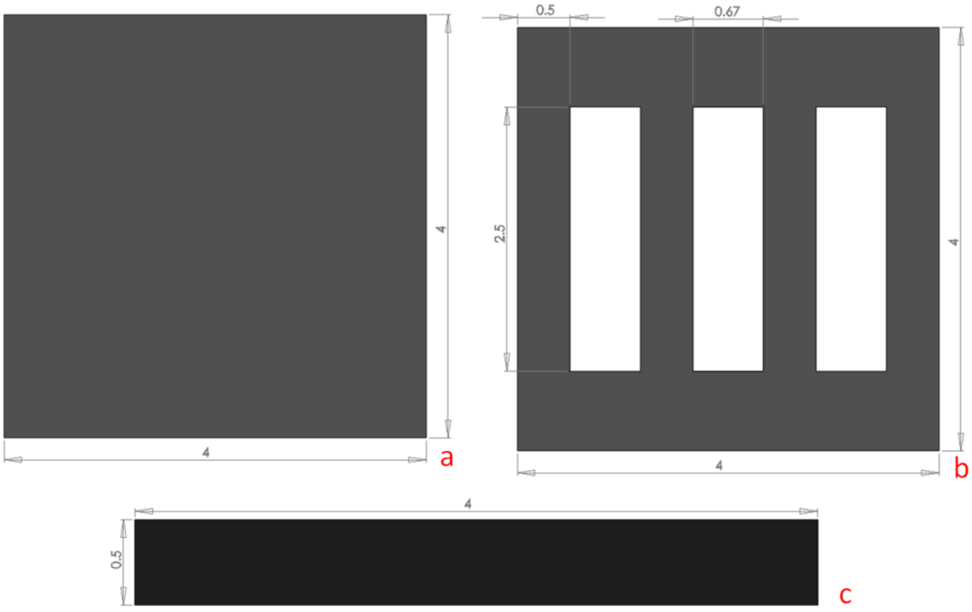

Figure 7.3 – Schematic diagrams of version 1 vapour sensing devices in (a) standard and (b) slotted sensor geometries along with (c) side profile (dimensions in mm)

The modified design had the same outer dimensions as the flat squares but included a set of three slots. The slots each had a length of 2.5 mm and width of 0.67 mm and were equally spaced across the device at 0.5 mm (Figure 7.3(b)). The motivation for this was that it was thought that it would allow increased permeation of the vapour into the structure of the device, therefore reducing the response time (or increasing the sensitivity if the exposure time doesn’t allow for the device to saturate).

7.4.2 Fabrication

The devices were fabricated using the custom MSL system described in chapter 3 using the build parameters shown in Table 7.2. Post processing of the devices consisted of rinsing them with propan-2-ol while they were still adhered to the build platform to remove the excess material on from the surface. Then they were removed using a flat bladed craft knife. This was then followed by further cleaning in a 5ml beaker half filled with propan-2-

ol, which was then placed into an ultrasonic water bath for 30 minutes. This was found to be necessary to remove any excess carbon particles from the edges of the devices and from in between the slots on the modified devices that didn't get removed during the initial wash. It was observed that if the devices were submerged in solvent without ultrasonic cleaning the connections to the devices failed soon after the connecting tracks had been painted (see below). Finally, the devices were post cured using an Otoflash G171 (NK-Optik GmbH, Germany) set to 500 flashes cycles (at a rate of 10 flashes per second) on each side.

Material	4:1 PEG w/ 5% CB
Component Height (mm)	0.5
Layer thickness (μm)	25
Number of Layers	20
Exposure time (s)	90
Separation (mm)	1
Peel speed (mm/s)	0.1
Levelling speed (mm/s)	0.2
Wait time after level (s)	2
Wait time after peel (s)	1
Total build time	36 minutes

Table 7.2 – Fabrication parameters for vapour sensor devices

7.4.3 Mounting

In order to electrically interface with the devices for testing, they were individually adhered onto stubs (Figure 7.4(a)) using superglue. The stubs had been designed previously with a 4 pin connector in order to interface to the connectors within the test chamber (Figure 7.4(b)) for the vapour test rig. The test rig and chamber had been designed previously for testing conductive polymer devices which required 2 connections for the sensing element with an additional 2 connections for an optional heating element. Usually, the silicon based devices are adhered to the stubs and then a wire bonder is used to make connections between the pad on the device to the pads on the stubs.

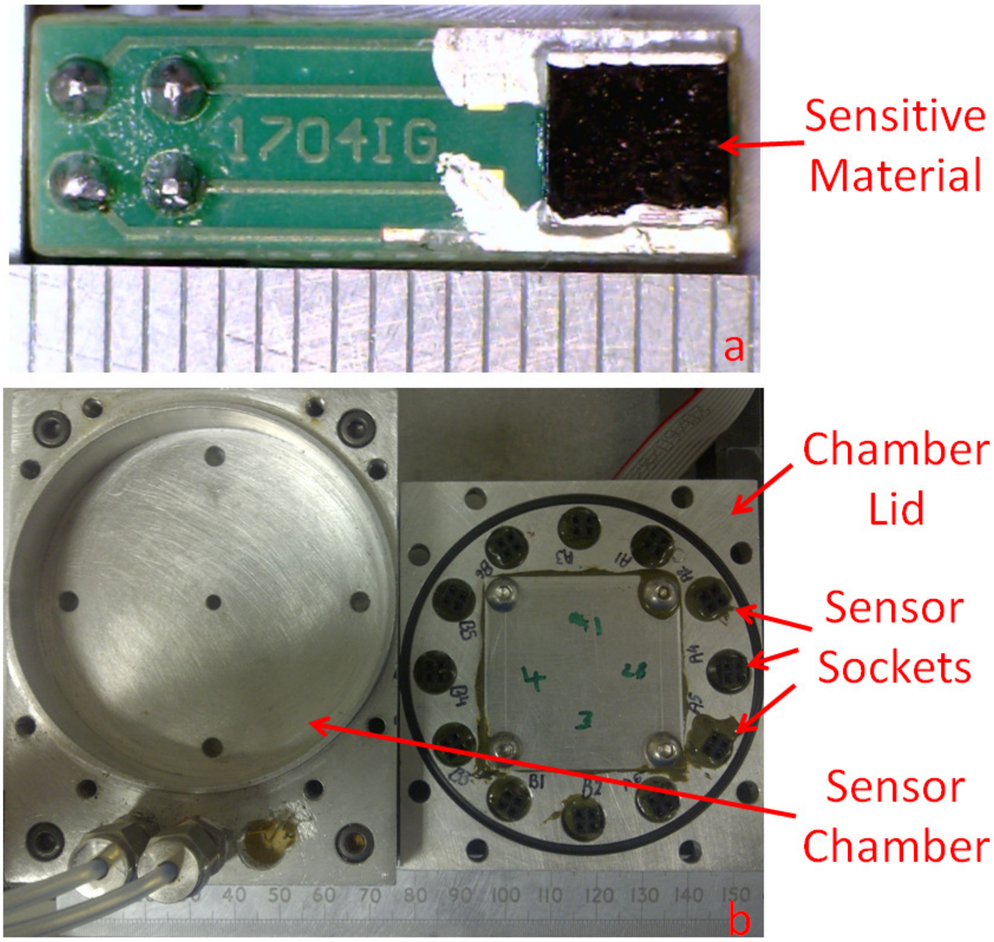

Figure 7.4 – Photographic images of (a) MSL fabricated vapour sensing devices on test stubs, (b) vapour test chamber

For the polymer composite sensors electrical connections were made by using silver conductive paint (Electrolube, UK) to paint a track from the pad on the stub to the edge of the device. The whole of the connecting edge of the device was also painted to ensure that the entire width of the devices sensing area was being used effectively. Care was also taken to avoid painting the remaining two sides as it would reduce the active area of the device. The painting procedure proved to be much simpler and quicker than wire bonding and did not require the assistance of an experienced technician, unlike wire bonding. However, care had to be taken to ensure that the painted track did not short with the two remaining pads on the stubs that were usually used for powering the heaters of previous polymer devices. As the polymer composite devices were designed to operate at room temperature, the connections for the heater were not required and so the tracks on the stubs were shortened using a scalpel to help ensure there were no short circuits to the other pads.

While the mounting orientation of the square pieces didn't matter as the side lengths were equal, the modified devices with slots were mounted such that the 4 bars were effectively created with 4 parallel sensing areas. This was to ensure that the maximum sensing area was being utilised. It was felt that by mounting the device with 90 degree rotation, the centre two bars would be negated.

The finished devices were then put in desiccator for 24 hours to ensure all the solvent from both the adhesive and conductive paint was removed as it would felt that this could otherwise have adversely affect any results from gas testing.

7.4.4 Design Improvement

Unfortunately, after assembling a number of devices onto the stubs, it was noticed that the measured resistance of the devices varied considerably before and after they were mounted. After further investigation it was apparent that both the processes of adhering the devices to the stubs and using the conductive paint to make electrical connection adversely affected the devices.

The first issue was that the adhesive was seeping into the micro-pores of the devices, created by small areas of aggregated carbon. It was believed that this reduced the sensitivity of the devices as it prevented swelling of the material. This was then proven by testing the response of 3 slotted devices to a toluene vapour both before and after adhesion to a sample stub. Before testing, it was also noticed that the baseline resistance of the devices was higher after being adhered to the stubs. In order to test the devices in this way, a composite epoxy with silver particles was used to adhere test wires to the sizes of the devices, extreme care had to be taken to apply as little force as possible to the wires to prevent damage to the devices or removal of the test leads. Table 7.3 shows results from these tests which demonstrate not only that the ΔR/R values were significantly increased after direct adhesion to the stubs, but also that the baseline resistance increased.

	Device 1	**Device 2**	**Device 3**
Baseline Resistance Before Adhesion (K ohm)	32.5	38.7	45.1
Baseline Resistance After Adhesion (K ohm)	54.1	53.6	74.4
ΔR/R Before Adhesion	0.18	0.18	0.21
ΔR/R After Adhesion	0.07	0.09	0.7

Table 7.3 – Characteristic of 3 MSL fabricated version 1 vapour sensing devices before and after adhesion to sample stubs

Additionally, it was also discovered that in a number of cases, the conductive silver paint had seeped into small gaps between the device and the stubs. This in turn reduced the devices resistance and further decreased the sensitivity as the change in resistance of the device was negligible when compared to the parallel resistance of the partial short beneath the device. In order to overcome these two problems, the design of the devices was modified to include an insulating base layer. The base layer was designed to be 0.5 mm thick and extend beyond the edges of the device by 0.5 mm on each side (Figure 7.5).

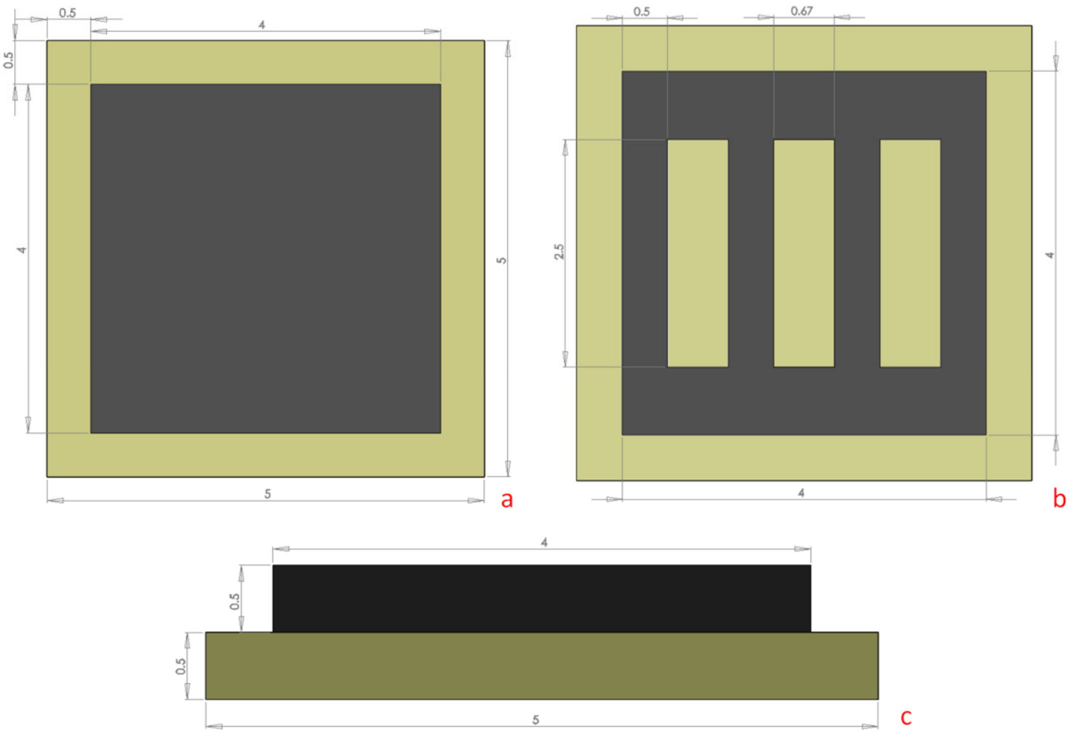

Figure 7.5 - Schematic diagrams of version 2 vapour sensing devices in (a) standard and (b) slotted sensor geometries along with (c) side profile (dimensions in mm)

The new devices were produced using a multi-material MSL fabrication process whereby the base and device areas were built in one fabrication process but with two different materials. To ensure that there was good adhesion between the base and the conductive composite, and to prevent the two part splitting at a later date due to the swelling process of the sensing mechanism, the same base photopolymer was used for both parts. A double quantity of the base PEG photopolymer was prepared and was then split equally into two vials. One was used to fabricate the base, while the other had the carbon black filler added and was used to fabricate the device area.

The CAD part was oriented in the slicer software such that the base layer was fabricated first, followed by the device area immediately after. The CAD design was also sliced such that the base layers were thicker 100 µm layers in order to speed up the fabrication process. As the base material contained no dye and there was no filler to restrict cure depth it was possible to build with these increased thicknesses. A set of 6 fabricated parts with the slotted design are shown in Figure 7.6.

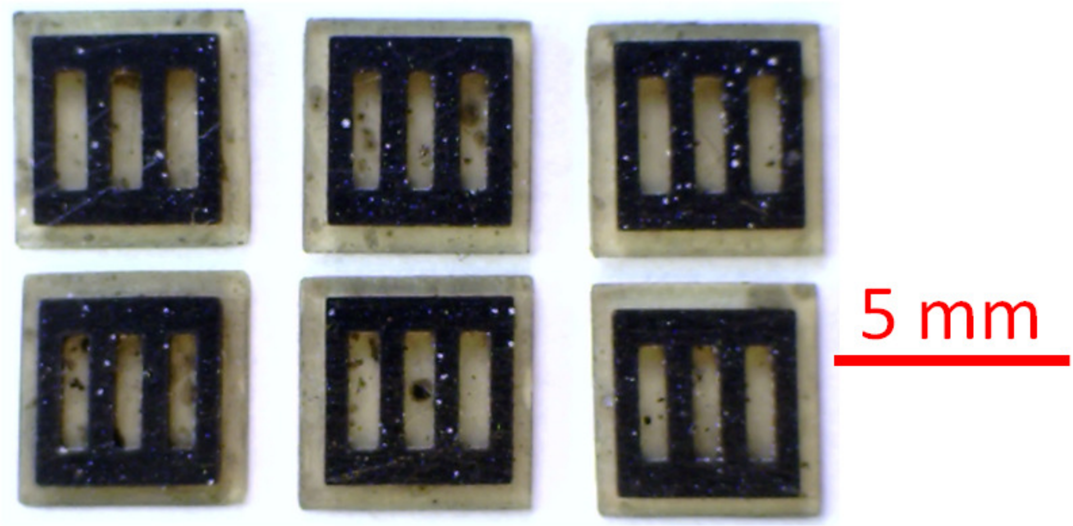

Figure 7.6 – Photographic image showing slotted version 2 vapour sensing devices

The fabricated devices were post processed and mounted to stubs in the same manner as the previous version of devices. The newer devices showed no variation in resistance while being adhered to the stubs and conductive paint seeping between the base and stub was no longer a problem providing that it didn't connect across both sides of the device; therefore care was taken to ensure this didn't happen. The addition of the base layer also made the devices easier to handle as they could be picked up using the base, which was less brittle and prone to damage than the composite material. Figure 7.7 shows the completed devices.

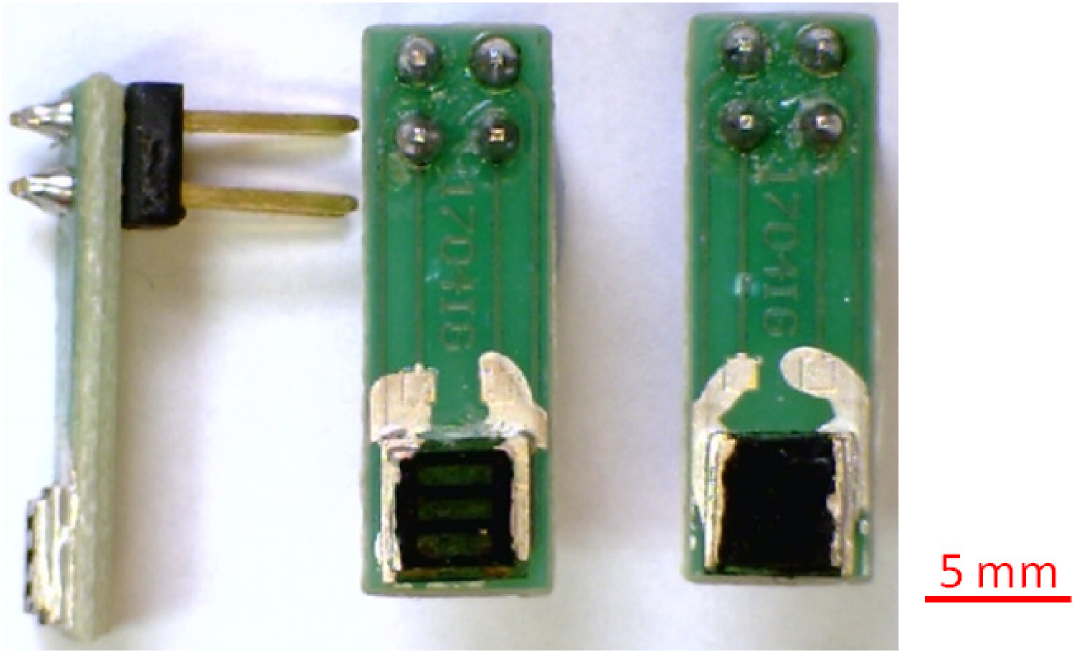

Figure 7.7 – Photographic image showing version 2 vapour sensing devices mounted onto test stubs. Image shows side view of a slotted device (left), top view of a slotted device (centre), and top view of a standard device (right)

7.5 Testing

Testing of the devices was conducted using a custom vapour delivery system that had been previously built. The system allows for the separate control of up to 2 sample vapours, wet air and dry air to the sensor chamber, a diagram of the setup is shown in Figure 7.8. The system is controlled using software written in LabView (National Instruments) and allows for both manual an automated control of the system for long tests.

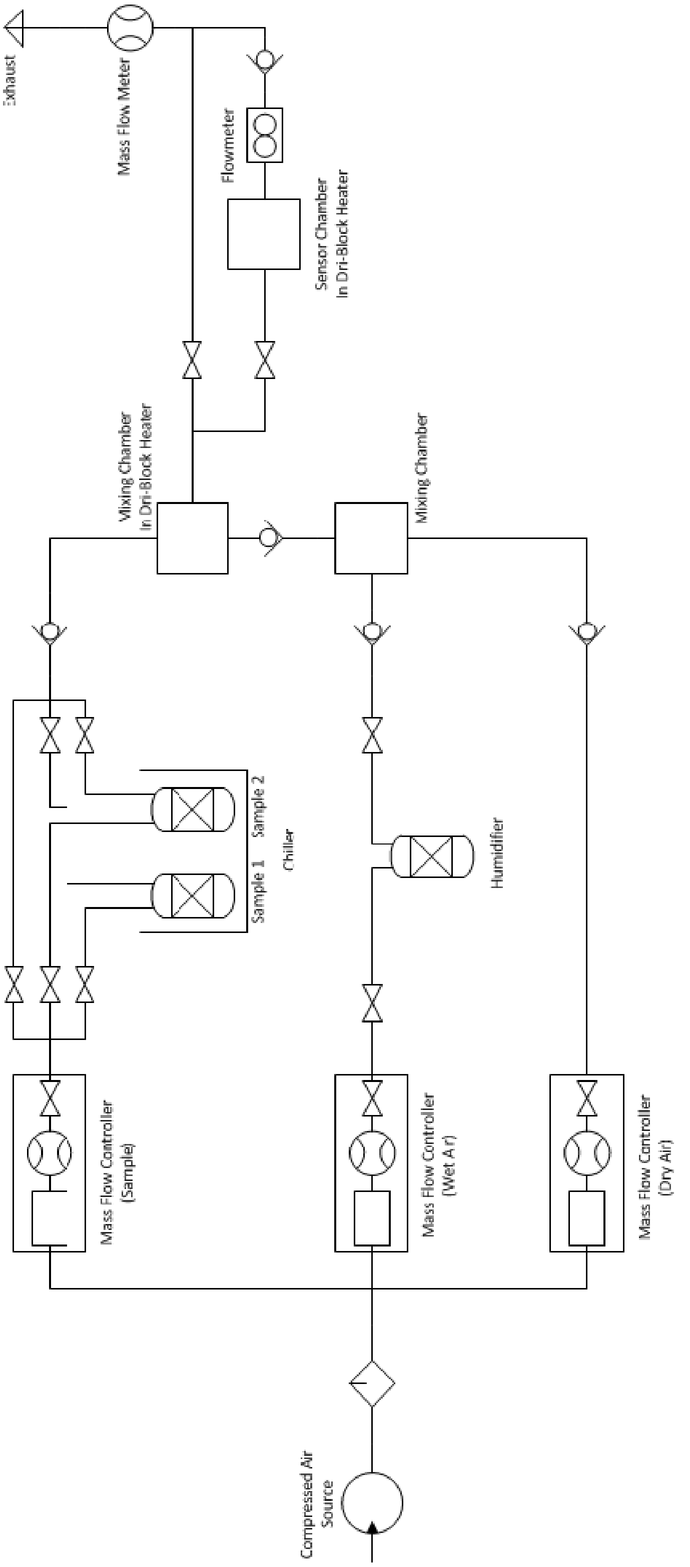

Figure 7.8 – Schematic diagram of vapour test rig

In order to measure the electrical responses of the sensors, a sensor interface system was designed to gather data from the polymer composite devices. This system consisted of a simple potential divider circuit (Figure 7.9) that was used to monitor the resistance of the devices under test. As the devices were predicted to have initial resistances of no less than 10 KΩ each, by using a 5 V supply and a matched second fixed resistor of similar value, the power dissipated by the devices was not expected to exceed 600 µW.

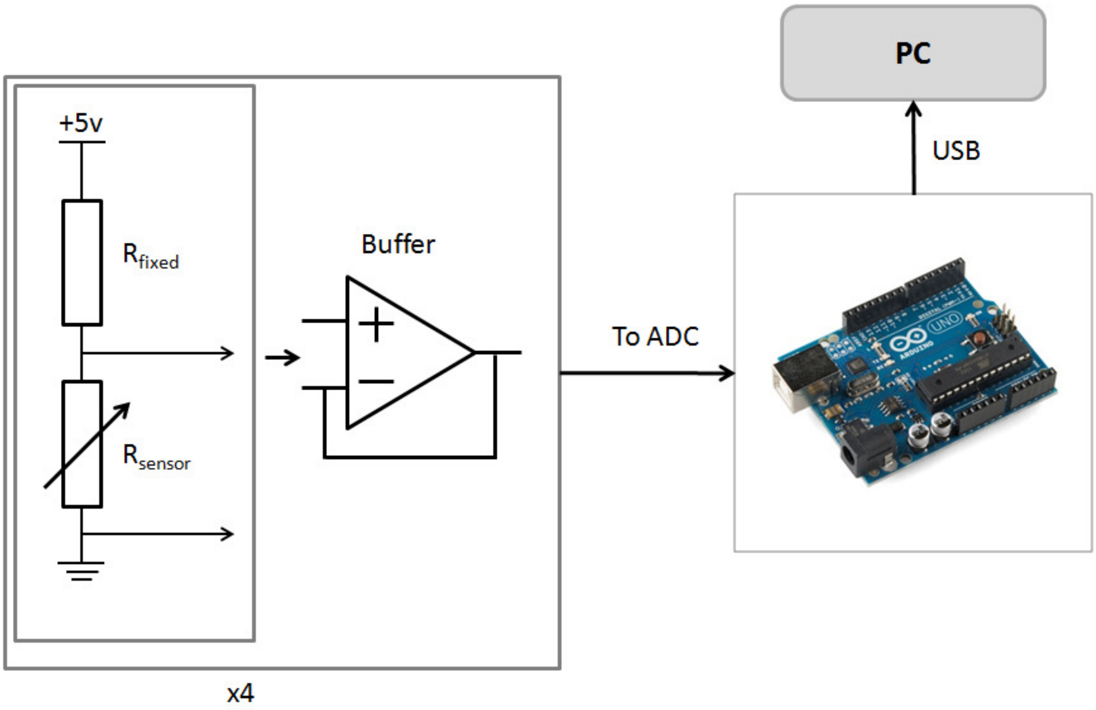

Figure 7.9 – Diagram of vapour senor device test circuit

The output from the potential divider was then buffered using an AD704 (Analog Devices Inc., USA) as unity gain amplifier and measured using the onboard analogue to digital converter on an ATMEGA328P microcontroller (Atmel Corperation, USA). The microcontroller was setup to monitor 4 sensing devices simultaneously along with the total flow through the chamber by using an AWM3300V mass flow meter (Honeywell, USA). The microcontroller was connected to a PC using a USB connection and communicated using an emulated serial (RS232) interface with a program (Figure 7.10) written using the

Microsoft's C# programming language. The program allowed for simultaneous live viewing and recording of all four sensors. The logged results could then be analysed at a later time.

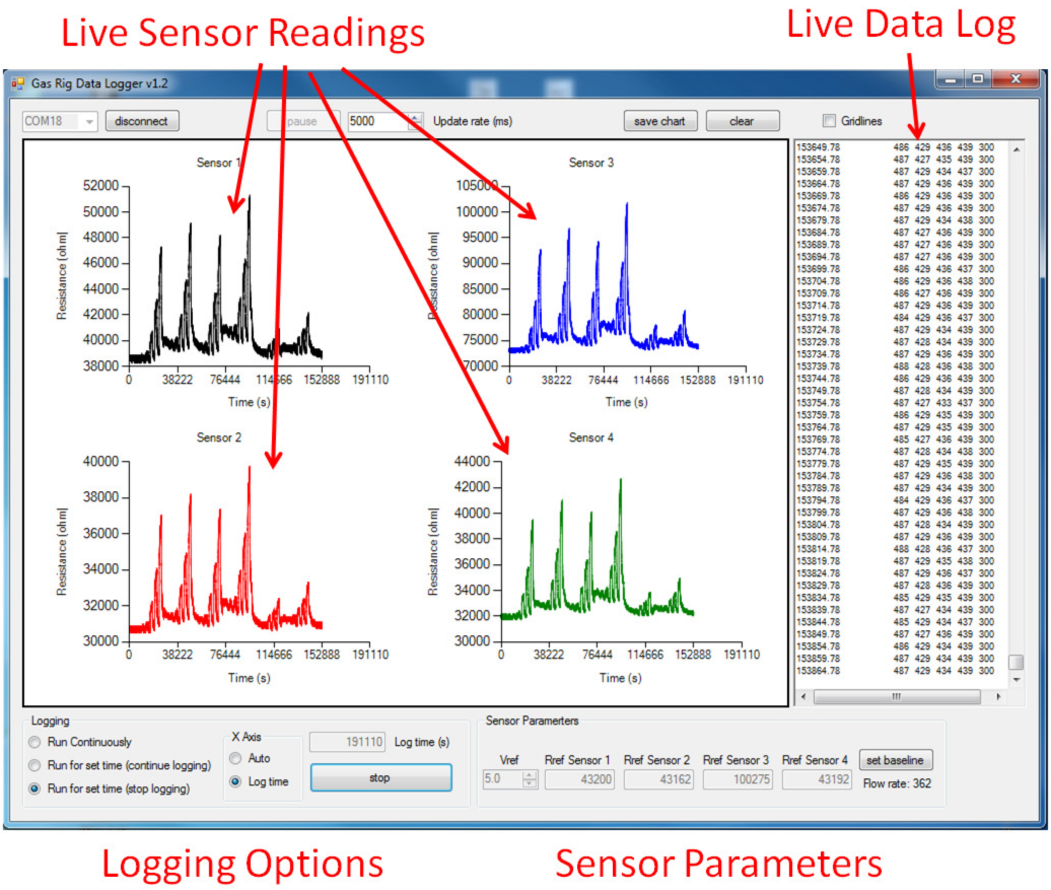
Live Sensor Readings

Live Data Log

Logging Options

Sensor Parameters

Gas Rig Data Logger v1.2

COM18 · 5000 Update rate (ms) · ☐ Gridlines

Logging: ○ Run Continuously · ○ Run for set time (continue logging) · ● Run for set time (stop logging)

X Axis: ○ Auto · ● Log time

191110 Log time (s)

Sensor Parameters: Vref 5.0 · Rref Sensor 1 43200 · Rref Sensor 2 43162 · Rref Sensor 3 100275 · Rref Sensor 4 43192 · Flow rate: 362

```
153649.78          486  429  436  439  300
153654.78          487  427  435  439  300
153659.78          487  429  434  437  300
153664.78          487  429  436  439  300
153669.78          486  429  436  439  300
153674.78          487  429  436  439  300
153679.78          487  429  434  438  300
153684.78          487  427  436  439  300
153689.78          487  427  436  439  300
153694.78          487  427  436  439  300
153699.78          486  429  436  437  300
153704.78          486  429  436  438  300
153709.78          486  427  436  439  300
153714.78          487  429  436  439  300
153719.78          484  429  436  437  300
153724.78          487  429  434  439  300
153729.78          487  428  434  439  300
153734.78          487  429  436  439  300
153739.78          488  428  436  438  300
153744.78          486  429  436  439  300
153749.78          487  428  434  439  300
153754.78          487  427  433  437  300
153759.78          486  429  435  439  300
153764.78          487  429  435  439  300
153769.78          485  427  436  439  300
153774.78          487  428  434  438  300
153779.78          487  429  435  439  300
153784.78          487  429  436  438  300
153789.78          487  429  434  439  300
153794.78          484  429  436  437  300
153799.78          487  429  436  438  300
153804.78          487  428  434  439  300
153809.78          487  429  436  439  300
153814.78          488  428  436  437  300
153819.78          487  429  435  438  300
153824.78          487  429  436  437  300
153829.78          487  428  436  439  300
153834.78          485  429  435  439  300
153839.78          487  427  434  439  300
153844.78          485  429  434  437  300
153849.78          487  427  436  439  300
153854.78          486  429  434  439  300
153859.78          487  429  434  439  300
153864.78          487  429  434  439  300
```

Figure 7.10 – Screenshot of interface and datalogging software for vapour sensing devices

7.5.1 *Testing of I/V*

An important feature of any sensing device is that it acts as an ohmic conductor and therefore responds linearly to changes in current flow. While non-ohmic devices can often be compensated for, this is not an ideal situation as the data obtained requires more processing in order to extract results and the results are often less repeatable. Therefore, to test the response of the devices, an Autolab PGSTAT12 (Metrohm, USA) was used to plot I/V curves for a selection of the devices. Additionally, it is important to know whether the response changes with increasing temperature, as such a test was conducted at 10 temperatures from 25 °C to 70 °C in 5 °C increments. This temperature range was chosen as it was felt that it would be representative of typical operating conditions and an amount of overhead, it was felt that temperatures above 70 °C would begin to degrade the material and therefore were outside of the normal operating range. Heating was achieved using a DB-3DL Dri-Block Heater (Techne, UK). The devices were tested over a range of -5V to +5V in 50 mV steps while measuring the current flow. All of the devices measured produced linear I/V curves for each temperature. Figure 7.11 shows a set of results from one of the slotted devices, which was typical of those seen for all devices. Figure 7.12 shows a subset of the same data. Figure 7.13 shows the variation in resistance of the device with increasing temperature which again, was a typical response.

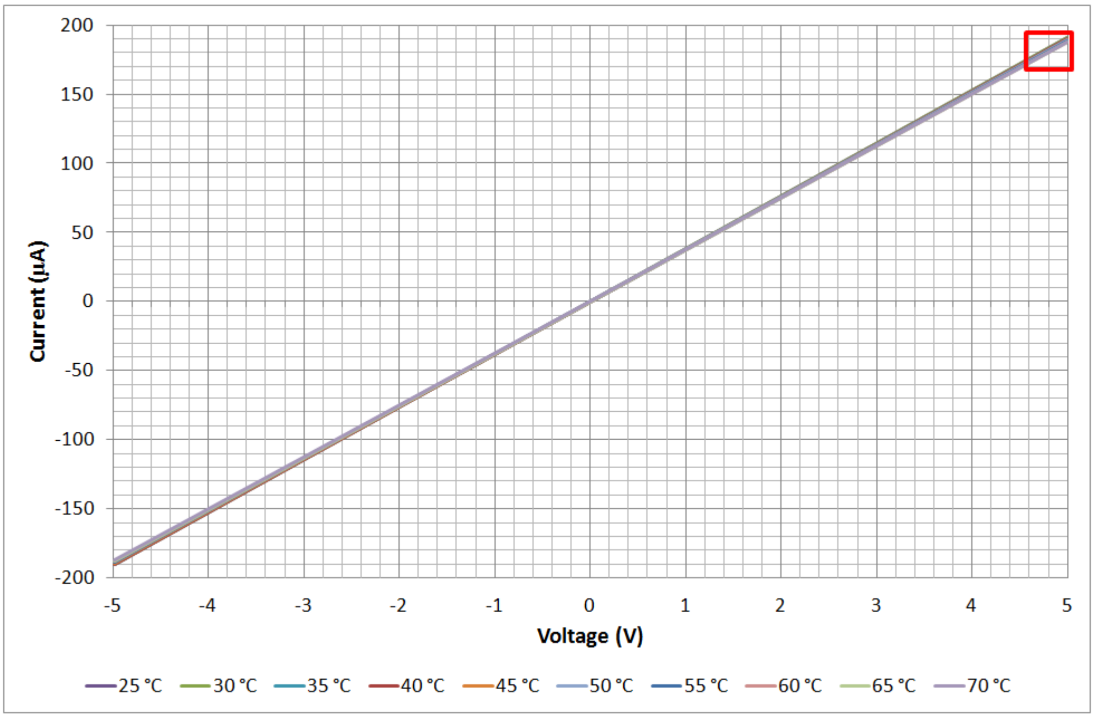

Figure 7.11 – I/V plot for a slotted version 2 vapour sensor tested at range of temperatures

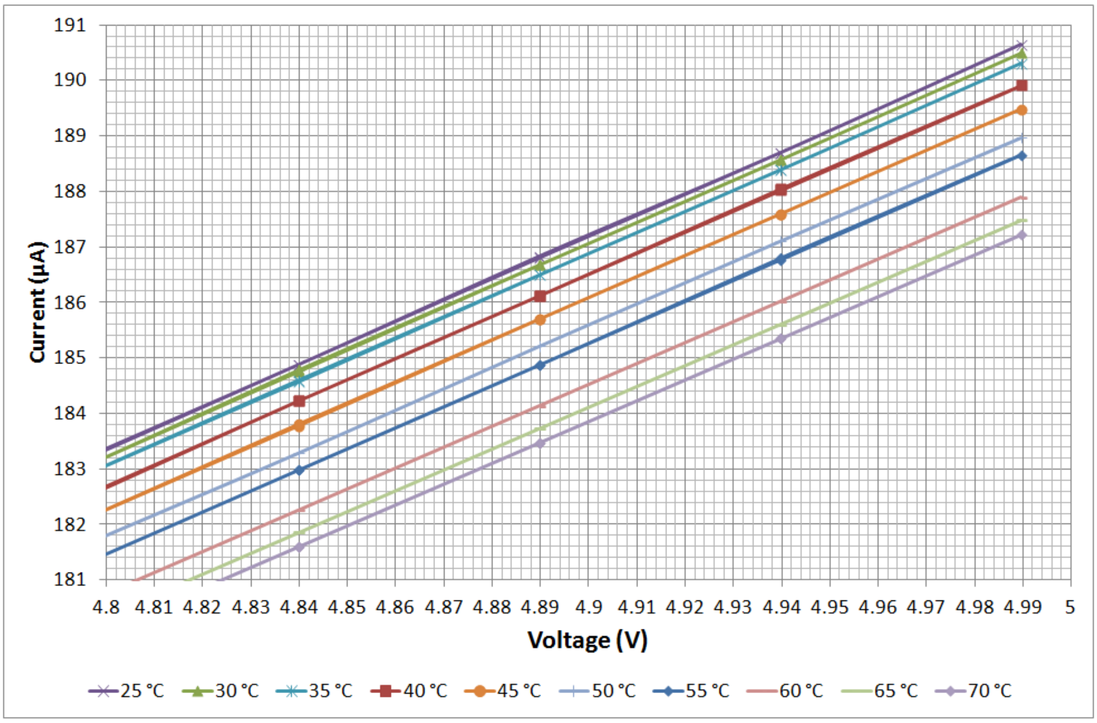

Figure 7.12 – I/V plot for a slotted version 2 vapour sensor tested at range of temperatures. (data shown over a restricted range to illustrate small variation)

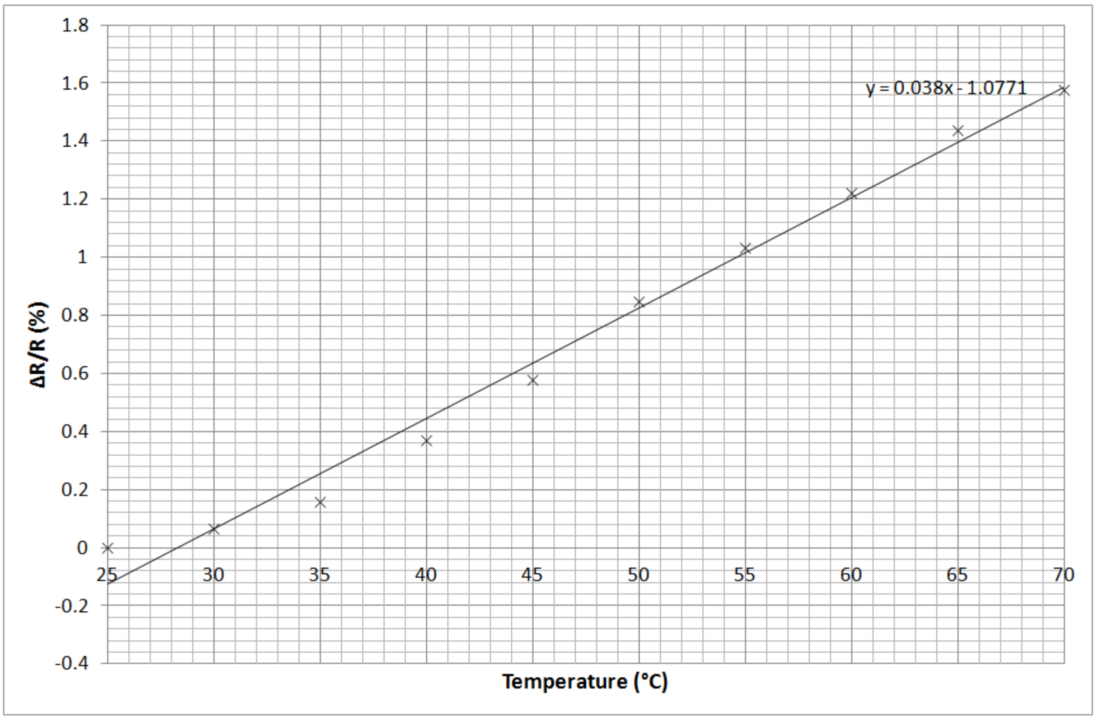

Figure 7.13 – Plot showing increase in baseline resistance of a version 2 slotted MSL fabricated vapour sensor with increase in ambient temperature

7.5.2 Calculating Vapour Concentrations

The flow rates required to achieve the desired concentration of the exposure vapours were calculated using the Antoine vapour pressure equation (Equation 7.1). This equation describes the relationship between the temperature and pressure of the equilibrium of the gas phase and condensed phase of the sample. The equation can be used to calculate the vapour pressure (p) for a given sample at a given temperature (t).

$$\log_{10} p = A - \frac{B}{t+C} \tag{7.1}$$

For each sample vapour, the constants A, B and C can be obtained from databooks that provide the necessary values for given temperature ranges, in this case constants were taken from Lange's Handbook of Chemistry [66] which provides a vapour pressure with the units in mm of Mercury (mmHg). The required flow rate (F_s in ml/min) of carrier air to achieve the desired concentration (c in ppm) was calculated using Equation 7.2, where F_t (ml/min) is the total flow rate, p is the vapour pressure and p_t is the total pressure (which had previously been measured at 760.0021 mmHg for the total flow rate of 300 ml/min – the standard total flow rate used on the gas test rig).

$$F_s = F_t \frac{c \times p_t}{p \times 10^6} \tag{7.2}$$

7.5.3 Test Procedure

The devices were tested for their response to 4 analyte vapours, Toluene, Ethyl Acetate, Ethanol and Propan-2-ol. The vapour pressure coefficients for these chemicals were obtained from Lange's Handbook of Chemistry [66] and are shown in Table 7.4.

	A	B	C
Toluene	6.9546	1344.8	219.5
Propan-2-ol	8.1178	1580.9	219.6
Ethanol	8.3211	1718.1	237.5
Ethyl Acetate	7.1018	1245	217.9

Table 7.4 – Constants for Antoine's Vapour Pressure Equation for toluene, propan-2-ol, ethanol and ethyl acetate

Each was tested at 4 different humidity levels to verify its effects on the sensitivity of the devices. 10%, 20%, 30% and 50% relative humidity were tested in an alternating pattern to ensure that any change detected was not an effect of gradual drift. Therefore the order tested was 10%, 30%, 20%, and then finally 50%. Equations 7.3 and 7.4 were used to calculate the required flow rates in order to achieve the desired level, where F_w is the flow rate of the wet air, F_d is the flow rate of the dry air, F_s is the flow rate of the sample air, F_t is the total flow rate.

$$F_w = \frac{\%RH \times F_t}{100} \tag{7.3}$$

$$F_d = F_t - F_w - F_s \tag{7.4}$$

The temperature of the samples was kept at a constant temperature of 10°C using an RTE-300 Refrigerated Chiller (Neslab, US). A range of analyte concentrations were used that were determined by the flow rate of the carrier gas through the sample vessels. The chosen sample flow rates were 15, 21, 30, 66, 99 and 141 ml/min, while the total flow rate used was 300 ml/min. Table 7.5 therefore shows the flow rates used at the different relative humidities. Using Equation 7.4 above, the resulting sample concentrations were then calculated. Table 7.6 shows the concentrations to the nearest 10 ppm.

		Sample Flow Rate (ml/min)						
		0	15	21	30	66	99	141
%RH	Wet Air	Dry Air Flow Rate (ml/min)						
10	30	270	255	249	240	204	171	129
20	60	240	225	219	210	174	141	99
30	90	210	195	189	180	144	111	69
50	150	150	135	129	120	84	51	9

Table 7.5 – Flow rate combinations used for testing of MSL fabricated vapour sensors to cover a range of humidity and sample vapour concentration

	Sample Flow Rate (ml/min)					
	15	21	30	66	99	141
	Sample Concentration (ppm)					
Toluene	820	1140	1640	3600	5400	7690
Propan-2-ol	1120	1570	2250	4940	7420	10560
Ethanol	1580	2200	3160	6940	10410	14830
Ethyl acetate	2860	4000	5730	12600	18890	26900

Table 7.6 – Calculated concentrations of sample vapours (to the nearest 10 ppm)

The test procedure was structured such that the sensors were exposed in turn to each of the vapours for 30 minutes. Between each exposure, there was a further period of 30 minutes to allow for sensor recovery where the total flow rate and humidity remained constant. There was also an additional period of 30 minutes after the humidity had been changed to allow for the devices to reach a steady state baseline resistance before being exposed to the next sample. Figure 7.14 shows a timing diagram of the test cycle.

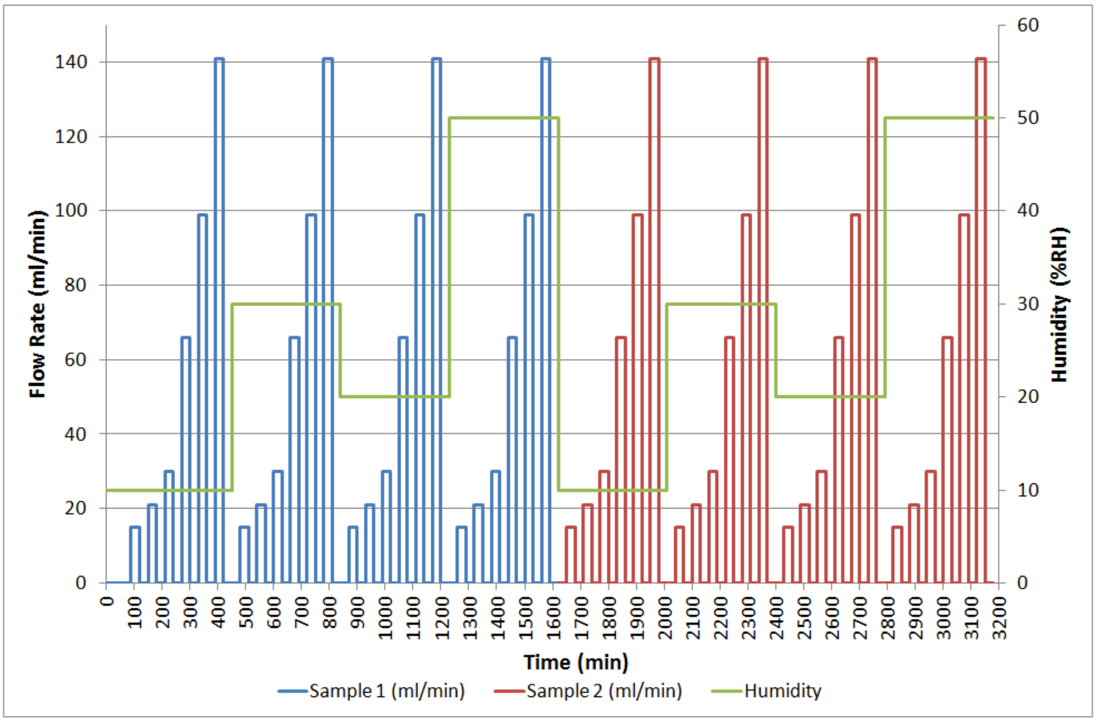

Figure 7.14 – Timing diagram for vapour test rig

7.5.4 Results

Figures 7.15 and 7.16 show the results obtained from two sets of devices (both standard, square devices and slotted types) with each of the 4 sample vapours. The results show a positive response (due to the reduction of conductive paths caused by the swelling of the polymer) by all devices to all of the sample vapours showing that the MSL process can successfully fabricate components that exhibit a change in their electrical properties on exposure to solvent vapours.

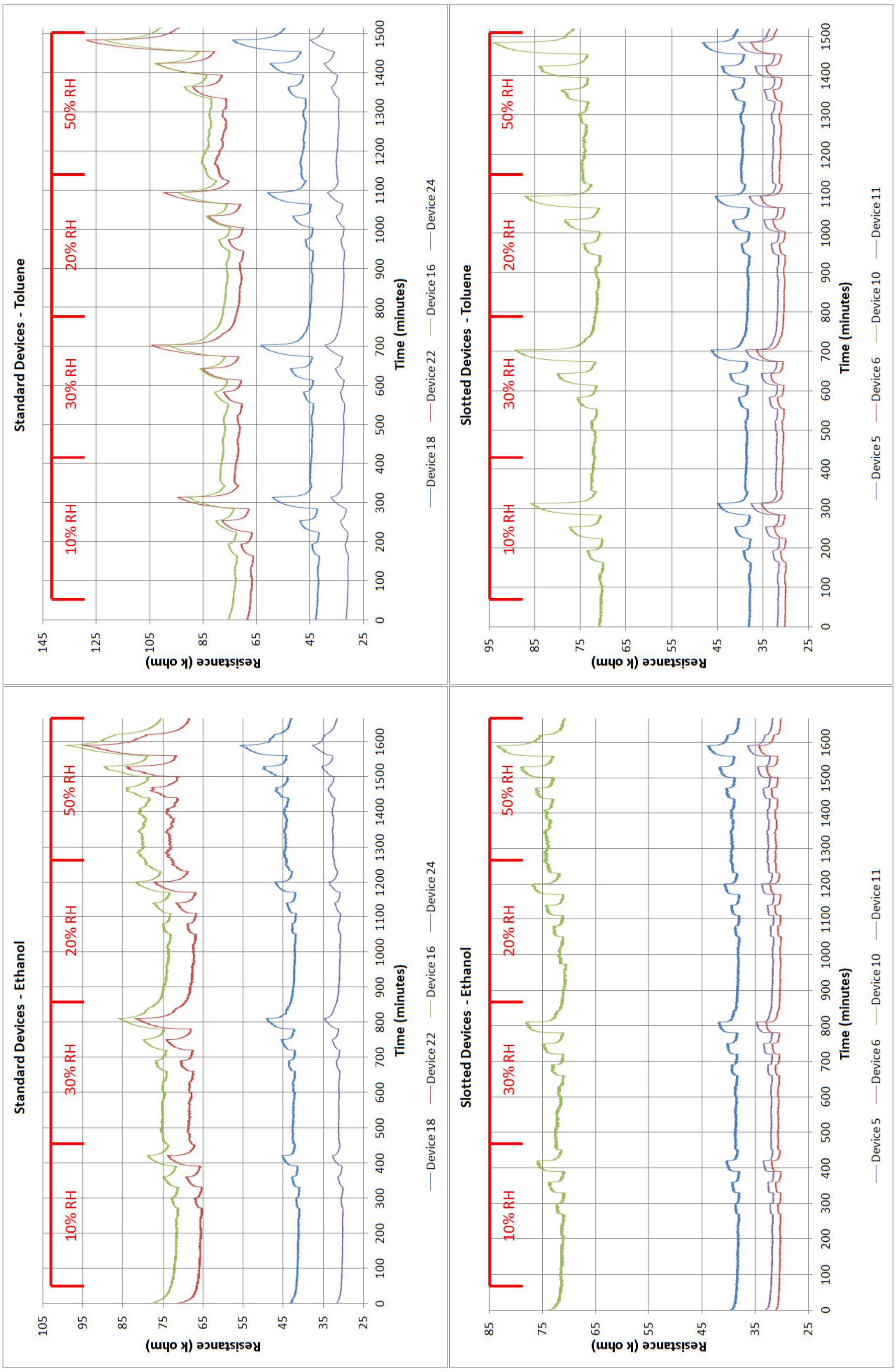

Figure 7.15 –Unprocessed results from testing of selection of standard and slotted devices with ethanol and toluene sample vapours

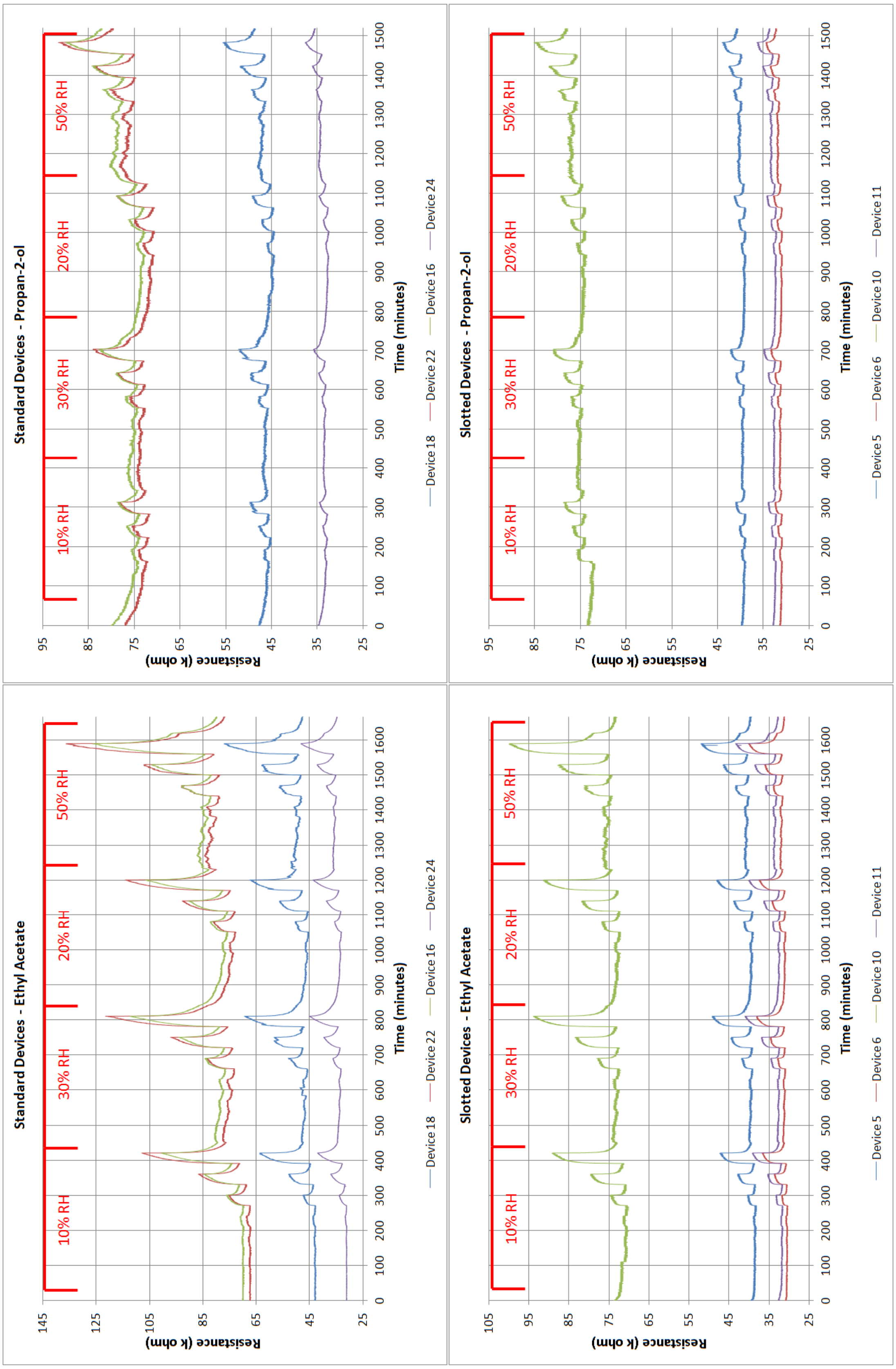

Figure 7.16 – Unprocessed results from testing of selection of standard and slotted devices with ethyl acetate and propan-2-ol

By visual inspection of the figures it can be seen that there is variation in the baseline resistances of the devices when compared to one another. On further inspection of the data, it can also be seen that, as was expected, an increased humidity of the sample air results in an increase of the baseline resistance of the sensor. This effect is due to the known swelling effects of PEG which is a polar sensitive molecule [67] and is therefore expected to respond to analytes with OH groups (although the magnitude of the response will be analyte specific). As a result of this pre-swelling effect, the device is taken closer to the percolation limit. As such, further swelling of the device caused by exposure to an analyte vapour then causes a response of greater magnitude when compared to using same sample concentration but at a lower humidity. While the change in baseline resistance can be clearly seen in the raw data, by calculating the response change from the baseline (Equation 7.5) the relative response magnitudes of the two device geometries at the different humidities could be directly compared. Figure 7.17 shows the response of the two sensors geometries at the minimum and maximum concentrations tested (a full set of results can be found in Appendix B) at increasing relative humidity of the carrier air. Table 7.7 then shows the equations for the fitted lines. It should be noted that these are empirical representations of the recorded data and not derived from the physical processes involved in the observed responses.

$$Response = \frac{R - R_0}{R_0} \tag{7.5}$$

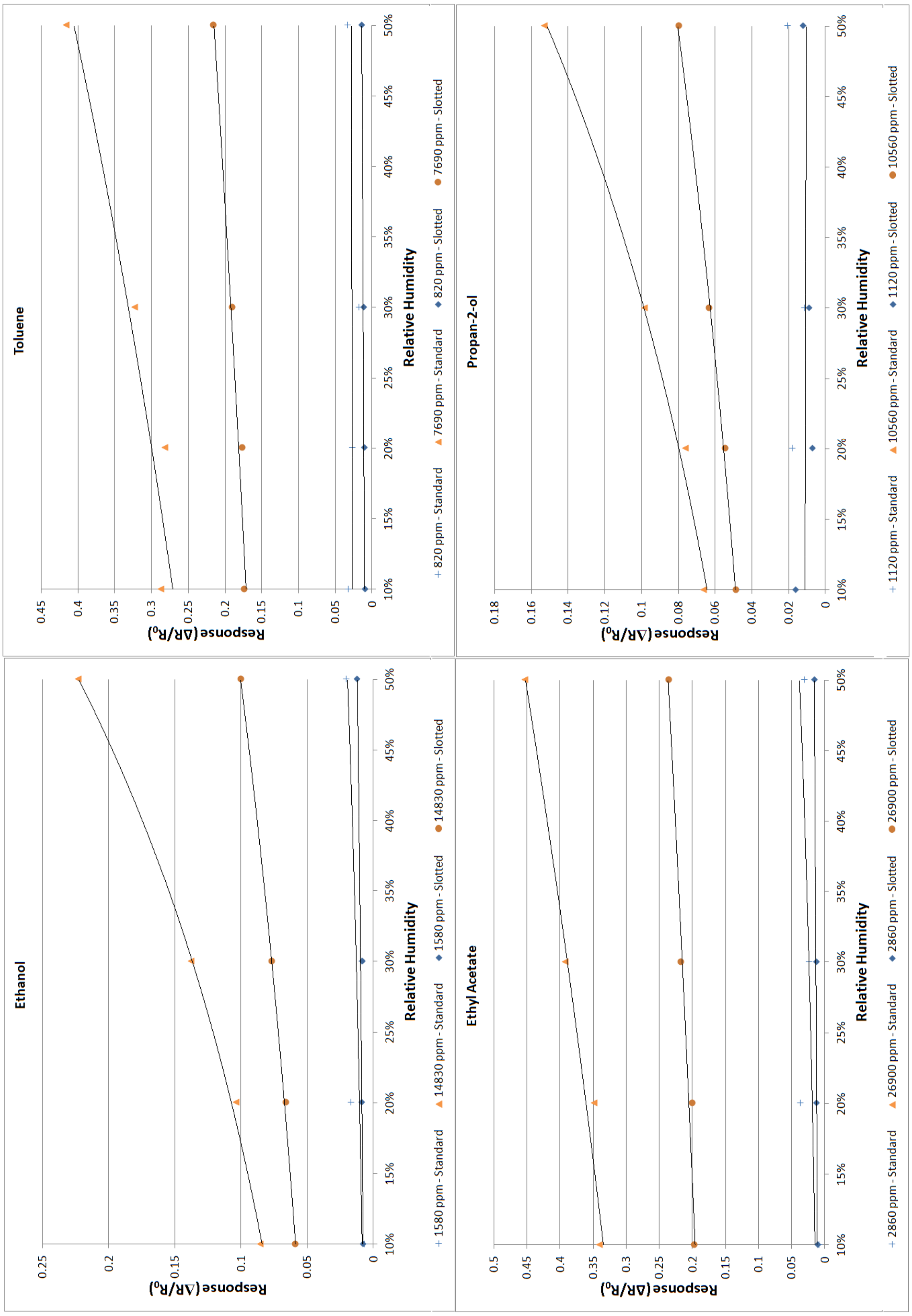

Figure 7.17 – ΔR/R0 results from testing of selection of standard and slotted devices with sample vapours of ethanol at 1580 and 14830 ppm, toluene at 802 and 7690 ppm, ethyl acetate at 2860 and 26900 ppm, and propan-2ol at 1120 and 10560 ppm at 10%, 20% 30% and 50% relative humidity

		Standard	Slotted
Ethanol (ppm)	1580	$0.007e^{2.086x}$	$0.007e^{1.103x}$
	2200	$0.005e^{2.805x}$	$0.005e^{2.333x}$
	3160	$0.006e^{3.240x}$	$0.006e^{2.419x}$
	6940	$0.017e^{2.875x}$	$0.018e^{1.766x}$
	10410	$0.032e^{2.828x}$	$0.031e^{1.715x}$
	14830	$0.066e^{2.434x}$	$0.051e^{1.336x}$
Toluene (ppm)	820	$0.027e^{0.066x}$	$0.010e^{0.785x}$
	1140	$0.011e^{1.296x}$	$0.006e^{1.621x}$
	1640	$0.016e^{0.438x}$	$0.010e^{1.775x}$
	3600	$0.041e^{2.053x}$	$0.039e^{1.216x}$
	5400	$0.106e^{1.425x}$	$0.081e^{0.895x}$
	7690	$0.250e^{1.007x}$	$0.162e^{0.567x}$

		Standard	Slotted
Ethyl Acetate (ppm)	2860	$0.012e^{2.372x}$	$0.010e^{0.885x}$
	4000	$0.010e^{2.520x}$	$0.008e^{2.154x}$
	5730	$0.016e^{2.318x}$	$0.013e^{1.258x}$
	12600	$0.079e^{1.173x}$	$0.042e^{1.366x}$
	18890	$0.169e^{0.849x}$	$0.096e^{0.880x}$
	26900	$0.310e^{0.754x}$	$0.187e^{0.474x}$
Propan-2-ol (ppm)	1120	$0.008e^{1.033x}$	$0.004e^{0.148x}$
	1570	$0.008e^{1.144x}$	$0.006e^{1.079x}$
	2250	$0.010e^{1.823x}$	$0.010e^{1.479x}$
	4940	$0.020e^{2.179x}$	$0.017e^{2.005x}$
	7420	$0.032e^{2.131x}$	$0.026e^{1.923x}$
	10560	$0.052e^{2.138x}$	$0.043e^{1.239x}$

Table 7.7 –Table of equations representing the responses of the two different device types to increases in relative humidity of the carrier air with different sample concentrations

The magnitude responses demonstrate a clear correlation between the exposure concentration and the magnitude of the signal received. However at the lower concentrations (below ~15000 ppm) the response of the devices was significantly small such that the noise from the analogue to digital converter (ADC) became significant. While this issue could potentially be overcome in future investigations by using an ADC with greater resolution, or altering the sensing circuit, it was felt that it would be more appropriate to investigate modification of the devices themselves. Suggested modifications would be to investigate thinner devices in order to increase the response time or by reducing the quantity of conductive loading such that the baseline resistance is closer to the percolation limit in order to increase the magnitude of the response.

Figures 7.18 & 7.19 show the magnitude response of the standard and slotted devices to the sample vapours. The results show that the slotted devices produced a smaller response than the solid square devices in all cases; however, the responses were marginally more linear. The slotted devices shows greater stability to changes in humidity with the maximum variation in signal response between 10% and 50% relative humidly being 4.3% compared to 13.8% variation for the plain, square devices. Additionally, although the devices responded to all sample vapours, all devices (and therefore the polymer composite mix used) displayed a significantly increased response to the toluene samples.

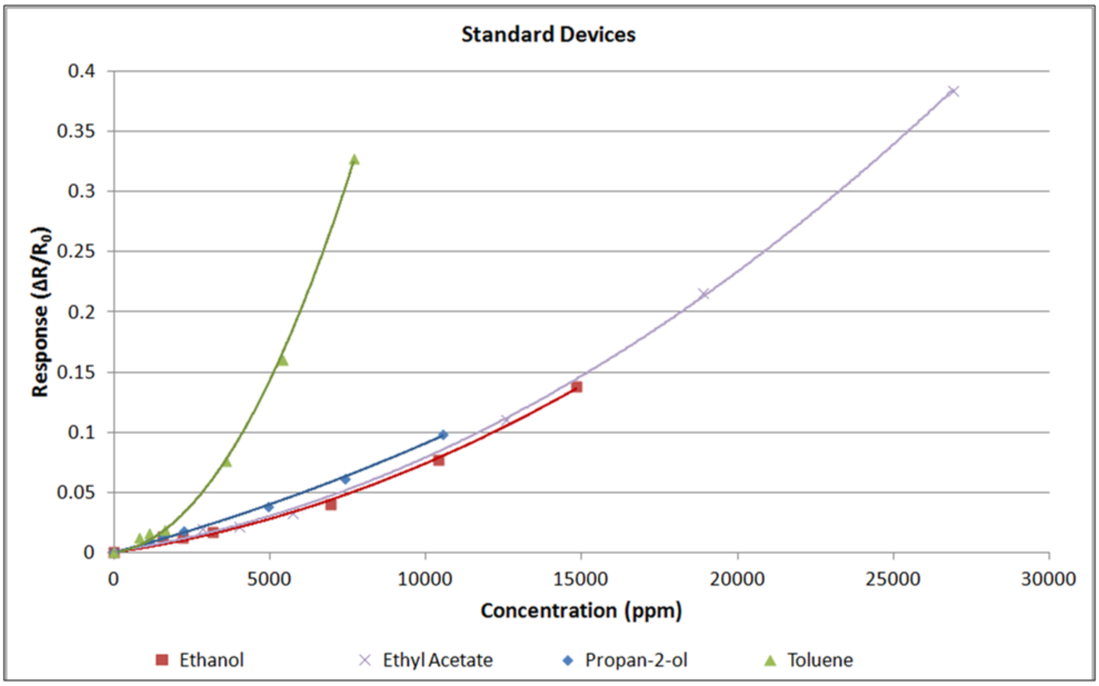

Figure 7.18 – Response magnitude of 1 mm thick standard, solid MSL fabricated vapour sensing devices to ethanol, toluene, ethyl acetate and propan-2-ol at a range of concentrations

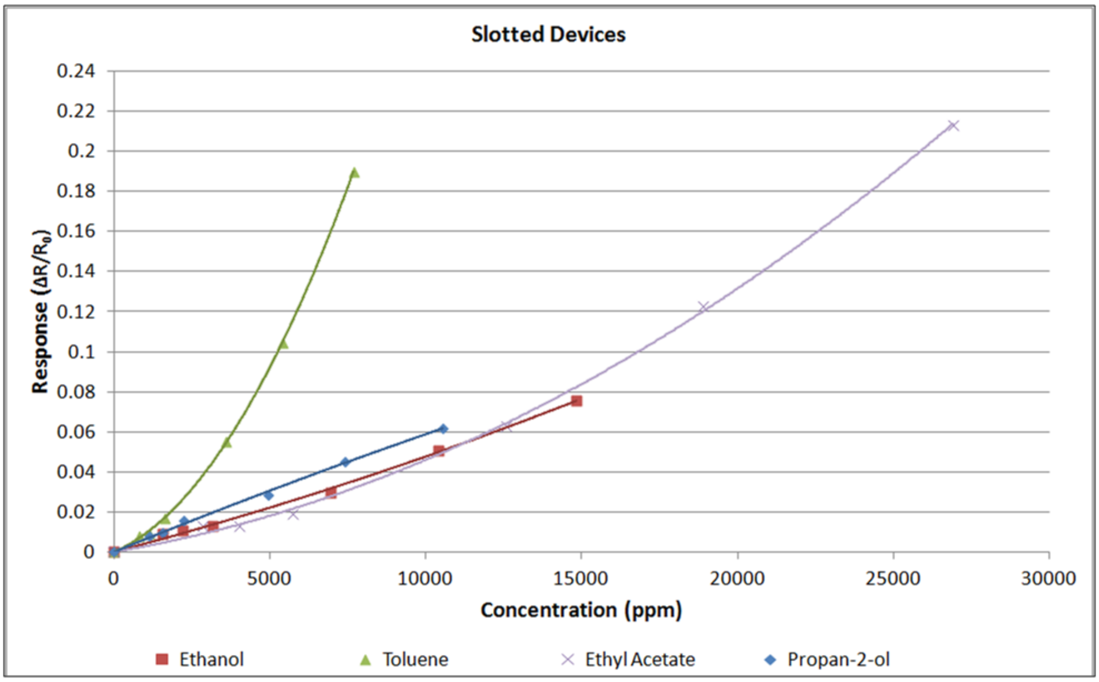

Figure 7.19 – Response magnitude of 1mm thick, slotted MSL fabricated vapour sensing devices to ethanol, toluene, ethyl acetate and propan-2-ol at a range of concentrations

When the magnitude of the responses are compared to the earlier investigation of temperature effect on the baseline value of the device, it can be seen that the observed response to sample vapours is generally much greater than the effects of background temperature, which was a maximum of 2.1% greater at 70 degrees compared to room temperature – a temperature which is beyond the expected normal operating range of the devices. To confirm the dynamic response to samples vapours at increasing temperatures, a selection of 4 slotted devices were retested at ambient temperatures of 30, 40, 50 and 60 degrees with the 3 higher concentrations of ethyl acetate and toluene at 20%, 30% and 50% relative humidity.

The results (shown in Figures 7.20 and 7.21) demonstrate a clear reduction in response to the sample vapours with increased temperature. The data shows that at 50°C and above the response is significantly reduced and at 60°C the responses are up to 76% lower magnitude than operating at 30°C. At 30°C and 40 °C it can also be seen that the humidity plays a larger factor that at the higher temperatures. The results recorded however do confirm the trend noted by similar experiments conducted by others [68-70] that conductive composite vapour sensors produce smaller responses at higher temperatures. This is due to the polymer being able to absorb less of the vapour at higher temperatures which results in less swelling and therefore a smaller response. This therefore indicates that for optimum operation, the devices should be used at a temperature approximately 5 - 10°C above room temperature to achieve maximum sensitivity while reducing the effect of change in the background room temperature.

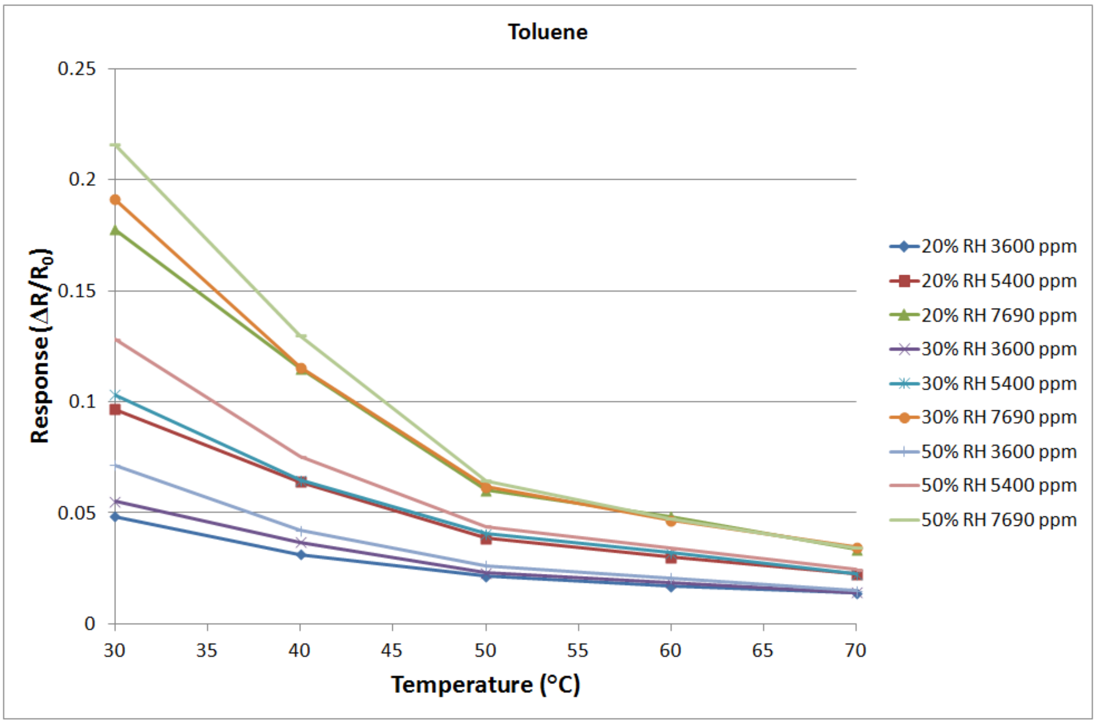

Figure 7.20 – Magnitude response of MSL fabricated slotted vapour sensing devices to toluene at a range of temperatures and air humidity

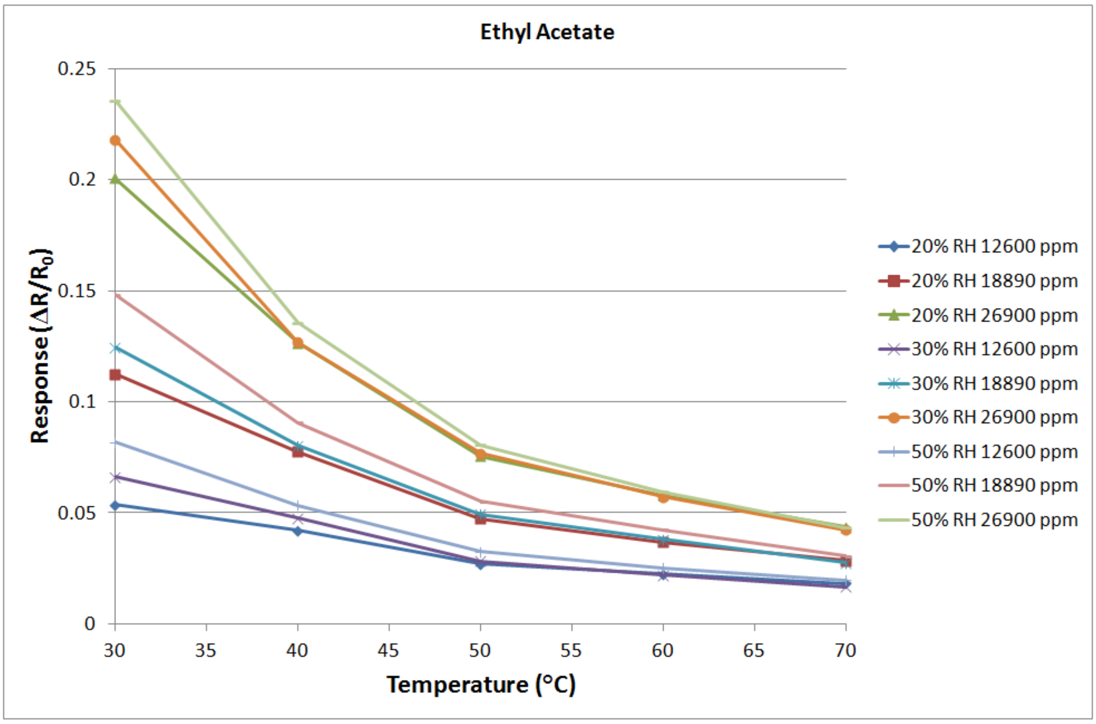

Figure 7.21 – Magnitude response of MSL fabricated slotted vapour sensing devices to ethyl acetate at a range of temperatures and air humidity

7.6 Conclusion

The concept of using conductive polymer composites for gas and vapour sensing applications is already well known, however, many of the fabrication techniques involved are complex and time consuming. In this chapter a novel method for the fabrication of chemoresistive carbon black / polymer composite vapour sensing devices using microstereolithography has been presented.

The base polymer material utilised a photopolymer component that allows the use of MSL in order to selectively and accurately fabricate and pattern devices of any required shape or size. Although only one material was tested here for verification of the feasibility of this technique, the method allows for a range of composite fill levels and the addition of other materials in order to alter the selectivity of the devices.

The PEG material explored has been seen previously in sensing by harnessing the swelling properties of the material when exposed to a sample vapour. Two geometries of sensor were fabricated to investigate whether the ability of MSL to fabricate complex 3D structures could be harnessed in order to achieve greater sensitivity by generating an increased surface area for the vapour to permeate. The solid square devices had a surface area of 24 mm^2 while the slotted devices had a surface area of 30.5 mm^2 (27% more). It was however discovered that modifications did not provide any increase in sensitivity although all devices tested did show satisfactory responses. Tables 7.8 and 7.9 show the average response sensitivity (with standard deviation) of the sensors to the sample analytes at range of humidities. The testing process also identified that the material showed selectivity towards toluene with magnitude responses up to 45% change at ~7500 ppm. As with many conductive polymer composites, there was shown to be a negative correlation between response and device temperature, the optimum operating temperature was found to be just above the room ambient temperature in order to prevent minor temperature changes affecting readings.

		Standard			
		10% RH	20% RH	30% RH	50% RH
Ethanol	Average	3.95	5.89	6.32	11.89
	Std Dev	1.07	2.79	1.64	2.08
Toluene	Average	22.97	22.45	23.38	33.57
	Std Dev	13.08	10.99	10.72	15.71
EA	Average	6.49	8.88	9.46	11.55
	Std Dev	4.19	3.77	3.18	3.38
Propan-2-ol	Average	13.34	8.14	8.39	13.02
	Std Dev	14.73	4.08	1.27	3.47

Table 7.8 – Average sensitivity (from fractional response) for standard square sensors for the range of tested analyte vapours at varying relative humidity of carrier air (response/ppm *10^{-6})

		Slotted			
		10% RH	20% RH	30% RH	50% RH
Ethanol	Average	3.52	4.11	4.75	6.99
	Std Dev	0.93	0.96	0.51	0.71
Toluene	Average	12.99	14.03	15.33	19.38
	Std Dev	6.03	5.93	6.16	5.86
EA	Average	4.21	4.68	5.18	6.36
	Std Dev	1.93	1.81	1.93	1.68
Propan-2-ol	Average	6.73	4.96	6.13	9.46
	Std Dev	3.97	0.80	1.04	1.27

Table 7.9 – Average sensitivity (from fractional response) for slotted sensors for the range of tested analyte vapours at varying relative humidity of carrier air (response/ppm $*10^{-6}$)

In the initial stages of testing it was discovered that the method of adhesion and connecting electrically of the sensors adversely affected their operation. Therefore a revised design was produced that utilised the multi-material capabilities of the custom MSL system by including a protective base for each device. Due to the simplicity of the fabrication method, this technique could see benefits in the cost of one-off or prototype devices for research or production situations. Additionally, although not demonstrated here, it is felt that the demonstrated multi-material compatibility of the devices suggests that future work should include investigation of the fabrication of one or more devices within complete flow channel housing in single build process.

7.7 References

[1] F.J. Santos, M.T. Galceran, Modern developments in gas chromatography–mass spectrometry-based environmental analysis, Journal of Chromatography A 1000 (2003) 125-151

[2] P.J. Marriott, P. Haglundb, R.C.Y. Ong, A review of environmental toxicant analysis by using multidimensional gas chromatography and comprehensive GC, Clinica Chimica Acta 328 (2003) 1-19

[3] N.S. Lewis, R.M. Goodman, R.H. Grubbs, A Conducting Polymer-based Electronic Nose for Landmine Detection, Technical report prepated for U.S. Army Soldier and

Biological Chemical Command Soldier Systems Center, Natick, Massachusetts (2001)

[4] A.M. Pisanelli, A.A. Qutob, P. Travers, S. Szysko, K.C. Persaud, Applications of Multi Array Polymer Sensors to Food Industries, Life Chemistry Reports 11 (1994) 303-308

[5] M. Penza, G. Cassano, F. Tortorella, G. Zaccaria, Classification of food, beverages and perfumes by WO3 thin-film sensors array and pattern recognition techniques, Sensors and Actuators B 73 (2001) 76-87

[6] A. Galdikas, A. Mironas, D. Senuliene, V. Strazdiene, A. Setkus , D. Zelenin, Response time based output of metal oxide gas sensors applied to evaluation of meat freshness with neural signal analysis, Sensors and Actuators B 69 (2000) 258–265

[7] J. Luo, J. Luo, L. Wang, X. Shi, Ju. Yin, E. Crewa, S. Lu, L.M. Lesperance, C-J. Zhong, Nanoparticle-structured thin film sensor arrays for breath sensing, Sensors and Actuators B 161 (2012) 845–854

[8] T. Hishinuma, Y. Koseki, J. Katayama, Y. Murai, T. Saito, M. Mizugaki, Changes of the thromboxane A2/prostacyclin balance in the urine of patients with renal diseases analyzed by gas chromatography/selected ion monitoring, Prostaglandins & other Lipid Mediators 60 (2000) 1–8

[9] F.K. Che Harun, J.A. Covington, J.W. Gardner, Portable e-Mucosa System: Mimicking the biological olfactory, Proceedings of the Eurosensors XXIII conference, Procedia Chemistry 1 (2009) 991–994

[10] A. Bhushan, D. Yemane, D. Trudell, E.B. Overton, J, Goettert, Fabrication of micro-gas chromatograph columns for fast chromatography, Microsystem Technologies 13 (2007) 361-368

[11] S. Ali, M. Ashraf-Khorassani, L.T. Taylor, M. Agah, MEMS-based semi-packed gas chromatography columns, Sensors and Actuators B 141 (2009) 309–315

[12] J.A. Dziuban, J. Mróz, M. Szczygielska, M. Malachowski, A. Górecka-Drzazga, R. Walczak, W. Bula, D. Zalewski, L. Nieradko, J. Lysko, J. Koszur, P. Kowalski, Portable gas chromatograph with integrated components, Sensors and Actuators A 115 (2004) 318–330

[13] J.P. Santosa, T. Arroyob, M. Aleixandrea, J. Lozanoa, I. Sayagoa, M. Garci´aa, M.J. Fernándeza, L. Arésa, J. Gutiérreza, J.M. Cabellosb, M. Gilb, M.C. Horrillo, A comparative study of sensor array and GC-MS: application to Madrid wines characterization, Sensors and Actuators B Chemical 102 (2004) 299-307

[14] Z. Xiaobo, Z. Jiewen, Comparative analyses of apple aroma by a tin-oxide gas sensor array device and GC/MS, Food Chemistry 107 (2008) 120–128

[15] A. Varpula, S. Novikov, A. Haarahiltunen, P. Kuivalainen, Transient characterization techniques for resistive metal-oxide gas sensors, Sensors and Actuators B 159 (2011) 12–26

[16] J.W Gardner, V.K. Varadan, O.O. Awadelkarim, Microsensors, MEMS and Smart Devices, John Wiley & Sons Ltd, New York, USA (2001)

[17] S. Pitcher, J.A. Thiele, H. Ren, J.F. Vetelino, Current/voltage characteristics of a semiconductor metal oxide gas sensor, Sensors and Actuators B 93 (2003) 454–462

[18] General Information for TGS Sensors, Figaro USA Inc, [online] Availabel: http://www.figarosensor.com/products/general.pdf, last accessed 09/02/2012

[19] H. Xu, X. Liu, D. Cui, M. Li, M, Jiang, A novel method for improving the performance of ZnO gas sensors, Sensors and Actuators B 114 (2006) 301–307

[20] M. Radecka, K. Zakrzewska, M. Rekas, SnO2–TiO2 solid solutions for gas sensors, Sensors and Actuators B 47 (1998) 194–204

[21] A. Haeusler, J-U. Meyer, A novel thick film conductive type CO2 sensor, Sensors and Actuators B 34 (1996) 388-395

[22] K. Zakrzewska, Mixed oxides as gas sensors, Thin Solid Films 391 2001 229-238

[23] J. Huang, Q. Wan, Gas Sensors Based on Semiconducting Metal Oxide One-Dimensional Nanostructures, Sensors 9 (2009) 9903-9924

[24] A. Berna, Metal Oxide Sensors for Electronic Noses and Their Application to Food Analysis, Sensors 10 (2012) 3882-3910

[25] G. Wiche, A. Berns, H. Steffes, E. Obermeier, Thermal analysis of silicon carbide based micro hotplates for metal oxide gas sensors, Sensors and Actuators A 123–124 (2005) 12–17

[26] J. Wagner, M. Schickfus, Inductively coupled, polymer coated surface acoustic wave sensor for organic vapors, Sensors and Actuators B: Chemical 76 (2001) 58–63

[27] H. Wohltjen, Mechanism of operation and design considerations for surface acoustic wave device vapour sensors, Sensors and Actuators 5 (1984) 307–325

[28] W.A. Groves, E.T. Zellers, Analysis of solvent vapors in breath and ambient air with a surface acoustic wave sensor array, The Annals of Occupational Hygiene 45 (2001) 609–623

[29] D. Amati, D. Arn, N. Blom, M. Ehrat, J. Saunois, H.M. Widmer, Sensitivity and selectivity of surface acoustic wave sensors for organic solvent vapour detection, Sensors and Actuators B: Chemical 7 (1992) 587–591

[30] J.W. Gardner, P.N. Bartlett, Application of Conducting Polymer Technology in Microsystems, Sensors and Actuators A 51 (1995) 57-66

[31] N. Andreadis, S. Chatzandroulis, D. Goustouridis, V. Kosma, K. Beltsios, I. Raptis, Fabrication of conductometric chemical sensors by photolithography of conductive polymer composites, Microelectronic Engineering 84 (2007) 1211–1214

[32] H. Lei, W.G. Pitt, L.K. McGrath, C.K. Ho, Modeling carbon black/polymer composite sensors, Sensors and Actuators B: Chemical 125 (2007) 396–407

[33] Y.S. Kim, Fabrication of carbon black–polymer composite sensors using a position-selective and thickness-controlled electrospray method, Sensors and Actuators B 147 (2010) 137–144

[34] N.K. Kanga, T.S. Juna, D-D. Laa, J.H. Ohb, Y.W. Choc, Y.S. Kim, Evaluation of the limit-of-detection capability of carbon black-polymer composite sensors for volatile breath biomarkers, Sensors and Actuators B: Chemical 147 (2010) 55–60

[35] X.M. Donga, R.W. Fua, M.Q. Zhangb, B. Zhanga, M.Z. Rong, Electrical resistance response of carbon black filled amorphous polymer composite sensors to organic vapors at low vapor concentrations, Carbon 42 (2004) 2551–2559

[36] B.C. Sisk, N.S. Lewis, Comparison of analytical methods and calibration methods for correction of detector response drift in arrays of carbon black-polymer composite vapor detectors, Sensors and Actuators B: Chemical 104 (2005) 249–268

[37] W. Zenga, M.Q. Zhangb, M.Z. Rongb, Q. Zheng, Conductive polymer composites as gas sensors with size-related molecular discrimination capability, Sensors and Actuators B: Chemical 124 (2007) 118–126

[38] J.P. Dakin, H.O. Edwards, B.H. Weigl, Progress with optical gas sensors using correlation spectroscopy, Sensors and Actuators B: Chemical 29 (1995) 87–93

[39] T.E. Brook, R. Narayanaswamy, Polymeric films in optical gas sensors, Sensors and Actuators B: Chemical 51 (1998) 77–83

[40] C. Massiea, G. Stewarta, G. McGregorb, J.R. Gilchrist, Design of a portable optical sensor for methane gas detection, Sensors and Actuators B: Chemical 113 (2006) 830–836

[41] M. Gall, The Si Planar Pellistor: a Low-power Pellistor Sensor in Si Thin-film Technology, Sensors and Actuators B: Chemical 4 (1991) 533-538

[42] M. Gall, The Si-Planar-Pellistor array, a detection unit for combustible gases, Sensors and Actuators B: Chemical 16 (1993) 260–264

[43] G. Williams, G.S.V. Coles, A study of tin-dioxide gas-sensor thermochemistry under conditions of varying oxygen partial pressure, Sensors and Actuators B: Chemical 25 (1995) 573–577

[44] N.T. Nagle, R. Gutierrez-Osuna, S.S. Schiffman, The How and Why of Electronic Noses, IEEE Spectrum 35 (1998) 22-31

[45] S. Pirsa, N. Alizadeh, Design and fabrication of gas sensor based on nanostructure conductive polypyrrole for determination of volatile organic solvents, Sensors and Actuators B 147 (2010) 461–466

[46] P.N. Bartlett, S.K. Ling-Chung, Conducting Polymer Gas Sensors Part III- Results for Four Different Polymers and Five Different Vapours, Sensors and Actuators 20 (1989) 287-292

[47] B-D. Parka, Y-S. Leeb, The effect of PEG groups on swelling properties of PEG-grafted-polystyrene resins in various solvents, Reactive & Functional Polymers 44 (2000) 41–46

[48] G.R. Ruschau, R.E. Newnham, J. Runt, B.E. Smith, 0-3 Ceramic/Polymer Composite Chemical Sensors, Sensors and Actuators, 20 (1989) 269-275

[49] B.J. Doleman, R.D. Sanner, E.J. Severin, R.H. Grubbs, N.S. Lewis, Use of Compatible Polymer Blends To Fabricate Arrays of Carbon Black-Polymer Composite Vapor Detectors, Analytical Chemistry 70 (1998) 2560-2564

[50] F.K. Che Harun, A.M. Jumadi, N.H. Mahmood, Carbon black polymer composite gas sensor for electronic nose, International Journal of Scientific & Engineering Research 11 (2011)

[51] M.C. Lonergan, E.J. Severin, B.J. Doleman, S.A. Beaber, R.H. Grubbs, N.S. Lewis, Array-Based Vapour Sensing Using Chemically Sensitive, Carbon Black-Polymer Resistors, Chemistry of Materials 8 (1996) 2298-2312

[52] Z. Hohercáková, F. Opekar, Au/PVC composite—a new material for solid-state gas sensors Detection of nitrogen dioxide in the air, Sensors and Actuators B 97 (2004) 379–386

[53] M.H. Al-Saleh, U. Sundararaj, A review of vapor grown carbon nanofiber/polymer conductive composites, Carbon 47 (2009) 2-22

[54] M. Wolf, R. Schmittgens, A. Nocke, D. Hecker, M. Liepelt, E. Schultheiß, Plasma deposition of conductive polymer composites for strain sensor applications, Procedia Chemistry 1 (2009) 879–882

[55] S.G. Wang, Qing Zhang, D.J. Yang, P.J. Sellin, G.F. Zhong, Multi-walled carbon nanotube-based gas sensors for NH3 detection, Diamond and Related Materials 13 (2004) 1327–1332

[56] K.H. An, S.Y. Jeong, H.R. Hwang, Y.H. Lee, Enhanced Sensitivity of a Gas Sensor Incorporating Single Walled Carbon Nanotube–Polypyrrole Nanocomposites, Advanced Materials 16 (2004) 1005-1009

[57] S.P. Khedkar, S. Radhakrishnan, Application of dip-coating process for depositing conducting polypyrrole films, Thin Solid Films 303 (1997) 167–172

[58] F. Zee, J.W. Judy, Micromachined polymer-based chemical gas sensor array, Sensors and Actuators B 72 (2001) 120-128

[59] F.K.C Harun, Mimicking the Human Olfactory System: A Portable e-Mucosa, PhD Thesis (2009)

[60] S. Kirkpatrick, Percolation and Conduction, Reviews of Moder Physics 45 (1973) 574-588

[61] F.K. Che Harun, J.E. Taylor, J.A. Covington, J.W. Gardner, An electronic nose employing dual-channel odour separation columns with large chemosensor arrays for advanced odour discrimination, Sensors and Actuators B 141 (2009) 134–140

[62] B.J. Doleman, M.C. Lonergan, E.J. Severin, T.P. Vaid, N.S. Lewis, Quantative Study of the Resolving Power of Arrays of Carbon Black-Polymer Composites in Various Vapor-Sensing Tasks, Analytical Chemistry 70 (1998) 4177-4190

[63] T. Iwaki, J.A. Covington, F. Udrea, J.W. Gardner, Identification and quantification of different vapours using a single polymer chemoresistor and the novel dual transient temperature modulation technique, Sensors and Actuators B 141 (2009) 370–380

[64] L. Niu, Y. Luo, Z. Li, A highly selective chemical gas sensor based on functionalization of multi-walled carbon nanotubes with poly(ethylene glycol), Sensors and Actuators B 126 (2007) 361–367

[65] M. Okazaki, K. Maruyama, M. Tsuchida, N. Tsubokawa, A Novel Gas Sensor from Poly(ethylene glycol)-Grafted Carbon Black. Responsibility of Electric Resistance of Poly(ethylene glycol)-Grafted Carbon Black against Humidity and Solvent Vapor, Polymer Journal 31 (1999) 672-676

[66] N.A. Lange, J.A. Dean, Lange's Handbook of Chemistry (Fifteenth Edition), McGraw-Hill New York (1999)

[67] A. Spietelun, M. Pilarczyk, A. Kloskowski, J. Namiesnik, Polyethylene glycol-coated solid-phase microextraction fibres for the extraction of polar analytes—A review, Talanta 87 (2011) 1–7

[68] Y.S. Kim, Microheater-integrated single gas sensor array chip fabricated on flexible polyimide substrate, Sensors and Actuators B: Chemical 114 (2006) 410–417

[69] M.L. Homer, J.R. Lim, K. Manatt, A. Kisor, L. Lara, A.D. Jewell, S-P.S.Yen, H. Zhou, A.V. Shevade, M.A. Ryan, Temperature effects on polymer-carbon composite sensors: evaluating the role of polymer molecular weight and carbon loading, Proceedings of IEEE Sensors 2003 2 (2003) 877-881

[70] T. Iwaki, J.A. Covington and J.W. Gardner, Identification of vapours using a single carbon black/polymer composite sensor and a novel temperature modulation technique, Proceedings of IEEE Sensors 2007 1-3 (2007) 1229-1232

Chapter 8

8 Microstereolithography for Ultrasonic NDE Applications

Ultrasonic non-destructive testing (NDT) is a means of measuring or examining the inherent properties or physical structures of components and materials without damaging or destroying the sample. Commonly, a transducer is used to generate a high frequency burst of sound which then interacts with the sample before being received either by the same transducer (in the case of pulse-echo inspection) or by another device. The method can be used as an inspection technique [1] to detect cracks [2] and defects in materials or their interfaces (such as weld joints), or can be used to image the surface [3, 4] of a sample. Imaging can be achieved either by using large arrays of devices, or by scanning smaller arrays or a single transducer in pulse-echo mode over the sample surface.

Ultrasonic non-destructive evaluation (NDE) applications [5-7] often require a focused beam of ultrasound to accurately analyse or image small features on samples. A transducer can be defined as a focusing device if the diameter of the beam emitted is condensed to a diameter which is less than the diameter of the transducer. A focused beam increases both lateral resolution and intensity which results in an improved ability to resolve features of interest. The transducer used in each application will generally be chosen such that it is optimally suited in terms of frequency, dimensions, bandwidth and focus. As such, it is often the case that while one transducer may be suitable for one application, it may not be suited to the next and so a different device would be required. Therefore, laboratories and test houses which work in the ultrasonic non-destructive testing (NDT) field require a significant number of different devices to ensure that for any given application a suitable device is available.

While there is a wide range of commercially available single element ultrasonic transducers available on the market which are suitable for applications involving inspection via pulse-echo immersion, keeping a suitably wide stock of devices represents a significant investment (as single transducers can cost >£100). However, the number of devices required could be significantly reduced by making use of an additional, bespoke beam forming element attached to the end of a standard unfocused transducer – a method not previously described in the literature.

Previous work has demonstrated the use of microstereolithography for fabricating capacitive air coupled transducers with some success [8]. This chapter instead investigates the feasibility of using microstereolithography as a rapid manufacturing technique for fabricating bespoke beam-forming devices for mounting onto the end of a standard, unfocused immersion ultrasonic transducer in order to enable it to be used in variety of non-destructive evaluation (NDE) applications.

The first section covers the design theory behind the device, this is then followed by a discussion of the fabrication of the device. The next sections cover characterisation experiments to map the output field of the device and to test its ability to be used as an imaging device to investigate the use of MSL fabricated devices for ultrasound for use in NDE applications. Parts of these sections were presented in poster format and as a conference paper [9] at the IEEE International Ultrasonics Symposium 2011 and have also been submitted as a journal paper [10]. The final section covers investigation for future improvements through the use of alternative materials.

8.1 Background

Sound can be described as a wave of pressure or change in molecular density that propagates through a medium, be it solid, liquid or gas. Humans and other animals can perceive sound waves by detecting the vibrations caused by these waves. It is generally acknowledged that for humans, the frequency of wave that can be detected is limited to a band ranging from approximately 20 Hz up to 20 KHz. Any frequency above 20 KHz is considered to be "ultrasonic".

As the sound wave propagates through a medium the speed of propagation of the vibrations (c) is determined both by the frequency of the vibration (f) of the particles in the medium and their wavelength (λ) as shown in Equation 8.1.

$$c = f\,\lambda \tag{8.1}$$

The acoustic resistance or characteristic acoustic impedance (Z) of a medium is determined by the density of the medium (ρ), and the sound speed (c) – the velocity of the wave through the medium. This is shown in equation 8.2.

$$Z = \rho\, c \tag{8.2}$$

When a wave meets an interface between its current medium and the next which has a different acoustic impedance (Figure 8.1), a proportion of the energy will be transmitted into the next medium and a proportion will be reflected. The acoustic impedance of a medium is required when calculating the likely reflection or transmission of a wave when it encounters the interface. Equations 8.3 and 8.4 describe these transmission (T) and reflection (R) coefficients at normal incidence, where (Z_1) is the acoustic impedance of the current medium and (Z_2) is that of the next [11].

$$T = \frac{4Z_1Z_2}{(Z_1+Z_2)^2} \tag{8.3}$$

$$R = \left(\frac{Z_1-Z_2}{Z_1+Z_2}\right)^2 \tag{8.4}$$

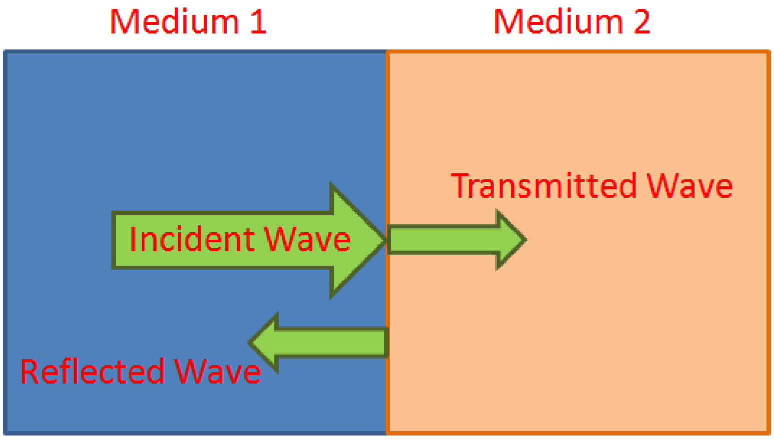

Figure 8.1 – Diagram illustrating transmission and reflection of an incident wave normal to the interface with two medium

Interference within the field causes a series of maxima of pressure amplitude to occur. The nearfield limit is the axial distance from the face of the transducer where the last pressure maximum occurs. Equation 8.5 describes the relationship between the nearfield limit (N) and the properties of the source (assuming the source is circular) – the radius of the source (r) and the wavelength in the medium (λ).

$$N = \frac{r^2}{\lambda} \tag{8.5}$$

8.2 Design

A number of designs were considered for the device including using an off-axis parabolic mirror [12], and a number of variations based on optical telescopes such as Cassegrain, Gregorian and Newtonian [13]. It was decided that the device would be based around the design of a Cassegrain reflector, this was because the off axis parabola and Newtonian varieties result in the focus not being located along the primary axis which was felt to add an unnecessary extra degree of complexity to this first design. The Gregorian style of focusing device was also considered, however, as it requires the beam to converge and then diverge between the primary and secondary reflector, there were concerns about the path length of the beam and the ability to keep the final focus within the nearfield region.

In a Cassegrain reflector, the primary reflecting surface has a concave shape with a parabolic profile. Its profile is such that the focal point lies at a point behind the secondary reflecting surface. The secondary, convex reflecting surface has a hyperbolic profile which serves to re-focus the converging wave front from the primary reflector to a final focal point behind the primary reflector. Using this configuration, the planar wave front being emitted from an ultrasound transducer can also be focused down to a point (Figure 8.2).

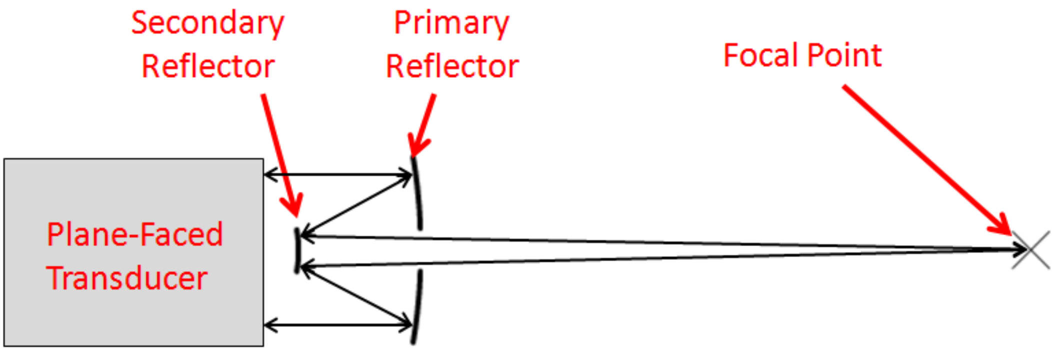

Figure 8.2 – Schematic diagram of illustrating the principal of operation of a focusing device based on a Cassegrain reflector

8.2.1 Theory of Focusing

The following equations can be used to generate the necessary parameters for a desired geometrical focus (note that this is not necessarily the same as the actual acoustic focus – discussed later). Below are the standard equations for defining the profile of a parabola (Equation 8.6), along with the location of its focal point f (Equation 8.7), and the profile of a hyperbola with a y-intercept at +/- a (Equation 8.8).

$$y_p = gx^2 \tag{8.6}$$

$$f = \frac{1}{4g} \tag{8.7}$$

$$\frac{{y_h}^2}{a^2} - \frac{x^2}{b^2} = 1 \tag{8.8}$$

For an equilateral (or rectangular) hyperbola where the 2 theta between the asymptotes is 90 degrees, $b = a$. So re-arranging for y then gives Equation 8.9.

$$y_h = a\sqrt{1 + \frac{x^2}{a^2}} \tag{8.9}$$

A theoretical hyperbolic function has two curves and, as such two focal points, a front and a rear. The distance between either of the focal points and the origin is c. The distance between the origin and the two y-intercepts are a and b, their relationship is shown in Equation 8.10. However, since it was previously stated that $b = a$, this can be simplified (Equation 8.11).

$$c = \sqrt{a^2 + b^2} \tag{8.10}$$

$$c = a\sqrt{2} \tag{8.11}$$

In order for the system to focus correctly the focal point of the parabola (f) and the rear focal point of the hyperbola (c) are coincident, this can be achieved by offsetting one from the other (Equation 8.12). The origin of the hyperbola can then be offset from that of the parabola by a distance d as shown Equation 8.13.

$$f = c + d \tag{8.12}$$

$$y_h = a\sqrt{1 + \frac{x^2}{a^2}} + d \tag{8.13}$$

If i and j are then defined as the distance between the two curves and the distance between the parabola and the system focus respectively at $x = 0$, then Equations 8.14 and 8.15 can be defined. Substituting Equation 8.11 into Equation 8.15 then gives Equation 8.16.

$$d = i - a \tag{8.14}$$

$$i + j = a + c \tag{8.15}$$

$$a = \frac{i+j}{1+\sqrt{2}} \tag{8.16}$$

Substituting Equations 8.12, 8.14 and 8.16 into Equations 8.6 and 8.123 then gives final defining equations for both the parabolic and hyperbolic surfaces given only the distances for required separation between the two surfaces at $x = 0$ and the desired final focal point relative to the primary mirror. These are shown in Equations 8.17 and 8.18 respectively. Figure 8.3 shows the relationship of the parameters mentioned.

$$y_p = \frac{x^2}{4\left[i+\frac{i+j}{1+\sqrt{2}}\left(\sqrt{2}-1\right)\right]} \tag{8.17}$$

$$y_h = i + \frac{i+j}{1+\sqrt{2}}\left[\sqrt{1+\frac{x^2}{\left(\frac{i+j}{1+\sqrt{2}}\right)^2}} - 1\right] \tag{8.18}$$

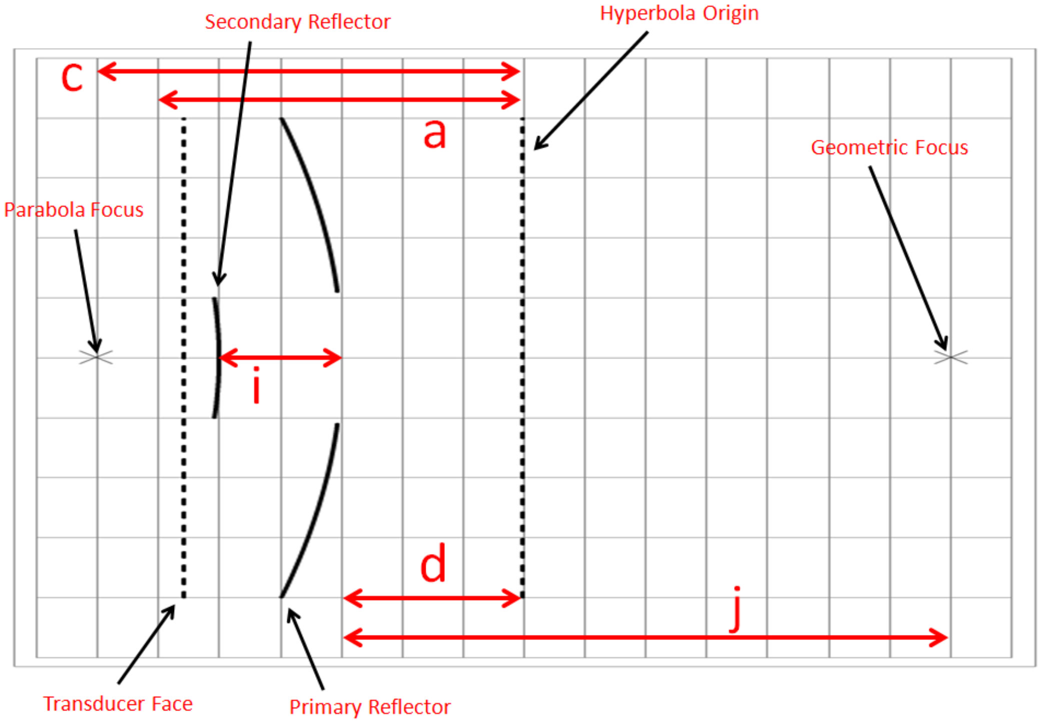

Figure 8.3 – Schematic diagram showing the key dimension of the design for the focusing device

It should be noted that, as with commercially available focused transducer devices, the geometric focal point is not the same as the actual acoustic focus that would be seen when the device is used in a test medium. However, as with commercially available focused devices, when used in a test medium, the geometrical focus deviates from the actual focus (the location of maximum pressure point) due to divergence of the field due to diffraction.

Huygens' principal [14] states that the wavefront of a propagating wave conforms to the envelope of the set of spherical wavelets formed at every point on the wavefront at the previous time instant. Fresnel [15] later furthered the work and stated that the amplitude of the wavefront at any point is equal to the superposition of the amplitude of all the wavelets present at that point which were formed at the previous time instant. This explains diffraction of the wavefront and divergence of the field. The specific geometry of the field is dependent on a number of factors including the transmission medium, the geometry of the source and the frequency of the signal. The divergence angle of the field, θ, about its mean path is approximately proportional to the ratio of the signal's wavelength, λ, to the diameter of the aperture of the source, D (Equation 8.19) [16].

$$\sin\theta \approx 1.22\,\frac{\lambda}{D} \tag{8.19}$$

The focal length is dependent on the acoustic velocity, and therefore the nearfield limit, N of the medium the device is being used in. Previous work [17-19] has detailed an equation that provides an approximation of the position of the focus along the beam axis, Equation 8.20.

$$p = \left| \frac{2}{1-\frac{x}{F}} \sin\left(\frac{N\pi}{2x}\left(1-\frac{x}{F}\right)\right) \right| \tag{8.20}$$

When plotted, the focal point occurs where p (relative pressure) is at its maximum – indicated by the dashed lines in Figure 8.4. Figure 8.4 shows typical plots of pressure amplitude with increasing axial distance and shows the boundary between near and farfield regions. After the last maxima, the amplitude will decrease to zero and so beyond this point the divergence of the beam prevents focusing. The distance at which this occurs is dependent on the wavelength of the acoustic signal and the diameter of the source. Therefore, the slower the speed of sound in the medium, the closer the actual focus will be to the geometric focal point. As there is no closed form solution for calculating what geometric focal length should be used in order to provide the desired actual focal length in a given medium, geometric foci for designs were found iteratively using software until the parameters for the desired focal length were found.

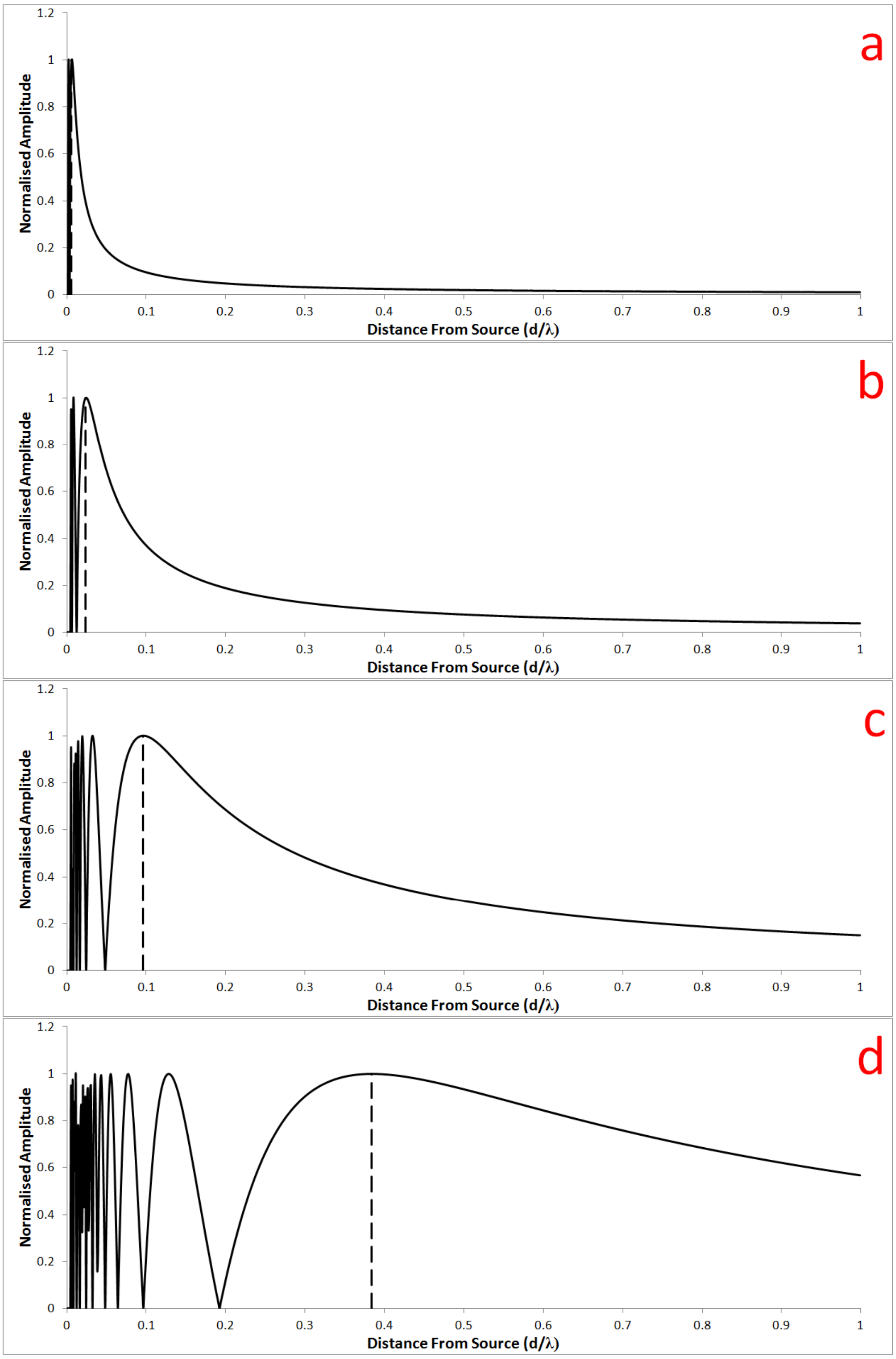

Figure 8.4 – Plots of normalised axial pressure for transducers with circular elements with diameters of (a) 4, (b) 8, (c) 16, and (d) 32 wavelengths

8.2.2 Calculating Parameters

As some of the key parameters for designing the system were dependant on the source of the ultrasound, the transducer's output frequency and field diameter were first measured. The transducer used was a Panametrics ½" diameter V311-SU immersion transducer with a nominal centre frequency of 10 MHz. In order to make the necessary measurements, the transducer was first clamped inside an immersion tank using a retort stand and clamp. A needle hydrophone with a 200 μm tip was then mounted on an XY motion stage. The motion stage allowed for automated movement of the hydrophone's tip in a plane parallel to the face of the transducer. Figure 8.5 shows the setup used.

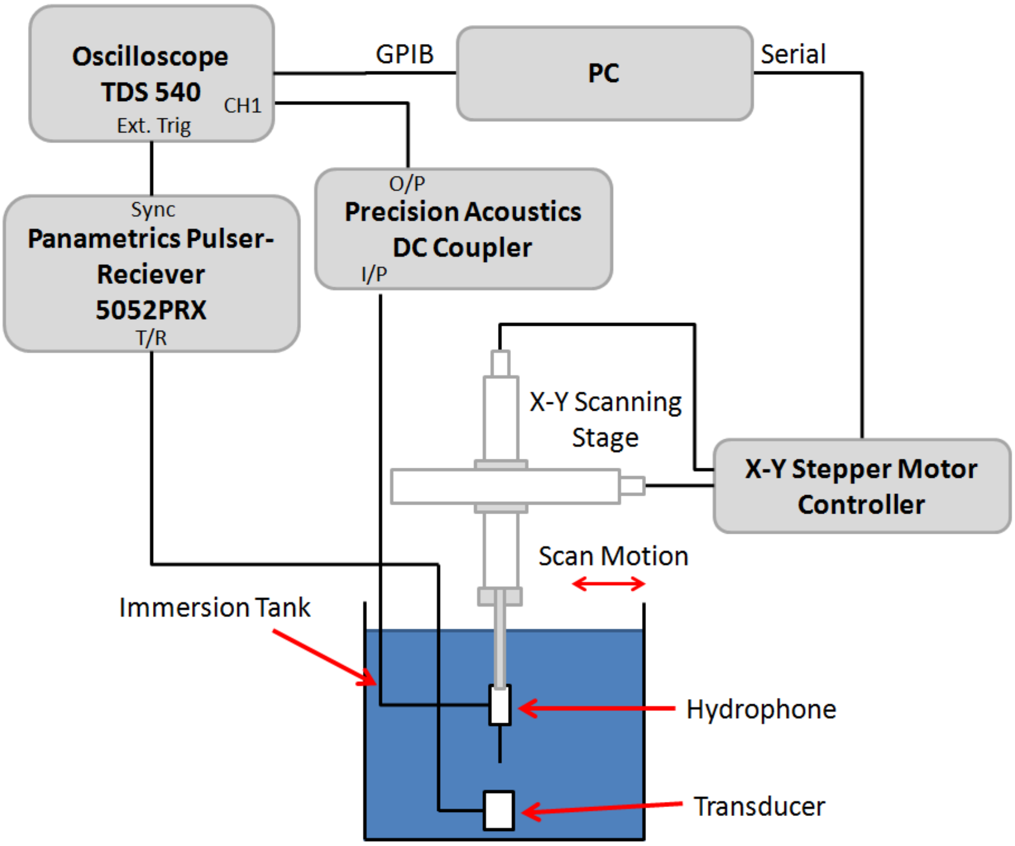

Figure 8.5 – Schematic diagram showing experimental setup for measurement of transducer parameters

The diameter of the field being emitted from the transducer was then measured. As the initial horizontal alignment was only done by eye, a number of line scans were taken either side of the initial scan to ensure that centreline was found. The scan was repeated 3 times at an offset of 0.5 mm and an additional 3 times at 90 degrees rotation with the same offset such that an average could be taken and any significant variation in diameter could be accounted for. The scanning process was automated using a program written in LabView (National Instruments, USA) which moved the hydrophone to the desired measuring point using the motion stage and then sent a request to the oscilloscope (Tektronix TDS 540) over a GPIB (general purpose interface bus) to make an acquisition and send the data back. The data from each of the points was then saved for processing and analysis at a later date. The raw data was then processed and exported using a further program written in LabView. Figure 8.6 show the result of the bare transducer scan. The diameter of the field was then measured at the full width half maximum as 12.5 mm +/ 0.2 mm.

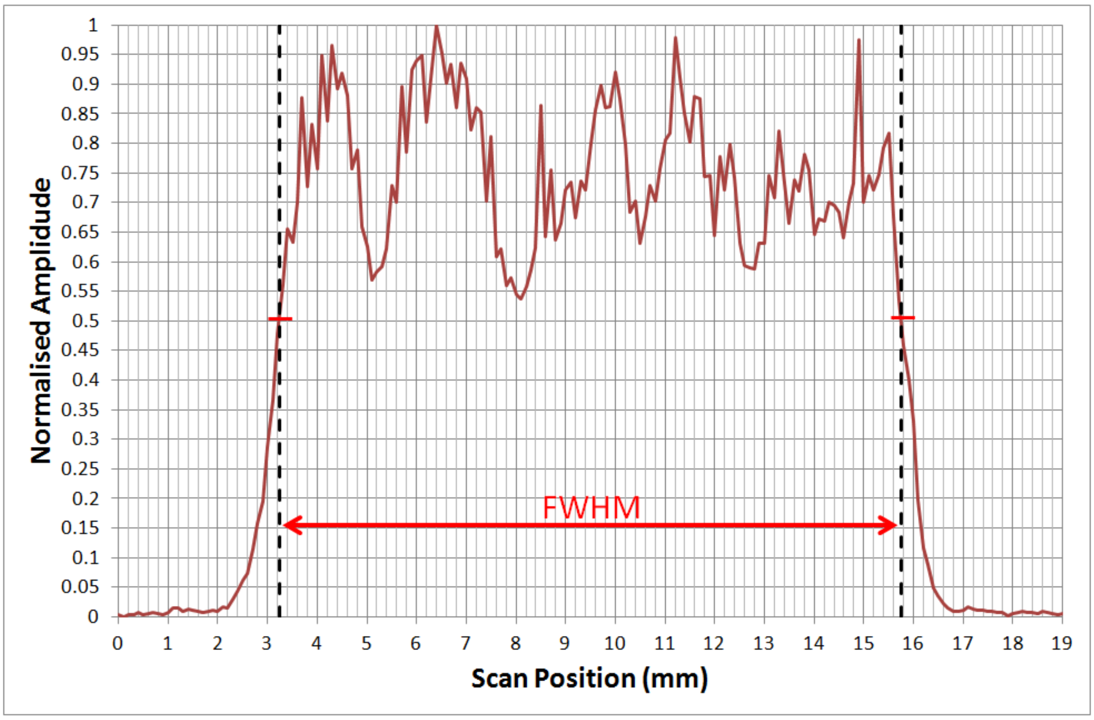

Figure 8.6 –Line scan of the radial cross section of the unfocused transducer at an axial distance of 0.5mm from the transducer face

In order to calculate the nearfield distance, N, of the transducer, the output frequency of the device was measured. This was done using a Tektronix TDS 3032C oscilloscope with the hydrophone and found to be ~9.6 MHz - Figure 8.7 shows the acquired FFT. However, when calculating N, it also had to be considered that, the secondary reflector and supports would partially obscure the transducer's output. Therefore, the effective radius of the transducer becomes a function of both the diameter of the transducer (d_T), the diameter of the secondary reflector (d_S) and the area of its supports as shown in Equation 8.21. Where d_I is the inner diameter of the body of the focusing device, n is the number of supports for the secondary reflector and w is the width of the supports.

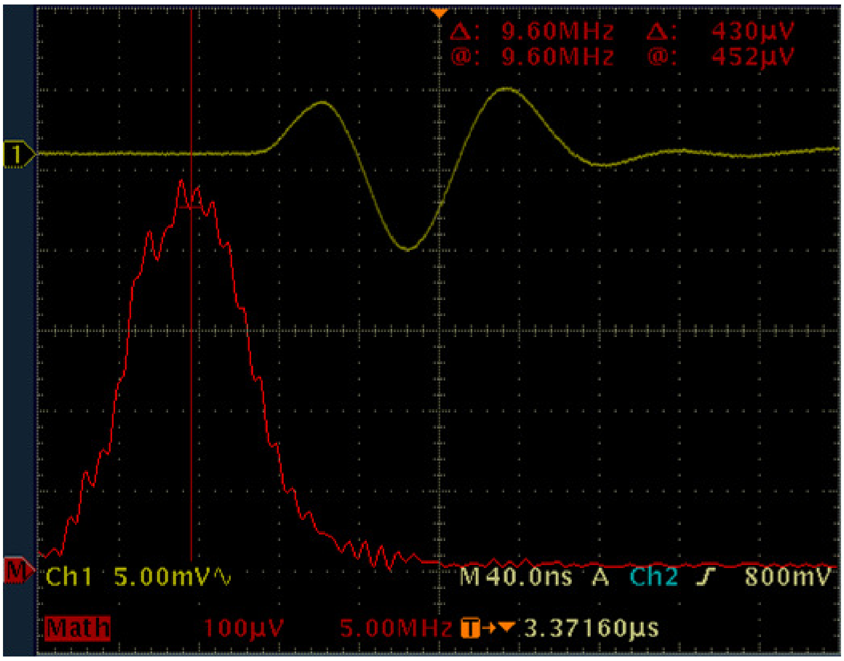

Figure 8.7 – FFT measurement of the transducer's nominal centre frequency

$$N = \frac{\pi\left(\frac{d_T}{2}\right)^2 - \pi\left(\frac{d_S}{2}\right)^2 - n\left(\frac{d_S - d_I}{2}\right)w}{\pi\lambda} \tag{8.21}$$

To keep the design compact, it was decided that the separation between the two reflecting surfaces (i) would be 10 mm and that the location of the final acoustic focus should be approximately 10 mm behind the primary reflector. In order to achieve this, a geometric focus (j) of 50 mm was used, giving a final focus at 9.6 mm behind the primary reflector. The design then has a nearfield distance of approximately 64 mm with a total focal length of 42.6 mm (Figure 8.8).

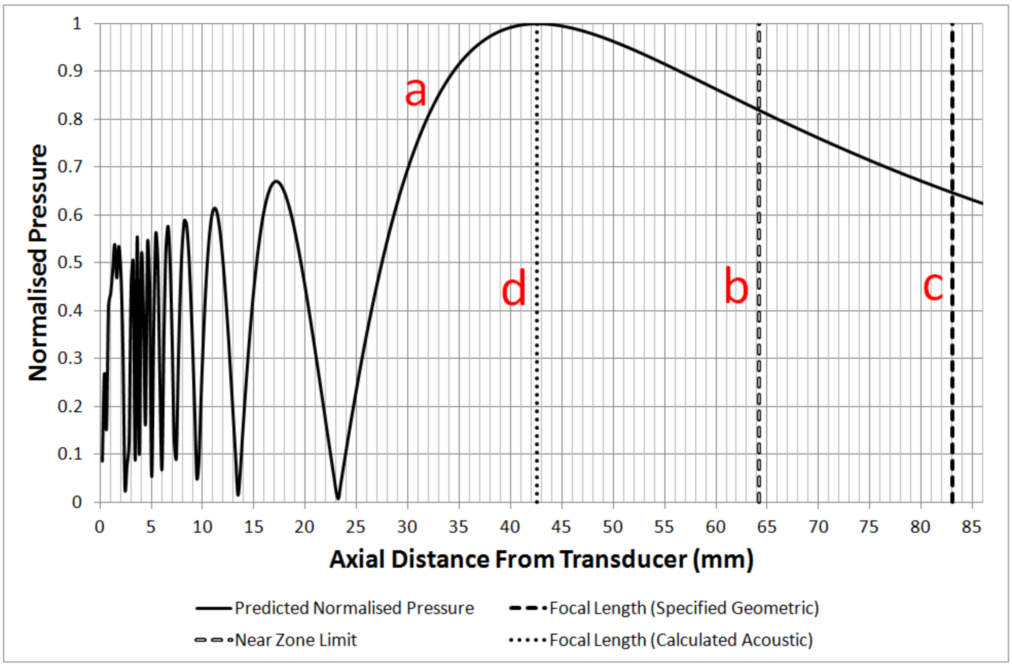

Figure 8.8 – Graph showing normalised axial pressure plot showing (a) predicted normalised axial pressure amplitude, (b) the calculate near zone limit, (c) the specified geometric focus, and (d) the expected acoustic focal length

8.3 CAD Design and Fabrication

Using the equations previously detailed, the parameters required to generate the surfaces can be used to calculate the coefficients g, a and d for Equations 8.7 and 8.12. The resulting coefficients are shown in Table 8.1.

Coefficient	Value
g	0.012
a	24.85
d	-14.86

Table 8.1 – Calculated coefficients for primary and secondary reflecting elements

The surfaces were then modelled using the equation driven curve tool in SolidWorks 2009 (Dassault Systèmes, France) CAD package and a supporting structure designed around them. The support structure was designed to maintain the correct distance between two surfaces to ensure correct operation. The device was also designed such that it could be mounted directly onto the end of the Panametrics transducer. As the device was to be used in an immersion tank, a series of six 2.5 mm holes were included in the design around the main body of the device. The holes were to ensure that the immersion fluid filled the entire cavity without having to assemble the device onto the transducer post-immersion.

Care also had to be taken when considering how the device would be fabricated. Typically, when fabricating components using MSL technologies it is usually favourable to align any faces which require a high quality final surface finish such that they are parallel to the build platform and fabricated last. This is due to the poorer surface finish on off-axis faces. However, in the case of the focusing device there are two such faces (the primary and secondary reflectors), indeed as these faces were directly opposite and facing each other, it would require that both of the faces be supported with an temporary support structure (Figure 8.9). While the use of a support structure behind the secondary mirror would not present a problem, the second support would be required to be in contact with the faces of both the primary and secondary reflectors (show in by the red circled areas on Figure 8.9). This would have severely compromised the surface finish of the face. As such it was necessary to design the device such that it would be fabricated in 2 (or more) parts.

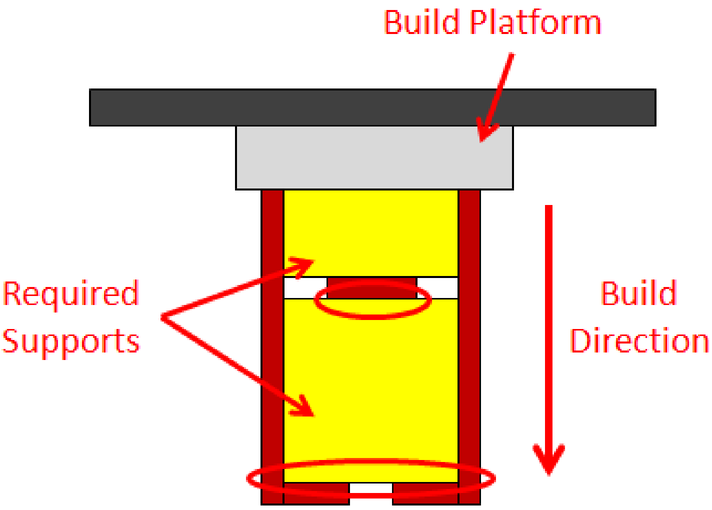

Figure 8.9 – Diagram illustrating the use of required support features if the focusing device were to be fabricated as one component. The circled regions highlight areas where the support structure would damage the reflecting surfaces.

The final design was split into 3 component parts consisting of the primary and secondary reflectors and a spacer ring which included the 6 filling holes. The component with the secondary reflector also included the additional ring necessary to mount directly onto the transducer. Figure 8.10 shows the component parts.

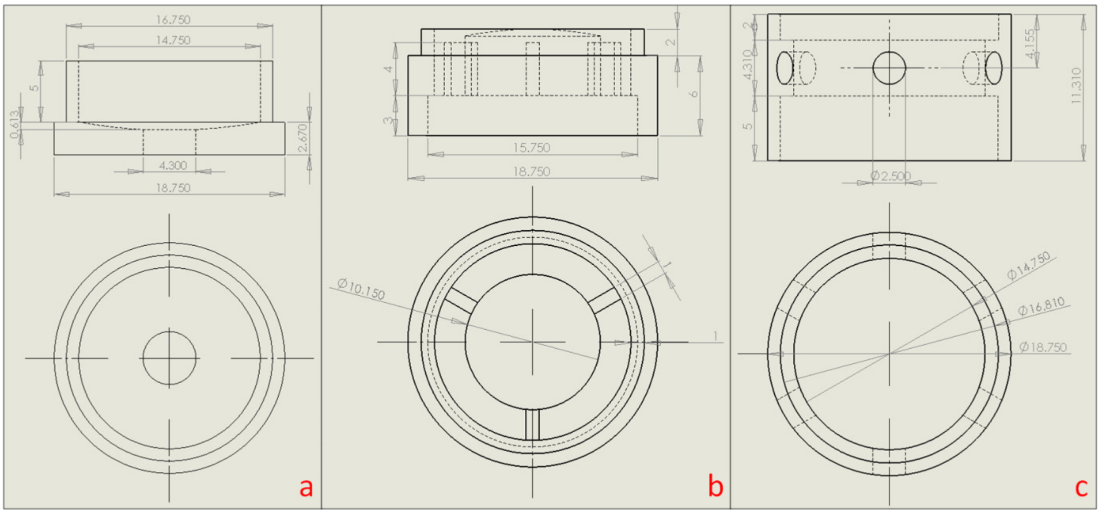

Figure 8.10 – Schematic diagrams of the components of the focusing device: (a) primary reflector, (b) secondary reflector with transducer mount, and (c) spacer ring (dimensions in mm)

The device was fabricated with the Perfactory Mini D (EnvisionTec GmBH, Germany) system using R11 photopolymer material in 50 µm voxel layers for the spacer ring (as the definition of its features was not critical) and 25 µm voxel layers for the others. This system was chosen for fabrication as it has an ERM (enhanced resolution module) which can be used to improve edge definition (discussed previously) and can cure layers of R11 faster than the custom system due to higher intensity exposure field. The fabrication process settings were kept at the manufacturer's suggested standards for R11 with the exception that the exposure time for standard layers was increased to 9.5 seconds (the same duration as the burn in range) to prevent delimitation effects. Table 8.2 details the build settings used and the total fabrication times for the component parts.

Component	**Primary**	**Secondary**	**Spacer**
Component Height (mm)	7.67	8	11.31
Layer thickness (µm)	25	25	50
Number of Layers	307	320	226
Exposure time (s)	9.5	9.5	9.5
Separation (mm)	5	5	5
Peel speed (mm/s)	0.8	0.8	0.8
Levelling speed (mm/s)	0.8	0.8	0.8
Wait time after level (s)	2	2	2
Wait time after peel (s)	1	1	1
Total build time	2h 8m	2h 13m	1h 34m

Table 8.2 – Fabrication settings and times for components of focusing device fabricated using MSL

As the process fabricates components with a discrete number of layers, each of a finite thickness, the curves of the reflecting surfaces were not smooth. Instead they consisted of a number of layers where the step size was equal to one layer thickness, which form a close approximation to the desired curve (Figure 8.11).

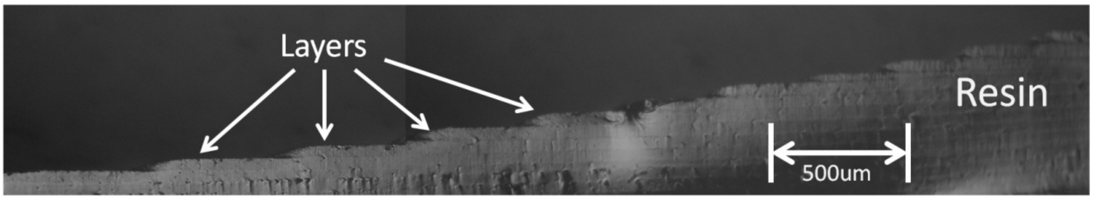

Figure 8.11 – Microscopy image of the cross section of an MSL fabricated primary reflector using 50 µm layers with the continuous curved profile being approximated by a finite number of layers

After the individual components were fabricated, they were rinsed with acetone to remove any excess uncured resin and blotted dry on paper towel before being post-cured in a UV flash box (Otoflash G171, NK-Optik GmbH) for 1000 flashes. The individual components (Figure 8.12(a)) were then adhered together using a standard cyanoacrylate based adhesive. The completed device, mounted to the end of the transducer is shown in Figure 8.12(b).

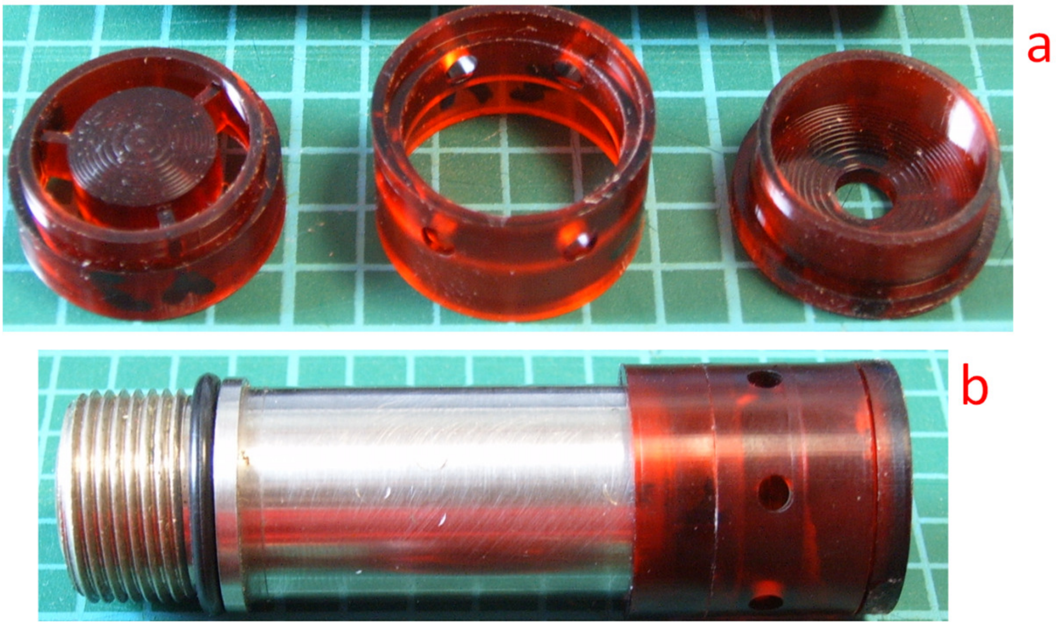

Figure 8.12 – Photographic images of (a) MSL fabricated component of focusing device, (b) assembled components mounted onto the end of the host transducer

8.4 Testing

In order to test the device, two sets of experiments were conducted. The first were to characterise the function and output of the device and compare to the original design. The second experiment was with the device being used in pulse-echo mode to investigate the device's performance in a typical imaging test.

For all the experiments discussed in this section the ultrasonic transducer used was a plane-faced broadband Panametrics ½" diameter V311-SU immersion transducer with a nominal centre frequency of 10 MHz. The transducer was driven using a Panametrics 5052PRX pulser-receiver, and a Precision Acoustics needle hydrophone with a 200 µm diameter tip was used for measuring the output of the device. A custom X-Y scanning stage with an accuracy of 5 µm and a manual Z height adjustment was mounted over the test tank. This was used to accurately position the hydrophone in order to produce 2D contour plots. A Tektronix TDS 540 oscilloscope controlled over a GPIB interface was used to record the detected signal. The system was automated using custom software written using National Instruments LabView.

8.4.1 Device Characterisation

The first test conducted on the device was to measure the axial distance of the focal point of the system from the device. This was achieved by mounting the focusing device onto the transducer and taking a series of X-Y plane scans parallel to the device's face at increasing axial distances (z-axis) starting with an initial offset of ~1 mm. To do this, the apparatus was setup as shown in Figure 8.13.

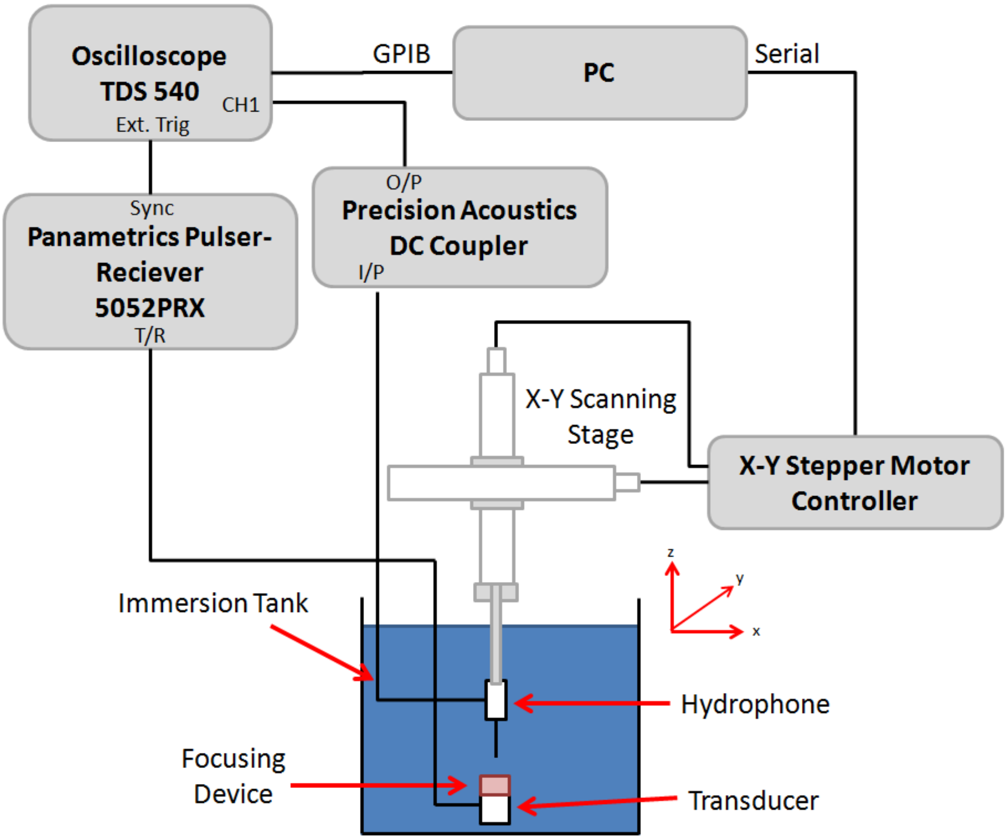

Figure 8.13 – Schematic diagram showing experimental setup for characterisation of focusing device

The movement of the hydrophone was such that centre of each X-Y scan was approximately centred about the output from the device. Each scan was 5 mm x 5 mm with a resolution of 250 µm/point (Figure 8.14). The maximum value from each scan was then plotted until a clear peak in the maxima was observed. Figure 8.15 shows the results obtained along with the normalised pressure curve from Equation 8.20 fit to the data.

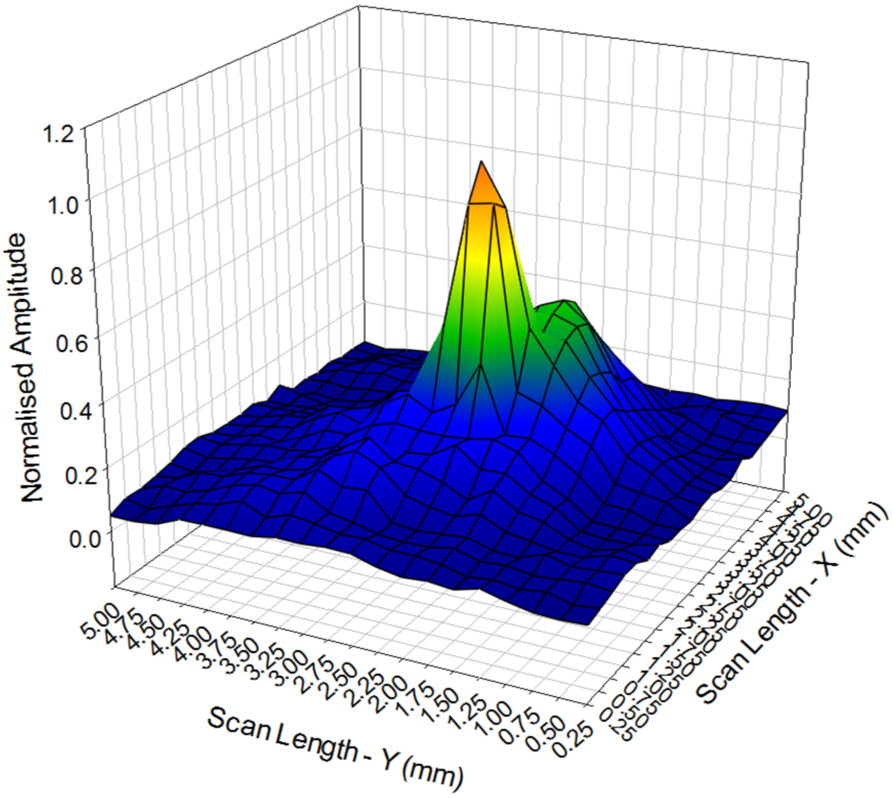

Figure 8.14 – 3D plot showing a sample measurement of the beam profile

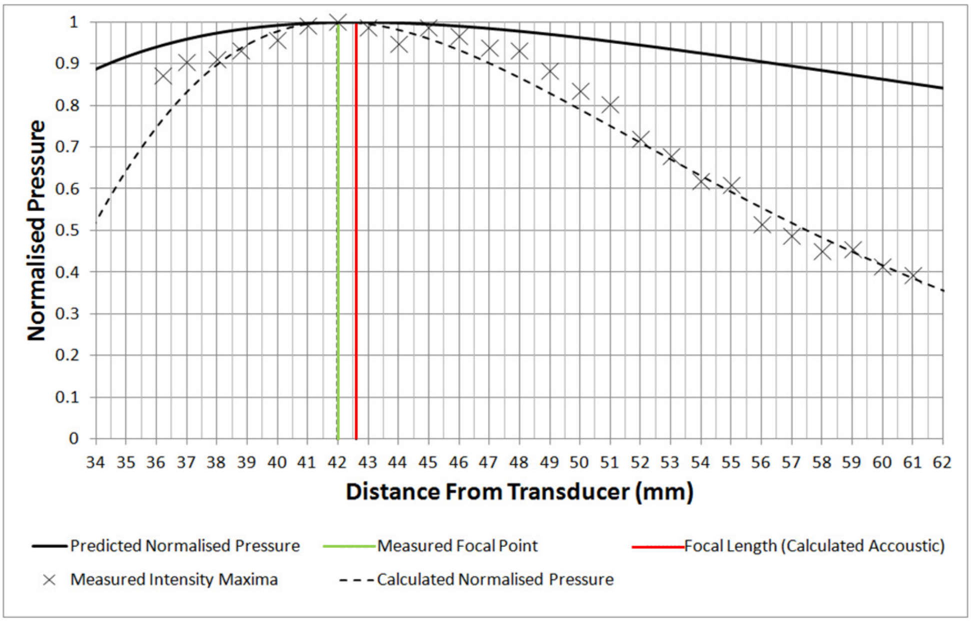

Figure 8.15 – Axial normalised pressure plots generated from initial design calculations and from maximum intensity measurements extracted from plane scans

From these scans it was discovered that the focal point of the system was at a distance of 8 mm (+/- 0.2 mm) from the back surface of the device. When taking into account the thickness of the material behind the primary reflector (1 mm) this then gave a total focal length of 42 mm which was a deviation of 1.4% from the calculated focal length of 42.6 mm which was considered to an acceptable error. Having located the position of the focal point, a finer resolution X-Y scan was then taken across the focal plane in order to measure the extent of the focus of the device (Figure 8.16). By extracting the horizontal and vertical lines that pass through the maximum point, the diameter of the focal spot can be measured along with profile of the intensity around the point. Figure 8.16 shows that the diameter of the focal spot at full width half maximum was measured to be 580 μm (+/- 10 μm).

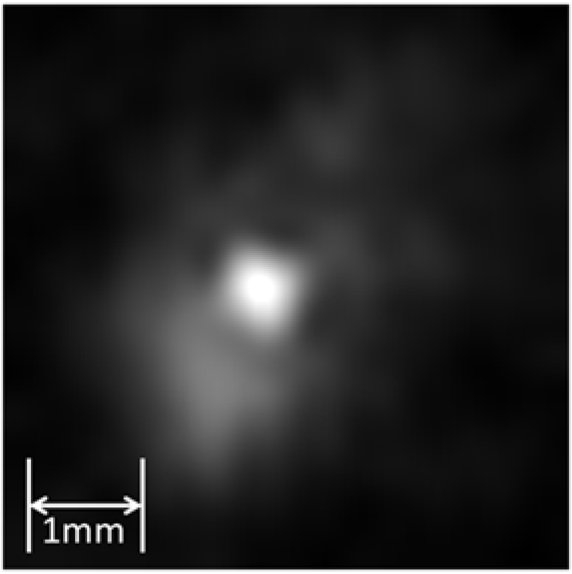

Figure 8.16 – Plot showing beam profile at focal plane

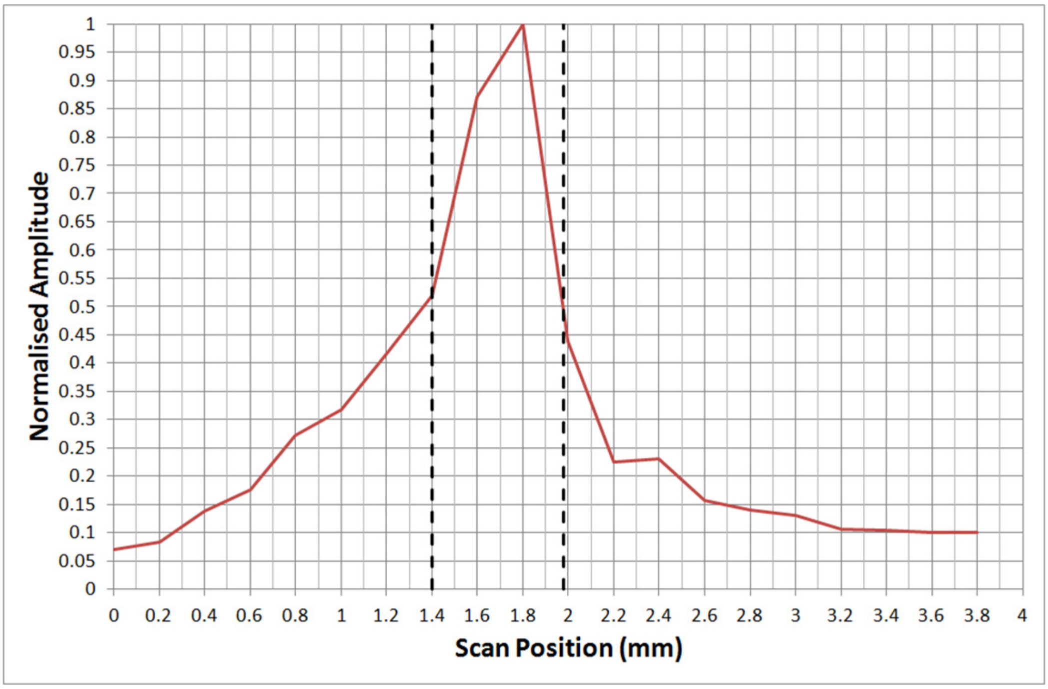

Figure 8.17 – Graph of radial line scan through focus maxima on focal plane

8.4.2 Imaging Using the Focusing Device

Once the location of the focal plane had been verified, the test apparatus was reconfigured such that the system could be used in pulse-echo mode for imaging the surface of a coin (Figure 8.18). Initially, the received signal (Figure 8.19) contained a number of other unexpected responses. It was discovered that the majority of the significantly sized extra responses were due to multiple reflections within the device as their position was unaffected by either repositioning of the target or by disturbances in the surface of the test medium.

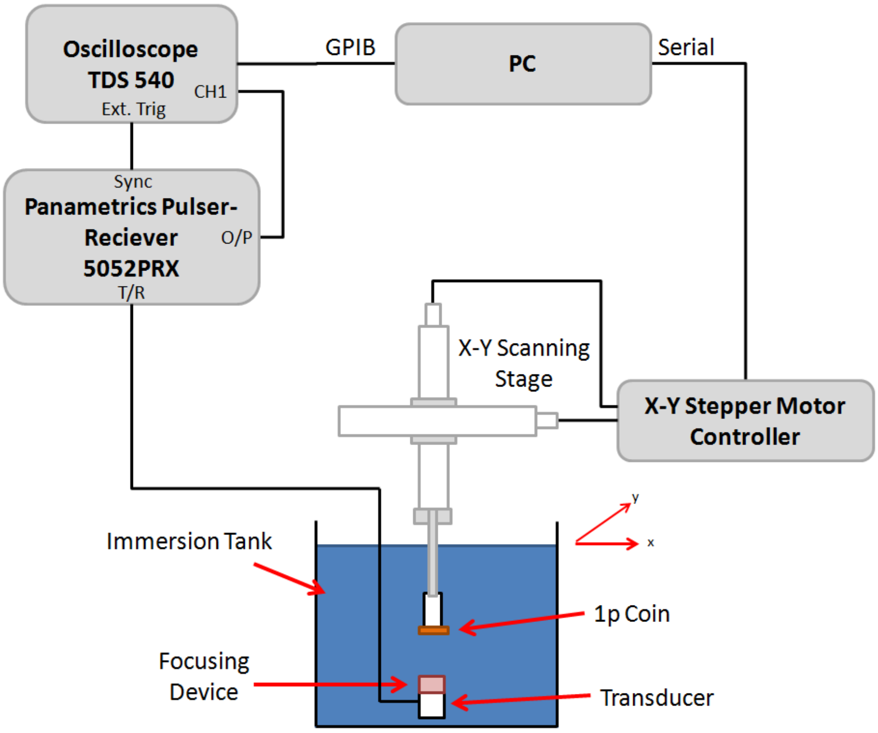

Figure 8.18 – Schematic diagram showing experimental setup used for pulse echo mode imaging of a coin using transducer with focusing device

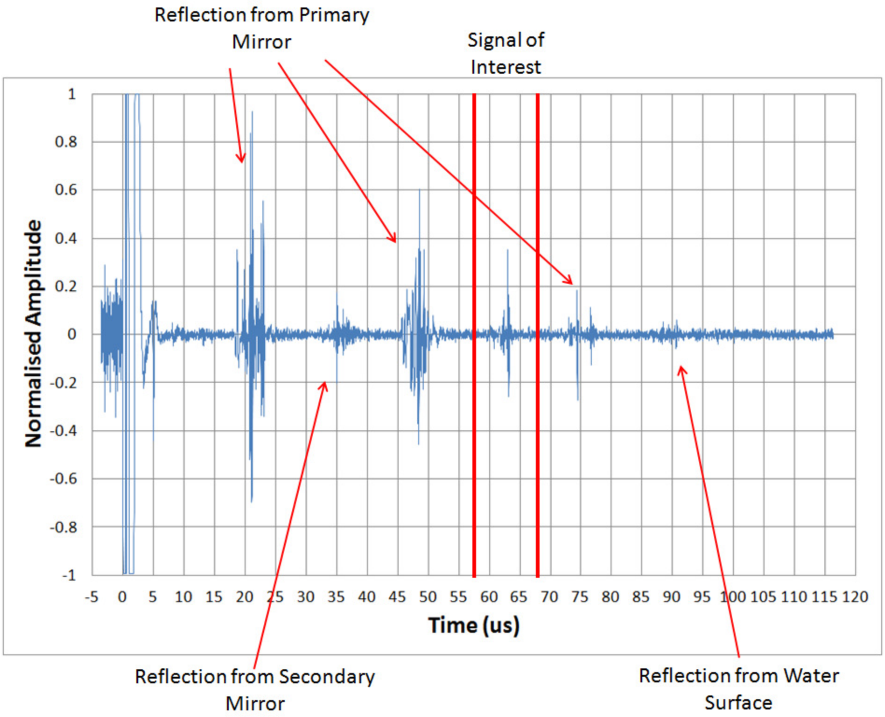

Figure 8.19 – Plot showing an example of a typical recorded signal including responses generated from multiple reflections within the focusing device

The extra responses occurred primarily from pulses reflecting from the rear of the secondary mirror which is located < 500 µm from the face of the transducer. Additional responses were thought to be caused by stray interferences due to the imperfect approximation of the reflection surfaced due to the fabrication procedure. A number of the smaller artefacts in the received signal were found to be caused by transmission into, and multiple reflections within, the part. Therefore, care had to be taken during processing of the data when used in pulse-echo mode to ensure that the areas of data representing reflections from the target were windowed out from signals generated by other reflections.

Scans were taken of both the front and rear of the coin (Figure 8.20(a)) and are shown in Figures 8.20(b) and 8.20(c). The darker areas seen on the plots were caused by air bubbles collecting on the surface of the coin during scanning. Additionally, the stripe artefacts seen in Figure 8.20(c) are thought to be due to the scan being conducted at a lower resolution and slight backlash in the lead screw of the motion stage.

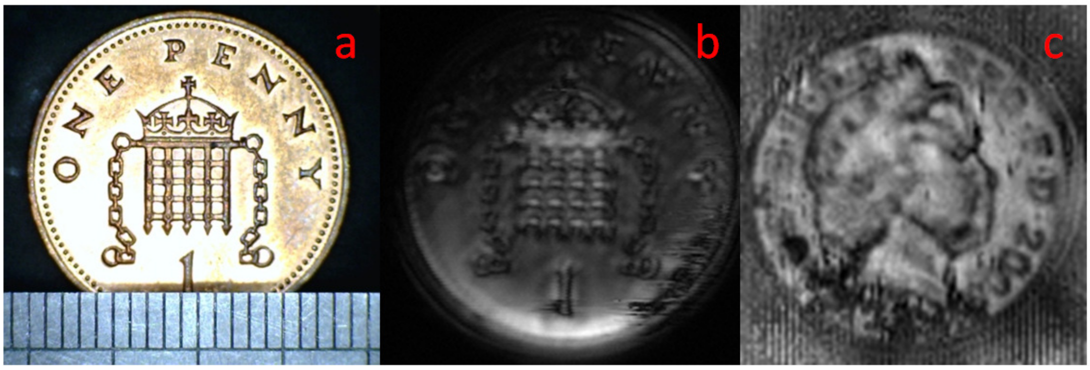

Figure 8.20 – (a) photographic image of UK 1p coin with additional plots generated from pulse echo scanning of (b) reverse and (c) front face using transducer with focusing device

8.5 Possible Improvements Using Alternative Materials

While the results of the device fabricated using R11 as a fabrication material demonstrate that the device functions, it is apparent that a significant amount of the signal is lost. The losses are primarily due to the transmission of the signal through the material. In an ideal situation, the material would be such that all of the signal would be reflected without any losses due to unwanted transmission or absorption. However, in practice, a more realistic aim is to use a material that has an increased reflection coefficient while absorbing any of the signal that is not reflected such that the amplitude of the received signal is greater. Therefore, while conducting work with the materials discussed in previous chapters, samples of the materials were produced to investigate the acoustic properties with a view to investigating whether any would exhibit properties that would be advantageous for ultrasound applications.

An additional sample was also made which incorporated a hollow micro-sphere material commercially known as Expancel (Akzo Nobel N.V., The Netherlands). Expancel micro-spheres are ~5-10 µm diameter gas filled polymer spheres that expand up to 5 times their initial size when heated to ~70°C. The Expancel samples tested were made by adhering a 0.5 mm thick layer to the reverse side of an R11 sample with 25 µm layers.

The samples were all designed to be fabricated to be 10 mm x 10 mm with a thickness of 1 mm. Table 8.3 shows the measured dimensions and weight of each sample along with an additional sample which was a section of aluminium sheet that was also measured for reference. The test apparatus was setup as in Figure 8.21. The pulser-reciever module was setup such that the transducer was being operated in pulse echo mode. The transducer used was the same plane-faced broadband Panametrics ½” diameter V311-SU immersion transducer with a nominal centre frequency of 10 MHz as used previously. The signal from both the hydrophone and transducer were recorded using a Tektronix DPO3034 oscilloscope. Both the time of flight and amplitude of the signals were recorded. The distance between the face of the transducer and the hydrophone tip was measured to be approximately 121.3 mm +/- 0.2 mm. This was verified as the time of flight of the signal was measured as 81.48 µS which equates to 121.37 mm using a speed of sound of 1489.6 ms^{-1} (calculated using formula detailed by Lubbers et al [20]).

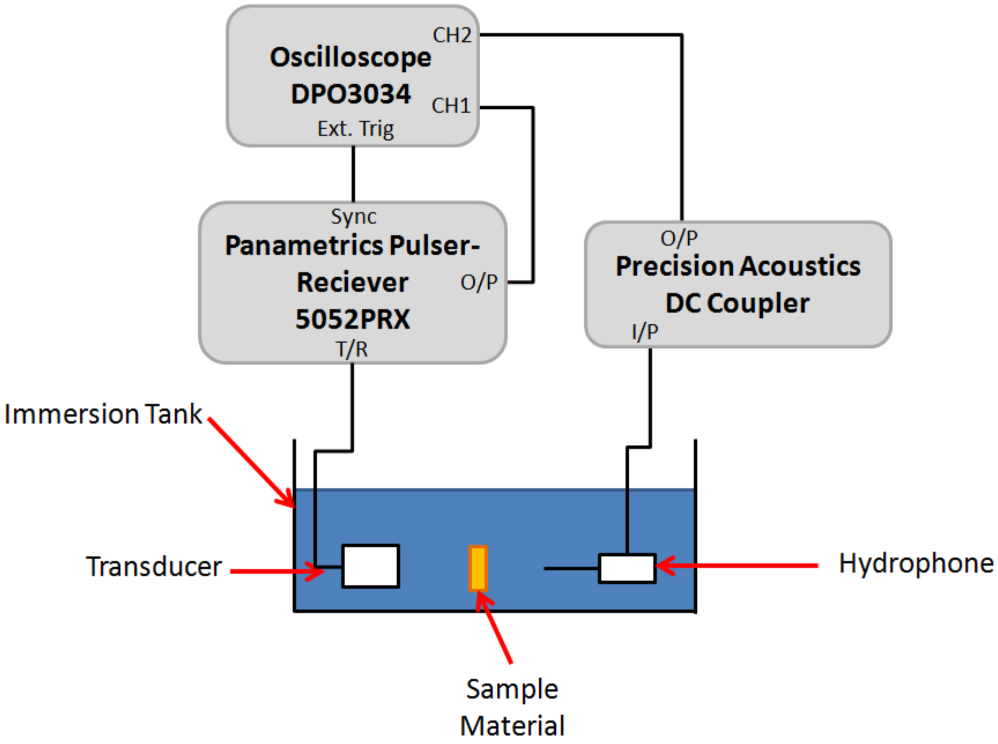

Figure 8.21 – Schematic diagram showing experimental setup used for testing of acoustic properties or a range of MSL compatible materials

Sample	Material	Thickness (mm)	Length (mm)	Width (mm)	Mass (g)	Density (Kg m^{-3})
A	R11 : 25um layers with ERM	1.76	9.92	9.93	0.204	1176.68
B	R11 : 25um layers with ERM	1.77	9.94	9.95	0.205	1171.04
C	R11 : 25um layers	1.74	10.00	9.97	0.205	1181.71
D	R11 : 25um layers	1.73	9.98	9.96	0.204	1186.30
E	R11 : 50um layers with ERM	1.77	10.02	10.01	0.204	1149.09
F	R11 : 50um layers with ERM	1.77	10.01	9.99	0.205	1158.19
G	R11 : 25um layers with ERM with Expancel	2.18	9.88	9.90	0.218	1022.37
H	R11 : 25um layers with ERM with pre-expamded Expancel	1.99	9.95	10.10	0.208	1040.08
I	3:1 of HDDA:DPPHA with 5%vol carbon black	0.97	9.47	9.70	0.096	1077.40
J	3:1 of HDDA:DPPHA with 5%vol carbon black	0.97	9.60	9.78	0.093	1021.18
K	1:2 of HDDA:DPPHA with 100%wt 30 um copper particles	1.04	10.15	10.01	0.185	1750.81
L	1:2 of HDDA:DPPHA with 100%wt 30 um copper particles	1.07	9.96	10.07	0.188	1751.80
M	1:2 of HDDA:DPPHA with 150%wt 30 um copper particles	0.68	9.79	9.95	0.142	2143.75
N	1:2 of HDDA:DPPHA with 150%wt 30 um copper particles	0.68	10.02	9.81	0.138	2064.59
O	1:2 of HDDA:DPPHA with 200%wt 30 um copper particles	0.51	9.77	9.97	0.132	2657.14
P	1:2 of HDDA:DPPHA with 200%wt 30 um copper particles	0.53	9.92	9.74	0.142	2772.95

Table 8.3 – Physical properties of material samples tested for their acoustic characteristics

Knowing the times of flight of the signal with and without a sample present, and the thickness of the sample, the speed of sound through the sample materials was calculated using Equation 8.21 - where (S_s) is the speed of sound through the sample material, (D_s) is the thickness of the sample, (S_w) is the speed of sound through the water, (T_0) is the time of flight of the signal without any sample present, and (T_{RX}) is the measure time of flight of the signal with the sample present.

$$S_s = \frac{D_s}{T_{RX} - \frac{T_0 S_w - D_s}{S_w}} \tag{8.21}$$

Using the calculated density (Table 8.3), along with the calculated speed of sound, the acoustic impedances of the materials were then calculated using Equation 8.3. Figure 8.22 show the measured results and acoustic impedance of the samples. The aluminium sheet used as a known sample to verify the integrity of the other results was calculated to have an acoustic impedance of 17.9x10^6 Kg m^{-2} s^{-1} which agrees with other sources [11].

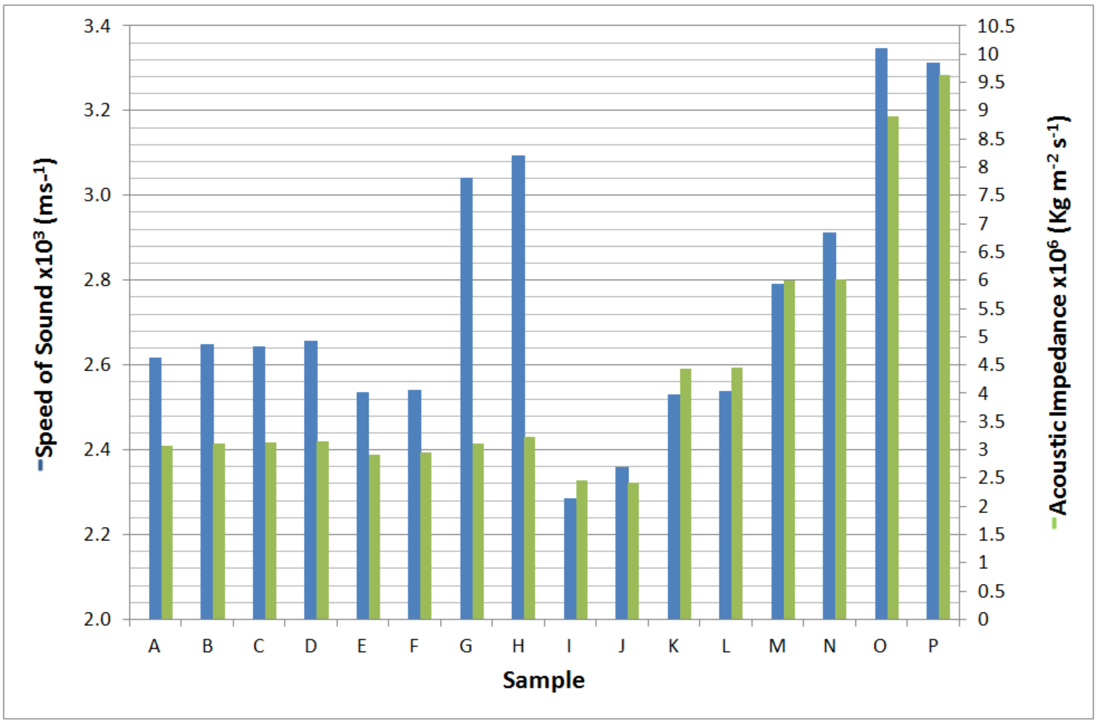

Figure 8.22 – Graph showing speed of sound and acoustic impedance for the sample MSL materials

The results indicate that the custom composite copper loaded materials exhibit a higher acoustic impedance than the standard commercial R11 material used to fabricate the focusing device. Indeed the observed trend with the copper composites is that the acoustic impedance approximately doubles with a doubling of the copper loading. The samples with 2:1 ratio by weight of copper loading to polymer show an acoustic impedance approximately three times greater than the R11 samples with 25 μm layers. This initially indicates that this material would more suitable for fabrication of the reflecting surfaces in the focusing device. Two other results of interest are that the samples fabricated using R11 exhibit different acoustic properties depending on the layer thickness used to fabricate the component – as can be seen when comparing samples A/B/C/D (R11 with 25 μm layers) with samples E/F (R11 with 50 μm layers). Additionally, it can be seen that the composite material with 5% carbon black loading exhibited noticeably lower acoustic impedance than the other samples.

Figure 8.23 shows the theoretical transmission percentages for the samples calculated using the measured acoustic impedances and Equation 8.3. Also shown is the measured % transmission based on the magnitude of the received signal with and without a sample present. It was not possible to record the measured % reflection due to the requirement of the accuracy required for alignment, however, the calculated reflection based on the acoustic impedance is presented in Table 8.4 below along with the calculated parameters.

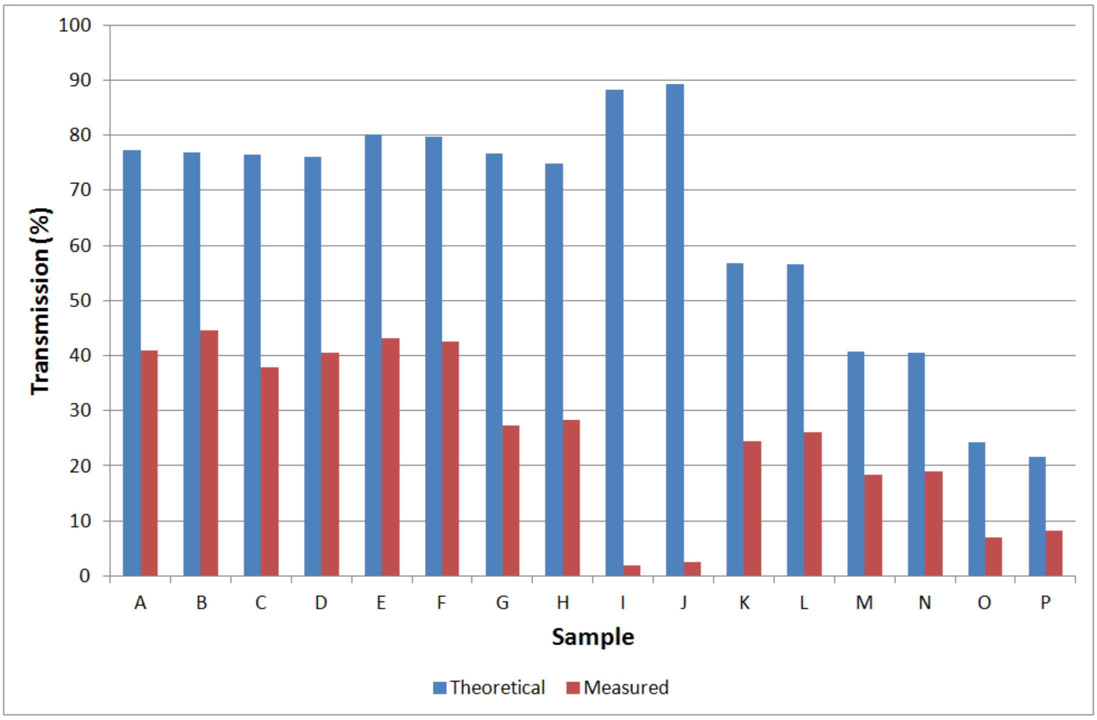

Figure 8.23 – Graph showing transmission percentages of sample materials

It can be seen that the amplitude of the signal received after being transmitted through the materials was consistently less than the theoretical values, in particular the carbon black composite samples (I & J) showed a difference of 86%. This difference can however, largely be accounted for by attenuation of the signal by means of absorption and scattering within the material. The attenuation of the signal through the materials can be described using Equation 8.22, where A is the measured amplitude, A_0 is the expected amplitude, l is the thickness of the material in meters, and α is the attenuation coefficient in nepers per meter (Np/m). Table 8.4 shows the calculated attenuation coefficients for each of the sample materials.

$$A = A_0 e^{-\alpha l} \tag{8.22}$$

Sample	Speed of Sound (ms^{-1})	Acoustic Impedance $*10^6$ ($Kg\ m^{-2}\ s^{-1}$)	Theoretical Reflection (%)	Theoretical Transmission (%)	Measured Transmission (%)	Attenuation ($Np\ m^{-1}$)
A	2617.00	3.08	12.1	77.3	40.9	361.21
B	2648.76	3.10	12.3	76.9	44.5	308.19
C	2643.98	3.12	12.6	76.5	38.0	402.58
D	2655.88	3.15	12.8	76.0	40.5	364.59
E	2534.95	2.91	10.5	80.2	43.2	349.70
F	2542.23	2.94	10.8	79.6	42.6	353.22
G	3042.65	3.11	12.4	76.7	27.3	474.35
H	3095.21	3.22	13.5	74.8	28.4	486.73
I	2286.76	2.46	6.1	88.2	2.0	3903.86
J	2359.06	2.41	5.6	89.2	2.5	3666.41
K	2529.34	4.43	25.7	56.8	24.4	810.55
L	2539.68	4.45	24.8	56.5	26.1	720.48
M	2792.63	5.99	36.2	40.7	18.3	1176.84
N	2912.23	6.01	36.3	40.5	19.0	1115.40
O	3347.03	8.89	50.8	24.2	6.9	2448.18
P	3313.94	9.63	57.6	21.6	8.2	1914.06

Table 8.4 – Measured acoustic properties from testing of a range of material samples

Due to the significantly larger reflection coefficients and attenuation of transmitted signal of the copper composite materials, the results suggest that fabricating the focusing device using a material with copper filler particles would produce improved signal intensity over the current R11 material due to its increased acoustic impedance. Additionally, the R11 samples suggest that while there is no observable difference acoustically between fabricating with or without ERM, fabricating with thinner layers (25 μm vs 50 μm) offers a marginal improvement in reflection (2%).

It is however felt that due to the difficulties associated with fabricating components using the copper composite with this material, the yield of attempting to fabricate entire components would be low. Instead, it is suggested that a multi-material approach is adopted whereby the bulk of the device's body is fabricated using a structural material (such as R11) and that only the key functional components (the reflection surfaces) are produced using the alternative material. It is felt that this approach would improve the functionality of the device while maintaining a desirable fabrication time and yield.

As tungsten is often used in the fabrication of commercial ultrasonic components by impregnating the particles in an epoxy resin [21] because of its high impedance, an attempt was made to utilise it as a further filler option. However, it was observed that once the particles had been added to the prepared photopolymer, droplets of the material failed to cure with exposure to the LED source of the custom fabrication system. Indeed, even using the post-curing unit (Ototflash 171, NK-Optik GmbH) only a thin skin of the material was cured, leaving the centre of the droplet as liquid. Although not proven by the author, it is believed that polymerisation is inhibited by absorption of the exposure light in the active region of the photoinitiator.

8.6 Conclusion

In this chapter the design and fabrication of a device for the focusing of ultrasound was discussed. The device was demonstrated to be able to focus a beam of ultrasound from a standard Panametrics immersion ultrasound transducer with a 12.5 mm plane wave output down to a spot of ~580 µm in diameter. The device was successfully used to perform a high resolution scan using the focused beam produced. When operating in pulse-echo mode, responses resulting from multiple reflections occurring within the device (due to the reflecting surfaces being comprised of a series of steps) were observed as a noise component of the received signal. However, they were easily identifiable and were windowed out during post processing of the data.

In addition to the multiple reflections, the acoustic properties of the R11 photopolymer used also contributed to the losses in signal amplitude attenuated through unwanted transmission through the material. Further investigation of the acoustic properties of alternative MSL compatible materials revealed that by using other composite materials the acoustic properties of the material could be altered. To potentially improve this class of device, reflection coefficients approaching 60% were observed using a 200% wt copper loaded composite material, a 46% increase on that seen with the commercial material used to fabricate the test device. However, it is felt that the fabrication technique would require further investigation in order to improve the reliability of the process for alternative materials.

The work undertaken has shown that fabricating parts for ultrasound applications with immersion transducers using existing MSL technology is feasible. The use of such a fabrication method has major advantages for NDT applications which have specific focussing requirements. The technology can also be used in the development of new NDT techniques which may require unusual or complex geometries. Due to the speed, ease and cost to produce components using MSL, the user is provided with the scope to tailor designs to specific applications and as such, fabricate a new design for each different application if required. Care must sill however be taken to consider the limitations of the technique such as restricted use of support structures that could compromise the reflection surfaces and that the continuous curve profile of the reflection surfaces will consist of a number of finite steps due to the nature of the fabrication process. It is suggested that further work should focus on materials with higher reflection coefficients and a multi material fabrication process that enables a higher z-axis resolution.

8.7 References

[1] G. Spositoa, C. Warda,P. Cawleya, P.B. Nagya, C. Scruby, A review of non-destructive techniques for the detection of creep damage in power plant steels, NDT & E International 43 (2010) 555–567

[2] T. Adachia, Y. Kondob, A. Yamajia, S-H. Yangc, I-Y. Yang, Nondestructive evaluation of micro-cracks in a ceramic ferrule by resonant ultrasound spectroscopy, NDT & E International8 (2005) 548–553

[3] A.G. Bashford, D.A. Hutchins, Non-destructive evaluation of green-state ceramics using micromachined air-coupled capacitance transducers, Ultrasonics 36 (1998) 121–126

[4] A.J. Hayman, P.D. Hanstead, Developments in Direct Ultrasonic Visualisation of Defects, Ultrasonics 17 (1979) 105-112

[5] D.W. Schindel, A.G. Bashford, D.A. Hutchins, Focussing of ultrasonic waves in air using a micromachined Fresnel zone-plate, Ultrasonics, 35 (1997) 275-285

[6] K. Kawashima, M. Murase, R. Yamada, M. Matsushima, M. Uematsu, F. Fujita, Nonlinear ultrasonic imaging of imperfectly bonded interfaces, Ultrasonics (2006) 1329-1333

[7] M. Spies, Ultrasonic field modelling for immersed components using Gaussian beam superposition, Ultrasonics, 46 (2007) 138-147

[8] R.J. Bradley, Capacitive Ultrasonic Transducers Fabricated Using Microstereolithography, PHD Thesis (2007)

[9] D.R. Billson, C.P. Purssell, S.J. Leigh, D.A. Hutchins, Rapid Prototyping technologies for ultrasonic beam focussing in NDE, 2011 IEEE International Ultrasonics Symposium Proceedings 2472-2474

[10] C.P. Purssell, S.J. Leigh, M. Thomas, D.R. Billson, D.A. Hutchins, Microstereolithography for Fabrication of Devices for Ultrasonic NDE Applications, in submission to Ultrasonics

[11] J.C. Drury, Ultrasonics Part 2. Properties of sound waves, Insight 46 (2004) 762-764

[12] T.J. Magner, J. Zaniewski, S. Rice, C. Fleetwood, Fabrication and testing of off-axis parabolic mirrors, Optics & Laser Technology 19 (1987) 91–96

[13] H.G.J Rutten, M.A.M. Van Venrooij, Telescope Optics: Evaluation and Design, Willmann-Bell Inc, Richmond Virginia (USA) (1988)

[14] O.S. Heavens, R.W. Ditchburn, Insight into Optics (1991) Wiley

[15] A. Fresnel, On the Diffraction of Light, Annales de Chimie et de Physique 1 (1816) 239-281

[16] G. Kossoff, Analysis of Focusing Action of Spherically Curved Transducers, Ultrasound in Medicine & Biology 4 (1979) 359-365

[17] I.N. Ermolov, A.Kh. Vopilkin, V.G. Badalyan, Calculations in Ultrasonic Testing, (Echo+, Moscow, 2000)

[18] E.A Ginzel, Near Field and Focusing Considerations with Wedges, Materials Research Institute, Canada, http://www.ndt.net/article/ndtnet/2009/ginzel2.pdf, last accessed: 24/01/2012

[19] Y.N. Makov, V. Espinosa, V. J. Sánchez-Morcillo, J. Ramis, J. Cruañes, and F. Camarena Departament, Strong on-axis focal shift and its nonlinear variation in low-Fresnel-number ultrasound beams, Journal of the Acoustical Society of America 119 (2006) 3618-3624

[20] J. Lubbers, R. Graaff, A simple and accurate formula for the sound velocity in water, Ultrasound in Medicine & Biology 24 (1998) 1065-1068

[21] W.R. Hendee, E.R. Ritenour, Medical Imaging Physics (4th Edition), Wiley-Liss Inc (2002)

Chapter 9

9 Conclusions and Further Work

Most methods of fabricating devices that contain functional micro-structures are still heavily based upon silicon fabrication processes. While such processes are suited to high volume, mass manufacture applications, the processes, turn around time and costs involved often make it prohibitive for lower volumes or groups without the equipment needed. Indeed, the structures that can be produced are also generally only pseudo 3D (essentially extruded 2D); true 3D complex structures are not viable with traditional techniques. Thus, there is a significant need for an alternative method that would allow small volumes batches of devices to be produced, cost effectively, have access to all three dimensions, without the requirement for extensive facilities and equipment.

Within the past 25 years, additive layer technologies have progressed from a concept, to a commonly used method of rapid prototyping for the assessment of aesthetics, form and fit of components. The technology has now reached a stage where it can be considered as an alternative method of manufacture, rather than just prototyping. Stereolithography (SL) and microstereolithography (MSL) in particular shows promise in this area with regard to micro-structures. While the advances in techniques and equipment mean that it is now relatively simple to fabricate mechanical components and structures on the micron scale [1], its uses beyond this are still somewhat limited. Some research has focused on using the technology for bio-compatible ceramics composites for bone scaffold applications. However, there has been little research in the area of functional materials beyond this, other than a few groups exploring the direct fabrication of piezoelectric films [2, 3].

The objective of this thesis was therefore to examine the further potentials of microstereolithography as an alternative method of fabrication for functional devices as an affordable, low volume alternative to traditional fabrication techniques. To this end, a number of new materials, techniques and applications were explored to understand the limits, in terms of equipment and materials, which can be applied to this process. This chapter first summarises the key findings and conclusions drawn from the conducted work. This is then followed by a number of suggestions of areas for further research.

9.1 Custom MSL System Design

In exploring the possibilities of MSL, initial work investigated existing methods, techniques and materials associated with microstereolithography. From this review it was clear that projection based MSL presented a number of favourable advantages over the traditional laser techniques. Such advantages included its ability to rapidly create layers due to the parallel exposure method, the simplicity of the machine operation (not having to align and focus lasers), and its increasing popularity as the main method of exposure in commercial systems – meaning that work conducted using this technology would be more applicable to future systems. It was also concluded that using a constrained surface approach would be ideal due its compatibility with the parallel projection method and not requiring large volumes of material (unlike free surface techniques) and are therefore easier to use as a development platform.

During the early stages of the work, it was apparent that the commercial systems available were not ideally suited for conducting development experiments. For example, it was often required to temporarily pause the fabrication process or alter the fabrication settings during the build, to ensure that the optimum setting could be established. As such, two custom MSL systems were designed and manufactured. Developed as part of the project, they enabled far greater control over the fabrication process to produce the optimum results. The systems were designed to have small build envelopes (a maximum size of 30 mm x 22.5 mm) so that small volumes of material could be used for testing - the minimum material volume for successful operation was found to be ~0.5 ml.

The systems employed LED technology as a means of photopolymisation. This investigation was driven by a number of factors, the main being that LEDs have a much narrower bandwidth that traditional lamp technology, which, when matched with an appropriate photoinitiator can provide increased control of the curing process. This is due to there being no fluctuating sideband wavelengths which are not uncommon in lamp exposure methods. One of the other key advantages of LED technology is that it has a much longer lifespan than traditional lamp technology (tens of thousands of hours compared to a few thousand at most for a typical lamp). Therefore, not only does LED technology prove to be cheaper in terms of initial cost, and power consumption, but it is also more cost effective due to extended lifespan. One of the initial concerns with using LED technology was whether the power output was sufficient to ensure photopolymerisation of the resin material occurred. However, during the course of the work, it was concluded it was sufficient and therefore could be considered a viable replacement. It should however be noted that due to the decreased intensity, compared to traditional bulbs, the required exposure time for commercial materials was increased.

One of the main advantages of the ALM technologies, over silicon based techniques, is that the fabrication process does not require human interaction once the process has started. However, it was acknowledged that to emulate the abilities of silicon processes to produce components with different functional layers, a similar technique was needed for MSL. Therefore, a second was designed and assembled for the purpose of fabricating components with up to 3 different materials. The design incorporated a simple carriage system that was automatically swapped depending on the required material – a method requiring little variation from the standard setup that could easily be implemented in a commercial system. The system shows significant time saving advantages over simply manually swapping materials, but highlighted potential issues with washing of the partially built component in between material changes (to prevent contamination). It is therefore suggested that this would be a suitable area for further investigation.

9.2 Materials

MSL technologies are already currently capable of fabricating components on scale necessary to create functional micro-devices. However, it is at present, severely limited in this area due to the current lack of compatible photocurable, functional materials necessary to produce such components.

9.2.1 Magnetic Material

Investigations were carried out into the development of a novel photocurable polymer material that exhibits ferromagnetic properties. A review of similar existing materials showed that researchers have previously synthesised organic polymer materials that could exhibit both ferromagnetic an anti-ferromagnetic properties [4]. However, such materials would not be compatible with the photopolymerisation process. Therefore, a composite material (consisting of filler particles being mixed into a base resin to form a suspension) approach was taken due to previous work showing successful use of similar composites using ceramics.

A number of filler materials were initially investigated including neodymium-iron-boron ($Nd_2Fe_{14}B$), aluminium-nickel-cobalt (AlNiCo) and magnetite (Fe_3O_4). The initial experiments highlighted issues that prevented the neodymium-iron-boron and aluminium-nickel-cobalt particles from being usable, so focus shifted to utilising the ferromagnetic magnetite nanoparticles. A suitable base resin material was found to be a 1:2 ratio of HDEDA to DPPHA, using 5% photoinitiator (by weight). A series of experiments showed that filler percentages of 35% (by weight) were suitable for a components with a low number of layers (up to ~5 using 25 μm layer thickness), however to maintain consistency in the material, a filler lower filler percentage of 25% was required for thicker parts. It was also observed that the duration of the stir time was critical for achieving a usable mix – 10 minutes being optimal.

A 100 µm test component was fabricated and subjected to an external magnetic field, causing it to deflect. The test highlighted that the material is prone to fatigue when used to fabricate thin components. The same design was fabricated using R11 and some blank material (using the same base material but no filler) but the same fatigue effects were not observed – indicating that the inclusion of the filler particles significantly altered the mechanical properties.

Mechanical testing of the material was performed on cube samples. The yield strength, when a compression force was applied through fabricate layers, was measured to be 164 MPa, which was comparable to that of R11 (200 MPa). However, when the force was applied across the layer planes, a yield strength of 47 MPa was recorded (compared to R11 at 164 MPa). Similar results were obtained when the material was tested in a tensile mode. Here, the Young's modulus of the material was measured to be 279 MPa with a tensile strength of 14 MPa, which was comparable to 354 MPa and 37 MPa respectively measured for R11. Testing of components with 50 µm layers showed a significant decrease in mechanical performance. In these cases, the Young's modulus and Tensile strength were observed to be only 83 MPa and 6 MPa respectively.

Analysis was conducted to assess the magnetic remanence of a typical component after being magnetised using a Neodymium permanent (B_r of 12000 Gauss) with a magnet as a means to ascertain what could be expected in a typical laboratory environment using the material. A remanence of 142 Gauss was observed in a 25 mm^3 cube after being poled. An exponential decay of the field was observed over a period of ~7 days over which time the magnitude of the field had reduced by 17.8%. Despite this drop, the presence of the material was still easily detectable using circuit containing an AMR (anisotropic magnetoresistive) sensor. This suggested that, in its current form, the material would not be suitable for the sensing displacement in long term applications (due to the decay of the field) but suitable for assessing relative displacement over shorter periods.

Exemplar microfluidic flow sensing devices were fabricated using the magnetite composite, to demonstrate the use of the material in a practical application. The material was used to fabricate the rotating impeller in the sensor. An AMR sensor was again used to detect the magnetic fluctuations caused by the rotation of the impeller. The first design was fabricated with an 8 mm diameter impeller housed inside a case fabricated using commercial R11. The device showed a proportional frequency of rotation between air flow rates of 2.5 l/min up to 5.5 l/min, below this value the response was found to be non linear. The device was then redesigned and optimised to have dimensions compatible with microfluidic devices previously created with the research group – of similar size to a lab-on-chip type device. The device used a 3.5 mm diameter impeller and demonstrated a proportional response over the entire working range (between 5 ml/min and 70 ml/min) when tested with liquid. The successful testing and characterisation of these devices illustrates that there is now a viable means to rapidly fabricate micro fluidic flow sensing devices using MSL technology.

9.2.2 Conductive Material

Investigations were carried out into creating a conductive photocurable material with the aim of using MSL to directly fabricate devices, sensors and embedded electrical interfaces (given sufficiently high conductivity). Initial work explored the use of metals for this purpose. However, the desired layer thickness (25 μm) restricted particle size, i.e. requiring particle and/or aggregate size to be sufficiently less than the target layer thickness. This resulted in the copper particles exhibiting non-conduction, which other research suggests is due to oxide layers forming on the surface of the particles. Nickel nanoparticles were also explored but showed excessive aggregation that caused failures when fabricating components.

Carbon nanoparticles were found to be compatible with the photopolymer material and did not exhibit the issues seen with the metal fillers. However, due to its lower conductivity than would be expected from a metal conductor, the fabricated components showed a measureable resistivity. While at first it would appear that this is not ideal, it is believed that such properties would be useful in the fabrication of sensing devices such as strain sensors. This is due to the observed resistance being dependent on the network of conductive paths through the matrix. Under strain, paths would be temporarily broken, increasing resistance. A range of samples was fabricated using various loading levels between 1.25% and 10% (by volume) such that the effect of filler level on component resistivity and mechanical properties could be assessed. It was discovered that a loading of 1.25% was below the percolation limit and therefore no measureable conductivity was observed. When factoring in the mechanical results, the optimum loading level is proposed to be 5% for standalone components. A loading higher that this was found to produce very fragile components.

By replacing the monomer in the material with a PEG monomer, it was discovered that the conductive composite photopolymer could also be effectively utilised for the direct fabrication of conductometric vapour sensors. Two geometries of sensors were fabricated in order to characterise their response to a range of standard vapours: ethanol, toluene, ethyl acetate and propan-2-ol.

The sensors operated on the principle of the base polymer swelling when exposed to a sample vapour, hence temporarily breaking conductive paths in the sensors and raising the resistance. The devices showed a response to each of the vapours, however, an increased sensitivity was observed towards toluene vapours – indicating a degree of selectivity. The devices were also characterised for their responses to variations in background humidity and temperature. The sensors were observed to have a linear response to both of these environmental factors up to 50% RH and 70°C – conditions which are beyond the typical working range of such sensors. Contrary to prediction, the sensors with a slotted geometry showed smaller responses than those fabricated with solid layers, although it is unclear as to why this is the case.

It is believe that this method of vapour sensor fabrication shows particular promise as an alternative to traditional methods of spray deposition due to the ease in achieving repeatable device geometries without the requirement for the use of deposition masks.

9.3 MSL for Ultrasonic NDE

In an effort to explore the range of applications for MSL, investigations were also carried out into using the technology for the fabrication of beam forming components for ultrasonic NDE applications. Although not typically considered to be micro-devices, the accuracy involved in the shaping of ultrasonic components is comparable to that required for micro-structures. As such, a beam focussing device was fabricated for this purpose. The device, designed to mount directly onto the end of a commercial, unfocused immersion ultrasound transducer was tested both for the accuracy in reproducing the focal point at the desired distance, and for the quality of the focus achieved.

The results observed show great promise for this application of MSL as the variation in focal point between the calculated design and fabricated device differed by no more than 2%. Additionally, with the focal spot measured to be ~580 μm in diameter (FWHM), the device was successfully used to image both sides of a 1p coin such that the features were clearly distinguishable.

Although the focusing capabilities were found to be acceptable for non-destructive imaging applications, one potential issue observed was the attenuation of the signal caused by unwanted transmission of the signal into the polymer. This was thought to be due to the R11 material used having a low reflection coefficient in water. A range of samples fabricated from different materials were analysed for their acoustic properties. The results confirmed that the commercial material initially used for fabrication had an acoustic impedance of $3.08\text{x}10^{6}$ Kg m^{-2} s^{-1} with a reflection coefficient of 0.12 when used in water. By contrast, it was also demonstrated that for ultrasonic immersion applications a composite material with a copper filler provided a significant increase in reflection performance. Indeed a loading of 200% (by weight) of copper particles increased reflection to 57%.

9.4 Conclusions

The research conducted has demonstrated further potential applications of microstereolithography in the field of functional micro-structure and device manufacture. It has shown that, given the necessary materials, microstereolithography presents an affordable alternative to traditional silicon processing techniques (with the added benefit of being able to fabricate true 3D micro structures) when there is a requirement for low volume manufacture and/or rapid turnaround of functional micro-components. This has been achieved through the development of alternative novel materials along with the fabrication of exemplar components using these materials.

For the first time, it has been shown that microstereolithography can be used for the direct manufacture of functional flow and gas sensors. Additionally, it has been demonstrated that microstereolithography can be used for the fabrication of ultrasonic beam forming devices, and that the use of different materials can be used to tune their acoustic properties.

9.5 Further Work

While this work has presented a number of new materials and applications for MSL, it is felt that there are a number of areas where the further investigation would lead to improvements in the technique:

- Further research should be carried out into the use of LED technology as an exposure source for parallel projection MSL technology. The main area of investigation would be in the area of dynamically adjusting the exposure intensity for different layers of the component. It is believed that by characterising the curing response of materials relative to combinations of exposure levels and intensities, fabrication speed could be increased by using higher intensities on areas of the component that don't have fine features.
- It is believed that further research into methods of washing of components mid-build on the multi-material fabrication system discussed in Chapter 3 would lead to improved results. While the current method of washing (agitating the component the bath of solvent) was shown to work, there were still some signs of cross contamination. It is suggested that a jetted washing method may provide improved results
- Further research should be carried out into the exploration of conductive materials with the MSL process. Carbon composites provide a good basis for the direct fabrication of sensor devices, however, the filler level required to create conductive tracks comparable to those on PCBs would make the material unusable. It is felt that using silver particles could provide the solution, but the cost of the resulting material may be significant. As an alternative approach, a hybrid approach may be considered where interfacing track could be printed mid-process using inkjet technology [5, 6].
- One of the key areas for development in MSL technology is the need for a soluble support material. Such a material would enable the fabrication of true fabrication multi-material mechanical components using MSL. Currently, similar materials are available for other ALM technologies, however, MSL still relies on support structures that require manual, mechanical removal.

- It is believe that greater selectivity could be achieved with MSL fabricated vapour sensing devices by developing a range of photocurable materials with different base monomers. Additionally, it is believed that the use of other particle additives combined within the composite material could increase response selectivity.
- Finally, it is believed that a number of the materials and principles presented could be transferable over to other AML technologies. Indeed, during this research, preliminary work has shown that it is possible to utilise carbon and magnetite composite thermoplastics in fused deposition modelling systems. Although the resolution is significantly poorer than that of MSL, it is felt that FDM may provide a solution to the rapid manufacture of macro sized functional components.

9.6 References

[1] H-W. Kang, I.H. Lee, D-W. Cho, Development of a micro-bellows actuator using micro-stereolithography technology, Microelectronic Engineering 83 (2006) 1201–1204

[2] X.N. Jiang, C. Sun, X. Zhang, B. Xub, Y.H. Ye, Microstereolithography of lead zirconate titanate thick film on silicon substrate, Sensors and Actuators 87 (2000) 72–77

[3] J.H Jang, S. Wang, S.M. Pilgrim, W.A. Schulze, Preparation and characterization of barium titanate suspensions for stereolithography, Journal of the American Ceramic Society 83 (2000) 1804-1806

[4] N. A. Zaidi, S. R. Giblin, I. Terry, A. P. Minkman, Room temperature magnetic order in an organic magnet derived from polyaniline, Polymer 45 (2004) 5683-5689

[5] Printed Electronics Limited (UK), [online] available from: www.printedelectronics.co.uk/AboutUs.asp (last accessed: 06/06/2012)

[6] Dimatix Inkjet Printheads, [online] available from: www.fujifilmusa.com/products/industrial_inkjet_printheads/index.html (last accessed: 06/06/2012)

Appendix A

A Multi-Material Controller Schematic

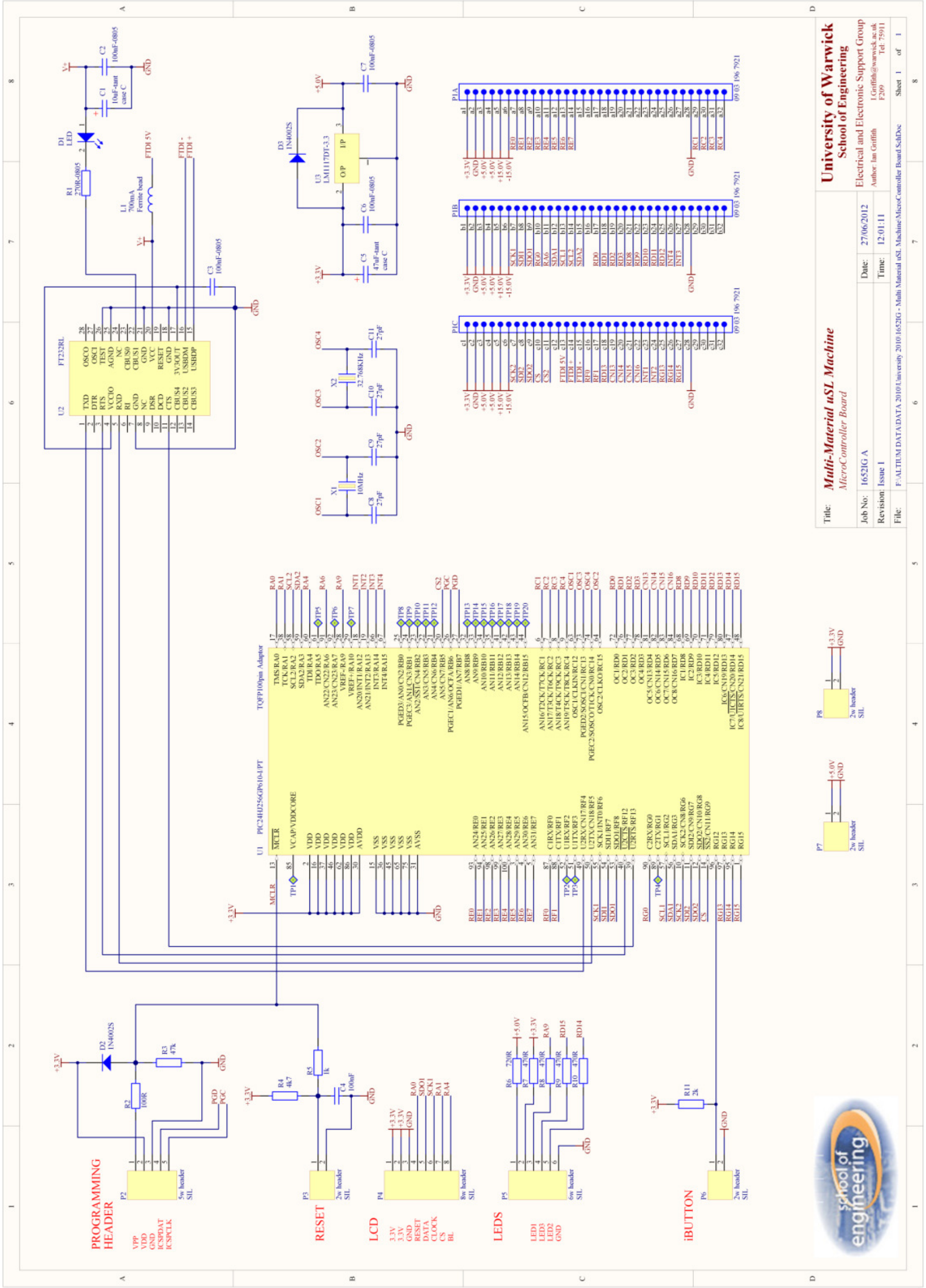

Figure A.1 – Schematic diagram of multi-material system controller

Appendix B

B Vapour Sensor Humidity Responses

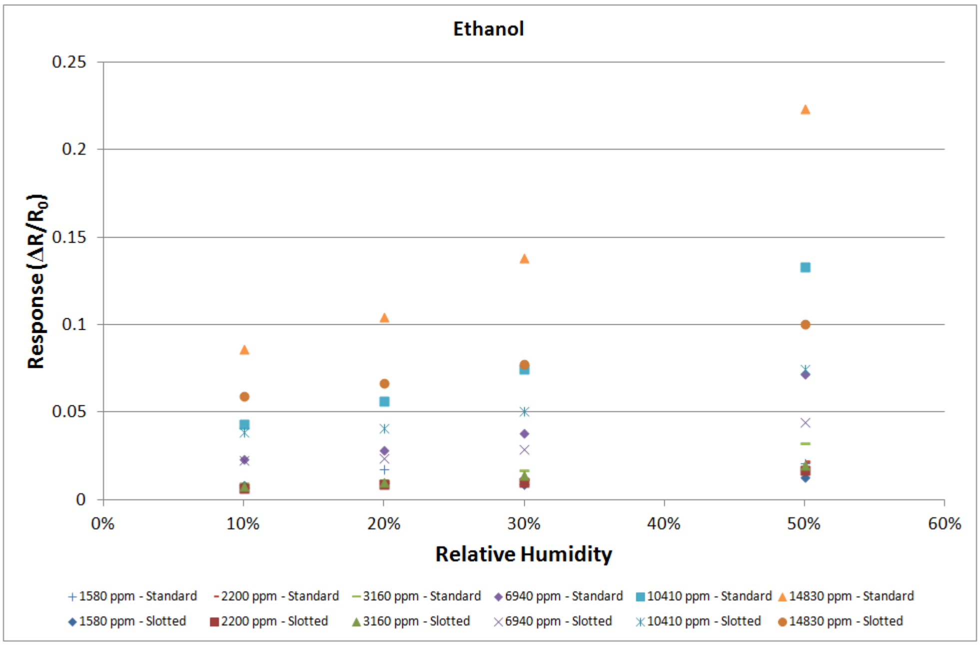

Figure B.1 – ΔR/R0 results from testing of selection of standard and slotted devices with sample vapours of ethanol at 1580, 2200, 3160, 10140, and 14830 ppm with 10%, 20% 30% and 50% relative humidity

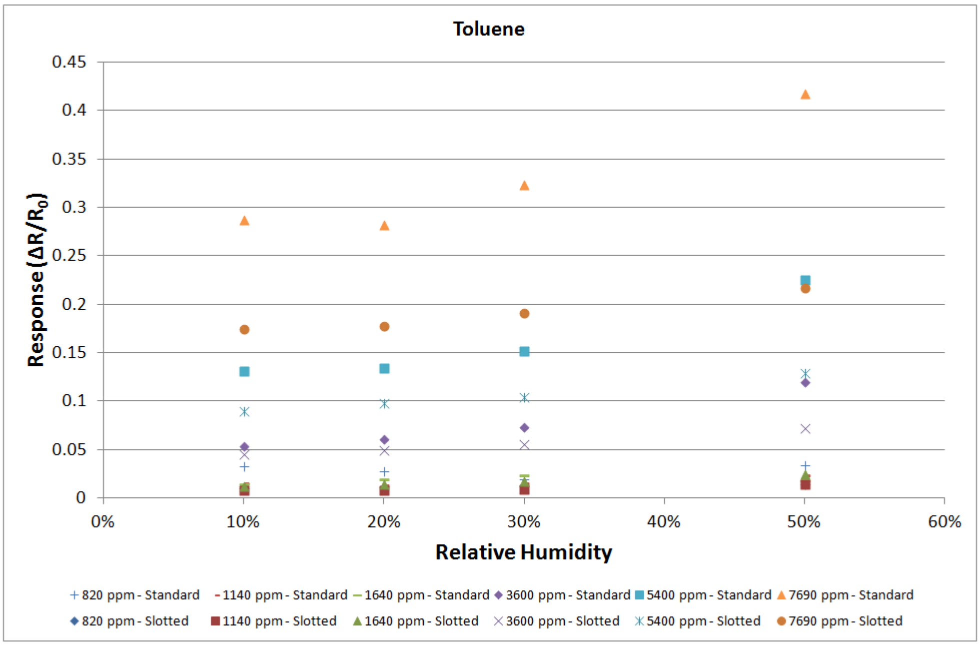

Figure B.2 – ΔR/R0 results from testing of selection of standard and slotted devices with sample vapours of toluene at 802, 1140, 1640, 3600, 5400, and 7690 ppm with 10%, 20% 30% and 50% relative humidity

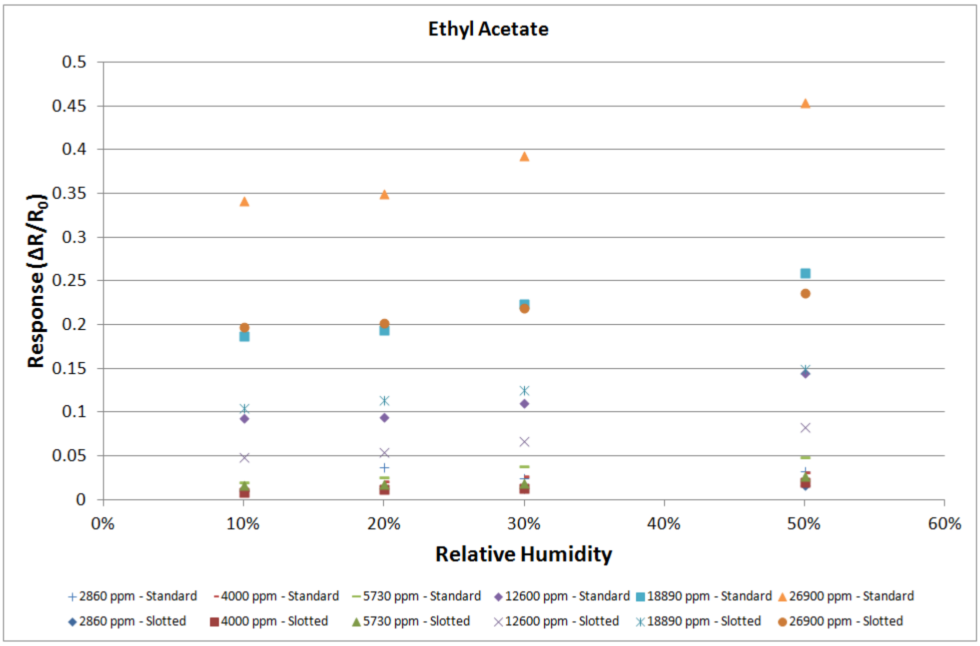

Figure B.3 – ΔR/R0 results from testing of selection of standard and slotted devices with sample vapours of ethyl acetate at 2860, 4000, 5730, 12600, 18890, and 26900 ppm with 10%, 20% 30% and 50% relative humidity

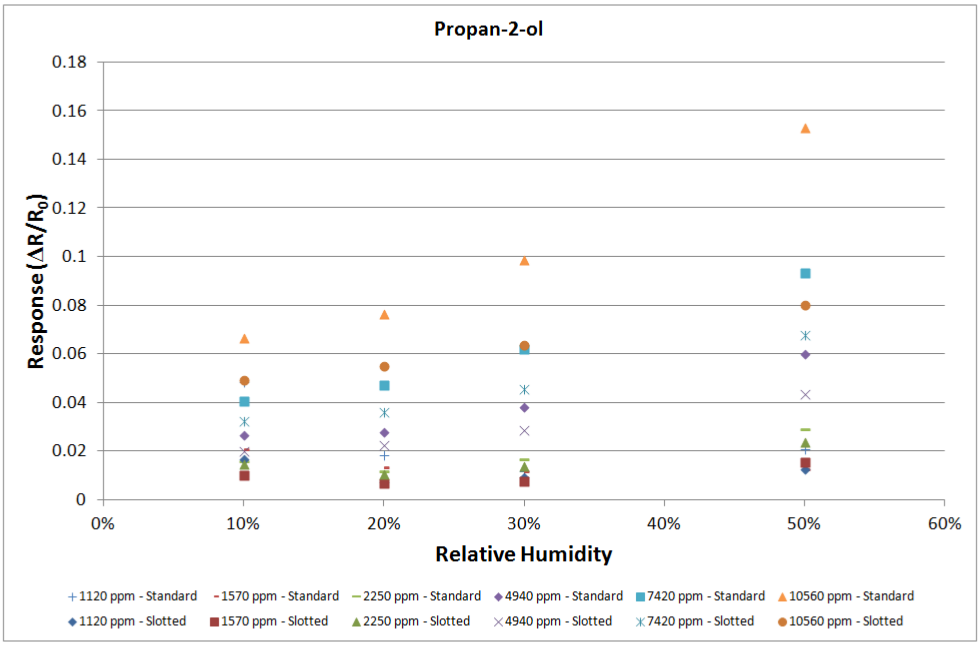

Figure B.4 – ΔR/R0 results from testing of selection of standard and slotted devices with sample vapours of propan-2ol at 1120, 1570, 2250, 4940, 7420, and 10560 ppm with 10%, 20% 30% and 50% relative humidity